Non-intrusive CdSe-based quantum dots for sensing pressure and temperature in lubricated contacts

Tarek Seoudi

N°d'ordre NNT : 2020LYSEI009

THESE de DOCTORAT DE L'UNIVERSITE DE LYON
opérée au sein de
L'INSA de LYON

Ecole Doctorale N° 162
Mécanique, Energétique, Génie civil, Acoustique (MEGA)

Spécialité/discipline de doctorat :
Mécanique

Soutenue publiquement le 20/02/2020, par :
Tarek Seoudi

Non-intrusive CdSe-based quantum dots for sensing pressure and temperature in lubricated contacts

Devant le jury composé de :

DWYER-JOYCE, Robert	Professeur (University of Sheffield)	Examinateur
HARTL, Martin	Professeur (University of Brno)	Rapporteur
SAN-MIGUEL, Alfonso	Professeur (Université Claude Bernard Lyon 1)	Examinateur
WONG, Janet	Senior lecturer (Imperial College London)	Rapporteur
PHILIPPON, David	Maître de Conférences (INSA-Lyon)	Co-directeur
VERGNE, Philippe	Directeur de Recherche CNRS (INSA-Lyon)	Directeur
MONDELIN, Alexandre	Development Engineer (SKF Aerospace)	Invité
FILLOT, Nicolas	Maître de Conférences (INSA-Lyon)	Invité

Département FEDORA – INSA Lyon - Ecoles Doctorales – Quinquennal 2016-2020

SIGLE	ECOLE DOCTORALE	NOM ET COORDONNEES DU RESPONSABLE
CHIMIE	**CHIMIE DE LYON** **http://www.edchimie-lyon.fr** Sec. : Renée EL MELHEM Bât. Blaise PASCAL, 3e étage **secretariat@edchimie-lyon.fr** INSA : R. GOURDON	M. Stéphane DANIELE Institut de recherches sur la catalyse et l'environnement de Lyon IRCELYON-UMR 5256 Équipe CDFA 2 Avenue Albert EINSTEIN 69 626 Villeurbanne CEDEX directeur@edchimie-lyon.fr
E.E.A.	**ÉLECTRONIQUE, ÉLECTROTECHNIQUE, AUTOMATIQUE** **http://edeea.ec-lyon.fr** Sec. : M.C. HAVGOUDOUKIAN **ecole-doctorale.eea@ec-lyon.fr**	M. Gérard SCORLETTI École Centrale de Lyon 36 Avenue Guy DE COLLONGUE 69 134 Écully Tél : 04.72.18.60.97 Fax 04.78.43.37.17 **gerard.scorletti@ec-lyon.fr**
E2M2	**ÉVOLUTION, ÉCOSYSTÈME, MICROBIOLOGIE, MODÉLISATION** **http://e2m2.universite-lyon.fr** Sec. : Sylvie ROBERJOT Bât. Atrium, UCB Lyon 1 Tél : 04.72.44.83.62 INSA : H. CHARLES **secretariat.e2m2@univ-lyon1.fr**	M. Philippe NORMAND UMR 5557 Lab. d'Ecologie Microbienne Université Claude Bernard Lyon 1 Bâtiment Mendel 43, boulevard du 11 Novembre 1918 69 622 Villeurbanne CEDEX **philippe.normand@univ-lyon1.fr**
EDISS	**INTERDISCIPLINAIRE SCIENCES-SANTÉ** **http://www.ediss-lyon.fr** Sec. : Sylvie ROBERJOT Bât. Atrium, UCB Lyon 1 Tél : 04.72.44.83.62 INSA : M. LAGARDE **secretariat.ediss@univ-lyon1.fr**	Mme Sylvie RICARD-BLUM Institut de Chimie et Biochimie Moléculaires et Supramoléculaires (ICBMS) - UMR 5246 CNRS - Université Lyon 1 Bâtiment Curien - 3ème étage Nord 43 Boulevard du 11 novembre 1918 69622 Villeurbanne Cedex Tel : +33(0)4 72 44 82 32 **sylvie.ricard-blum@univ-lyon1.fr**
INFOMATHS	**INFORMATIQUE ET MATHÉMATIQUES** **http://edinfomaths.universite-lyon.fr** Sec. : Renée EL MELHEM Bât. Blaise PASCAL, 3e étage Tél : 04.72.43.80.46 **infomaths@univ-lyon1.fr**	M. Hamamache KHEDDOUCI Bât. Nautibus 43, Boulevard du 11 novembre 1918 69 622 Villeurbanne Cedex France Tel : 04.72.44.83.69 **hamamache.kheddouci@univ-lyon1.fr**
Matériaux	**MATÉRIAUX DE LYON** **http://ed34.universite-lyon.fr** Sec. : Stéphanie CAUVIN Tél : 04.72.43.71.70 Bât. Direction **ed.materiaux@insa-lyon.fr**	M. Jean-Yves BUFFIÈRE INSA de Lyon MATEIS - Bât. Saint-Exupéry 7 Avenue Jean CAPELLE 69 621 Villeurbanne CEDEX Tél : 04.72.43.71.70 Fax : 04.72.43.85.28 **jean-yves.buffiere@insa-lyon.fr**
MEGA	**MÉCANIQUE, ÉNERGÉTIQUE, GÉNIE CIVIL, ACOUSTIQUE** **http://edmega.universite-lyon.fr** Sec. : Stéphanie CAUVIN Tél : 04.72.43.71.70 Bât. Direction **mega@insa-lyon.fr**	M. Jocelyn BONJOUR INSA de Lyon Laboratoire CETHIL Bâtiment Sadi-Carnot 9, rue de la Physique 69 621 Villeurbanne CEDEX **jocelyn.bonjour@insa-lyon.fr**
ScSo	**ScSo*** **http://ed483.univ-lyon2.fr** Sec. : Véronique GUICHARD INSA : J.Y. TOUSSAINT Tél : 04.78.69.72.76 **veronique.cervantes@univ-lyon2.fr**	M. Christian MONTES Université Lyon 2 86 Rue Pasteur 69 365 Lyon CEDEX 07 **christian.montes@univ-lyon2.fr**

*ScSo : Histoire, Géographie, Aménagement, Urbanisme, Archéologie, Science politique, Sociologie, Anthropologie

Non-intrusive CdSe-based quantum dots for sensing pressure and temperature in lubricated contacts

Abstract
This thesis is dedicated to the measurement of local pressure and temperature and to compare the heat generation in all-steel and silicon nitride-steel (hybrid) elastohydrodynamic (EHD) contacts. The ultimate goal of this work is to develop a new non-intrusive *in situ* technique, exploiting the sensitivity of the photoluminescence (PL) of CdSe/CdS/ZnS quantum dots (QDs) to pressure and temperature. Dispersible in small concentration in lubricants, it is shown that the QDs doesn't modify the rheological behavior of the carrier fluid and that shearing is not perturbative to the QDs PL response. The calibration of QDs in the suspension confirms the QDs PL dependence on temperature and pressure. The *in situ* measurements were conducted in EHD contacts using a ball-on-disc test rig. Comparisons between pressure and temperature measurements and predictions, using an in–house finite element thermal EHD model, showed a good agreement which demonstrates the feasibility of the proposed methodology. The effects of sliding and normal loading on pressure, temperature and heat generation are indicated. The effect of the thermal properties of the solid materials is underlined and the partition of the generated heat between the contacting solids is investigated. The energy equilibrium between the mechanical energy and the internal thermal energy generated by compression and shearing is demonstrated by comparing experimental power losses and numerical heat generation, in steel-steel and hybrid contacts.

Keywords: Elastohydrodynamic lubrication, hybrid contacts, *in situ* measurement, photoluminescence, quantum dots, temperature & pressure sensing, power losses and heat generation

Boîtes quantiques non-intrusives à base de CdSe pour la mesure de la pression et de la température dans des contacts lubrifiés

Résumé
Cette thèse est dédiée à la mesure des pressions et des températures locales et à la comparaison de la génération de chaleur dans les contacts élastohydrodynamiques (EHD) de type tout acier et hybride (nitrure de silicium-acier). Le but ultime de ce travail est de développer une nouvelle technique *in situ* non-intrusive, exploitant la sensibilité de la photoluminescence (PL) des boîtes quantiques (QDs) de CdSe/CdS/ZnS aux variations de pression et température, afin de cartographier ces deux paramètres dans les contacts EHD. Dispersible à faible concentration dans les lubrifiants, il est montré que les QDs ne modifient pas le comportement rhéologique du fluide porteur et que le cisaillement n'est pas perturbateur à la réponse en PL. La calibration des QDs en suspension confirme la dépendance de la réponse en PL des QDs à la pression et à la température. Les mesures *in situ* sont effectuées en utilisant un banc d'essai bille-disque. La comparaison entre les mesures *in situ* de pression et de température et celles prédites à l'aide d'un modèle éléments finis TEHD interne montre une bonne concordance, ce qui démontre la faisabilité de la méthodologie proposée. Les effets du glissement et du chargement normal sur la pression, la température et la chaleur générée sont reportés. L'effet des propriétés thermiques des solides est souligné et la répartition de la chaleur générée entre les solides en contact est étudiée. L'équilibre énergétique entre l'énergie mécanique et l'énergie thermique interne générée par compression et cisaillement est démontré en comparant les pertes de puissance expérimentales et la chaleur générée issue du modèle numérique, pour des contacts acier-acier et hybrides.

Mots-clés : Lubrification élastohydrodynamique, contacts hybrides, mesure *in situ*, photoluminescence, boîtes quantiques, mesure de pression et température, pertes de puissances et génération de chaleur

Preface

This work was carried out at the laboratory of Contact and Structure Mechanics (LaMCoS - INSA de Lyon, France). It resulted from a collaboration between LaMCoS lab and SKF Company.

I would like to thank my thesis directors, Philippe Vergne and David Philippon who offered me the opportunity to carry out this thesis at LaMCoS together with Nicolas Fillot and Guillermo Morales-Espejel who discussed with me, gave me their suggestions and advised me throughout this work. I wish to express my gratitude to SKF Aerospace team in Valence with whom I had the chance to work, and more particularly Yves Maheo and Alexandre Mondelin for their support. Personally, I have learned a lot!

I would like to thank Pr. M. Hartl and Dr. J. Wong for their interest in this work and for accepting to review this manuscript. I also thank them along with Pr. R. Dwyer-Joyce and Pr. A. San-Miguel for being part of the jury.

I would also like to thank Dr. N. Bouscharain, Mr. N. Devaux, Dr. H. Diaf and Mr. L. Lafarge without whom much of the experimental part in this work wouldn't have been possible. I want to salute the entire staff of the laboratory for their welcome and their kindness.

Finally, I wish to thank all my friends and family for their presence and support, thank you for helping me to get to where I am today. Special thanks goes to Bayan who has always been there on my side and shared good moments with me during the last five years.

Table of contents

Preface **7**
Table of contents **9**
Résumé étendu **13**
Introduction 15
Première partie: Contexte et état de l'art 16
Deuxième partie: Possibilité de sonder la pression et la température à l'aide des QDs de CdSe/CdS/ZnS 21
Troisième partie: Mesure *in situ* de pression et température dans les contacts EHD 25
Quatrième partie: Comparaison entre les contacts tout-acier et hybride 30
Conclusion 37
Nomenclature **39**
General Introduction **45**
Chapter 1: Context & state of the art **49**
1.1 Introduction 51
1.2 Rolling element bearings 51
1.2.1 Rolling element bearings types 51
1.2.2 Rolling element bearings materials 52
1.2.3 Rolling element bearings lubrication - Elastohydrodynamic lubrication 52
1.3 Experimental techniques for studying EHD contact 56
1.3.1 Optical interferometry for film thickness measurement 56
1.3.2 Raman spectroscopy for pressure measurement 57
1.3.3 Infrared thermography for temperature measurement 59
1.3.1 Electrical resistance for pressure and temperature measurement 63
1.4 Pressure and temperature in steel and hybrid EHD contacts - Industrial challenge 65
1.5 Heat generation in hybrid and all-steel bearings - Literature overview 67
1.6 Summary and aim of the work 68
Chapter 2: Potential of the CdSe/CdS/ZnS QDs for probing pressure and temperature **71**
2.1 Introduction 73
2.2 Overview on the quantum mechanical atomic model 73
2.3 Semiconductor Materials 75
2.3.1 Band gap 75
2.3.2 Electronic transitions in semiconductors - Photoluminescence 77
2.4 Quantum dots 78
2.4.1 Semiconductor hetero-nanostructured QDs 79

2.4.2 QDs emission spectrum 81
2.5 Calibration of CdSe/CdS/ZnS QDs - Methodology 83
2.5.1 High pressure experiments 84
2.5.2 Thermal dynamic experiments 85
2.5.3 Fluorescence measurements tools 86
2.6 QDs pressure and temperature sensitivities - Results and discussion 87
2.6.1 High pressure calibration results 87
2.6.2 Results of the thermal dynamic calibration 92
2.7 Conclusion 94
Chapter 3: *in situ* measurement of pressure and temperature in EHD contacts 95
3.1 Experimental setup 97
3.1.1 EHD tribometer 97
3.1.2 Coupling the EHD tribometer with the photoluminescence equipment 99
3.2 Spatial measurement resolution 100
3.2.1 Laser spot size 100
3.2.2 Depth of focus 101
3.2.3 The uncertainty on the position of a measuring point 102
3.3 Experimental preparation 102
3.3.1 QDs suspensions 102
3.3.2 Parameters of importance and operating conditions 104
3.4 *In situ* pressure and temperature measurement 109
3.4.1 Pressure measurements - Isothermal contacts with dispersion N°1 109
3.4.2 Pressure measurements - Isothermal contacts with non-calibrated dispersions 110
3.4.3 Temperature measurement - Non-isothermal contacts 114
3.5 Summary and conclusion 118
Chapter 4: Comparison between all-steel and hybrid EHD contacts 123
4.1 Effect of sliding and normal load in sapphire-steel and sapphire-Si_3N_4 contacts 125
4.1.1 Operating conditions 125
4.1.2 Temperature rise 126
4.2 Effect of sliding and normal load in steel-steel and steel-Si_3N_4 contacts 130
4.2.1 Operating conditions 130
4.2.2 Pressure distribution 131
4.2.3 Temperature rise 133

4.2.4 Heat generation 135
4.2.5 Heat fluxes 137
4.3 Summary and discussion 140
General conclusion 143
Recommendations for future work 145
Annexes 147
5.1 Themo-elastohydrodynamic Numerical model 149
5.1.1 Lubricant Transport Properties 149
5.1.2 Numerical computation 151
5.2 Emission energy and Full width at half maximum uncertainties 154
5.3 Pressure and temperature sensitivities uncertainties 154
5.4 Pressure and temperature uncertainties 155
5.4.1 High pressure cell 155
5.4.2 Elastohydrodynamic contact 155
5.5 Pearson VII and SplitPearson VII functions 155
5.6 Determination of the laser spot size using cleaved silicon sample 156
References 161

Résumé étendu

Résumé étendu..... 13
Introduction..... 15
Première partie: Contexte et état de l'art..... 16
Deuxième partie: Possibilité de sonder la pression et la température à l'aide des QDs de CdSe/CdS/ZnS..... 21
Troisième partie: Mesure *in situ* de pression et température dans les contacts EHD..... 25
Quatrième partie: Comparaison entre les contacts tout-acier et hybride..... 30
Conclusion..... 37

Introduction

Cette thèse s'intéresse aux contacts mécaniques lubrifiés, en particulier à ceux que l'on retrouve dans les roulements. Les roulements sont des éléments clés pour le bon fonctionnement de nombreux mécanismes. Ils permettent notamment de réduire le frottement entre deux pièces en mouvement relatif par la mise en rotation des éléments roulants qui le compose (billes, rouleaux ...). Réduire le frottement et décroitre les pertes d'énergie, afin d'améliorer la longévité des mécanismes, est l'un des défis actuels de l'industrie aérospatiale. Afin d'optimiser la lubrification, il est nécessaire de maitriser les différents phénomènes physiques qui entrent en jeu. La plupart des roulements fonctionne en régime de lubrification élastohydrodynamique (EHL). Dans de telles conditions, le lubrifiant est soumis à des gradients de pression pouvant dépasser 1 GPa, à des contraintes de cisaillement de plusieurs MPa qui ont pour effet de provoquer une dissipation d'énergie importante conduisant à une élévation de température de plusieurs dizaines de degrés. Ces effets ont une influence sur le comportement rhéologique du lubrifiant, l'épaisseur de film et le frottement dans le contact.

L'objectif de cette thèse est de développer une nouvelle méthode expérimentale pour mesurer la pression et la température dans les contacts lubrifiés élastohydrodynamiques (EHD) circulaires. En particulier, de comparer les variations de températures dans un contact tout acier et dans un contact hybride (céramique-acier). En effet, les roulements hybrides sont de plus en plus utilisés dans le secteur aéronautique. Quantifier et comparer les pertes d'énergie dans ces types de roulements est un enjeu industriel.

Diverses méthodes expérimentales, telles que la spectroscopie Raman, la mesure de résistance électrique et la thermographie infrarouge, ont été développée pour sonder les contacts (EHD) en termes de pression ou de température. Malgré les résultats obtenus avec les méthodes précédents, il s'avère que le développement des méthodes de mesure avec une résolution et une précision plus fine est encore nécessaire afin d'acquérir une meilleure compréhension de l'EHL dans toute sa complexité. Pour cela, dans le cadre de cette thèse, une nouvelle technique de mesure *in situ* est développée afin de mesurer, si possible, simultanément la pression et la température dans les contacts EHD. Afin de valider les mesures obtenues, celles-ci seront comparées aux résultats obtenus avec un modèle numérique thermique EHD (TEHD) développé antérieurement.

La technique expérimentale utilisée ici consiste à disperser des nanosondes photoluminescentes, appelées boîtes quantiques (QDs), dont la photoluminescence (PL) est sensible aux variations de pression et de température dans le lubrifiant. Dans ce travail, les nanosondes utilisées sont des semi-conducteurs développés sous forme de QD cœur / coquille / coquille CdSe / CdS / ZnS, fonctionnalisés pour être dispersés dans un fluide alcane. D'abord une procédure d'étalonnage est effectuée afin d'évaluer la sensibilité à la pression et de la température de ces QD. Puis, la faisabilité de la méthodologie proposée est étudiée par la comparaison entre les valeurs de pression/température mesurées et simulées, obtenues dans des contacts EHD fonctionnant sous différentes conditions (vitesses, charges, températures, nature des matériaux…). Enfin cette nouvelle technique est utilisée pour quantifier l'échauffement dans des contacts glissants représentatifs des contacts tout acier ou hybride dans les roulements.

Une première partie présente le contact étudié et le régime EHL rencontré dans les roulements industriels, les principales méthodes expérimentales développées dans la littérature pour mesurer la pression et la température dans les contacts EHD.

Une deuxième partie fournit une description de la nature et des propriétés des nanosondes choisies (CdSe/CdS/ZnS QDs). Puis la procédure et les résultats de la calibration de ses nanosondes sont présentés. Les paramètres spectroscopiques ainsi que leur sensibilité à la pression et à la température sont donnés. De plus, cette partie met en évidence l'influence du cisaillement sur la réponse des QDs dans des conditions contrôlées de température. Enfin, les limites de l'utilisation de cette méthode sont posées pour la mise en œuvre, par la suite, dans le contact EHD.

Une troisième partie est consacrée à la mise en œuvre et la faisabilité de la méthode proposée dans le contact EHD. Pour cela, des mesures de pression et température sont réalisées dans des contacts isothermes puis non-isothermes pour des contacts simulant des contacts « tout acier » et « hybrides » (verre-acier, saphir-acier, verre-Si_3N_4 et saphir-Si_3N_4). Les profils de pression et température effectués le long de la ligne centrale du contact dans la direction de roulement sont comparés avec ceux obtenus avec le modèle numérique.

Dans la quatrième partie, l'influence du taux de glissement sur l'échauffement du lubrifiant dans le contact est mesurée. Différentes combinaisons de matériaux « hybride » ou « tout acier » ont été étudiées, à charges normales puis pressions hertziennes équivalentes. Une comparaison entre génération de chaleur simulée et pertes de puissance expérimentale est effectuée afin de valider la cohérence entre l'énergie mécanique transmise et l'énergie générée (chaleur) au sein du contact, et également pour fournir des résultats pertinents à l'application industrielle.

Pour conclure, une dernière section résume les principaux résultats de ce travail et suggère quelques perspectives.

Première partie: Contexte et état de l'art

Les roulements employés dans l'aéronautiques varient quant à leur géométrie d'une part (roulement à billes, à rouleau, etc…) mais également par la nature des matériaux employés (tout acier ou hybride acier-céramique). Les choix sont faits en fonction des exigences de l'application (charges supportées, vitesses, températures, …).

Dans la majorité des applications les roulements sont lubrifiés. Le lubrifiant intervient dans les contacts en régime de lubrification élastohydrodynamique (EHL). Son rôle principal, dans ce régime, est de réduire le frottement et l'usure en assurant une séparation minimale entre les solides en contact. Cette stratégie prolonge la durée de vie du contact lubrifié dans les roulements, diminue les pertes de puissance et permet l'accommodation des vitesses / contraintes de cisaillement élevées.

En effet, en régime EHL, la charge est concentrée sur une zone très réduite, ce qui génère des pressions extrêmement élevées (0.5 à 3 GPa). Par conséquence, cela provoque une déformation élastique importante des corps en mouvement (d'au moins un ordre de grandeur supérieur à

l'épaisseur du film) et une énorme augmentation de la viscosité du lubrifiant (d'un ordre de grandeur tous les 25 à 250 MPa). Dès lors, cela empêche le lubrifiant d'être entièrement expulsé et permet ainsi la formation d'un film lubrifiant au niveau du contact. Le diamètre de contact est de l'ordre de quelques centaines de µm et l'épaisseur du film est bien inférieure à 1 µm. Cela signifie que seuls quelques pico-litres du lubrifiant sont confinés en continu. Avec des contraintes de cisaillement allant de quelques KPa à quelques MPa et des taux de cisaillement de 10^5 à 10^7 s^{-1}, cela provoque un échauffement du lubrifiant atteignant plusieurs dizaines de degrés.

La mise en évidence et la compréhension du contact EHD est le résultat de nombreuses études expérimentales, numériques et analytiques. La complexité de l'étude du comportement d'un contact lubrifié provient principalement du couplage entre les sollicitations locales induites par les solides en contact et le comportement physique et rhéologique du lubrifiant. L'épaisseur du film lubrifiant est plus précisément contrôlée par son comportement rhéologique à l'entrée du contact. Quant aux propriétés rhéologiques du lubrifiant, elles sont directement liées aux températures et pressions locales rencontrées en chaque point de la zone du contact. Le développement de méthodes de mesure *in situ* de ses paramètres dans le contact est une étape nécessaire dans la meilleure compréhension du fonctionnement du contact EHD.

Différentes méthodes *in situ* ont été développées pour sonder l'épaisseur du film, la pression, la température, la viscosité, la contrainte de cisaillement, etc ... dans les contacts EHD. Spikes [1], Albahrani et al. [2] et Kumar et al. [3] ont rapporté la plupart de ces méthodes dans des revues de littérature.

La section suivante ne fournit pas une base complète de toutes les méthodologies *in situ* développées pour étudier l'EHL. Elle vise à donner un aperçu des principales méthodes développées pour mesurer les paramètres pertinents tels que la pression et la température.

- Spectroscopie Raman pour la mesure de pression

L'effet Raman désigne la diffusion inélastique de la lumière d'un échantillon éclairé par une lumière monochromatique. Le spectre Raman représente l'énergie vibratoire de l'échantillon et fournit des informations sur la structure chimique et les liaisons de ses molécules. La pression et la température influencent la structure de la molécule / la distance interatomique et provoquent par conséquent le déplacement des pics Raman (i.e un changement d'énergie vibratoire). Celui-ci permet donc de mesurer la pression et la température avec une précision de 30 MPa [4] et 5 à 10 K [5], respectivement. La température peut être déterminée grâce au rapport des intensités relatives des pics de Stokes et anti-Stokes. Jubault et al. [24] ont utilisé le 5P4E, ont réussi à extraire des profils de pression, comme illustré dans la Figure 0-1.

La très petite taille de la sonde, entre 5 et 10 µm (diamètre du spot laser) par rapport au diamètre du contact (200 à 550 µm), donne un avantage à cette technique en termes de résolution spatiale. En revanche, son principal inconvénient réside dans la faible intensité du signal mesuré et qui conduit à des durée d'acquisition très longs. Cela est la conséquence d'une part de la faiblesse du signal Raman de la plupart des lubrifiants étudiés et d'autre part les très faibles épaisseurs des films lubrifiants étudiés.

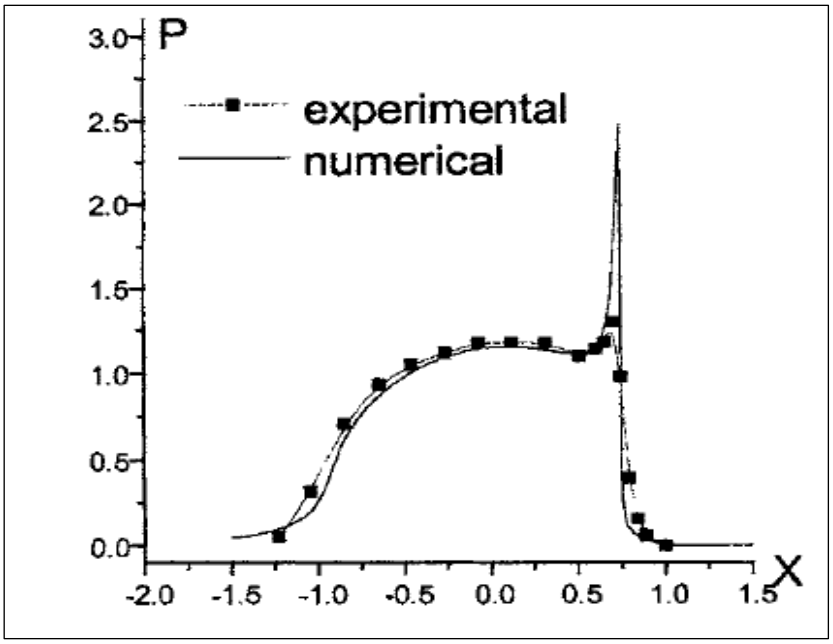

Figure 0-1:comparaison entre les distributions adimensionnées de la pression expérimental et numérique obtenues par spectroscopie Raman, par le modèle numérique EHD. Pour w = 17 N, u_e = 0.3 m/s, T_0 = 323 K [6].

- Thermographie infrarouge pour la mesure de la température

La thermographie infrarouge est une technique utilisée pour mesurer le rayonnement infrarouge émis par les échantillons. En général, ce rayonnement est converti en température en utilisant à la fois des étalonnages et des techniques analytiques. Les résultats, présentés sur la Figure 0-2, montrent un exemple de comparaison entre l'échauffement de la surface bille d'acier et les surfaces des disques en saphir. Généralement, la méthodologie implique l'utilisation d'un détecteur radiométrique IR et de filtres. Elle nécessite également d'effectuer des étalonnages afin de séparer quatre sources de rayonnement : fond, disque transparent (saphir), film lubrifiant et bille en acier. Cependant, l'application d'une telle technique pour mesurer la température dans l'EHL s'avère complexe en termes d'étalonnage en ce qui concerne la soustraction des radiations de fond et la dépendance de l'émissivité du lubrifiant à la température et à l'épaisseur du film (qui varient tous les deux sur toute la région de contact). L'approche expérimentale est considérée intrusive dans une certaine mesure car elle nécessite l'utilisation de matériaux réfléchissants infrarouges comme un revêtement de chrome. Ce dernier est appliqué à la surface inférieure du disque transparent pour isoler son rayonnement. Il est d'environ 120 nm d'épaisseur et possède une diffusivité thermique différente de celle du disque. Cette technique a permis de sonder la température avec une résolution spatiale de 6 μm.

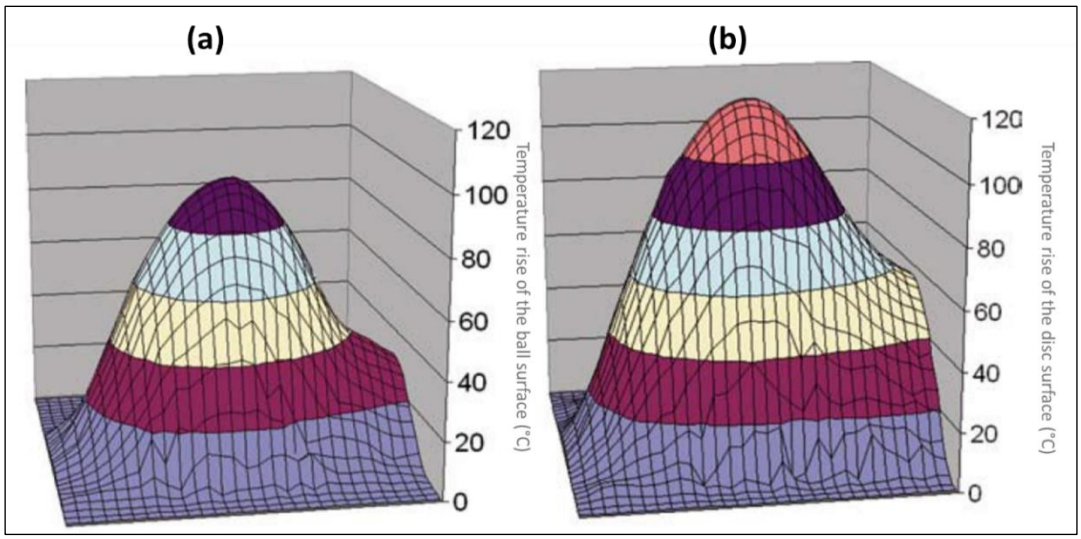

Figure 0-2: Les échauffement mesurées par thermographie IR de (a) la surface de la bille en acier et (b) la surface du disque en saphir partiellement revêtu dans un contact EHD fonctionnant pour w=50N (P_h=1.34GPa), T_0=40°C, u_e =1.113 m/s and SRR= -100% (i.e. u_b=1.6695 m/s and u_d=0.5565 m/s)[7]. L'entrée de contact est à gauche.

- Résistance électrique pour la mesure de pression et de température

La méthode de résistivité électrique a également été utilisée pour mesure la température et la pression dans le contact EHD. Cette dernière consiste à évaluer la variation de la résistance électrique dans une couche mince qui joue le rôle de micro-capteur lorsqu'elle traverse le contact lubrifié. Pour détecter la température, les matériaux (en couche mince) les plus largement utilisés sont le platine et le titane. En effet, leur résistance électrique présente une forte dépendance vis-à-vis de la température et une faible dépendance vis-à-vis de la pression. En revanche, la manganine (Cu – Mn – Ni) est couramment utilisée comme transducteur de pression car sa résistance électrique est très sensible à la pression et moins sensible à la température. Généralement, les capteurs à couches minces sont déposés sur des matériaux isolants électriques comme des substrats en céramique (saphir, zircone, nitrite de silicium, etc.) ou sur des revêtements isolants protecteurs (généralement en oxyde d'aluminium ou en oxyde de silicium) lorsqu'il s'agit de son emploi sur des surfaces métalliques.

Grâce à cette méthode, des profils de pression et/ou de température ont été obtenus pour divers lubrifiants, dans des conditions de charge et de vitesse variées [8]–[14], voir Figure 0-3. Néanmoins, la technique du micro-capteur est considérée comme intrusive car l'épaisseur du revêtement (0,1 μm) n'est pas négligeable par rapport à la plage d'épaisseur de film typique en EHL ; c'est-à-dire que les dimensions du capteur peuvent perturber l'entrainement du lubrifiant à l'intérieur du contact. De plus, les propriétés thermiques des matériaux qui constituent le micro-capteur sont différentes de celles du substrat massif. Pour cette raison, la génération de chaleur / l'élévation de température peut être influencée par la présence du capteur à l'intérieur du contact EHD. Enfin, la durabilité du capteur soumis à des conditions EHD sévères reste un problème majeur. D'autre part, la technique nécessite de nombreux étalonnages individuels des micro-capteurs car une faible variation des propriétés mécaniques (lors des processus de fabrication et de dépôt ou lors du test) peut avoir un effet significatif sur la réponse des capteurs.

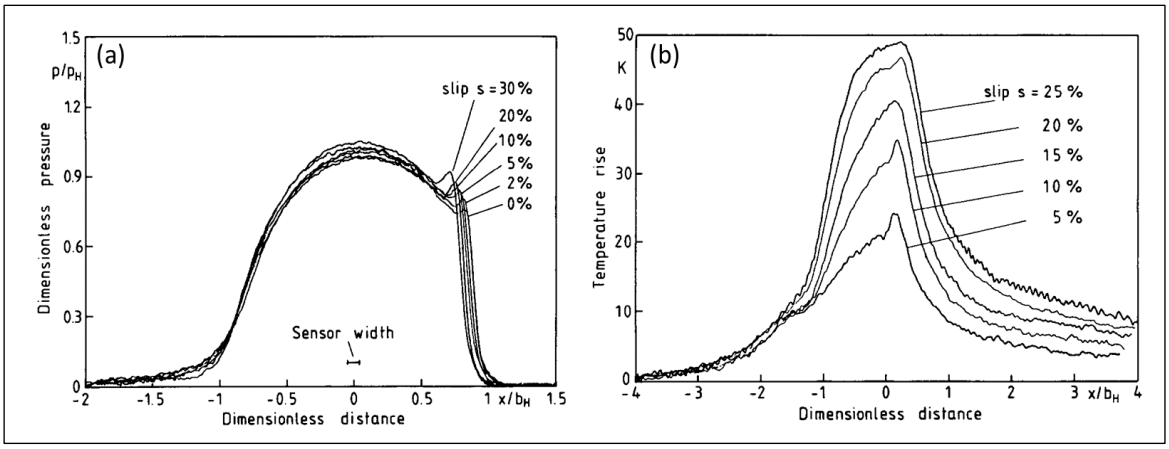

Figure 0-3: profils de (a) pression et (b) de température mesurés à l'aide de capteurs à couche mince en manganine et en platine dans diverses conditions de glissement [12].

Malgré les acquis des précédentes approches expérimentales, il existe un besoin continu pour développer une technique expérimentale (moins intrusive pour les conditions de contact, détectable en réponse, durable, fiable, résistante aux conditions sévères de l'EHD, simple à mettre en œuvre, plus précise) afin de mesurer plus finement la pression et la température dans les contacts EHD.

Ce travail vise à répondre à un défi industriel, qui consiste à quantifier et à comparer la pression, l'élévation de température et la chaleur générée dans les contacts EHD circulaires tout acier 100C6 et hybrides (acier 100C6-Si_3N_4). Ceci est très utile et instructif pour définir la route à suivre pour minimiser les pertes d'énergie, améliorer l'efficacité et prolonger la durée de vie de ces contacts sous des vitesses/contraintes de cisaillement élevées. Plusieurs résultats sur la génération de chaleur/ pertes de puissance et l' élévation de température dans les roulements tout acier et hybrides fonctionnant sous conditions opératoires identiques ont été rapportés dans la littérature [15]–[20]. Cependant, dans la plupart de ses études, la température du roulement est essentiellement mesurée à l'aide de thermocouples à travers le palier (sur les surfaces de bagues extérieurs des roulements) et pas au niveau du contact bille-bague. Cela est dû à l'accessibilité limitée, à la complexité de la structure des roulements et à la vitesse de rotation élevée de ses composants.

Pour cela, dans ce contexte, l'objectif des travaux en cours est de développer une nouvelle technique *in situ* fournissant des mesures locales de pression et de température dans les contacts EHD, avec éventuellement une détectabilité, une précision et une fiabilité meilleures que les techniques développées précédemment telles que la spectroscopie Raman, la thermographie infrarouge et la résistance électrique, respectivement. Cette technique consiste à exploiter la photoluminescence (PL) de nanosondes photoluminescentes, appelés boîtes quantiques (QDs), sensible aux variations de pression et de température dans le lubrifiant. De plus, afin de comparer/valider les mesures obtenues, un modèle numérique thermique non-newtonien (TEHD), inspiré des travaux Habchi et al. [16], sera utilisé.

Deuxième partie: Possibilité de sonder la pression et la température à l'aide des QDs de CdSe/CdS/ZnS

Les boîtes quantiques (QDs) sont des nanocristaux de semi-conducteurs photoluminescents. Généralement, elles sont d'un diamètre compris entre 2 et 10 nm et contiennent de 100 à 100 000 atomes. Elles sont désignées comme des atomes artificiels en raison de leurs niveaux d'énergie discrets, ce qui les rend plus proches de la structure électronique des atomes que des matériaux massifs. Leur photoluminescence varie essentiellement en fonction de leur taille. Cet effet est connu sous le nom de confinement quantique. Ce dernier implique la dépendance de l'énergie de la bande interdite E_g des matériaux à la pression et la température. Ces paramètres affectent à la fois la taille des QDs, la structure cristalline et l'interaction exciton-phonon.

Concernant l'application de ces nanostructures comme sondes dans les lubrifiants en milieu très confiné, les QDs cœur/coquille/coquille CdSe/CdS/ZnS (voir Figure 0-4) semblent être d'excellents candidats. En effet, plusieurs travaux ont indiqué la sensibilité des QDs à base de CdSe aux variations de la pression et de la température [21], [22]. Dans le cadre de ce travail, les QDs utilisés ont été synthétisé par l'équipe STEP du laboratoire SyMMES (INAC / CEA-Grenoble) selon le procédé décrit dans [23]. Leur diamètre moyen est de 6 nm. Ces QDs ont été fonctionnalisé à leur surface avec un ligand organique constitué d'acide stéarique afin de pouvoir stabiliser leur dispersion dans des fluides tels que les lubrifiants, alcanes et esters en particulier dans ce travail. Ces mêmes QDs ont par ailleurs un rendement quantique (rapport entre le nombre de photons émis et le nombre de photons absorbés) de 81% [23] ce qui est très élevé en comparaison avec d'autres familles de QDs.

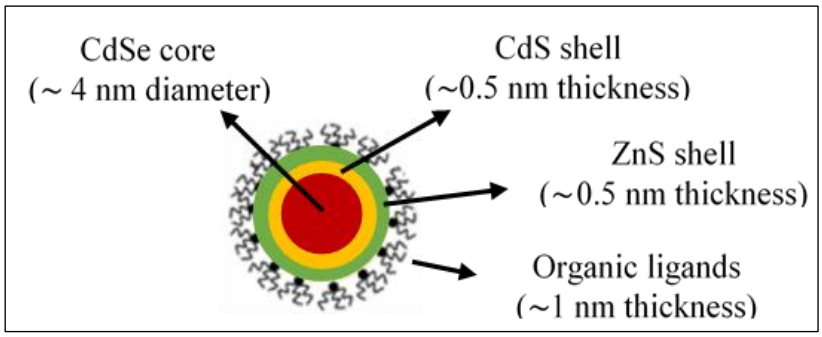

Figure 0-4: représentation schématique des QD cœur/coquille/coquille CdSe/CdS/ZnS [24].

Dans ce travail, les QDs sont dispersés à une concentration très faible de 0,125 mg /mL dans un lubrifiant de référence bien caractérisé, à savoir le squalane ($C_{30}H_{62}$). Ce liquide est un alcane ramifié dont les propriétés rhéologiques se retrouvent dans [25]. Cette faible concentration, recommandée par Albahrani [24], est sélectionnée premièrement afin d'éviter de modifier la viscosité du squalane et deuxièmement pour diminuer les interactions entre les QD qui pourraient modifier les caractéristiques du spectre d'émission dues aux processus de réabsorption [26].

Calibration statique

Avant de mesurer *in situ* dans le contact EHD la pression et la température, il est nécessaire de calibrer la réponse en PL de ces nanosondes. La réponse en PL de ces QDs peut-être approximé par une Gaussienne. Pour cela 2 paramètres spectroscopiques sont retenus : l'énergie (ou longueur d'onde) et la largeur à mi-hauteur (FWHM). Les sensibilités de ces deux paramètres à la pression et température ont été déterminées par des mesures réalisées dans des cellules haute pression (DAC) régulées en température.

Les résultats de la Figure 0-5 et Figure 0-6 indiquent la variation de l'énergie d'émission et de la largeur à mi-hauteur des QDs en fonction de la pression, respectivement à 296 K, 323 K et 348 K. En effet, l'énergie d'émission augmente avec la pression et diminue avec la température comme montré dans des études existantes [24],[21], [22], [27]–[29]. Quant à la largeur à mi-hauteur, elle est constante à faible pression et augmente avec la température. La tendance des courbes de calibration semble être quadratique sur toute la plage de pression, comme mentionné par des travaux précédents [21], [28]. Globalement, on peut voir qu'à mesure que la température augmente, les courbes deviennent relativement plus linéaires. En d'autres termes, lorsque la température de l'expérience augmente, le changement de pente apparait à des pressions plus élevées. Cela pourrait être associé à la transition de phase du liquide porteur (squalane) ou à celle des CdSe QD. Le second cas est à écarter car la réponse en PL est modifiée à des pressions bien supérieures à 3 GPa à température ambiante [30].

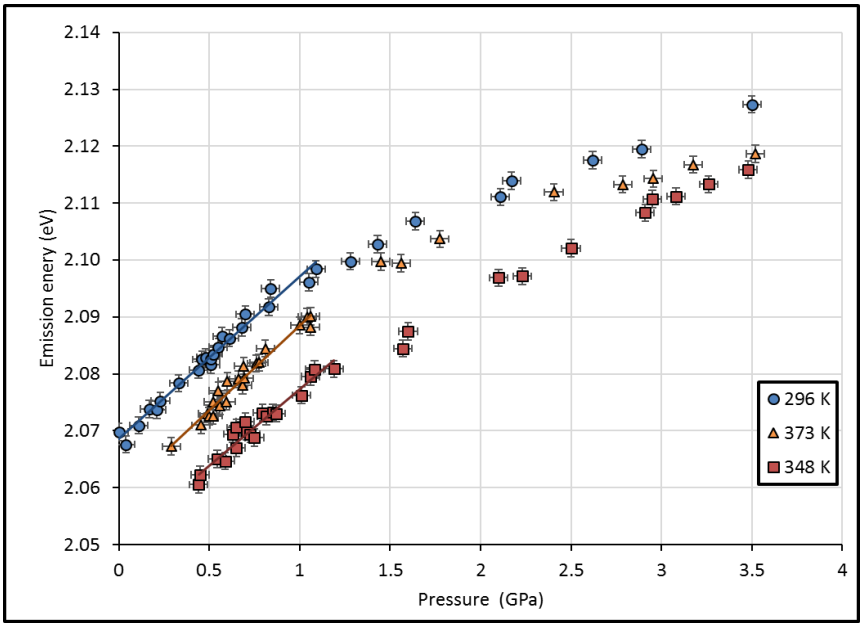

Figure 0-5: dépendance à la pression de l'énergie d'émission des QDs de CdSe /CdS /ZnS dispersés dans du squalane à trois températures (épaisseur de film de l'échantillon dans la DAC ≤ 0,07 mm).

Cependant, la discussion sur la transition de phase du squalane dérivée des conditions de pression stationnaires pourrait être trompeuse et incomplète car elle pourrait se produire différemment dans les conditions EHD, c'est-à-dire dans les conditions de pression dynamique. C'est pourquoi notre analyse se concentrera sur la région inférieure ou égale à 1.3 GPa et pour

une température supérieure à 296 K. Cela signifie que, pour les mesures EHD en perspective, la charge appliquée doit être soigneusement choisie pour induire une pression maximale de 1.3 GPa au contact.

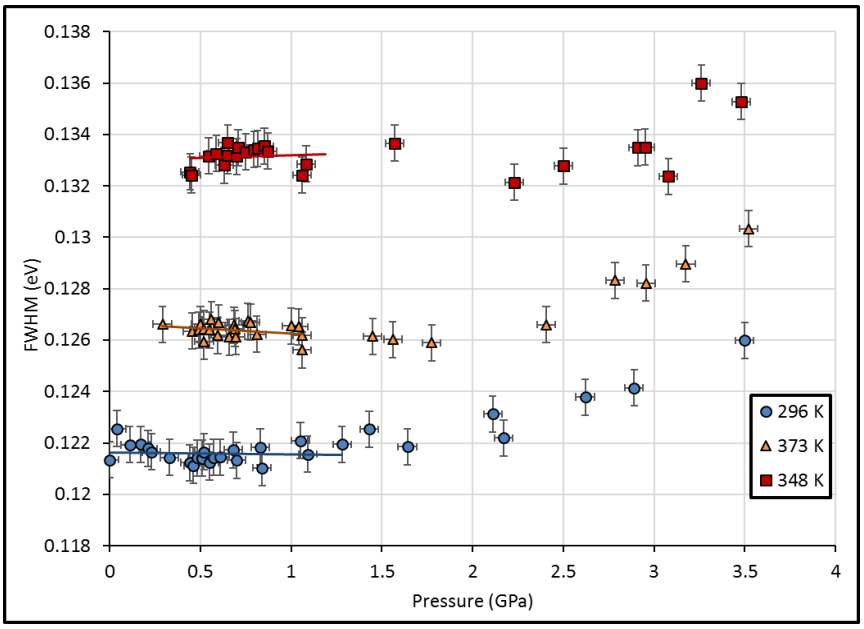

Figure 0-6: dépendance à la pression de la largeur à mi-hauteur du pic en PL des QDs de CdSe /CdS /ZnS dispersés dans du squalane à trois températures (épaisseur de film de l'échantillon dans le DAC ≤ 0,07 mm).

Dans cette plage de pression [0, 1.3GPa] sur laquelle les régressions sont effectuées, on peut remarquer que les courbes d'étalonnage sont linéaires et ont des pentes similaires pour chaque température. Ces tendances donnent lieu à deux corrélations de premier ordre : l'une pour l'énergie d'émission (Eg) et l'autre pour la largeur à mi-hauteur (FWHM) en fonction de la pression et de la température.

Concernant l'énergie d'émission, la recherche d'une meilleure régression a conduit à la relation suivante :

$$E_g(P,T) = E_{g0} + S_p P + S_T \qquad 0.1$$

En ce qui concerne la FWHM, la relation linéaire résultante peut s'écrire:

$$FWHM(T) = FWHM_0 + S'_T T \qquad 0.2$$

Ces équations permettent de découpler les influences de la pression et de la température à partir d'un seul spectre acquis de PL des QDs (au moins dans des conditions statiques). En effet, la température peut être déduite de la FWHM (équation 0.2). Ensuite, elle est substituée dans l'équation linéaire (0.1), qui inclut l'énergie d'émission des QDs, pour extraire la valeur de pression.

- Calibration dynamique

La calibration dynamique est effectuée à l'aide du rhéomètre optique à pression ambiante. Les effets de la température et de la contrainte de cisaillement sont étudiés sur la réponse en PL de la suspension colloïdale de QDs dans le squalane réalisée précédemment. Cette calibration est essentielle pour isoler et identifier l'effet possible de la contrainte de cisaillement induite par l'écoulement sur la réponse QDs PL. Il est particulièrement important de calibrer dans de telles conditions car i) la suspension subira un cisaillement intense lors de la mesure *in situ* dans les contacts EHD et ii) dans le rhéomètre, la température est régulée plus précisément et plus facilement contrôlée que dans les DAC.

Les résultats présentés sur la Figure 0-7 montrent la variation de l'énergie d'émission et de la FWHM en fonction de la contrainte de cisaillement à trois températures différentes (293, 333 et 373 K). L'énergie d'émission et la FWHM sont quasi constantes malgré l'effet de l'écoulement et de la contrainte de cisaillement, ce qui signifie que les réponses des QD sont indépendantes de la contrainte de cisaillement dans la plage expérimentée. L'exclusion de ce paramètre (contrainte de cisaillement) conforte l'application des corrélations linéaires obtenues à partir de la calibration statique en utilisant la DAC pour sonder la pression et à la température dans des conditions dynamiques (contacts EHD).

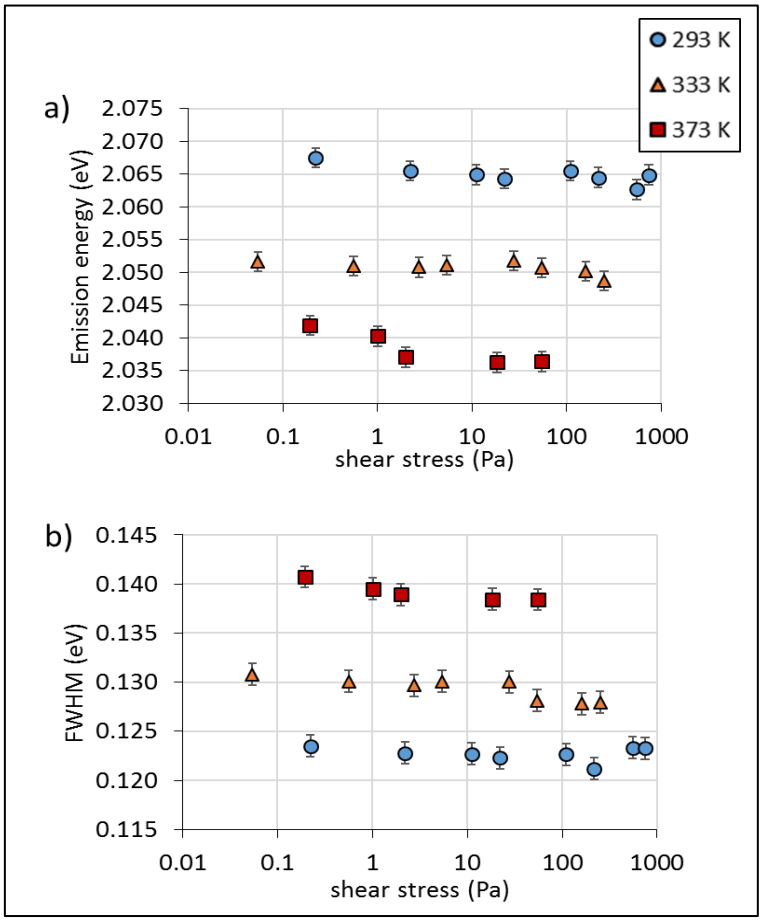

Figure 0-7: variation de l'énergie d'émission et de la FWHM des QDs de CdSe/CdS/ZnS dispersés dans le squalane en fonction de la contrainte de cisaillement, à différentes températures.

Troisième partie: Mesure *in situ* de pression et température dans les contacts EHD

Dans cette partie, diverses dispersions de QDs dans le squalane vont être mise en œuvre dans le contact EHD pour mesurer la pression et la température. Diverses conditions de fonctionnement vont être étudiées : roulement pur ou roulement-glissement, charge normale, température à l'entrée du contact, ainsi que la nature des matériaux solides en contact. Le but est d'évaluer les performances de la méthode de mesure développée ici, et ce dans un large éventail de conditions de fonctionnement, dans la limite des pressions et températures définies lors de la calibration. Des comparaisons avec les résultats obtenus à partir d'outils numériques seront également proposées.

- Tribomètre bille-disque

Pour simuler expérimentalement le contact EHD circulaire, le banc d'essai utilisé dans ce travail est un tribomètre bille-disque appelé «Jerotrib» (développé par Molimard et al. [31]).

Des billes en acier 100C6 ou en nitrure de silicium (Si3N4) sont employées. Des disques transparents, en verre (BK7) ou en saphir, sont utilisés. En effet, les mesures spectroscopiques nécessitent au moins que l'un des deux solides soit transparent. Le disque en verre est utilisé pour une plage de pression de contact moyenne (0.5–0.8 GPa) et le disque en saphir pour des pressions proches ou supérieures à 1 GPa. En termes de propriétés thermiques, le verre peut être considéré comme un matériau isolant thermique qui n'absorbe / dissipe pas facilement la chaleur et améliore ainsi la génération de chaleur dans le lubrifiant. En revanche, le saphir présente une diffusivité thermique (D) similaire à celle de l'acier 100C6. La bille et le disque sont entrainés par deux moteurs indépendants afin de contrôler précisément le taux de glissement. La température des deux solides ainsi que celle de l'huile sont maintenues constantes à l'aide d'un bain thermostaté. Le tribomètre est couplé avec un système optique qui comprend une source laser, un microscope et un spectromètre (voir Figure 0-8).

Il est important de préciser que, comme le faisceau laser se déplace à travers le disque en saphir/verre de 10 mm d'épaisseur, un signal de fond fluorescent émis par le disque transparent se superpose à la ligne de base du spectre de PL des QDs. Il est alors difficile d'extraire la largeur à mi-hauteur (FWHM) même après avoir appliqué une fonction de correction de la ligne de base. En revanche, le rapport signal sur bruit des QDs permet d'évaluer l'énergie d'émission des QDs (position de crête indiquée en haut du spectre des QD). Cette dernière n'est pas affectée par le fond parasite car les QD n'absorbent pas d'énergie de l'ordre de celle émise par le disque transparent, comme rapporté dans la référence [23]. Pour ces raisons, l'analyse de la FWHM ne sera pas exploitée et seule l'énergie d'émission sera évaluée pour étudier les contacts EHD. Cela implique qu'avant de mesurer la température, il est nécessaire d'effectuer un contact isotherme en roulement pur pour isoler la variation d'énergie d'émission des QDs due à la pression.

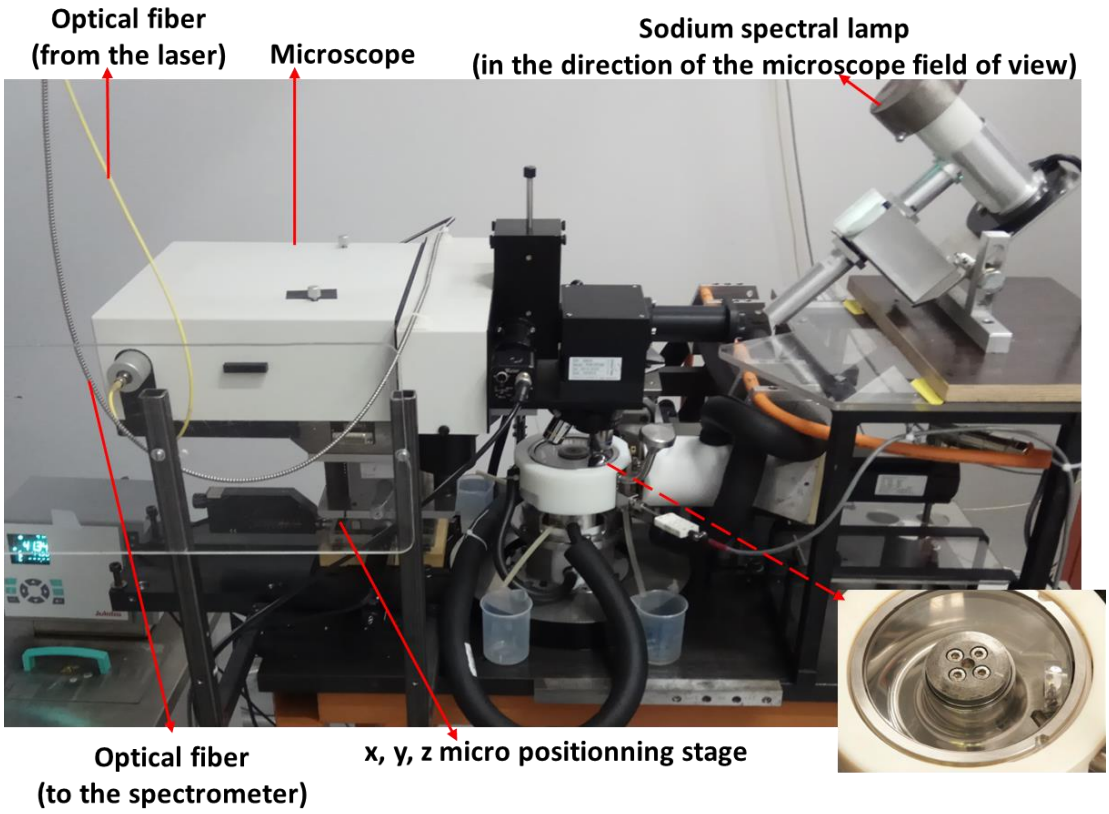

Figure 0-8:Le couplage du banc d'essai Jerotrib avec le système optique (microscope, laser, fibres optiques, lampe spectrale et spectromètre. Le laser et le spectromètre ne sont pas illustré ici.

- Mesure *in situ* de la pression dans des contacts isothermes

La Figure 0-9 de gauche montre les variations d'énergie d'émission des QDs, enregistrées le long de la ligne centrale du contact, dans la direction de roulement, de l'entrée vers la sortie du contact pour différentes configurations de matériaux (verre-acier, verre-Si_3N_4 et acier saphir) en conditions isothermes (roulement pur et faibles vitesses d'entrainement afin d'éviter l'échauffement du au cisaillement du fluide à l'entrée du contact).

La Figure 0-9 de droite montre que les pressions expérimentales, obtenues en utilisant le modèle linéaire de calibration, sont en bon accord avec celles prédites par le modèle numérique avec un écart inférieur à 3% au centre du contact. De plus, les valeurs d'énergie d'émission/pression mesurées sont reproductibles pour différentes positions de mesure.

Les profils obtenus sont quasi-hertziens, et proche des profils de pression obtenus avec la simulation numérique. On peut également remarquer que, au fur et à mesure que la charge augmente, le profil de pression tend vers une distribution de plus en plus hertzienne, comme le révèle l'analyse expérimentale effectuée dans [4]. Cette tendance est également mise en évidence dans les travaux précédents de Kagerer et al. [12], Safa et al. [13] et Habchi et al. [28].

Cependant, on peut remarquer que les profils de pression expérimentaux sont légèrement surdimensionnés, en termes de diamètre de contact dans le sens de l'axe x sans dimension, par rapport aux profils simulés : ~ 14% pour le verre-acier, ~ 13% pour le verre -Si3N4 et ~ 14% pour les contacts en acier saphir.

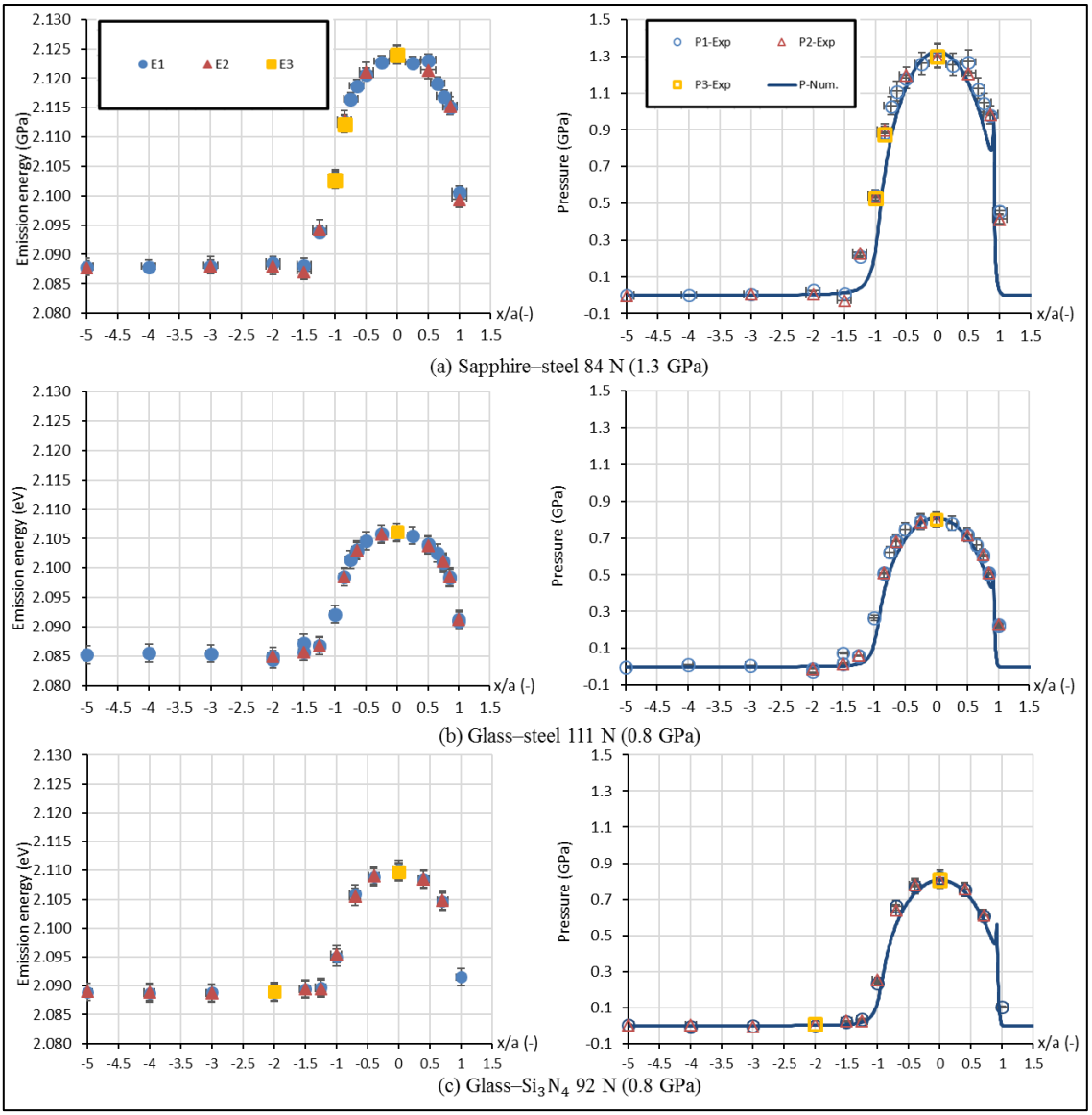

Figure 0-9: comparaison entre les profils d'énergie d'émission (à gauche) et les profils de pression mesurés et simulés (à droite) le long de l'axe x adimensionné et y = 0 pour des contacts isothermes (a) acier-saphir, (b) acier-verre et (c) verre-Si_3N_4 fonctionnant à T_0 = 298 K avec u_e = 1.8 m/s en roulement pur (SRR = 0%). E_i représente l'énergie d'émission détectée et P_i-Exp représente les valeurs de pression mesurées, avec "i" le numéro de répétition de la mesure enregistrée pour une même position d'un même test.

- Mesure *in situ* de la température dans des contacts non-isothermes

Les contacts non-isotherme sont opérés à des charges et pour des couples de matériaux identiques au cas isothermes. En revanche, la vitesse d'entrainement est plus importante, ce qui génère de l'échauffement par cisaillement du fluide à l'entrée du contact. La température du fluide à l'entrée du contact est de 313K. Des tests en roulement pur (SRR = 0%) et en roulement-

glissement à SRR= 10% sont étudiés. Ce dernier est appliqué également pour induire une augmentation supplémentaire de température dans la zone centrale sous pression.

La Figure 0-10 montre une comparaison entre les températures mesurées et simulées de contacts (a) verre-acier, (b) verre-Si3N4, (c) saphir-acier et (d) saphir-Si3N4. Les tests sont réalisés en roulement pur pour les différentes charges normales appliquées. Il est important de noter que les variations de température mesurées et calculées, dans cette étude, représentent des moyennes de températures à travers l'épaisseur du film.

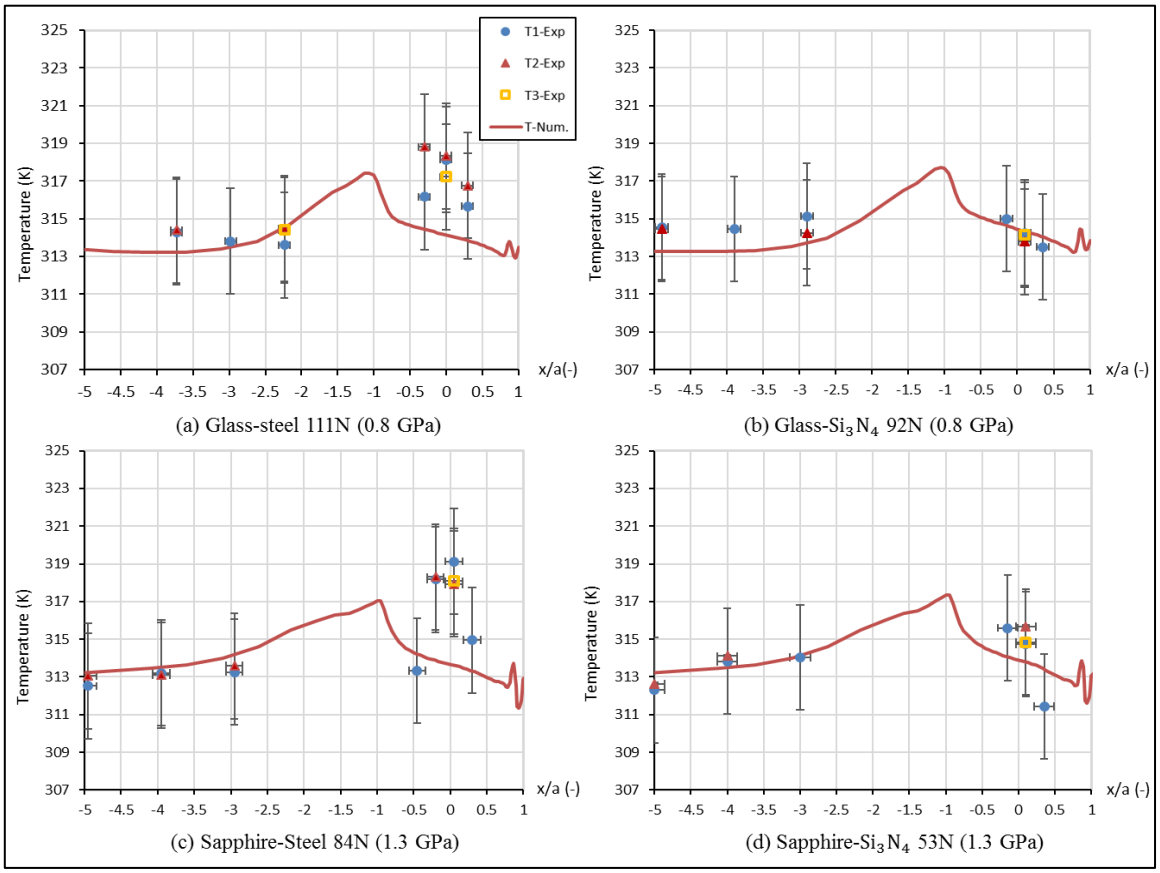

Figure 0-10: comparaison entre les profils de température mesurés et simulés le long de l'axe x adimensionné pour y = 0 pour des contacts non-isothermes (a) verre-acier, (b) verre-Si3N4, (c) saphir-acier et (d) saphir-Si_3N_4 fonctionnant à T_0 = 313 K avec u_e = 5 m/s en roulement pur (SRR = 0%). T_i-Exp représente les valeurs de température mesurées, avec «i» le numéro de répétition de la mesure enregistrée pour une même position d'un même test .

L'écart-type des températures mesurées vaut ± 3K, comparable aux variations de température simulées. Par conséquent, bien qu'une bonne répétabilité des résultats des tests est obtenue pour chaque position et configuration de contact, une comparaison quantitative sur la dominance de l'échauffement par friction ou par compression ne peut pas être déduite de ces mesures.

Cependant, il existe un bon accord entre résultats expérimentaux et résultats numériques pour les cas (b) et (d) et, bien que les variations restent faibles, des différences plus importantes pour les cas (a) et (c). Pour toutes les conditions opératoires, les simulations révèlent une très faible élévation de température (de quelques degrés Kelvin) au voisinage des contacts (x/a= - 1). Cela découle i) d'un échauffement par cisaillement à l'entrée du contact favorisé par la vitesse

d'entraînement relativement élevée, comme le prédit le coefficient thermique de réduction d'épaisseur du film de Cheng [6], [32], et ii) de la compression du lubrifiant à l'entrée de contact.

Ces profils de température simulés sont en bon accord avec les résultats précédents de simulation de Habchi et al. [33] et des mesures par Safa et al. [13]. Dans tous les cas, l'effet l'échauffement visqueux apparu à l'entrée du contact se poursuit par une étape de refroidissement lors du passage du lubrifiant la zone de haute pression de contact, puis par une deuxième faible montée en température à proximité de la sortie, dans la zone de conjonction. Ces tendances sont qualitativement similaires à celles obtenues par Cheng et al. [9].

La Figure 0-11 montre des résultats dans les mêmes conditions que les précédentes avec du glissement (SRR = 10%). Cette fois-ci, les variations de température sont plus importantes et en meilleur accord avec les augmentations de température simulées, quelle que soit la nature des matériaux en contact et les charges appliquées. Globalement, l'écart entre l'élévation de température expérimentale et simulée est inférieur à 5 K, alors que l'incertitude de température est de 4-5 K. Encore une fois, les résultats expérimentaux sont reproductibles.

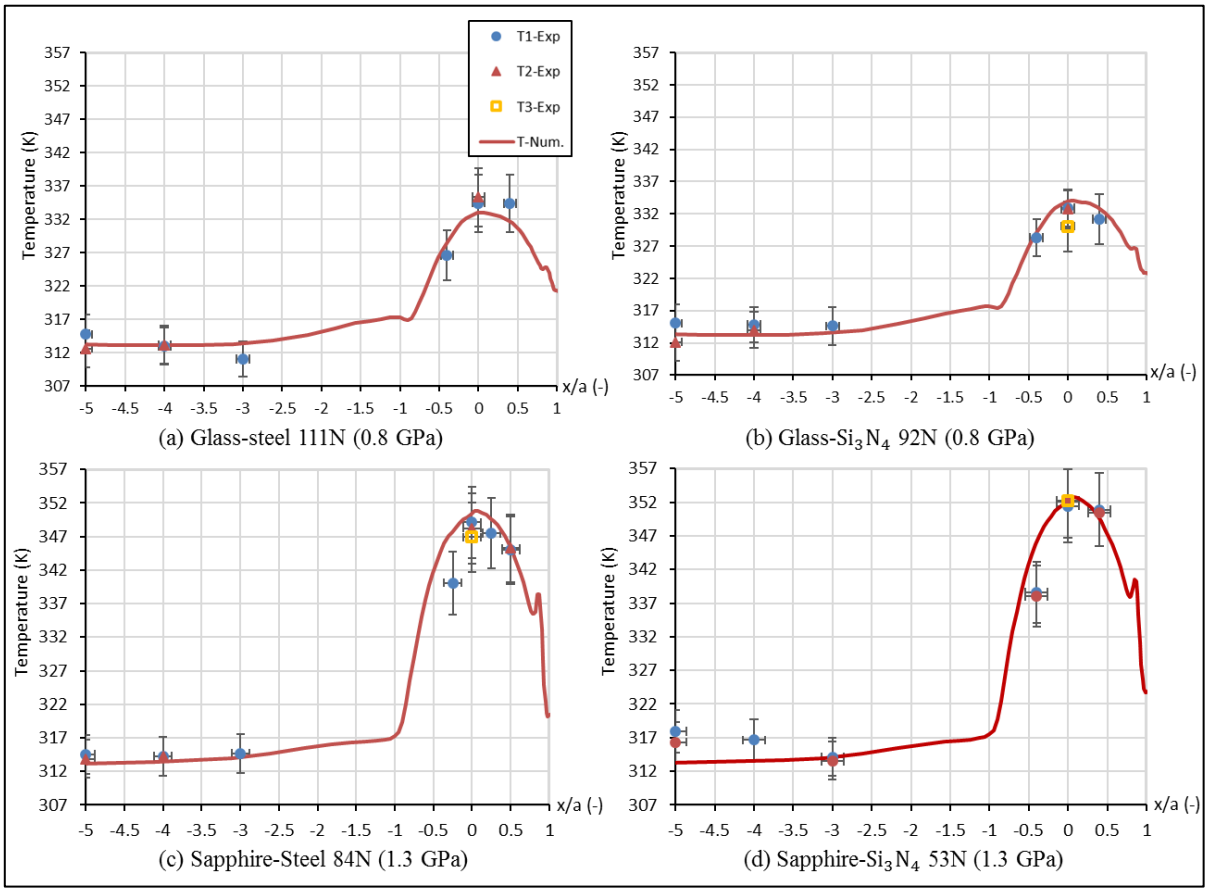

Figure 0-11: comparaison entre les profils de température mesurés et simulés le long de l'axe x adimensionné pour y = 0 pour des contacts non-isothermes (a) verre-acier, (b) verre-Si3N4, (c) saphir-acier et (d) saphir-Si_3N_4 fonctionnant à T_0 = 313 K avec u_e = 5 m/s en roulement-glissement (SRR = 10%). T_i-Exp représente les valeurs de température mesurées, avec «i» le numéro de répétition de la mesure enregistrée pour une même position d'un même test .

À l'entrée de contact, l'élévation de température simulée à cause de l'échauffement par cisaillement existe toujours en condition de roulement-glissement sans changement substantiel d'amplitude par rapport à celles obtenues en roulement pur pour la même vitesse d'entraînement, comme prédit par les coefficients de Cheng [6], [32]. Ensuite, dans la région sous pression, l'élévation de la température devient plus intense et atteint sa valeur maximale au centre de contact, principalement en raison du cisaillement sous haute pression, car les vitesses des surfaces des corps en contact sont maintenant différentes. Par la suite, la température chute fortement au niveau de la zone de sortie. Les profils de température, très probablement influencés par la distribution de pression (voir l'apparition d'un pic de température à 1,3 GPa), sont comparables à ceux trouvés dans les travaux précédents [11]–[14], [34], [35].

La validation et la reproductibilité des résultats expérimentaux mettent en évidence la fiabilité des QD utilisés comme nanosondes pour mesurer la pression et la température dans des conditions de cisaillement et de pression sévères. La méthode développée est non intrusive et a une résolution spatiale appropriée (~ 10 µm) par rapport à la taille d'un contact EHD typique. Cependant, le principal inconvénient de cette technique réside dans la nécessité d'utiliser un matériau transparent comme le verre ou le saphir à travers lequel le faisceau laser et le signal de photoluminescence des QDs passent. C'est néanmoins une caractéristique inhérente à toutes les méthodes optiques. Dans notre cas, cependant, on peut noter qu'il n'est pas nécessaire de revêtir la surface transparente d'un revêtement métallique, comme c'est le cas pour les techniques interférométrique ou thermographie infrarouge. Un deuxième inconvénient est l'impossibilité de mesurer simultanément pression et température du fait de la non-utilisation de la largeur à mi-hauteur (FWHM). Il est donc nécessaire d'effectuer un contact isotherme dans des conditions de roulement pur pour isoler la variation d'énergie d'émission des QDs due à la pression.

Quatrième partie: Comparaison entre les contacts tout-acier et hybride

Cette partie est dédiée à l'étude de l'effet de la nature des matériaux solides sur les températures dans des contacts EHD, opérés en roulement-glissement. En particulier, l'effet du taux de glissement et de la charge normale sur l'élévation de température, les pertes de chaleur et des puissances dissipées seront quantifiées et comparés pour les contacts EHD tout acier et hybrides (acier- Si_3N_4). De plus, grâce à l'utilisation d'un modèle numérique TEHD, la répartition de la chaleur générée entre les solides en contact sera étudiée à travers l'évaluation des flux de chaleur transférés aux surfaces en contact.

- Effet du glissement et de la charge normale sur les contacts en saphir-acier et saphir-Si_3N_4

Comme mentionné précédemment, les techniques spectroscopiques nécessitent le déploiement d'au moins un corps de contact transparent. Par conséquent, un disque en saphir est utilisé pour effectuer les mesures de PL.

La Figure 0-12 montre les variations de l'énergie d'émission et les variations de température correspondantes, ainsi que les résultats donnés par le modèle numérique. Toutes les mesures sont prises au centre du contact avec un SRR variant de 0 à 50%. Dans cette gamme de taux de glissement, la pression au centre du contact ne varie pas [4], [12], [36]. Les variations de température mesurées et calculées représentent les changements de températures moyennes à travers l'épaisseur du film. On peut clairement voir que la température mesurée augmente avec le taux de glissement (i.e le cisaillement du lubrifiant).

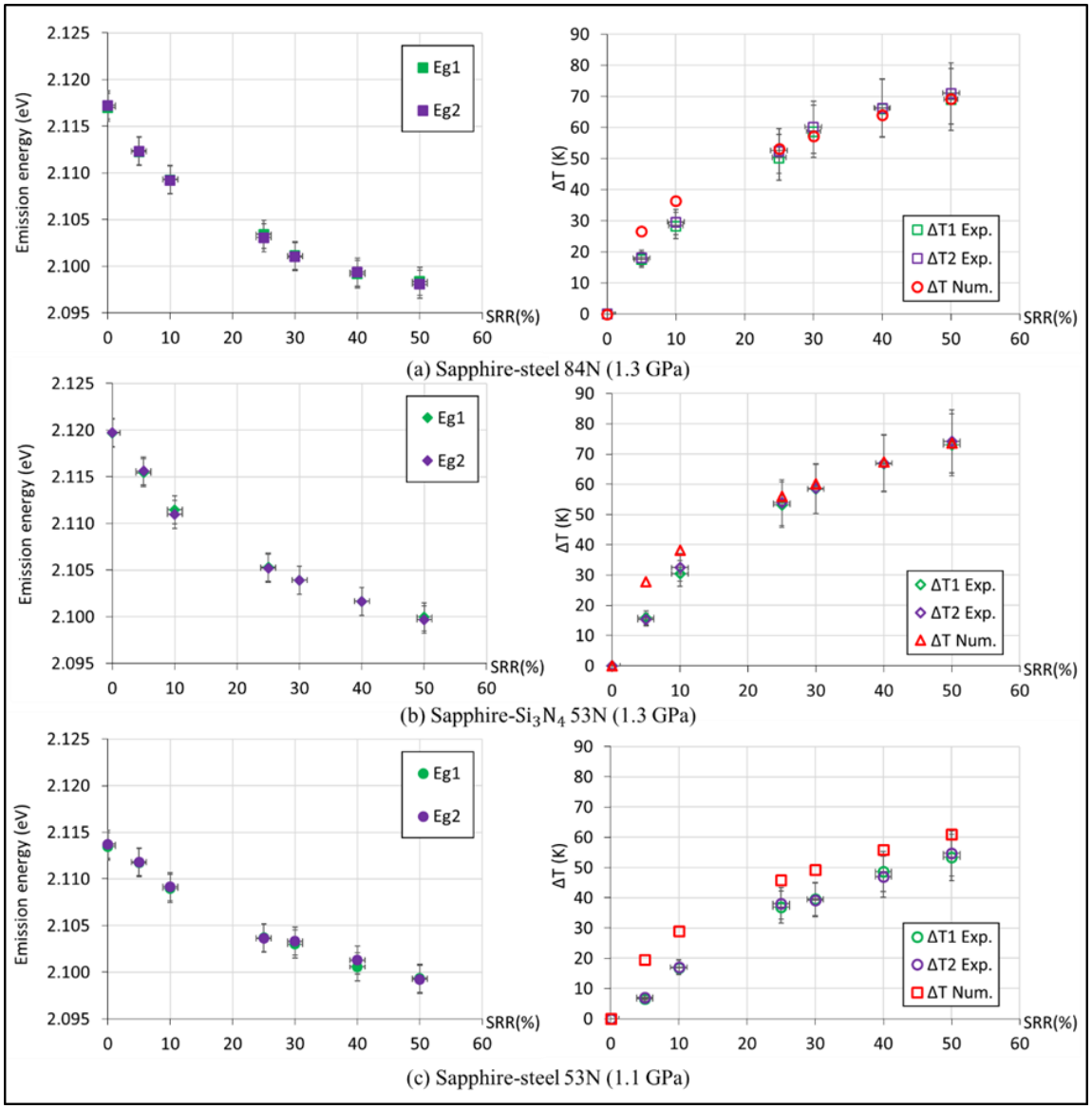

Figure 0-12: variation de l'énergie d'émission (à gauche) et de la moyenne des températures mesurées et simulées (à droite) en fonction du taux de glissement (SRR) pour des contacts : (a) saphir-acier (84N), (b) saphir-Si_3N_4 (53N) et (c) saphir-acier (53N) fonctionnant à T_0 = 313 K et u_e = 5 m/s.Egi et ΔTi-Exp représentent les valeurs de température mesurées, avec «i» le numéro de répétition de la mesure enregistrée au centre du contact d'un même test.

Les résultats montrent que, pour la même pression centrale (P_H = 1.3 GPa), les élévations de température mesurées et simulées dans le contact saphir-Si_3N_4 sont légèrement supérieures de ~ 1 à 5 K à celles obtenues dans le cas en saphir-acier. Cependant, cette différence est proche de l'incertitude de mesure. Par conséquence, l'effet thermique dû au remplacement d'une bille en acier par une bille en Si_3N_4 ne peut pas être quantifié clairement.

À une pression centrale inférieure P_H = 1.1 GPa, les augmentations de température simulées et mesurées dans le contact saphir-acier sont réduites de ~ 10-15 K par rapport aux cas où les charges appliquées génèrent une pression hertzienne de 1.3 GPa. Ces résultats expérimentaux et numériques soulignent l'effet significatif de la pression combinée au cisaillement sur l'élévation de la température au centre du contact. Les résultats semblent également être en cohérence avec les propriétés thermiques des solides, mais ici, cet effet est limité et de la même amplitude que les incertitudes numériques et expérimentales. L'importance de cet effet pourrait être clairement observée en utilisant un solide avec une très faible diffusivité thermique comme le verre (D = 0.05 × 10-5 m2/s).

- Effet du glissement et de la charge normale sur les contacts en acier-acier et acier-Si_3N_4

Dans cette partie, l'effet de la nature des matériaux en contact (en particulier acier-acier et acier-Si_3N_4) sur l'élévation de la pression, de la température et de la dissipation thermique est analysée. Notez que pour ces solides opaques, la spectroscopie de photoluminescence ne peut plus être utilisée pour effectuer des mesures *in situ*. Une autre approche est proposée : des tests de frottement sont effectués pour évaluer les pertes de puissance qui correspondent à la chaleur générée dans ces contacts.

Champ de pression

La Figure 0-13 compare les profils de pression simulés le long de la direction x pour les contacts acier-acier et acier-Si_3N_4, à la même charge normale (256 N) et à différentes charges générant la même pression maximale (1,6 GPa) au centre du contact, pour trois rapports de glissement-roulement différents (SRR = 5, 25, 50%) à 298K. Tous les profils obtenus s'expliquent par les propriétés élastiques des corps en contact (et des déformations correspondantes) induites par l'application de charges normales.

En effet, pour les mêmes matériaux en contact (acier-Si_3N_4 dans ce cas), au fur et à mesure que la charge augmente, la pression EHD augmente et sa distribution (en largeur) augmente. Dans le cas présent, une augmentation de 41% de la charge normale entraîne une augmentation de 12% de la pression et une augmentation de 11% de la largeur de contact. Sous charge normale équivalente, la pression maximale dans un contact hybride est plus élevée que dans un contact tout acier (12% ici). La distribution de pression dans le contact tout acier est plus grande (en largeur) que dans le contact hybride acier-Si_3N_4 que ce soit pour une charge normale équivalente (6% plus large) ou une pression centrale générée équivalente (16% plus large).

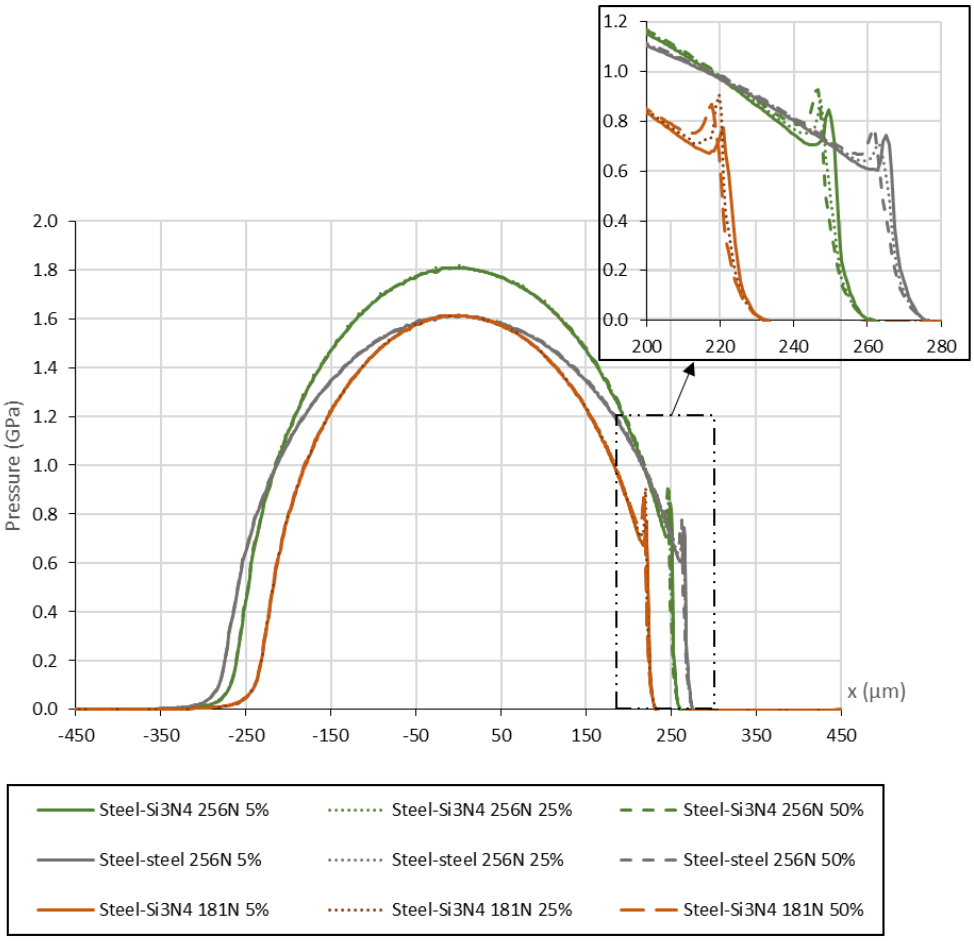

Figure 0-13: profils de pression simulés le long de la ligne centrale (y=0) des contacts: acier-Si_3N_4 (w=256N P_H=1.8 GPa), acier-acier (w=256N P_H=1.6 GPa) and acier-Si_3N_4 (w=181N P_H=1.6 GPa) opérés à T_0=298 K, u_e=0.5 m/s and SRR= 5, 25, 50%.

Plus important encore, on peut clairement remarquer que la forme de distribution caractéristique de la pression EHD reste quasi inchangée dans sur la plage de SRR étudiée, ici jusqu'à SRR = 50%. Les différences se trouvent principalement dans l'emplacement et l'amplitude du pic de pression proche de la sortie du contact. Ces résultats sont conformes aux résultats publiés dans [12], [36], [37]. On peut remarquer que lorsque SRR augmente, la position du pic de pression se déplace vers la zone du contact. Ceci est en bon accord avec les résultats expérimentaux de Kagerer et al. [12].

Elévation de température

La Figure 0-14 montre les profils de température simulés le long de la direction de roulement (axe x) dans les contacts acier-acier (charge de 256N) et acier-Si_3N_4 (charge de 256N et 181N) fonctionnant en roulement-glissement (SRR = 5, 25, 50%) et à une vitesse d'entraînement de 0.5 m/s. Notez que les températures affichées sont des valeurs moyennes dans l'épaisseur du film de lubrifiant.

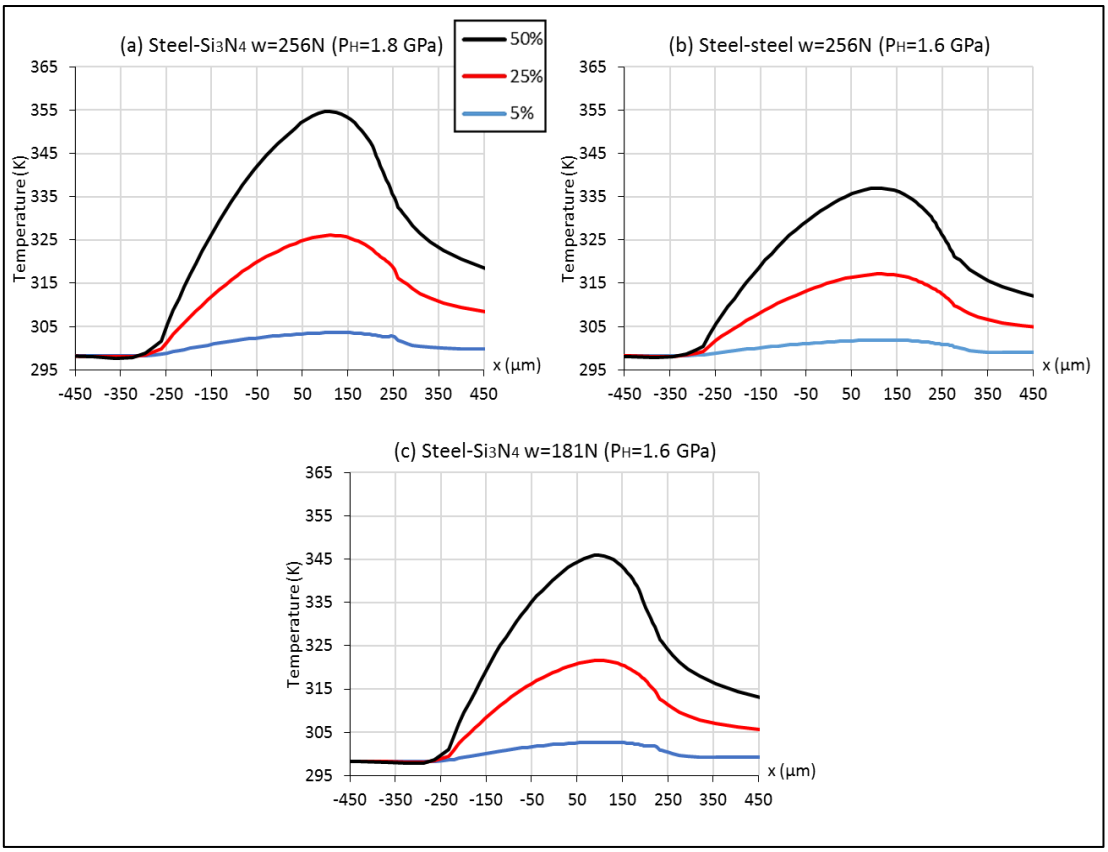

Figure 0-14: profils de température moyenne simulée sur la ligne centrale (y=0) des contacts*: (a) acier-Si_3N_4 (w=256N P_H=1.8 GPa), (b) acier- acier (w=256N P_H=1.6 GPa) and (c) acier-Si_3N_4 (w=181N P_H=1.6 GPa) opérés à T_0=298 K, u_e=0.5 m/s avec SRR=5, 25 and 50%.*

Globalement, en contraste aux profils de pression, la température commence à augmenter à l'entrée du contact pour atteindre son maximum au-delà du centre, puis elle diminue avec une queue au niveau et au-delà de la zone de sortie du contact. Les résultats montrent également que le profil de température est un peu perturbé à l'endroit où se situe le petit pic de pression, selon les profils de pression affichés sur la Figure 0-13. Ces résultats sont en bon accord avec les travaux expérimentaux et numériques d'Ebner et al. [14]. Par ailleurs les résultats montrent que, en moyenne, la différence d'augmentation de température entre le contact acier-acier et acier-Si3N4 est deux fois plus élevée dans le cas d'une charge normale équivalente que dans le cas d'une pression centrale équivalente.

Génération de chaleur

Afin de valider les résultats précédents, une approche alternative qui fait le bilan énergétique dans le contact EHD est proposée. Elle consiste à comparer les pertes de puissance expérimentales et la génération de chaleur numérique. En effet, à la conjonction des solides en contact, la puissance est transmise via le contact EHD fortement chargé qui, à son tour, génère des pertes de puissance dues à l'action de cisaillement du lubrifiant, considéré comme une source de chaleur localisée.

La Figure 0-15 compare les pertes de puissance expérimentales (dérivées des essais de frottement) et la génération de chaleur simulée dans les contacts acier-acier et acier-Si_3N_4 pour des conditions de glissement variables. Ces résultats révèlent un bon accord global et une dépendance linéaire de ces deux paramètres en fonction du taux de glissement. Ces résultats mettent en évidence la cohérence entre l'énergie mécanique transmise et l'énergie générée au sein des contacts testés.

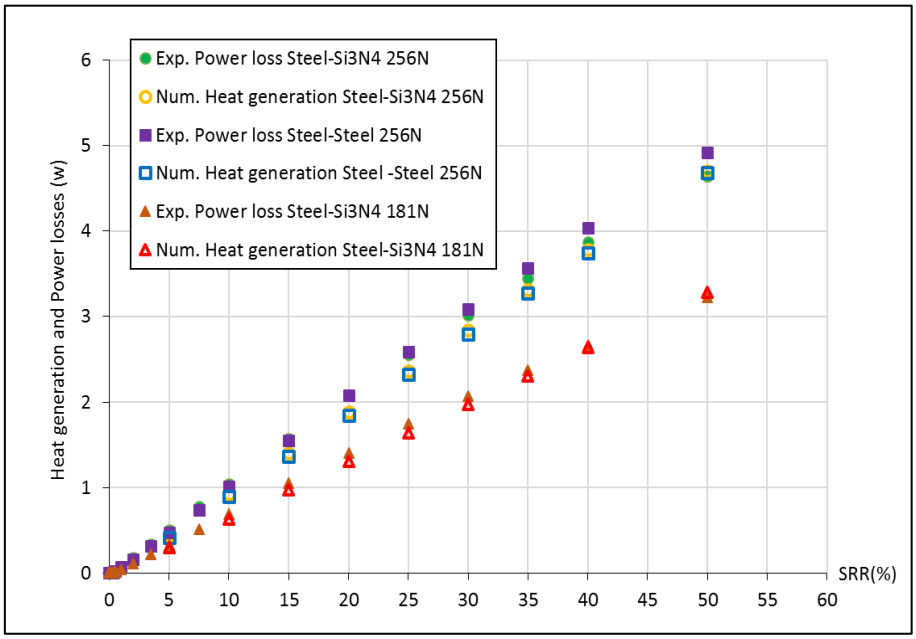

Figure 0-15: perte de puissance expérimentale et génération de chaleur simulée par rapport au taux de glissement pour différents contacts: acier-Si_3N_4 (w = 256N, P_H = 1.8 GPa), acier-acier (w = 256N, P_H = 1,6 GPa) et acier-Si_3N_4 (w = 181N, P_H = 1.6 GPa) contacts opérés à T_0 = 298 K et u_e = 0,5 m/s.

En effet, les résultats montrent que, sous une charge normale constante de 256 N, la chaleur générée dans le contact acier-Si_3N_4 (P_H = 1.8 GPa), est légèrement supérieure à celle dans l'acier-acier (P_H = 1.6 GPa), sur la gamme appliquée de SRR [0; 50%]. En revanche, à une pression constante (P_H = 1.6 GPa) mais une charge normale inférieure de 181 N (acier-Si_3N_4), la chaleur générée dans le contact acier-Si_3N_4 est réduite d'environ 30% sur l'ensemble de SRRs appliqués, par rapport aux cas à charge plus élevée (256 N, acier-acier). En d'autres termes, on peut dire que la charge normale domine l'effet de la pression sur la génération de chaleur, indépendamment du fait que les solides en contact soient acier-acier ou acier-Si_3N_4. Notez que le concept d'élévation de température est étroitement lié à celui de génération de chaleur, mais ne doit pas être confondu. Contrairement à la température, la quantité de chaleur est proportionnelle à la masse du lubrifiant considéré. Cette dernière dépend des dimensions du contact. Cela implique le volume de fluide sous pression (aire de contact et épaisseur de film) et le transfert de chaleur dans les solides en mouvement.

L'accord expérience-simulation numérique en termes de pression (partie 3) et de température (fin de la partie 3 & début de la partie 4) et les résultats de la Figure 0-15, fait du modèle numérique un moyen complémentaire utile pour aller plus loin dans l'étude de la répartition de la chaleur dans les deux solides en contact. Ce sujet sera évoqué dans la section suivante.

Flux de chaleur

Afin de prendre en compte tous les transferts d'énergie thermiques dans les corps solides en contact et dans le film lubrifiant, les différents flux thermiques peuvent être intégrés. Ils peuvent être présentés comme indiqué sur la Figure 0-16, pour différents natures de matériaux en contact, taux de glissement et charges.

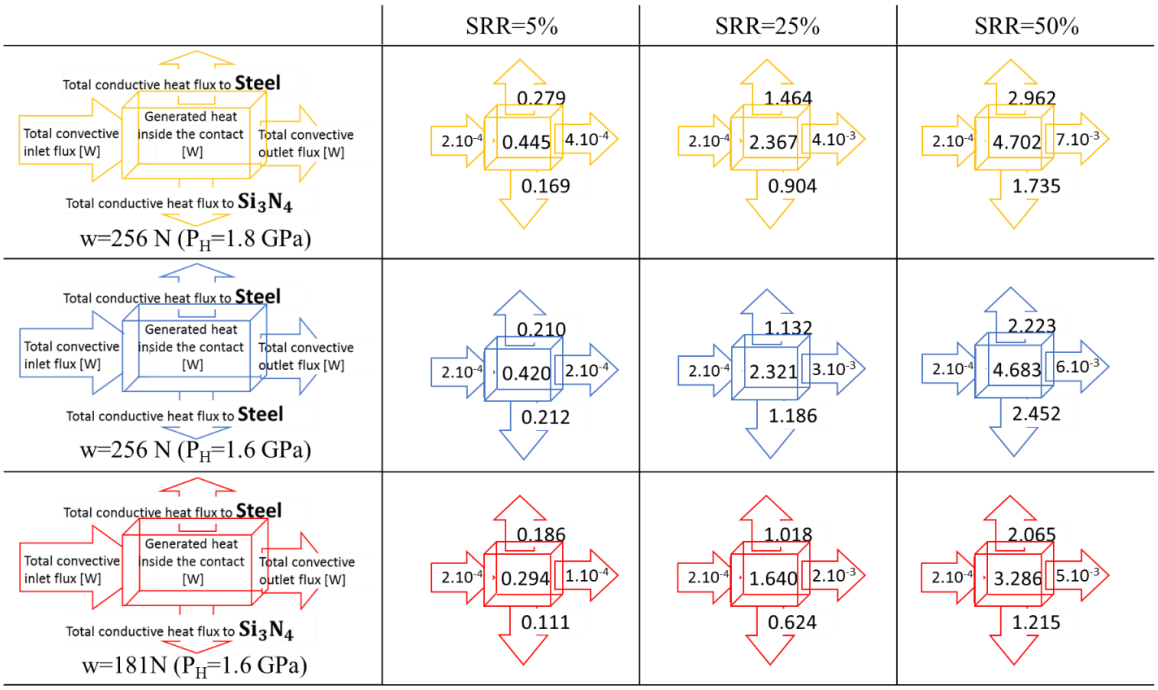

*Figure 0-16: flux de chaleur par convection/*conduction *et chaleur générée dans le volume de lubrifiant dans les contacts - acier-Si_3N_4 (w=256N P_H=1.8 GPa), acier - acier (w=256N P_H=1.6 GPa) and acier -Si_3N_4 (w=181N P_H=1.6 GPa) opérés à T_0=298 K, u_e=0.5 m/s for SRR=5, 25 and 50%.*

On peut noter que, dans ces simulations, le bilan énergétique est pleinement satisfait: la chaleur générée à l'intérieur du lubrifiant est transférée par les différents flux aux 3 éléments qui constituent le contact lubrifié.

Pour une analyse plus détaillée, on peut observer les rapports de flux de chaleur intégrés entre le disque et la bille et comparer l'influence du glissement (SRR) et de la charge normale sur le transfert de chaleur entre les différentes combinaisons de matériaux solides en contact. Ces rapports sont relativement constants pour une combinaison donnée de solides en contact et de charge normale appliquée, indépendamment de la valeur du SRR. En effet, dans les contacts acier-acier, le rapport est proche de 1 car le disque et la bille sont un même matériau. En revanche, dans le cas des contacts acier-Si_3N_4, le rapport est supérieur à 1 car la chaleur est plus facilement conduite dans le disque en acier que dans la bille en céramique (isolant).

Conclusion

Le travail présenté dans ce manuscrit a été motivé par un besoin industriel de mesurer les pressions et températures locales et de comparer la génération de chaleur dans les contacts élastohydrodynamiques (EHD) tout acier et hybrides. Répondre à ce défi représente une voie possible pour une meilleure sélection de la conception (choix des matériaux, conditions de fonctionnement, lubrification, …) des roulements (REB).

Pour atteindre cet objectif, une méthode *in situ* non-intrusive, exploitant la sensibilité de la photoluminescence des boîtes quantiques (QDs) à la pression et à la température, a été développée. Cette technique a un rendement plus efficace en termes de détectabilité, de précision et de fiabilité que les techniques développées précédemment telles que la spectroscopie Raman, la thermographie infrarouge et la résistance électrique, respectivement. Par ailleurs, les résultats expérimentaux ont été comparés aux résultats obtenus à l'aide d'un modèle numérique thermique-EHD.

La première étape de ce travail visait à calibrer la photoluminescence des QDs aux variations de pression et de température dans des conditions statiques et à analyser l'influence des contraintes de cisaillement sur leur réponse dans des conditions contrôlées de température et de cisaillement. Cette calibration a montré le potentiel de cette technique pour mesurer la pression et la température, grâce aux paramètres spectroscopiques que sont l'énergie d'émission et la largeur à mi-hauteur du spectre de photoluminescence des QDs, et ceci malgré l'effet de l'écoulement ou du cisaillement. Les dépendances à la pression et à la température se sont avérées linéaires pour des pressions allant jusqu'à 1.3 GPa et pour des températures de 296 K à 373 K (ou dans des plages inférieures au changement de phase du fluide lubrifiant porteur).

L'étape suivante a été consacrée à la réalisation des mesures de pression et de température *in situ* dans les contacts EHD à l'aide d'un tribomètre bille-disque. Pour employer la technique de photoluminescence, il est impératif d'utiliser au moins un matériau transparent (verre ou saphir) à travers lequel passent à la fois le faisceau laser incident et l'émission en photoluminescence des QDs. Cependant, ces disques transparents présentent une fluorescence parasitique qui, bien que faible, ne permet pas de décorréler le signal de ces disques de celui de QDs en ce qui concerne la largeur à mi-hauteur du signal. Seule l'énergie d'émission, qui dépend à la fois de la pression et de la température, peut être utilisée. Pour découpler les effets, l'approche consiste à d'abord réaliser des mesures en conditions isothermes (roulement pur, vitesses d'entrainement faibles) afin d'extraire les variations de pression. Puis, pour des conditions de fonctionnement identiques, mais en ajoutant du glissement, réaliser à nouveau des mesures pour extraire les variations de températures dues à l'échauffement du lubrifiant.

Les mesures *in situ* ont été effectuées pour différentes combinaisons de solides en contact : verre-acier, saphir-acier, verre-Si_3N_4 et saphir-Si_3N_4. Un bon accord entre les résultats expérimentaux et numériques en termes de pression et de température ont été révélés; ce qui démontre la faisabilité de la méthodologie proposée. Une étude numérique a été élaborée pour

quantifier la pression, la température ainsi que la génération de chaleur dans les contacts EHD acier-acier et acier-Si_3N_4 (qui sont contacts représentatifs des contacts réels). Les effets de glissement, de la charge normale et des propriétés thermiques des matériaux ont été mis en évidence. Les principaux résultats trouvés sont les suivants:

- pour une combinaison de matériaux en contact, l'augmentation de la charge normale augmente la pression, la température et la chaleur générée dans le volume de lubrifiant comprimé.

- sous une même charge normale, l'utilisation d'une bille en Si_3N_4 au lieu d'une bille en acier 100C6 entraîne une augmentation à la fois de la pression locale (en raison du module d'Young plus élevé) et de la température (en raison de l'influence de la pression plus élevée et des propriétés des lubrifiants et de la chaleur spécifique de la céramique).

- quels que soient les solides en contact, acier-acier ou acier-Si_3N_4, la charge normale appliquée et la vitesse de glissement se révèlent être les paramètres clés qui modifient la génération de chaleur à l'intérieur du contact.

- la relation proportionnalité des flux thermiques transférées par conduction entre le disque et la bille qui reste constante malgré les effets de glissement et de la charge normale.

La validité de ces résultats a été corroborée avec succès grâce aux comparaisons entre la chaleur générée (calculée à l’aide du modèle numérique) et les pertes de puissance (dérivées des essais de frottements) dans des conditions de roulement-glissement. En effet, ces résultats confirment l'équilibre énergétique entre l'énergie mécanique et l'énergie thermique interne (chaleur générée).

Nomenclature

Variable	Unit	Description
		Roman characters
a	$[m]$	Contact Radius (circular contact)
a_0	$[GPa^{-1}]$	Hybrid model constant
a_1	$[K.GPa^{-1}]$	Hybrid model constant
a_2	$[K^2.GPa^{-1}]$	Hybrid model constant
A_k, C_k, s	$[\ -\ ]$	Lubricant thermal conductivity scaling rule parameters
a_v	$[K^{-1}]$	Coefficient of thermal expansion of the Tait model
B	$none$	Number of atoms and molecular orbitals
b_H	$[m]$	Hertzian half width of the Contact
b_0	$[\ -\ ]$	Hybrid model constant
b_1	$[K]$	Hybrid model constant
C_F	$[\ -\ ]$	Hybrid model constant
c	$[g.L^{-1}]$	concentration
c_0	$[GPa^{-1}]$	Hybrid model constant
c_1	$[K.GPa^{-1}]$	Hybrid model constant
c_2	$[K^2.GPa^{-1}]$	Hybrid model constant
C_0	$[J.m^{-3}.K^{-1}]$	Lubricant volumetric heat capacity scaling rule parameter
C_{pf}	$[J.kg^{-1}.K^{-1}]$	Lubricant heat capacity
C_{pd}, C_{pb}	$[J.kg^{-1}.K^{-1}]$	Heat capacities of the disc and the ball
C_v	$[J.m^{-3}.K^{-1}]$	Lubricant's volumetric heat capacity
d_{spot}	$[m]$	Spot diameter
d_{beam}	$[m]$	diameter of the incident beam
D_F	$[\ -\ ]$	Fragility parameter in the Hybrid model
D	$[\ m^2.s^{-1}]$	Thermal diffusivity
D_d, D_b	$[\ m^2.s^{-1}]$	Thermal diffusivities of the disc and the ball
DoF	$[\ -\ ]$	Degree of freedom
E	$[eV]$	Energy
E_{eq}	$[Pa]$	Equivalent Young modulus
E_{inlet}	$[eV]$	Inlet emission energy
E_g	$[eV]$	Bandgap energy
E_{g0}	$[eV]$	Bandgap energy at zero kelvin and atmospheric pressure
E_r	$[Pa]$	Reduced Young modulus $(2/E_r\ = (1-\nu_t^2)/E_t + (1-\nu_b^2)/E_b)$
E_d, E_b	$[Pa]$	Young moduli of the disc and the ball
f	$[m]$	Focal distance
F_x	$[N]$	Force in the *x*-direction
$FWHM$	$[eV]$	Full-width at half maximum
$FWHM_0$	$[eV]$	Full-width at half maximum at zero kelvin and atmospheric pressure

G_C	$[-]$	Chittenden dimensionless material parameter ($G_C = \alpha^* E_{eq}$)
h	$[m]$	Film thickness
$\hbar$	$[m^2.kg.s^{-1}]$	Reduced Planck constant
H, H_0	$[m]$	Gap between the rotating disc and the plate in the rheometer
H_C	$[-]$	Chittenden dimensionless film thickness
h_0	$[m]$	EHD gap between the rigid bodies at O
h_c	$[m]$	Film thickness at the contact centre, $(x; y) = (0; 0)$
h_{min}	$[m]$	Minimum film thickness
$HWHM$	$[eV]$	Half-width at half maximum
I	$[u.a]$	Intensity
I_{max}	$[u.a]$	Maximum intensity
K	$[-]$	Chittenden parameter
k	$[cm^{-1}]$	Wave number
k_f	$[W.m^{-1}.K^{-1}]$	Lubricant thermal conductivity
κ_f	$[-]$	Thermal conductivity parameter
k_d, k_b	$[W.m^{-1}.K^{-1}]$	Thermal Conductivities of the disc and the ball
K_0	$[Pa]$	Isothermal bulk modulus at atmospheric pressure
K_0'	$[-]$	Pressure rate of change of isothermal bulk modulus
K_{00}	$[Pa]$	Isothermal bulk modulus at zero absolute temperature
L	$[-]$	Moes dimensionless material parameter $L = G_C(2U_C)^{1/4}$
M	$[-]$	Moes dimensionless load parameter $M = W_C(2U_C)^{-3/4}$
M_p	$[kg.m.s^{-1}]$	Particle momentum
m	$[kg]$	Particle or quasi-particle mass
m^*	$[J.m^{-3}.K^{-1}]$	Lubricant volumetric heat capacity scaling rule parameter
m_{pear}	$[-]$	Pearson VII shape parameter
N	$none$	Quantum number
n	$none$	Power law exponent of the Carreau equation
n_t	$none$	Total number of data
P	$[Pa]$	Pressure
P_0	$[Pa]$	Atmospheric pressure
P_∞	$[Pa]$	Hybrid model parameter
P_{center}	$[Pa]$	Central EHD pressure
P_{exp}, P_{num}	$[Pa]$	Experimental and numerical pressures
P_H	$[Pa]$	Hertz pressure
P_{iso}	$[Pa]$	Isothermal experimental pressure
P_g	$[Pa]$	Glass transition pressure at a given temperature
PWL	$[W]$	Power losses
PWL_{hybrid}	$[W]$	Power losses in a hybrid contact
PWL_{steel}	$[W]$	Power losses in all-steel contact
Q_{comp}	$[J]$	Compression heat source

Q_{shear}	$[J]$	Shearing heat source
Q_{th}	$[-]$	Dimensionless thermal parameter $Q_{th} = (-\partial\eta/\partial T)\left(u_e^2/k_f\right)$
q	$[-]$	Hybrid model parameter
q^*	$[-]$	Coefficient in the dimensionless conductivity scaling parameter
R	$[m]$	Radius of the rotating plate in the rheometer
R_{corr}^2	$[-]$	Coefficient of correlation in regressions
R_{eq}	$[m]$	Equivalent radius of curvature
R_x	$[m]$	Radius of curvature of equivalent elastic solid in the x-axis (in the entrainment direction)
R_y	$[m]$	Radius of curvature of equivalent elastic solid in the y-axis
R_{dx}, R_{bx}	$[m]$	Principal curvature radii of the disc (d) and ball (b) surfaces, in the xz-plane.
r	$[m]$	Radius from the rotational axis in the rheometer
r_{Bohr}	$[m]$	Bohr radius
r_{spot}	$[m]$	spot radius
r_{QD}	$[m]$	Quantum dot radius
S	$[m^2]$	Contact surface
S_p	$[\,eV.GPa^{-1}\,]$	Pressure sensitivity of the energy peak (linear relation)
S_T	$[\,meV.K^{-1}\,]$	Temperature sensitivity of the energy peak (linear relation)
S_T'	$[\,meV.K^{-1}\,]$	Temperature sensitivity of peak full-width at half maximum
SCE	$[-]$	sum-of-squares of deviations
SRR	$[\%]$	Slide to roll ratio
T	$[K]$	Temperature
T_0	$[K]$	Inlet or environmental temperature
T_g	$[K]$	Glass transition temperature at a given pressure
T_R	$[K]$	Reference conditions temperature
T_∞	$[K]$	Divergence temperature Hybrid model
ΔT	$[K]$	Temperature rise
ΔT_{exp}	$[K]$	Experimental temperature rise
ΔT_{num}	$[K]$	Numerical temperature rise
U_C	$[-]$	Dimensionless Chittenden velocity ($U_C = \mu_0 u_e/(E_{eq}R_b)$)
u_e	$[m.s^{-1}]$	Mean entrainment velocity
u_{top}, u_{bottom}	$[m.s^{-1}]$	Velocities of top and bottom solids
u_d, u_b	$[m.s^{-1}]$	Velocities of the disc and the ball
Δu	$[m.s^{-1}]$	Sliding veleocity
u_f	$[m.s^{-1}]$	Lubricant velocity field
u_{fx} , u_{fy}	$[m.s^{-1}]$	Lubricant velocity field components, in the x and y directions, respectively
V	$[m^{-3}]$	Volume
V_0	$[m^{-3}]$	Volume at the contact environment conditions

V_R	$[m^3]$	Volume at the reference conditions
w	$[N]$	Normal Load
W_C	$[-]$	Chittenden dimensionless load parameter ($W_C = w/(E_{eq}R_b^2)$
x, y, z	$[-]$	Coordinates of the 3D space
X, Y, Z	$[-]$	Coordinates of the dimensionless 3D space

Greek characters

α^*	$[Pa^{-1}]$	Reciprocal asymptotic isoviscous pressure coefficient
α'	$[meV.K^{-1}]$	Temperature coefficient in Varshni law
α_0	$[Pa^{-1}]$	Initial pressure–viscosity coefficient in the Hybrid model
α_1	$[meV.K^{-1}]$	Temperature coefficient in the linear approximation of Varshni law
α_2	$[meV.GPa^{-1}]$	Constant in the linear and quadratic approximations of $E_g$variation with pressure
β	$[K]$	Temperature close to the Debye temperature in Varshni law
β_2	$[meV.GPa^{-2}]$	Constant in the quadratic approximation of Eg variation with pressure
β_K	$[K^{-1}]$	Bulk modulus-temperature coefficient
$\dot{\gamma}$	$[s^{-1}]$	Shear rate
δ	$[m]$	Deformation sum of the mating bodies, in the z direction
θ_D	$[K]$	Debye temperature
λ	$[m]$	wavelength
λ_h	$[-]$	The ratio of the minimum film thickness to the combined surface roughness of the bounding solids
λ_R	$[s]$	Relaxation time at T_R and ambient pressure
$\mu\ /\ \eta$	$[Pa.s]$	Newtonian viscosity / non-Newtonian viscosity
μ_e, η_e	$[Pa.s]$	Viscosity integral number 1
μ_e', η_e'	$[Pa.s]$	Viscosity integral number 2
μ_R	$[Pa.s]$	Low shear viscosity at T_R and ambient pressure
μ_0	$[Pa.s]$	Viscosity at ambient pressure and at $T = T_0$
$\mu_{0\infty}$	$[Pa.s]$	Low-shear viscosity for zero argument of the exponential in the Hybrid model
μ_{decay}	$[m]$	Mean of cumulative distribution function
ν	$[-]$	Equivalent Poisson ratio
ν_d, ν_b	$[-]$	Poisson ratios of the disc and the ball
ρ	$[kg.m^{-3}]$	Lubricant density
ρ_0	$[kg.m^{-3}]$	Density at the contact environment conditions
ρ_e, ρ_e'	$[kg.m^{-3}]$	Density integral number 1 and 2
ρ_d, ρ_b	$[kg.m^{-3}]$	Densities of the disc and the ball
ρ_R	$[kg.m^{-3}]$	Density at the reference conditions
σ	$[Pa]$	Stress tensor
$\sigma_{deviation}$	$[-]$	Standard deviation
σ_{RA}	$[nm]$	Arithmetical average of the surface roughness

σ_{RMS}	$[nm]$	Root mean squared of the surface roughness
σ_1, σ_2	$[nm]$	the root mean square roughness of contacting solids 1 and 2
τ	$[Pa]$	Shear stress
ϕ	$[-]$	Cumulative distribution function
ω	$[rd.s^{-1}]$	Angular velocity
φ_T	$[-]$	Cheng thermal coefficient

Abbreviations

B&W	Black and white image
CCD	Charge-coupled device
DAC	Diamond anvil cell
DLC	Diamond-Like Carbon
EHD	Elastohydrodynamic
EHL	Elastohydrodynamic lubrication
IR	Infrared
LSS	Limiting shear stress
NP	Nanoparticle
PL	Photoluminescence
PRI	Pure rolling isothermal tests
PRNI	Pure rolling non-isothermal tests
QDs	Quantum dots
REBs	Rolling element bearings
RMS	Root mean square
RSNI	Rolling-sliding non-isothermal tests
SQ	Squalane
Si_3N_4	Silicon nitrite
TEM	Transmission electron microscopy
TEHD	Thermal elastohydrodynamic model
5P4E	Polyphenyl ether (m-bis(mphenoxyphenoxy)benzene)

General Introduction

Minimizing friction and heat dissipation for longer high-speed operations is the main challenge of aerospace and automotive industry. Over decades, numerous studies have been conducted on optimizing the elastohydrodynamic lubrication (EHL) regime under which most of the rolling element bearings (REBs) are operated. In such conditions, the lubricant is subjected to high pressure, shear stress and temperature rise that influence its rheological and frictional behavior within the contact.

In this work, the industrial goal is to quantify pressure and temperature profiles as well as to compare dissipated heat in all-steel and hybrid (ceramic (Si_3N_4)-steel) circular elastohydrodynamic (EHD) contacts, like the ones found in rolling element bearings.

It is important to note that various experimental methods, such as Raman spectroscopy, electrical resistance and infrared thermography, were carried out to probe (EHD) contacts in terms of pressure or temperature. However, despite achievements, there is a continuous need to measure, with finer resolution and accuracy and, if possible, simultaneously these two relevant thermodynamic parameters in order to acquire a better understanding of the EHL in all its complexity. For that, within this framework, a new *in situ* technique is chosen to be developed in order to measure both the pressure and temperature throughout EHD contacts. Moreover, in this study, a thermal EHD (TEHD) numerical model is used in order to validate measurements.

The experimental technique consists in dispersing photoluminescent (PL) nanosensors, called quantum dots (QDs), sensitive to the temperature and pressure variations in the lubricant. In this work, the used nanosensors are semiconductors developed in the form of CdSe/CdS/ZnS core/shell/shell QDs, and functionalized to be dispersed in an alkane fluid.

In this regard, a calibration procedure is performed in order to evaluate the QDs pressure and temperature photoluminescence sensitivity. Subsequently, the feasibility of the proposed methodology is investigated through the comparison between the measured and the simulated pressure/temperature values, obtained within EHD contacts of different operating conditions and combinations of contacting solids.

The manuscript consists of four chapters. The first chapter begins by introducing general notions about the REBs and lubrication regimes. Then, two important aspects are described: the EHL regime and its encountered parameters. Some widely used methods to probe EHD contacts are presented. The necessity to develop a new *in situ* technique, to fulfil the industrial challenge, is supported.

The second chapter provides a description of the physics and properties of the chosen nanosensors (CdSe/CdS/ZnS QDs). It also presents the calibration tools and procedures. The calibration curves reveal the pressure and temperature sensitivity of the photoluminescence spectroscopy parameters of the QDs.

In the third chapter, the experimental tool simulating representative EHD contacts is described. Measurement of pressure and temperature are performed for different combinations of contacting solids: glass-steel, sapphire-steel, glass-Si_3N_4 and sapphire-Si_3N_4. In order to verify the validity of the PL spectroscopic method, comparisons between experimental results and

numerical solutions in terms of pressure and temperature distributions along the contact centerline are elaborated and discussed. The performance of the developed method among the state of the art competing techniques is summarized.

In chapter four, the influence of the slide-to-roll ratio (SRR) on the temperature rise at equivalent normal loads and Hertzian pressures is studied, again for different combinations of contacting solid materials. Comparison between simulated heat generation and experimental power losses is carried out in order to validate the conservation between the transmitted mechanical energy and the internally generated energy within the contact, and also to provide relevant results to the industrial application. This closing chapter offers a discussion about the findings, achievements and limitations of this work.

Finally, a general conclusion is proposed to summarize the main outcomes of this work and to suggest some perspectives.

Chapter 1: Context & state of the art

Chapter 1: Context & state of the art 49
1.1 Introduction 51
1.2 Rolling element bearings 51
1.2.1 Rolling element bearings types 51
1.2.2 Rolling element bearings materials 52
1.2.3 Rolling element bearings lubrication - Elastohydrodynamic lubrication 52
1.3 Experimental techniques for studying EHD contact 56
1.3.1 Optical interferometry for film thickness measurement 56
1.3.2 Raman spectroscopy for pressure measurement 57
1.3.3 Infrared thermography for temperature measurement 59
1.3.1 Electrical resistance for pressure and temperature measurement 63
1.4 Pressure and temperature in steel and hybrid EHD contacts - Industrial challenge .. 65
1.5 Heat generation in hybrid and all-steel bearings - Literature overview 67
1.6 Summary and aim of the work 68

1.1 Introduction

This chapter aims to present the context and the industrial challenge to overcome. A general framework on rolling element bearings (REBs) is reviewed. The selection of the elastohydrodynamic lubrication (EHL) regime is justified. Some experimental works devoted to study elastohydrodynamic (EHD) contacts that have found a wide acceptance are covered. A brief description of the tribological behavior of steel–steel and hybrid (ceramic–steel) lubricated contacts is reported. Finally, the interest of developing *in situ* technique to measure pressure and temperature throughout EHD contacts is defended.

1.2 Rolling element bearings

Rolling element bearings (REBs) consists of two rings which maintain a set of rolling elements (such as balls or rollers) arranged in a row and held within a cage. This setup allows reducing massively rotational friction while supporting radial loads (transmitted through the discrete contacts between the rolling elements and the two rings). Thus, this enables REBs to sustain high loads, to achieve relatively high rotational speeds while reducing energy consumption. In most of applications, REBs are lubricated I) to ensure the separation between moving surfaces II) to carry away the heat generated by friction, and III) to carry away internally generated debris and external contaminants from the rolling tracks. Otherwise, fatigue and abrasion will lead to the bearing failure. Most of research up to date has focused on optimizing REBs design and lubrication thereby enhance their performances.

1.2.1 Rolling element bearings types

There are two basic types of REBs: ball bearings and roller bearings (see Figure 1-1). Ball bearings may transmit not only radial but also axial loads through the balls from one ring to the other. Balls induce point contacts with the ring raceways. By increasing the load, the contacts develop into circular or elliptical areas.

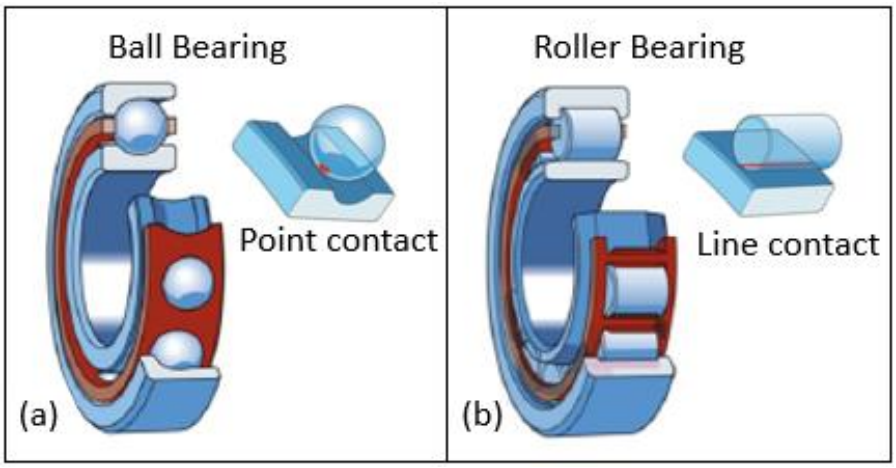

Figure 1-1: Two most common REBs. (a) Angular contact ball bearing. (b) Cylindrical roller bearing (source: SKF).

In general, contact areas are small and allow the ball bearings to accommodate higher speeds compared to the ones formed in roller bearings (rectangular shape contacts). However, significant normal load may cause large deformation of the balls and rings, thus leading to bearing failure. This is why ball bearings are used to carry lighter loads than roller bearings in which the load is distributed over a larger area of contact. Nevertheless it is important to underline that even under moderate normal load, the stresses nearby the contact zone are quite high.

1.2.2 Rolling element bearings materials

Under service conditions, especially in aerospace applications, REBs have to endure high loads, high rotating speeds and high temperatures. The choice of the bearing's materials is therefore crucial. It is important to note that one cannot fulfill all the requirements for a given application with only one material [38]. This is why, in order to prevent failure of REBs in operation, bearing materials must be selected based on essential properties like elasticity, thermal conductivity, hardness, fatigue resistance, wear resistance, corrosion resistance, etc...

Generally, bearings are entirely made of ferrous alloys like steel, especially with low carbon content like the widely used 100C6 (or AISI 52100) steel. In the last decades, researches have introduced new harder and lighter materials like ceramics [39]. These latter may exhibit more resistive behavior to corrosion, heat and wear than ferrous alloys [40]. However, they have lower toughness, fracture resistance and are not able to sustain shocks. Today, a rather large number of bearings are made, more often partially, from a variety of ceramics including alumina, silicon carbide, titanium carbide, and silicon nitride [39].

1.2.3 Rolling element bearings lubrication - Elastohydrodynamic lubrication

The main role of REBs lubrication is to reduce friction and wear by ensuring a minimum separation between the contacting solids (see Figure 1-2). This strategy extends the contact lifetime, lessens the power losses and allows to accommodate high velocities/shear stresses. The lubricant is most commonly oil or pasty, like grease: it is chosen based on the application requirement. In both cases, it is found that the lubricant acts like oil at the infinitesimal contact level. Indeed, grease can be considered as a static oil sponge that releases oil from the contact borders (under mechanical stress) [41].

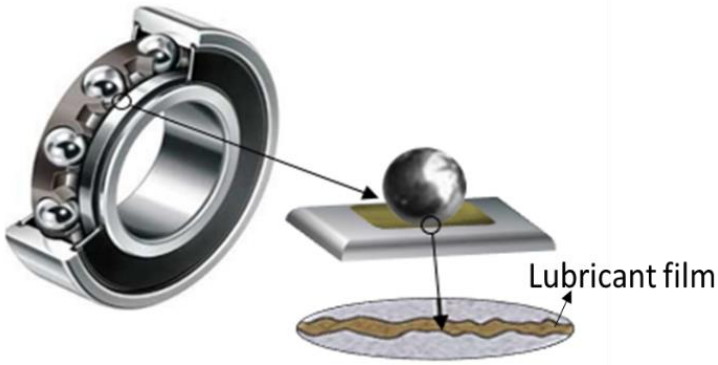

Figure 1-2: Lubrication observed in the contact between the inner ring and a ball in an all-steel ball bearing.

The longevity of the contact depends on many parameters such as the lubricant's viscosity, load stresses, sliding speed, presence of particles etc… Improving the lubricant efficiency may rely on adapting the viscosity characteristics of the base oil and the chemistry of the additives. Despite the fact that the use of low viscosity oils is favored for a better fuel economy, their use is limited by durability concerns. There are three different regimes of lubrication which can be identified from the so-called Stribeck curve: I) Hydrodynamic, II) Mixed and III) Boundary lubrication (Figure 1-3).

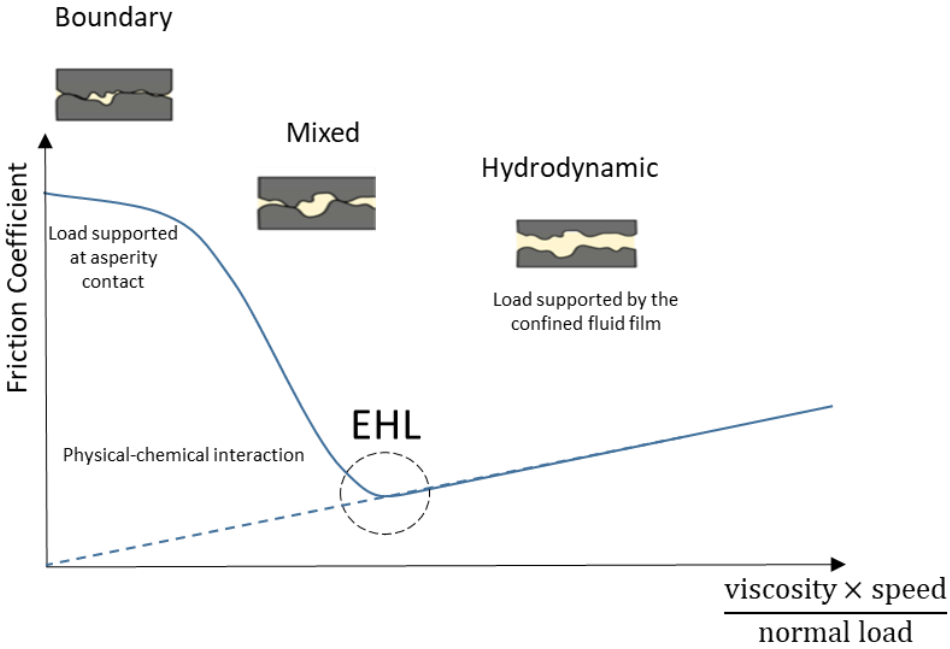

Figure 1-3: Stribeck curve.

The Stribeck curve describes the different operating conditions by a mean of a parameter defined as the product of sliding speed and lubricant viscosity divided by the applied normal load. The Stribeck curve can also be expressed as a function of the ratio (λ_h) of the contact minimum film thickness (h_{min}) to the combined surface roughness of the bounding solids. This ratio can be written as follows:

$$\lambda_h = \frac{h_{min}}{\sqrt{({\sigma_1}^2 + {\sigma_2}^2)}} \qquad 1.1$$

where σ_1, σ_2 the RMS (root mean square) roughness of contacting solids 1 and 2.

λ_h is considered as a useful indicator to distinguish between different lubrication regimes, and thus to evaluate the level of surface interaction between rolling elements (see Table 1-1).

$\mathbf{3 < \lambda_h}$	Hydrodynamic (full-film) regime
$\mathbf{1 \leq \lambda_h \leq 3}$	Mixed regime
$\mathbf{\lambda_h < 1}$	Boundary regime

Table 1-1: Lubrication regimes in function of the ratio λ_h [42].

In the case of hydrodynamic lubrication, the lubricant film completely separates the contacting surfaces. Elastohydrodynamic lubrication (EHL) is a particular case of hydrodynamic lubrication. Among the different lubrication regimes, EHL lies in the compromising lowest region of the hydrodynamic regime at which friction and film thickness are at the lowest (see Figure 1-3 and Table 1-1). This is the typical lubrication regime of non-conformal contacts such as those found in REBs. As displayed in Figure 1-2, within an EHL contact, the lubricant film is severely confined between sliding and supporting surfaces (ring raceways and rolling elements). The concentrated pressure in this small region is extremely high. This causes an important elastic deformation of the rubbing bodies and a huge increase of the lubricant viscosity which prevents the lubricant from being entirely squeezed out and thus allows the formation of a lubricating film at the contact level. That is why the place of the EHD regime in the Stribeck curve corresponds to the piezo-viscous elastic regime in the classification based on the liquid and solid behaviors; piezo-viscous as the liquid's viscosity is pressure dependent, and elastic as the solid is elastically deformed.

Indeed, the lubricant properties (viscosity and density) varies with pressure and temperature. Moreover, viscosity which can be defined as the degree of the fluid resistance to motion, may be affected significantly by shear stress. For this reason, the lubricant viscosity at the contact inlet, where the lubricant recirculation is the main cause of the shearing between its layers, has a direct impact on the formation of the lubricant film within the contact, and thus influences its frictional behavior. For example, fluids with higher viscosity (which do not flow easily) form thicker films between the moving surfaces, hence can support higher loads. However, higher viscosity leads to higher friction and excessive heating. To avoid this as much as possible, a good compromise on viscosity must be found by selecting a proper lubricant in function of the applications and the specifications required by the manufacturer.

In EHL, the contact diameter is about a few hundred µm and the film thickness is much less than 1 µm. This means that only some picoliters of the lubricant are continuously confined. Pressure ranges from 0.5 to 3 GPa, causes elastic deformation of the contacting solids (by an order of magnitude at least larger than film thickness) and a significant increase of the lubricant's viscosity (by an order of magnitude every 25 to 250 MPa). With shear stresses ranging from some KPa to some MPa and strain rates from 10^5 to $10^7 s^{-1}$, friction causes self-heating of the lubricant which can reach several tens of degrees. It is important to mention that at some point (beyond a certain temperature and pressure) for a given lubricant, the shear stress may become insensitive to shear rate. This phenomenon is known as the limiting shear stress (LSS). Its origin is not fully understood up to date [43].

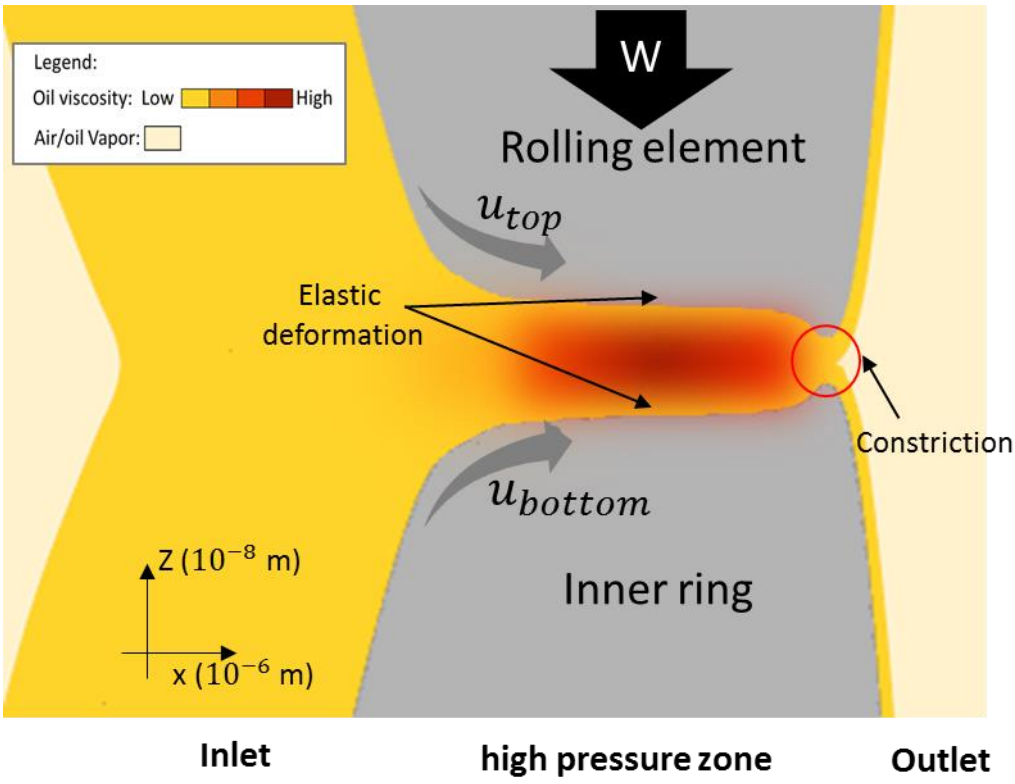

Figure 1-4: Schematic of the lubricant film approximate viscosity gradient within the EHD contact, inspired from [44].

To be more precise, the EHD contact can be divided into three distinctive zones, as illustrated in Figure 1-4:

I. The inlet or the hydrodynamic zone, where the lubricant is entrained first through a Couette flow. It is important to know that the inlet's relative position depends, among other parameters, on the speed magnitude and direction of the two moving solid surfaces.

II. The high pressure zone: the lubricant is entrained in the reduced gap between the elastically deformed solids surfaces leading to its severe compression. This forms an almost constant film thickness where the oil viscosity increases almost exponentially with pressure (piezo-viscous effect).

III. The outlet: the lubricant is dragged to the outlet away from the contact mostly through a Poiseuille flow. A sudden steep pressure drop provokes a breakdown of the film and leads to the formation of the liquid/vapor meniscus (under pure rolling). Notice that just before the outlet, there is a constriction in which a sudden decrease in the film thickness associated to a narrow pressure peak, known as the Petrusevich spike, occurs. This flow constriction is required to maintain the continuity of the flow and to prevent the lubricant from leaking out.

1.3 Experimental techniques for studying EHD contact

The determination of the EHD regime circumstances have been the result of numerous experimental, numerical and analytical studies. The complexity of understanding the behavior of a lubricated contact arises mainly, apart from its very reduced dimensions and the presence of high gradients, from the coupling between the local stresses induced by the contacting solids and the physical and rheological behavior of the lubricant. Indeed, in the EHD regime, the lubricant film thickness is mainly controlled by its rheological behavior at the contact inlet. In turn, the rheological properties of the lubricant are directly related to the local temperature and pressure that are encountered at each point of the contact area.

Various numerical models/approaches have emerged providing more or less relevant tools to investigate the effect of viscosity, pressure and temperature on EHD parameters such as film thickness. Dowson and Higginson were the first to investigate EHD point contacts and to obtain a numerical solution under isothermal Newtonian conditions [45]. Najji et al.[46], Habchi et al.[47] and Peiran et al. [48] introduced non-Newtonian and thermal effects in order to reach more realistic predictions of rolling-sliding contacts. Canzi, Venner and Lubrecht have developed a model that predicts the lubricant film thickness for various contact ellipticity ratios [49], [50]. Despite these achievements, the search for more physical results is always ongoing by incorporating critical parameters, for instance like the limiting shear stress of the lubricant and the surface roughness of the solids.

Parallel to the numerical modeling progress, different *in situ* methods have been developed to probe EHD contacts. Indeed, it is crucial to compare and validate the numerical solutions with experimental results via one or more parameters such as film thickness, pressure, temperature, viscosity, shear stress, etc... Spikes [1], Albahrani et al. [2] and Kumar et al. [3] have reported most of these methods in literature reviews. Generally, the experimental techniques are classified into three categories: optical, electrical and acoustic.

The next sections do not provide a full picture of all the developed *in situ* methodologies for studying EHL. They aim to give an overview of the main developed methods to measure relevant parameters such as pressure, temperature as well as film thickness.

1.3.1 Optical interferometry for film thickness measurement

Optical (white light) interferometry is considered as the most effective technique to measure the lubricant film thickness in EHD contacts. Since its introduction by Gohar and Cameron [51] to validate the emerging EHL theory, development in terms of image analysis procedure by Gustaffson et al. [52] and the introduction of a spacer layer which allows the measurements of the film thickness down to few nanometers by Westlake and Cameron [53], it becomes the most widely used *in situ* method. Indeed, it is of considerable interest to evaluate in real-time a key parameter such as film thickness in the contact, in particular the minimum thickness with respect to the surface roughness. This evaluation indicates the evolution of lubrication regime

(see Table 1-1). Hence, it allows a better prediction of service operating conditions, and thus, allows optimizing the mechanical system performance.

It is important to highlight that the main advantage of optical interferometry is that a single captured image (interferogram) gives a full quantitative picture of the film thickness formed in the contact zone and surrounding (see Figure 1-5). On the other hand, the major drawback of this technique lies in the necessity of using one transparent smooth material like glass or sapphire through which optical visualization can take place. Thanks to the performed intensive experimental studies, semi analytical models were established for predicting central and minimal film thicknesses in circular contacts with an uncertainty reaching the average values of 9% and 37% respectively, based on predictions from a full numerical model [54].

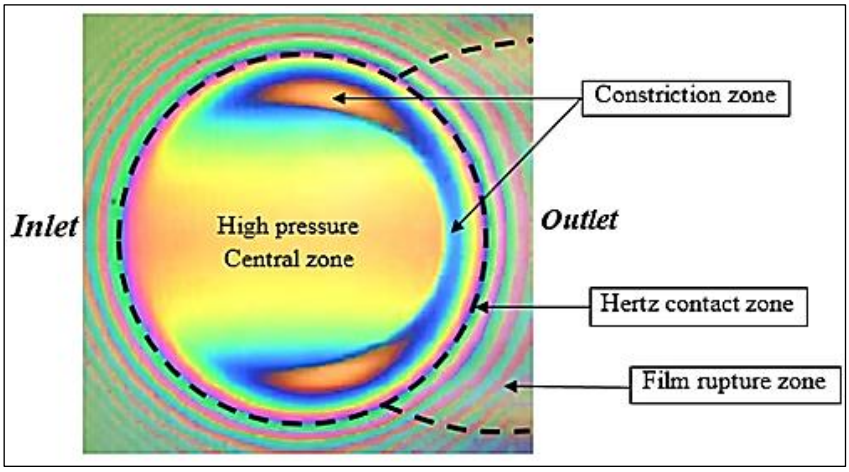

Figure 1-5: The different zones of an EHD contact on a white-light interferogram [24].

1.3.2 Raman spectroscopy for pressure measurement

Raman effect designates the inelastic light diffusion of a sample illuminated by a monochromatic light. The Raman spectrum represents the vibrational energy of the sample and provides information about the chemical structure and bonds of its molecules. This fact also offers the possibilities for measuring:

- The pressure and temperature that influence the molecule structure/interatomic distance and consequently provokes shifts in vibrational energy. It is important to notice that the temperature can be determined in another way through the ratio of Stokes and anti-Stokes peaks relative intensities.

- The film thickness by exploiting the intensity of the Stokes line, which is proportional to the number of excited molecules.

Gardiner et al. [55] were among the first to introduce Raman spectroscopy for pressure measurement in a lubricated contact. They used polyphenyl ether (5P4E) which is an excellent Raman scatterer. The pressure-sensitivity of this fluid was calibrated in a high-pressure hydrostatic cell. Then, Hutchinson et al. [56] measured the film thickness profile in a static

highly-loaded contact between a steel ball and a diamond window (see Figure 1-6). This was done after elaborating a calibration procedure for film thicknesses between 0.1 to 10 µm.

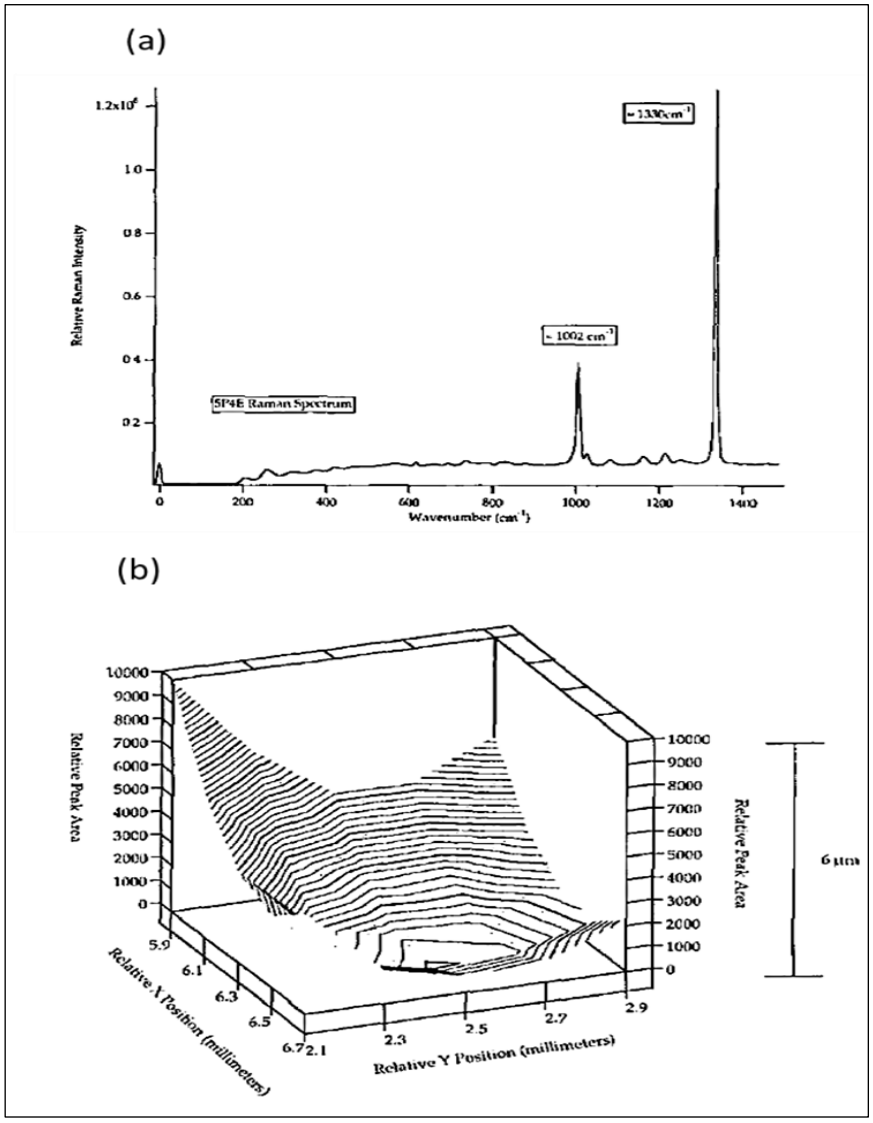

Figure 1-6: (a) Raman spectrum of 5P4E with a peak located at 1002 cm^{-1}, and the diamond window band at 1330 cm^{-1}. (b) Raman film thickness mapping: 5P4E in ball-on-plane static contact [56].

Jubault et al. [57] used the same liquid and performed some EHD validation tests using the pressure and temperature sensitivity of the molecules vibrational frequency reported in the literature: [58]. As results, they have confirmed that the molecules vibrational frequency is sensitive of about 3.3 cm^{-1}/GPa and its temperature sensitivity is negligible by comparing their experimental results with the analytical and numerical predictions. By using a coupled system consisting of an EHD tribometer and a high-resolution Raman spectrometer, they succeeded to extract pressure profiles and even observed the Petrusevich pressure spike located at the contact exit, as illustrated in Figure 1-7.

It is important to note that Jubault et al. used a two-stage monochromator with two 600 gr/mm gratings to disperse the Raman spectra on a CCD detector. This results in a spatial dispersion less than 0.4 cm^{-1}/pixel, and thus provides an excellent resolution of ±0.1 cm^{-1}, yielding a pressure precision of ±0.03 GPa. On the other hand, they increased the acquisition time of each spectrum in order to get a sufficient signal-to-noise ratio.

This method has the advantage of a very small probe size which is approximately 11 µm (laser spot diameter) comparing to the contact diameter in the range of 200-550 µm. However, its main drawback lies in the intrinsic weakness of the Raman signal of most lubricants like mineral oils, esters, alkanes, etc. Furthermore, this technique seems to be inoperable for contacts in which a very little amount of lubricant film is present (i.e. with very thin films), because of the very low signal to noise ratio, but this issue is common to all spectroscopic methodologies. This fact becomes difficult to overcome by simply using a powerful laser source that in turn may generate stronger Raman peak because it may provoke heating and even breakdown the lubricant film or the lubricant molecular bonds.

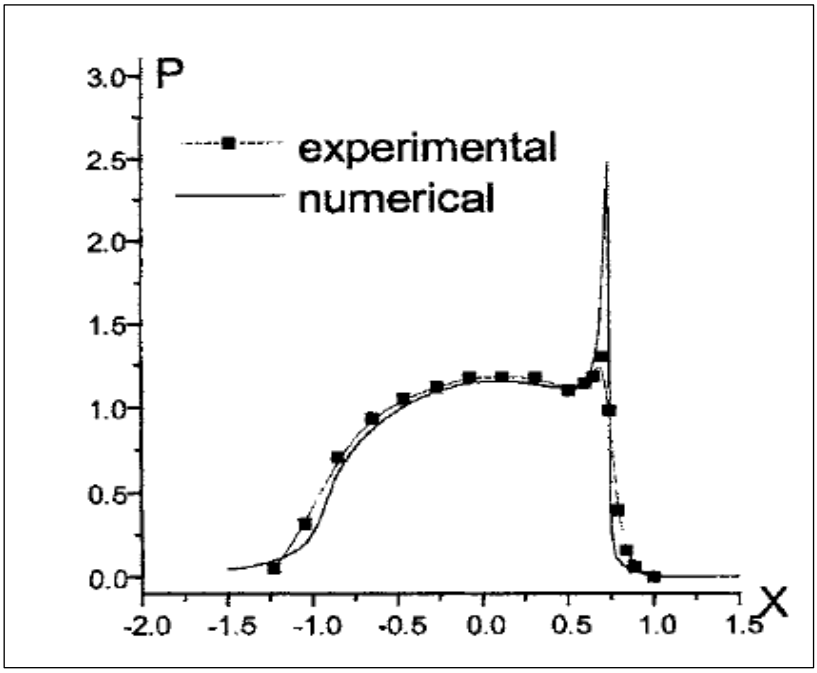

Figure 1-7: Comparison between an experimental dimensionless central pressure profile obtained by Raman spectroscopy and the numerical solution of the EHD problem. For w = 17 N, u_e = 0.3 m/s, T_0 = 323 K [6].

1.3.3 Infrared thermography for temperature measurement

Infrared thermography is a technique used to measure the infrared radiation emitted from samples. In general, this radiation is converted into temperature using combined calibration/analytical techniques. In the 1970s, Winer and co-workers were the first to use such technique to measure average temperatures in EHD contacts formed between a sapphire disc and a steel ball [59], [60]. Their experimental methodology involves the use of IR radiometric detector and filters. It also requires to perform some calibrations in order to separate four

sources of radiation: background, transparent disc (sapphire), lubricant film and steel ball. Their setup allowed probing temperature with a spatial resolution of 35.6 µm (over three time higher than that with Raman spectroscopy).

Later, Spikes et al. used an infrared microscope with an InSb detector with which the spatial resolution was approximately of 11 µm [7]. They improved the method to measure the surface temperature of rolling-sliding contacts formed between a steel ball and a sapphire disc lubricated with a traction fluid, namely Santotrac 50. This methodology consists on distinguishing the radiation emitted from surfaces of the ball and the disc and from the bulk sapphire disc (the background radiation) using a partially coated sapphire disc which is divided into 3 sectors at its lower surface:

I. 120° coated sector with a 120 nm thick aluminum layer (opaque to infrared and of low emissivity of ~ 0.04) to collect the radiation of the bulk disc.

II. 120° coated sector with a 120 nm thick chromium layer (opaque to infrared and of emissivity of ~0.4.) to isolate the infrared emission of the disc lower surface.

III. 120° uncoated sector to isolate the radiation emanated from the steel surface.

The results, displayed in Figure 1-8, show an example of comparison between the temperature rise of the steel ball and the sapphire disc surfaces.

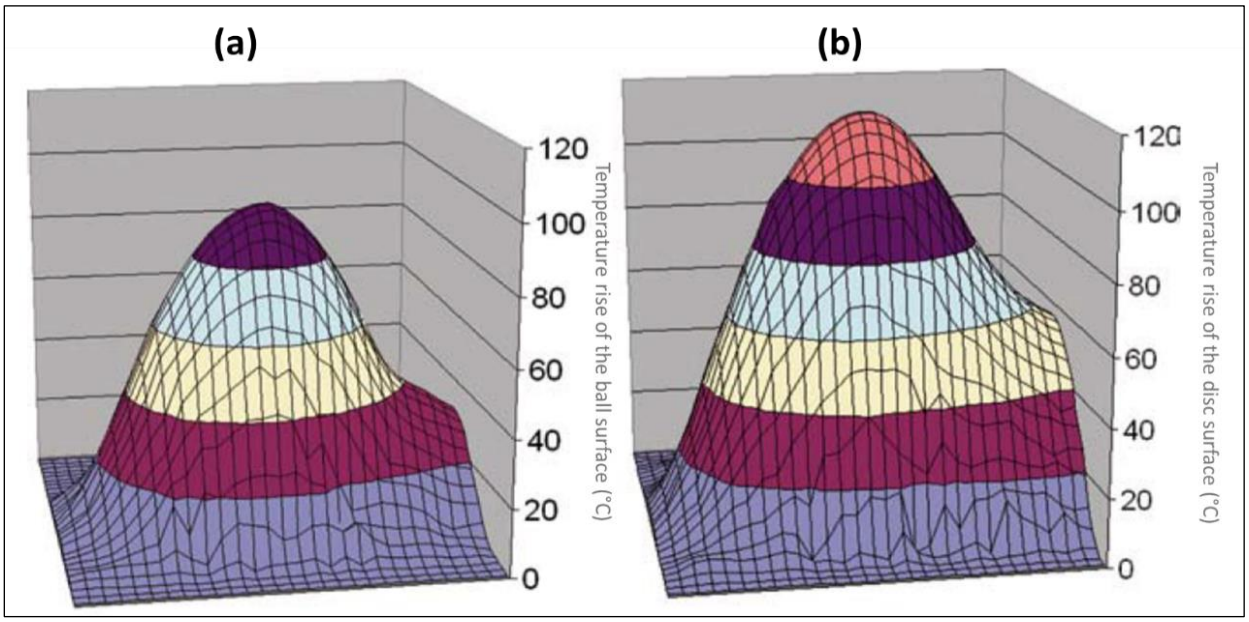

Figure 1-8: Temperature rise maps measured by IR thermography over (a) the steel ball and (b) the partially coated sapphire disc surfaces in an EHD contact operated at w=50N (P_H=1.34 GPa) T_0=40°C, u_e =1.113 m/s and SRR= -100% (i.e. u_b=1.6695 m/s and u_d=0.5565 m/s) [7]. Contact inlet is on the left.

Reddyhoff et al. [61] used the same experimental approach as Spikes et al. to explore the effect of compressive heating/cooling on temperature rise in EHD contacts using different lubricants. They attempt to enhance the accuracy of temperature measurement down to 0.1°C and the spatial resolution down to 6 µm by employing a high sensitivity infrared microscope lens and by using stepping microscope techniques, respectively. Figure 1-9 shows an example of the measured maximum temperature rise of the sapphire disc surface as a function of wide range of low entrainment speed in pure rolling (SRR=0%) and in rolling-sliding (SRR=50%). However, as they did not have a direct access to the local temperature rise within the lubricant film, they could not really distinguish the part of the temperature rise due to the compressive heating/cooling effect as compared to the shear heating effect.

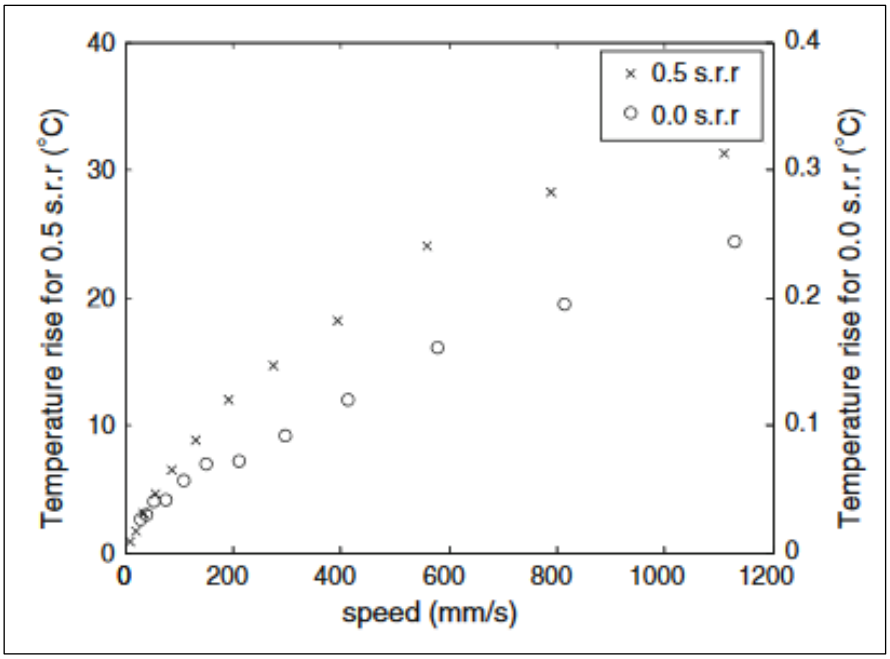

Figure 1-9: The influence of entrainment speed on the maximum disc surface temperature rise measured by IR thermography in an sapphire(disc)-steel (ball) EHD contact lubricated with Santotrac 50 operated at T_0=40°C , under w= 40 N, with SRR=0 and 50% (disc is moving faster than the ball) [61].

Lu et al. tried to reconstruct the oil film three-dimensional temperature distribution by using two-band pass filters and a second chromium coated sapphire disc to isolate the disc surface radiation [62]. Knowing that oil emissivity depends on both film thickness and temperature, they repeated the calibration procedure (performed under pure rolling) by changing temperature and entrainment speed (therefore film thickness) in order to establish a relationship between oil emissivity as a function of both temperature and film thickness.

After these complex preliminary calibrations, they measured the oil emissivity and deduced the temperature distribution in different parts of the contact at a given central film thickness (see Figure 1-10).

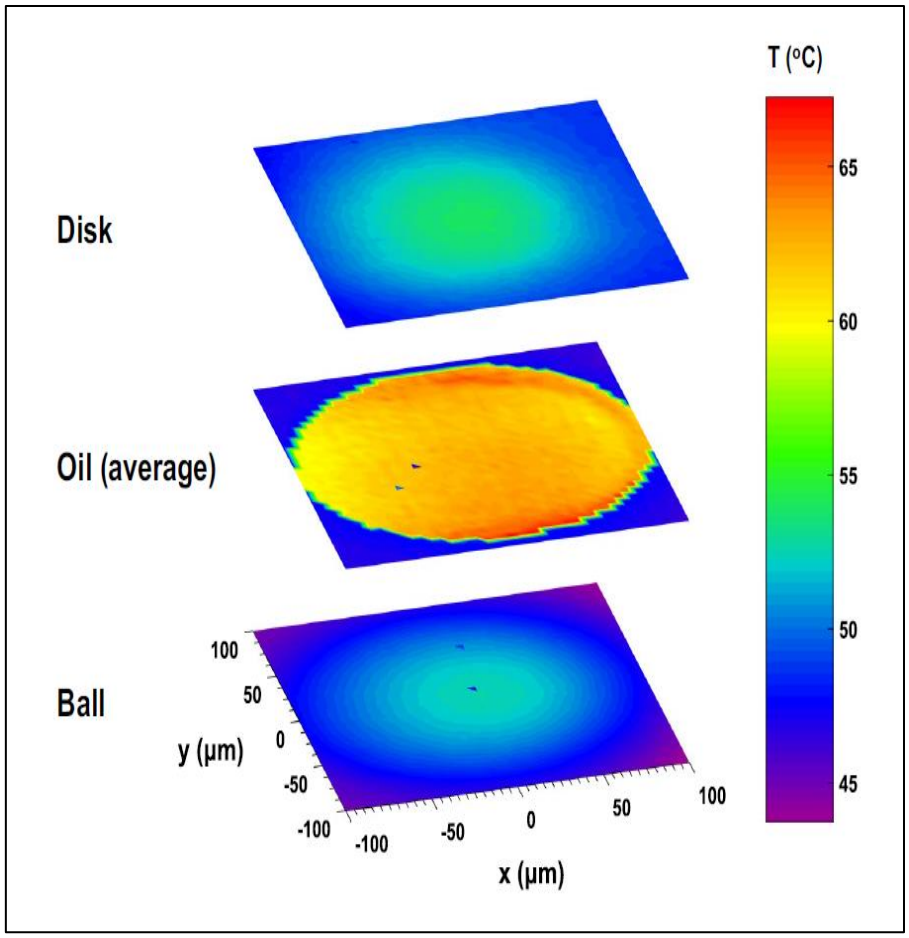

Figure 1-10: Temperature distributions of the oil film (average values across the film thickness) and at the two bounding surfaces (disc and ball) at SRR = 100%, with an inlet oil temperature of 40 °C [62].

Although the spatial resolution of IR thermography have been improved over time, the application of such technique to probe temperature in EHL is considered complex in terms of calibration when it comes to the subtraction of the background radiations and the lubricant emissivity dependence on temperature and film thickness (which both vary over the whole contact region). The experimental approach is also intrusive to some extent because it requires the use of infrared reflective material like chromium coating (of 120 nm thick and of different thermal diffusivity than that of the disc) to be applied at the lower surface of the transparent disc to isolate its radiation. Unlike the made assumption, this latter cannot be the same when it comes to use of the uncoated sapphire disc to collect the ball surface radiation.

In addition, Spikes et al. [7], Reddyhoff et al. [61], and Lu et al. [62] attempted to map the shear stress throughout the contact using the moving heat source theory and semi-analytical developments combined with their temperature measurements but their approach and their assumptions may be subject to criticism.

1.3.1 Electrical resistance for pressure and temperature measurement

Throughout the EHD contact, temperature and pressure can be measured using the electrical resistance sensor method. This latter consists on assessing the variation of the electrical resistance in thin film sensors when it get through the lubricated contact. For sensing temperature, the most widely employed thin film materials are platinum and titanium because their electrical resistance exhibits high dependence with respect to temperature and low dependence with respect to pressure. In contrast, manganin (Cu–Mn–Ni) is commonly used as a pressure transducer because its electrical resistance is highly sensitive to pressure and less sensitive to temperature. Generally, thin film sensors are deposited on electrical insulating materials like ceramic substrates (sapphire, zirconia, silicon nitrite, etc.) or on protective insulating coatings (usually of aluminum oxide or silicon oxide) when it comes its employment on metallic surfaces made from bearing steel.

In 1964, Kannel et al. [8] used for the first time manganin thin film sensors for measuring pressure distribution in EHD contacts performed in a twin-disk test rig. Cheng and Orcutt [9], Dow et al. [10], Mokhtar and Ghany [11], Kagerer and Königer [12] and Safa et al. [13] used manganin and platinum sensors to measure both pressure and temperature in EHD contacts. They found that temperature profiles have similar trend to pressure distributions, as shown in Figure 1-11 for example. However, most of the authors evoked the low durability of these sensors under the severe conditions imposed in rolling-sliding highly-loaded EHD contacts.

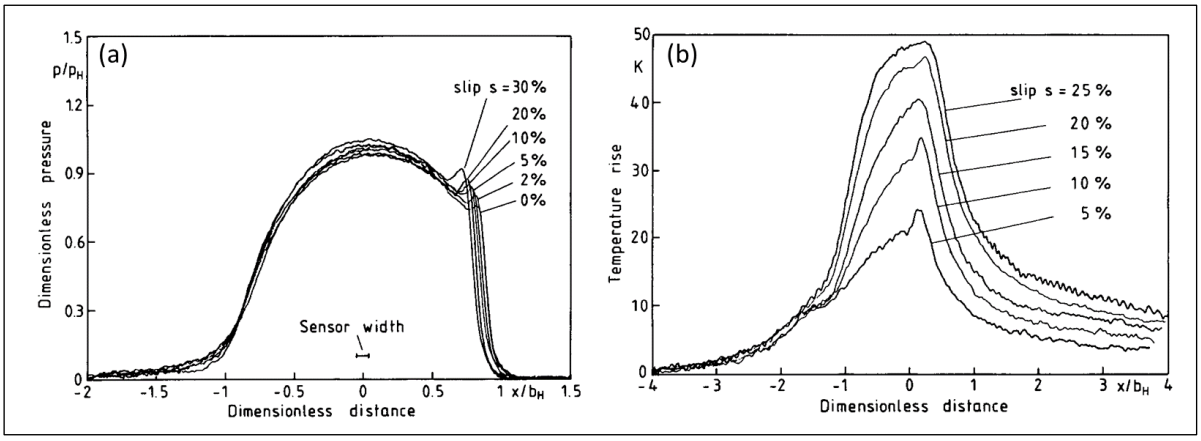

Figure 1-11: Measured (a) pressure (b) temperature profiles using thin film sensors made of manganin and platinum at various slip conditions (SRR) [12].

Ebner et al. [14] measured temperature distributions in EHD contacts for different bulk and coated (DLC) materials on a twin-disk test rig. They deposited thin film sensors made of platinum on zirconia (ZrO_2) and alumina (Al_2O_3) discs (see Figure 1-12). It is important to know that the calibration was carried out for each thin film sensor before each experiment to determine the temperature and pressure coefficients.

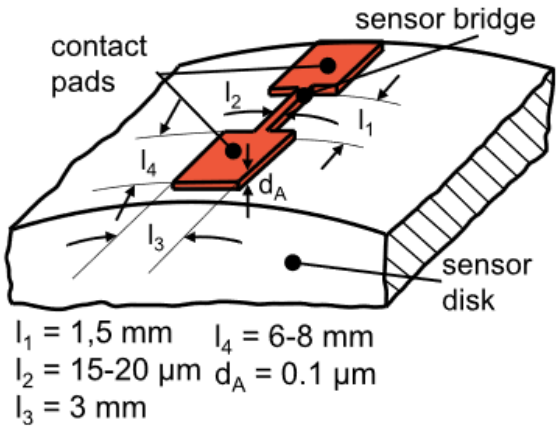

Figure 1-12: Geometry of the thin film sensor used in [14].

According to their calibration, the platinum film ohmic resistance is found to be highly sensitive to temperature but it slightly decreases with an increase of pressure. In order to determine the resistance change due to temperature rise at the contact level, the authors calculated the pressure distribution using TEHL simulations (complementary tool) for each operating condition and substituted the computed pressure values in their calibration model. They deduced the temperature rise under multiple operating conditions. As a result, they found a qualitative accordance between experimental and simulated temperature rise profiles; for example as it is shown in Figure 1-13, for the rolling-sliding tests denoted 1.2 and 3.2 for which different disc materials were used (z=0.9*h corresponds to the gap height close to the surface of the sensor disc). In addition, they confirmed the significance of thermal insulation effect of DLC coatings. However, the authors claimed that the existence of oscillations in the measurements of test denoted 1.2 in Figure 1-13(a) is likely due to the continuing deterioration of the thin film sensor, as a result of small lubricant film thickness.

It can be concluded that the film sensor technique may be considered intrusive because the thickness of the thin film sensor (0.1 µm) is comparable to the typical EHL film thickness range and the thermal properties of the sensor material is different from that of the bulk substrate. For this reason, the heat generation/temperature rise may be influenced by the presence of the sensor film inside the EHD contact. In addition, the durability of the film sensor for withstanding severe EHD conditions is a major issue, as mentioned by most of the authors. Furthermore, the technique requires many calibrations per film sensor/per experiment because a small variation in the mechanical properties (during the manufacturing and deposition processes or during the test) may have a significant effect on the sensor response.

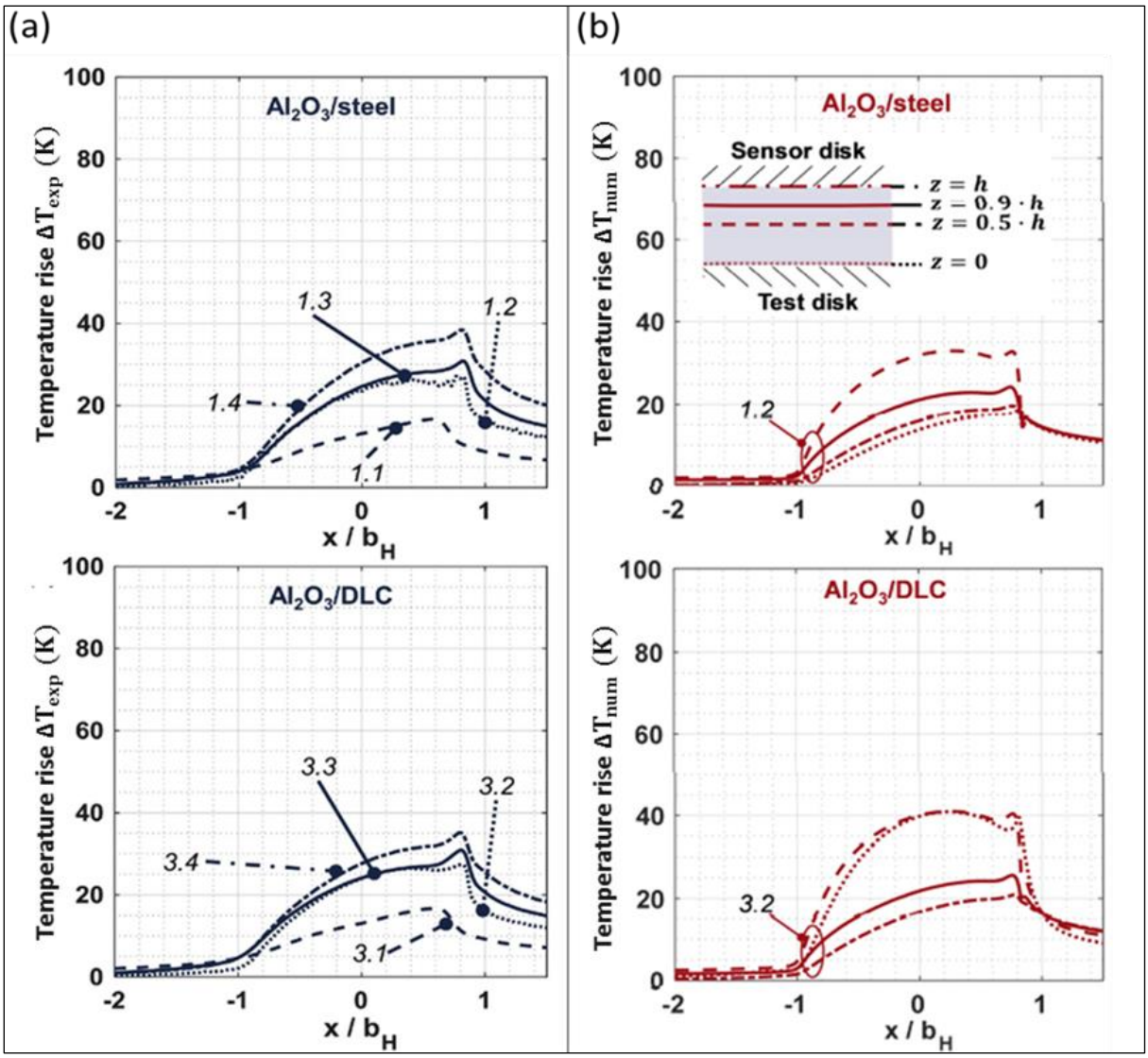

Figure 1-13: (a) Measured temperature rises ΔT_{exp} as a function of dimensionless x-axis, with b_H hertzian contact radius, obtained for different rolling-sliding tests. (b) Simulated temperature rise ΔT_{num} at different gap height positions [14]. Tests, denoted 1.2 and 3.2, run at T_0=335.5 K under P_H=1000 N/mm^2 for u_e=16 m/s with SRR=20%. The other tests represent other experimental conditions.

1.4 Pressure and temperature in steel and hybrid EHD contacts - Industrial challenge

Hybrid bearings are most commonly composed of steel-based bearing rings and ceramic (most of the time silicon nitride (Si_3N_4)) rolling elements, as illustrated in Figure 1-14. In most applications, they better withstand extreme conditions (poor lubrication and contaminated environments) and provide longer life than all-steel bearings [63]. However, early fatigue may occur if Si_3N_4 contains manufacturing defects [64]. Si_3N_4 is characterized by a combination of favorable properties for high-speed bearings, such as high hardness, high elasticity, great

stiffness, low density, low coefficient of thermal expansion, high electrical resistivity and no response to magnetic fields [40].

Regarding the tribological behavior of EHD contacts, Si_3N_4 in hybrid bearings generates smaller contact areas compared to steel in conventional all-steel bearings due to its higher elastic modulus. Thus, for a hybrid bearing, this can result in lower friction which is the integral of shear stress over the (lower) contact area. However, under the same operating conditions, the hybrid contact yields higher contact pressures and, consequently, this leads to increase friction. The technical challenge lies in modifying, whenever possible, the geometry of the rings of hybrid bearings to locally increase the curvature radii, and thus reduce the contact pressure and ultimately friction.

Figure 1-14: Example of all-steel and hybrid (Si_3N_4 –steel) ball bearings (inspired source: SKF).

Besides, the simultaneous shearing and compression of the lubricant promote the temperature rise through the lubricant film. The variation in temperature affects the lubricant viscosity thereby modifies parameters such as the film thickness and shear stress (i.e. friction). Moreover, at the contact level, the lubricant acts like an energy carrier whereby the generated heat dissipates through the flow and bounding solids. Apart from the normal load, the rolling and sliding velocities, the heat / temperature distribution depends on the contact size and most importantly on the thermal properties of the materials in contact [65]. For these reasons, in order to improve bearings design and operation, there is an industrial need for bearing manufacturers to reliably predict and quantify the contact temperature rise and heat generation within steel-steel and hybrid (Si_3N_4 – steel) contacts.

1.5 Heat generation in hybrid and all-steel bearings - Literature overview

Results of heat generation/power losses and temperature rise in lubricated all-steel and hybrid bearings operated under identical operating conditions were reported in the literature. Reddecliff and Valori showed that the hybrid and M50 steel bearing outer ring temperatures are identical (using thermocouples) [15]. However, they reported that the estimated heat generated in hybrid ball bearings is less than that of M50 steel bearings of about 10 to 20% [15]. Miner et al. used thermocouples in contact with the surface of the bearing outer ring and employed separate thermocouples to measure the oil–in and oil–out temperatures [16]. As results, they did not show remarkable differences between the measured temperatures of outer rings and oil-outs in all-M50 steel and hybrid bearings, operated under high-speed conditions. Paleu et al. [17] have found that the total power loss (caused by slip on ball-to-race contacts) in hybrid ball bearings is smaller of about 27 to 52 % than the total power loss in conventional all-100C6 steel ball bearings, in accordance with the results given in [18],[19]. Figure 1-15 shows the variation of the power loss ratio (hybrid over all-100C6 steel) observed over a speed range of 5000 up to 35000 rpm and for a load of 200 N obtained by [17].

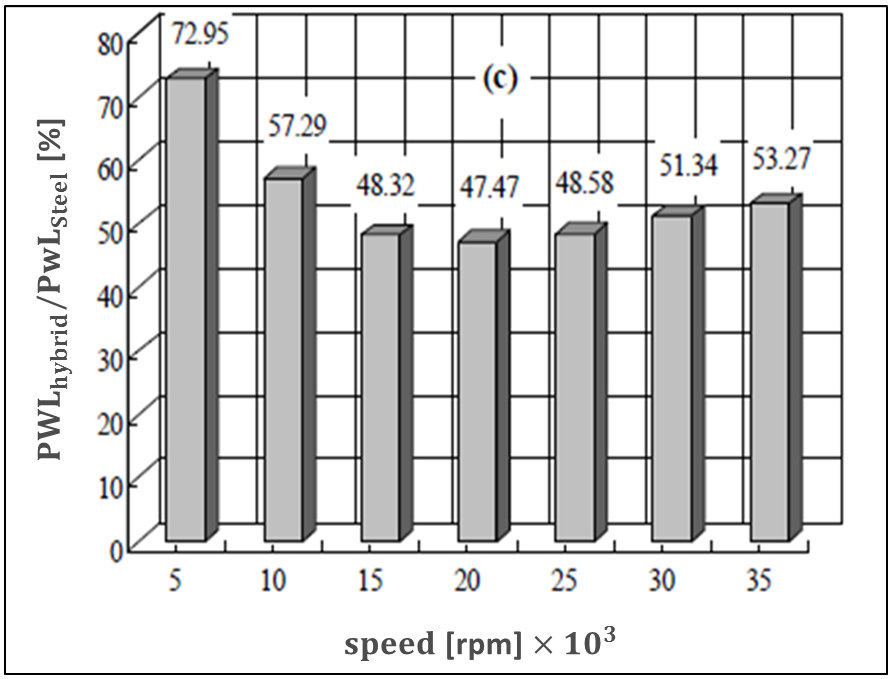

Figure 1-15: Hybrid to all-steel REBs total power losses ratio (PWL_{hybrid} / PWL_{steel}) versus speed, (normal load: w=200 N) [17].

Shoda et al. [20] measured the temperature rise at the outer and the inner rings of the hybrid and all-M50 steel bearings. They found that the temperature differences between the two rings of the hybrid bearing were lower than that of the M50 steel bearing over a wide range of entrainment speed. In addition, they reported that, at low entrainment speed, the heat generation of the M50 steel bearing was higher than that of the hybrid bearing. However, the heat

generation of this latter increased progressively with the entrainment speed and get closer to that of the M50 steel bearing starting at 1500 rpm.

In most of the studies, one can notice that the temperature of the bearing is essentially measured through bearing housing using thermocouples. This is due to the limited cavity, the complexity of the REBs structure and the high rotational speed of its components. Nevertheless, other measurement technique like infrared thermography can be used to extract temperature; however, the emissivity of the measured elements requires complex calibration. Recently, Yan et al. [66] have proposed an alternative technique based on CdTe quantum dots (QDs) fluorescence thermometry to measure the temperature bearing inner ring /cage at high speed (5000-6000 rpm). Nevertheless, since the authors glued their QDs sensor film to the cage/inner ring by silica gel (low thermal conductive material), their method may be considered as intrusive. In addition, their way to demonstrate the feasibility of their proposed methodology, by comparing the roller bearing cage temperature measured using the QDs sensor (during rotation) and the one recorded by thermocouple sensor after the bearing-spindle system shut down, may be subject to criticism.

1.6 Summary and aim of the work

The determination of the EHL regime circumstances has been the motivation of numerous experimental, numerical and analytical studies. The brief description of some well-known EHD contact characterization methods provides a critical analysis of their possibilities. It also illustrates the needed criteria for an experimental *in situ* technique (less intrusive to the contact conditions, detectable in response, durable, reliable, withstand EHD severe conditions, simple to implement, accurate and highly sensitive) in order to conduct a proper investigation of the physical parameters encountered in EHD contacts.

This work focuses on fulfilling an industrial challenge, which is to quantify and compare the pressure, temperature rise and the generated heat in both all-100C6 steel and hybrid (100C6 steel-Si_3N_4) circular EHD contacts. This is very helpful and instructive in defining the route to take for minimizing the energy losses and thus enhance the efficiency for such contacts.

The aim of the current work is thus to develop a new *in situ* technique providing local measurements of pressure and temperature in EHD contacts, eventually with more enhanced detectability, accuracy and reliability than the previously developed techniques such as Raman spectroscopy, infrared thermography and electrical resistance, respectively. Furthermore, a non-Newtonian thermal (TEHD) numerical model, inspired by the work Habchi et al. [67], will be used in order to compare/validate the experimental results.

Our idea consists in dispersing quantum dots undergoing observable changes as a function of temperature and pressure in a lubricant. Thus, these quantum dots will be used as nanoscale sensors to map pressure and temperature in EHD contacts. It is important to emphasize that the chosen lubricant in this work does not contain additives and the film thickness that it forms has

been chosen as to guarantee a full separation of the contacting bodies. That is to say that, in this study, only EHD mechanisms are considered and no chemical reaction will be involved.

The next chapter provides a brief description on the composition, physics and properties of the chosen photoluminescent nanosensors. In order to evaluate their pressure and temperature sensitivities, calibration procedures are established, and their results are presented.

In the third chapter, experimental tool used to simulate the EHD contact are described. The feasibility of the proposed methodology is investigated by measuring the pressure and temperature under isothermal and then non-isothermal conditions, using a steel or Si_3N_4 ball on a sapphire or glass disc, as spectral measurements require employing at least one transparent specimen. The pressure and the temperature profiles from the experiments are compared with the ones obtained using a numerical model (described in annex 5.1) for validation.

In the last chapter, numerical and experimental studies are performed to analyze the influence of the slide to roll ratio, normal load and nature of the contacting materials on the temperature rise. Furthermore, to get closer to the industrial application, an alternative method is proposed in order to evaluate the correlation between power losses and generated heat calculated inside rolling-sliding EHD contacts (to validate the equilibrium between the mechanical energy and the internally generated energy or heat within the contact).

Finally, a general conclusion summarizes the outcomes of this work and set out some prospects.

Chapter 2: Potential of the CdSe/CdS/ZnS QDs for probing pressure and temperature

Chapter 2: Potential of the CdSe/CdS/ZnS QDs for probing pressure and temperature 71
2.1 Introduction.... 73
2.2 Overview on the quantum mechanical atomic model 73
2.3 Semiconductor Materials.... 75
2.3.1 Band gap 75
2.3.2 Electronic transitions in semiconductors - Photoluminescence.... 77
2.4 Quantum dots 78
2.4.1 Semiconductor hetero-nanostructured QDs.... 79
2.4.2 QDs emission spectrum.... 81
2.5 Calibration of CdSe/CdS/ZnS QDs - Methodology.... 83
2.5.1 High pressure experiments 84
2.5.2 Thermal dynamic experiments.... 85
2.5.3 Fluorescence measurements tools.... 86
2.6 QDs pressure and temperature sensitivities - Results and discussion 87
2.6.1 High pressure calibration results 87
2.6.2 Results of the thermal dynamic calibration 92
2.7 Conclusion.... 94

2.1 Introduction

In the previous chapter, the industrial objectives and scientific context are presented. A description of coupled effects that influence the local thermodynamic and mechanical conditions in the EHD contact is reviewed. The various experimental techniques developed up to date and their limitations are pointed out. All this confirms a clear need for *in situ* experimental techniques with appropriate spatial resolution and time scale.

This chapter addresses the potentiality of probing pressure and temperature in very thin films found in EHD contacts, using photoluminescent CdSe/CdS/ZnS quantum dots (QDs). Albahrani et al. [68] have already shown the potential of the CdSe/CdS/ZnS QDs for either measuring the pressure up to 1 GPa at ambient temperature (under isothermal dynamic conditions) or measuring the temperature up to 373 K under ambient pressure (i.e. under isobaric static conditions). Meaning that, the challenge of measuring simultaneously the variations of these two parameters is not achieved yet. However, their work constitutes a basis that allows us to develop a deeper study of this nanosensors. Firstly, into the calibration of the CdSe/CdS/ZnS QDs for higher pressure and temperature ranges. Subsequently, into the decoupling of the temperature and pressure influences in the perspective of establishing profiles of each of these parameters from representative EHD contacts.

The first part of this chapter is dedicated to a brief description of the quantum theory, the mechanism of photoluminescence (PL) in semiconductor crystals and the optical properties of QDs. Afterwards, the focus is on the selected CdSe/CdS/ZnS QDs and susceptible factors that may modify their PL emission. This is followed by the presentation of calibration results of the QDs responses to temperature and pressure variations. Subsequently, an investigation on the possible influence of shear stress on the QDs fluorescence emission is presented. This is in the purpose of this work to establish accurate empirical laws to be able to probe local pressure and temperature throughout EHD contacts.

2.2 Overview on the quantum mechanical atomic model

The quantum mechanical atomic model is considered as the most accurate model of the atom. Based on this model, the atom consists of a positively charged central nucleus of protons and neutrons surrounded by a cloud of negatively charged electrons (see Figure 2-1). Electrons exhibit properties of both particles and waves. The electron two-sided nature is known as the Wave-Particle Duality. Electrons move so fast around the nucleus so that one can define a volume of space where an electron can be found most of the time. Theses volumes are called orbitals. These orbitals have characteristic shapes, labeled s, p, d and f, with discrete energy levels at different distances from the nucleus.

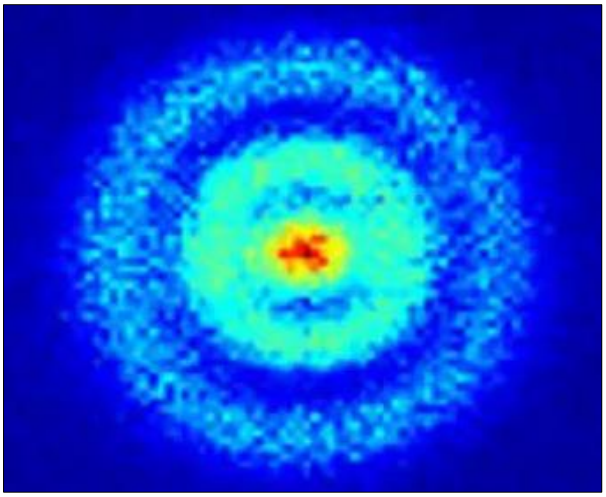

Figure 2-1:The first direct observation of an atom's electron orbital captured using a quantum microscope [69].

Between energy levels there are regions where electrons cannot persist in a stable way. These regions are called energy gaps. In order to describe the distribution and trajectories of each electron in the atom, scientists have assigned to each electron a unique set of four numbers called the quantum numbers (N). These numbers designate the shells, subshells, orbitals, and spins of each electron. According to Pauli Exclusion Principle, two electrons cannot have the same quantum numbers in an atom or in a molecule (a group of two or more atoms).

Consistently to this principle, when B identical atoms bind together to form a molecule or a crystal lattice, this leads to an overlapping and splitting of their atomic orbitals into B discrete molecular orbitals of different energy.

Since a large number of atoms join each other (~10^{22} in case of a piece of bulk material), the available energy of adjacent levels becomes so close together to form packages of energy states. In these packages, the states are spaced by ~10^{-22} eV. Thus, each package of states can be considered as continuous energy bands. The highest energy band, completely filled of electrons (the outermost shell of the atom), is labeled the valence band. The lowest energy band, not completely filled of electrons (area where the electrons can escape easily), is labeled the conduction band.

As an example, the splitting of the energy levels of carbon atoms in diamond is shown in Figure 2-2 .

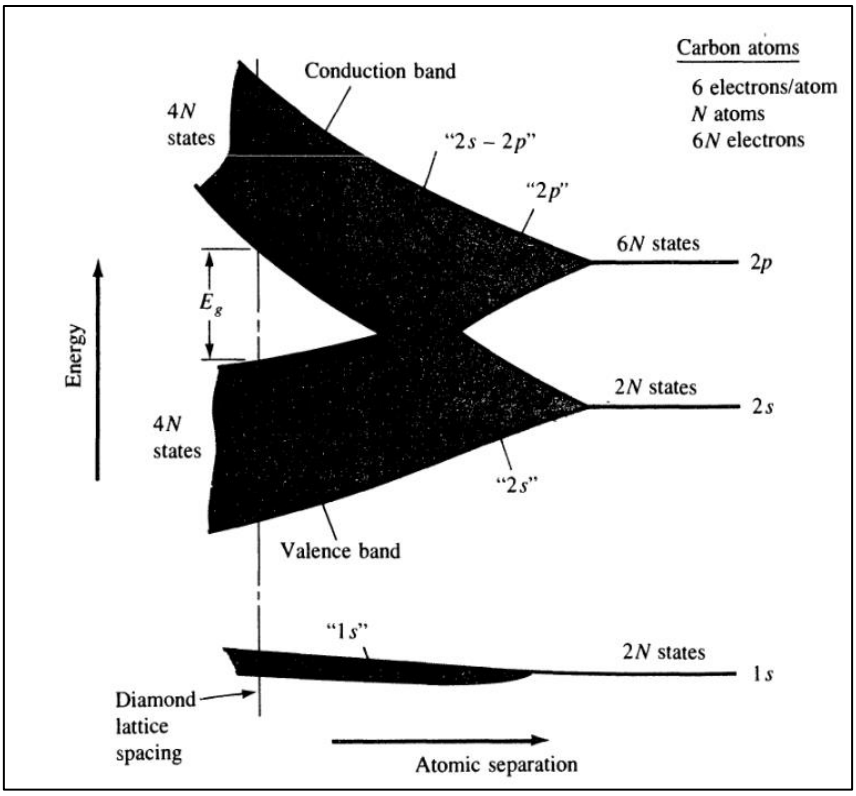

Figure 2-2: Energy bands for diamond versus the atomic separation [70].

2.3 Semiconductor Materials

Semiconductors are a group of materials that possess electrical conductivity lying between that of metals and insulators. Thermal excitation, optical excitation, impurity content may vary significantly their conductivity from insulator-like to metal-like materials and vice-versa. That is because the conductivity of intrinsic semiconductors depends mainly on the band gap.

2.3.1 Band gap

In the electronic band structure of solids, the band gap is the forbidden zone between the top valence band of electrons and the bottom conduction band, where no electronic energy level can exist (see Figure 2-2). It represents the minimum energy that is required to make an electron migrate from the valence band up to the conduction band, where it can contribute in conduction.

Figure 2-3 illustrates in energy diagrams both the existence and the difference in size of bands gap between conductors, semiconductors and insulators. In insulators, electrons of the valence band are very far apart from the conduction band. This large band gap prevents electrons from the valence band to be excited up to the conduction band. In metals, the valence band partially overlaps with the conduction band. This allows a portion of valence band electrons to be free to move into the conduction band and participate in electrical conduction. Finally, in intrinsic semiconductors, the gap is small enough that it allows some electrons to be promoted into the conduction band by some sort of excitation, such as thermal excitation, or by the absorption of energy from a photon.

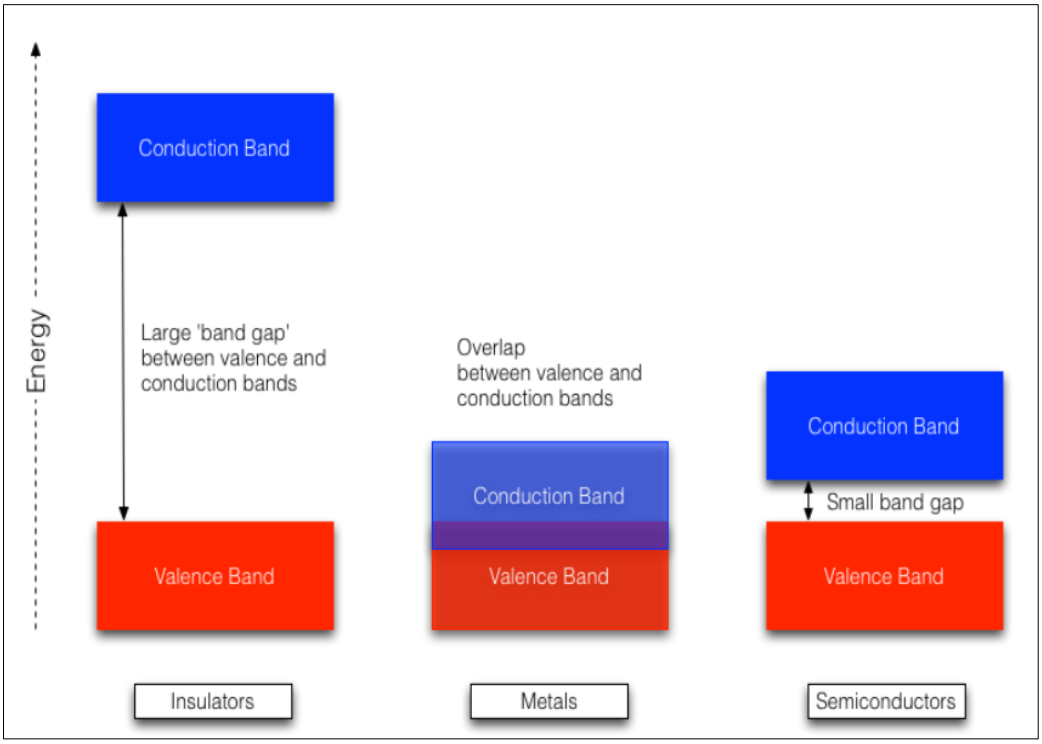

Figure 2-3: Description of the electronic bands in solids inspired from [71].

It should be noted that, in a semiconductor material, when the excitation leads an electron to leave its initial position (in the valence band), it also generates the formation of a hole. That is to say that the hole is considered as a vacant place previously occupied by an electron. This hole behaves as a positive charge (that is equal in magnitude but opposite in polarity to the charge that the electron has) able to migrate within the material. This theoretical concept of holes is introduced to simplify the analysis because it is easier to keep track of the missing electrons of the valence band rather to keep track of the existing electrons in an almost full band (valence band). It is quite often, in quantum mechanics, to describe a large number of interacting particles as possible non-interacting particles called 'quasi-particles', e.g. holes, excitons, etc. [72]. Exciton in semiconductors is defined as an electron-hole pair where both of them are bounded together by the electrostatic Coulomb force. The distance in an electron-hole pair is labeled the exciton Bohr radius. It is important to point out that the decay of this exciton (or the recombination of the electron and hole) is vital to the creation of current, light emission or even the production of heat.

The band gap is the main parameter that characterizes a semiconductor material. It is represented in an E-k dispersion diagram. This diagram shows the relationship between the electron energy states versus the crystalline wavenumber k (which can be seen as a spatial frequency). The wavenumber k is linearly related to the momentum (*M*) as following:

$$M_p = \hbar k \qquad 2.1$$

where $\hbar$ is the reduced Planck's constant and k the magnitude of the wavevector $\vec{k}$.This latter orientation indicates the direction along which electrons move. The equation which relates the energy E and the momentum, may be written as:

$$E = \frac{{M_p}^2}{2m} = \frac{\hbar^2 k^2}{2m} \qquad 2.2$$

In 3D crystal structures, the interatomic distance (lattice constant) may be different for different directions. A complete description of k-space (3D-space) and energy E requires a 4-dimensional plot which is evidently not possible to visualize. The solution is to plot the 2D diagrams separately for different directions represented by Miller indices (three lattice vectors [$\mathbf{x_1}$ $\mathbf{x_2}$ $\mathbf{x_3}$]), as illustrated in Figure 2-4.

There are two types of band gaps, direct and indirect.

In the direct band gap, the top of the valence band and the bottom of the conduction band are aligned at the same k value like in case of GaAs, CdSe, CdS, ZnS, etc.

In the indirect band gap, the top of the valence band and the bottom of the conduction band are located at a different k value like in Si, Ge, etc.

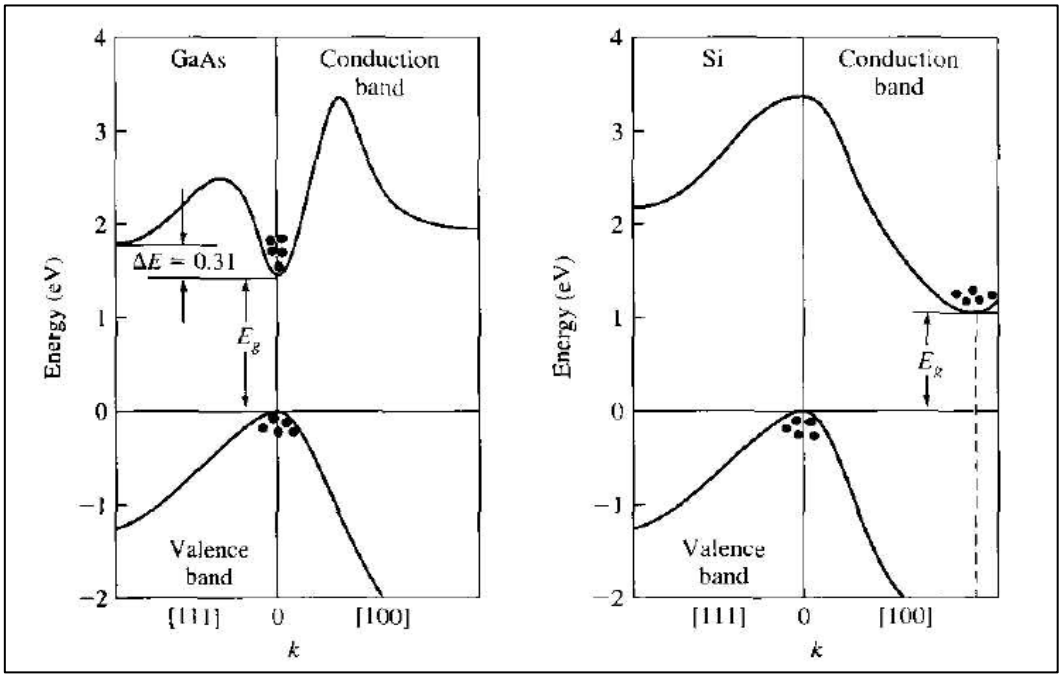

Figure 2-4: Direct and indirect band gaps for GaAs (left) and Si (right)[73].

2.3.2 Electronic transitions in semiconductors - Photoluminescence

The section focuses on radiative transition, especially on photoluminescence (PL). To introduce this concept, it is important to know that when an electromagnetic wave propagates through a pure bulk semiconductor material, two classes of photonic transitions may occur:

- Interband transitions in which the excited electron moves from an occupied state (valence band) to an unoccupied state (conduction band).
- Intraband transitions in which the electron jumps to a state in the same band.

The interband transition process is ensured if, and only if, the incident photon has an equal or higher energy than the energy gap. This transition can exist in either a direct or indirect band gap. But, as an incoming photon has a negligible momentum (due to its negligible mass) compared to that of the electron, the absorbing electron gets energy and bridges the band gap without changing its wavevector. However, for an indirect gap material like silicon, the excited electron needs additional momentum to reach the conduction band bottom at a non-zero wavevector. This additional momentum may be induced by the interaction with a phonon (crystal lattice vibration giving off energy difference as heat). Consequently, due to the electron and hole momentum mismatch in the indirect band gap, the probability of a photon emission in an indirect band gap is much lower (one photon emission per thousand excitons) than that of in a direct band gap (~999 per thousand excitons).

The intraband transition usually involves a non-radiative recombination in which the generated electron-hole pair recombines without releasing any photon. A phonon is released instead.

PL is defined as photons emission by a molecule after the absorption of photons. This process occurs within a very short time, between 10^{-9} and 10^{-7} s. In the case of an ideal pure semiconductor crystal, PL is generally triggered from interband radiative transitions. This makes PL, to some extent, a sensitive tool to probe semiconductor bands as it shows a fingerprint peak related to the energy of each excited level. It should be emphasized that both the PL and the states of energy depend not only on the semiconductor material but also on its size, pressure, temperature, the nature of its surrounded environment, etc.

2.4 Quantum dots

Quantum dots are photoluminescent semiconductor nanocrystals with a diameter between 2 and 10 nm and 100 to 100,000 atoms within their volume. They are designated as artificial atoms because of their discrete quantized energy levels, which make them more closely similar to atoms than to bulk material. Their discrete quantized energy levels arise at the band-edges of both the conduction and valence bands. This involves a size-dependent discrete energy level and, more importantly, a size-dependent bandgap energy E_g, as shown in Figure 2-5.

Indeed, as the size of the QDs becomes comparable to the exciton Bohr radius (r_{Bohr}), the exciton becomes spatially confined. This effect is known as quantum confinement. It is worth noting that r_{Bohr} and QDs radius r_{QD} are parameters which indicate the established degree of confinement within the nanostructure. Generally, there are two main degrees of quantum confinement:

-Strong quantum confinement, where $r_{QD} << r_{Bohr}$. In this regime, the Coulomb interaction between electrons and holes is no longer sufficiently strong to form bound excitons.

-Weak quantum confinement, where $r_{QD} > r_{Bohr}$. In this regime, the excitons are considered as particles in spherical potentials.

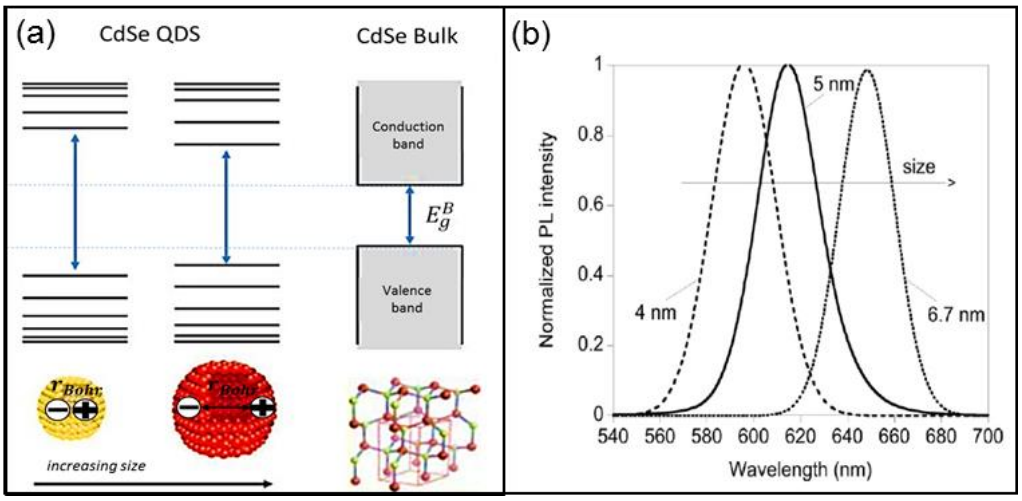

Figure 2-5: (a) Schematic representation of the effect of quantum confinement on the electronic structure of CdSe QDs and bulk CdSe. Modified image from [74]. (b) Normalized PL spectra (excitation wavelength, 450 nm) for 4.0, 5.0, and 6.7 nm CdSe nanocrystals [23].

The separation of the energy levels (which influence PL) in the strong confinement regime is much larger than that in the weak confinement regime. That means that, by reducing the size of the semiconductor nanocrystal, the band gap becomes larger and the exciton becomes strongly confined (see Figure 2-5). The impact of quantum confinement becomes negligible usually for sizes larger than 2-3 times the exciton Bohr radius [72].

2.4.1 Semiconductor hetero-nanostructured QDs

Semiconductor hetero-nanostructured QDs are composed of a semiconducting nanocrystal core material and one or two shells of distinct semiconducting materials, usually covered by organic ligands. The main reason of such incorporation of multicomponent materials is to enhance the photoluminescence efficiency and the stability against photodegradation.

Indeed, at the surface of pure semiconducting nanocrystals, the periodicity brusquely stops. Numerous rearrangements in the atomic positions occur, resulting in surface atoms having a lower coordination number than the interior atoms. This incomplete bonding results in atomic orbitals that point away from the surface and called "dangling orbitals" [75]. In an E-k dispersion diagram, these latter energy levels lie within the energetically forbidden gap [76]. These surface states act as traps for electrons or holes and reduce the material optical transmissivity and emissivity. For example, in CdSe nanocrystals, Cd dangling orbitals act as electron traps while Se dangling orbitals act as hole traps. That is why it is crucial to remove all the energy levels inside the gap, i.e. eliminate dangling bonds. This can be achieved by controlling the surface quality of the semiconductor nanocrystals by performing a chemical process known as passivation [76]. This latter consists in overgrowing a shell of another semiconductor material of larger band gap and/or by coating the surface with ligands (see Figure 2-6). Using appropriate ligands is also required to ensure the affinity of QDs with its

surrounding environment and to allow a stable colloidal dispersion in the liquid medium for protecting the QDs surface from interaction or degradation. In Figure 2-7, one can notice that the emission wavelength of the coated CdSe with CdS and ZnS shells is slightly higher compared to uncoated CdSe. This indicates the partial delocalization of the excitons in the shell.

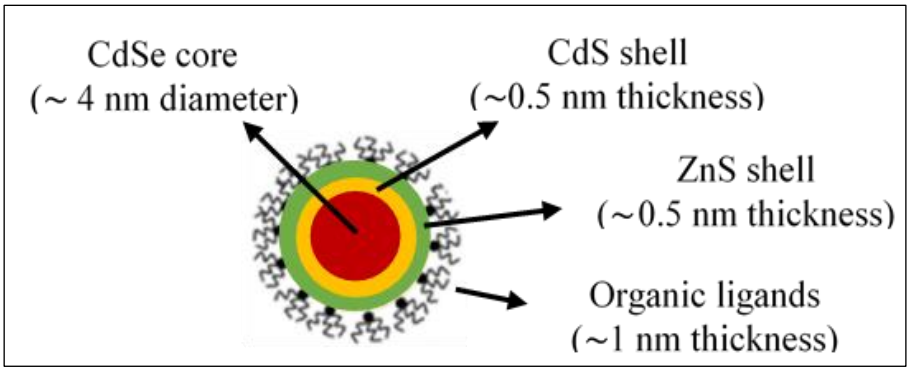

Figure 2-6: A schematic representation of the CdSe/CdS/ZnS core-shell-shell QDs [24].

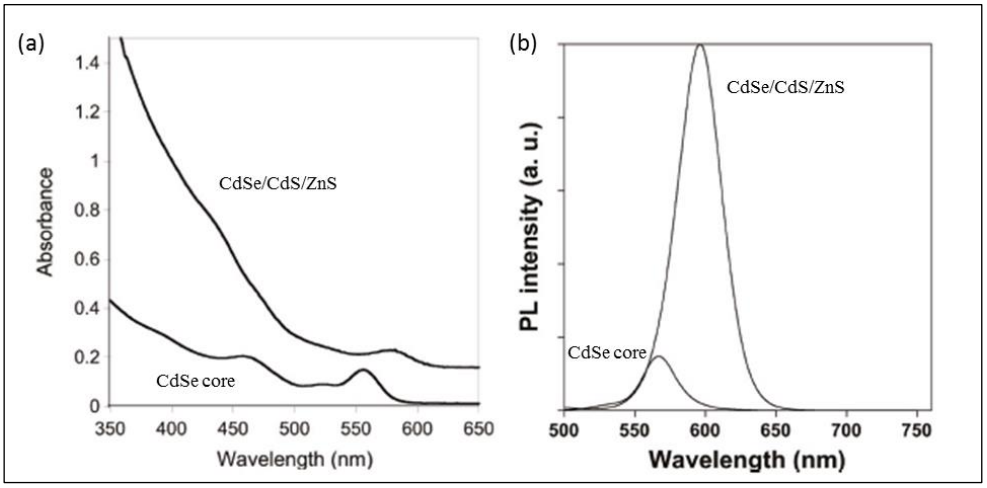

Figure 2-7:(a) UV-vis absorption spectra; (b) PL spectra (excitation wavelength, 400 nm) of the core and core/shell/shell nanocrystals [23].

In this work, CdSe/CdS/ZnS core-shell-shell QDs (see Figure 2-6) appeared to be excellent candidates for our sensing application in highly confined lubricant. Indeed, the well-documented Bohr radii of CdSe (r_{Bohr}=5.4 nm [77]), CdS (r_{Bohr}=3.00 nm [78]) , ZnS (r_{Bohr}= 2.5 nm [79]) are higher than their dimensional size within the QD, displayed in Figure 2-6, which evidenced the quantum confinement effect. In addition, all of the QD compounds (CdSe, CdS and ZnS) have direct band gaps enabling the emission of photon. The CdSe core can cover most of the visible spectrum depending on its size. CdS middle shell with an intermediate lattice constant reduces the strain between the CdSe core and ZnS outer shell [80]. ZnS outer shell with its large bandgap improves the confinement of the charge carriers (electron and hole). Photoluminescence of the CdSe/CdS/ZnS QDs corroborates these influences, as a significant increase in the PL intensity is observed relatively to the CdSe/CdS and CdSe/ZnS systems [81]. As illustrated in Figure 2-8, the PL mechanism of CdSe/CdS/ZnS QDs is promoted as follows: firstly, the electron-hole pairs are generated by the exciting high-energy photons in the shell

region. Secondly, these charge carriers are relaxed to the band-edge states of the core region. Finally, they are directly recombined to emit lower-energy photons [80].

Since most of the industrial lubricants are alkane and ester based oils, the CdSe/CdS/ZnS nanoparticles are covered by an organic ligand made of stearic acid in order to stabilize their dispersion in such liquids. The absorption and PL spectra of CdSe/CdS/ZnS QDs show dominant excitonic transitions. Their quantum yield (ratio between the number of emitted photons and the number of absorbed photons) accounts for 81% [23].

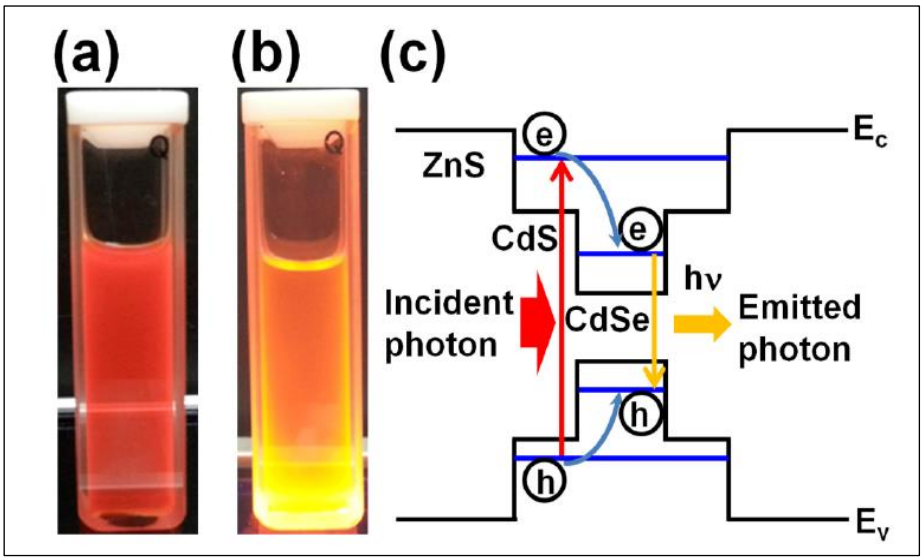

Figure 2-8: Images of (a) before and (b) after exposure to UV excitation wavelength of 365 nm of CdSe/CdS/ZnS core-shell-shell quantum dots. (c) Schematic diagram of the optical processes in the CdSe/CdS/ZnS core-shell-shell quantum dots [80].

2.4.2 QDs emission spectrum

There are three main parameters to characterize the Gaussian shape of the steady-state emission spectrum of QDs which have shown temperature and pressure dependencies: PL peak energy, PL bandwidth (full width at half maximum, FWHM) and PL intensity.

i. PL peak energy

The PL peak energy or Emission energy (E_g), which corresponds to the mean bandgap energy of the QDs, is very sensitive to temperature and pressure changes. These two parameters affect the crystalline lattice of the semiconductor nanocrystals (by dilation or compression) and consequently affect the confinement of the exciton within QDs.

Regarding temperature influence, it is useful to note that a minor impact arises from the shift in the relative position of the valence and conduction bands due to the lattice thermal expansion. However, a major contribution arises from the temperature dependence of the electron-lattice interaction (electron-phonon coupling) [82].

The Varshni law can describe the relationship between the bandgap energy and temperature as follows [82]:

$$E_g(T) = E_{g0} - \frac{\alpha' T^2}{(T + \beta)} \quad 2.3$$

where E_{g0} is the bandgap energy at 0 K and atmospheric pressure, α' a temperature coefficient and β a temperature close to the Debye temperature θ_D.

Theoretical treatments show a linear effect with temperature at higher temperatures, in particular temperatures higher than the Debye temperature θ_D [24].

$$E_g(T) = E_{g0} - \alpha_1 T \quad 2.4$$

where α_1 is a constant.

Regarding the pressure dependence, an increase in pressure induces a shift in relative position of the valence and conduction bands due to the lattice compressibility and the pressure dependence of the electron lattice interaction. Linear and non-linear pressure dependencies of the bandgap energy are observed [21], [27], [28].

$$E_g(P) = E_{g0} + \alpha_2 P \quad 2.5$$

$$E_g(P) = E_{g0} + \alpha_2 P + \beta_2 P^2 \quad 2.6$$

where α_2 and β_2 are constants.

ii. Full width at half maximum

The full width at half maximum (FWHM) represents the distribution of the bandgap energy and thus is representative of the size distribution of the QDs. Its broadening depends mainly on associated vibrational levels inside the QDs due to the scattering of excitons with phonons which may be involved with the temperature [22], [29]. More precisely, there are two kinds of broadening, homogenous and inhomogeneous.

- The homogenous broadening arises from the interactions of electrons and holes with lattice vibrations (excitons-phonons interactions).

- The inhomogeneous broadening is caused by the distribution of band gaps which may change with the size, shape, composition, crystalline structure (including phase transition), surface defects, microenvironment, etc. of the QDs.

The variation of FWHM with pressure remains unclear. Indeed, pressure may reduce or increase the surface defects or the interfacial mismatch between the QDs materials and thereby narrow or broaden the FWHM. In the case of CdSe/ZnS, Fan *et al.* suggested that the pressure reduces the surface defects between the CdSe and the ZnS and consequently lessens the FWHM [21].

iii. PL intensity

PL intensity of QDs does not only depend on pressure and temperature. PL quenching at higher pressure and temperature is caused by an escape of electrons and holes via a non-radiative recombination path. PL intensity depends also, in conformity with our sensing application in EHD contacts, on parameters that experimentally may not be precisely adjusted or quantified such as excitation power, concentration per unit volume, film thickness, etc. This fact makes the PL intensity less appropriate for our quantitative investigation as it doesn't allow providing reliable results. That is why PL intensity analysis will be excluded in our study.

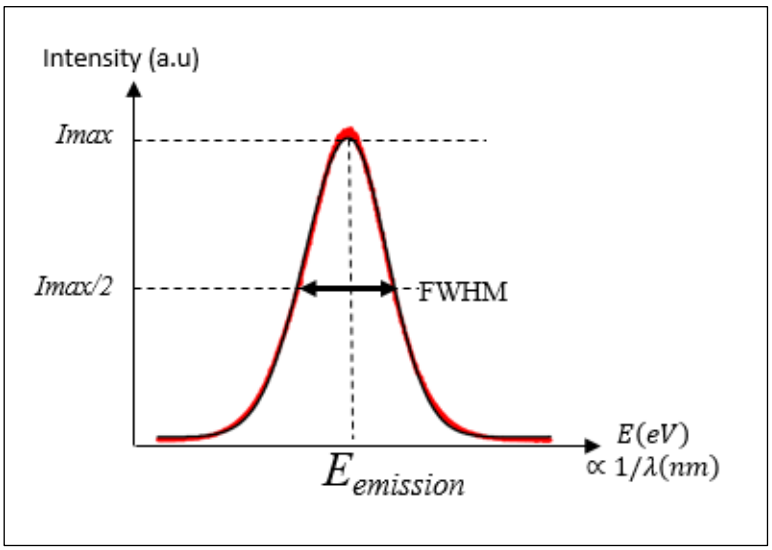

Figure 2-9: Typical Cdse/CdS/ZnS QDs emission spectrum [24].

Note that additional parameters such as the viscosity and polarity of the carrier fluid, as well as the interactions between photoluminescent substances, non-hydrostatic pressure of the surrounding medium etc. may also affect the QDs PL emission spectra [24].

2.5 Calibration of CdSe/CdS/ZnS QDs - Methodology

The CdSe/CdS/ZnS QDs have been synthetized by N. Nerambourg et al. [23] at INAC/CEA-Grenoble. Their mean diameter is of 6 nm (see Figure 2-10), are dispersed at a concentration of 0.125 mg/ml in a well-characterized reference lubricant, namely squalane ($C_{30}H_{62}$, SQ). This liquid is a branched alkane whose rheological properties can be found in [25]. This low concentration, recommended by Albahrani [24], is selected first in order to avoid altering the squalane viscosity and second to lessen interactions between QDs that might change the emission spectrum features due to reabsorption processes [26].

The calibration of CdSe/CdS/ZnS QDs in suspension aims to evaluate their PL sensitivity to changes in pressure and temperature. This will enable these QDs to be used as nanosensors in representative EHD contacts. In this work, only the steady-state emission spectra, and especially the emission energy and the FWHM are evaluated, with in mind to measure precisely pressure and temperature.

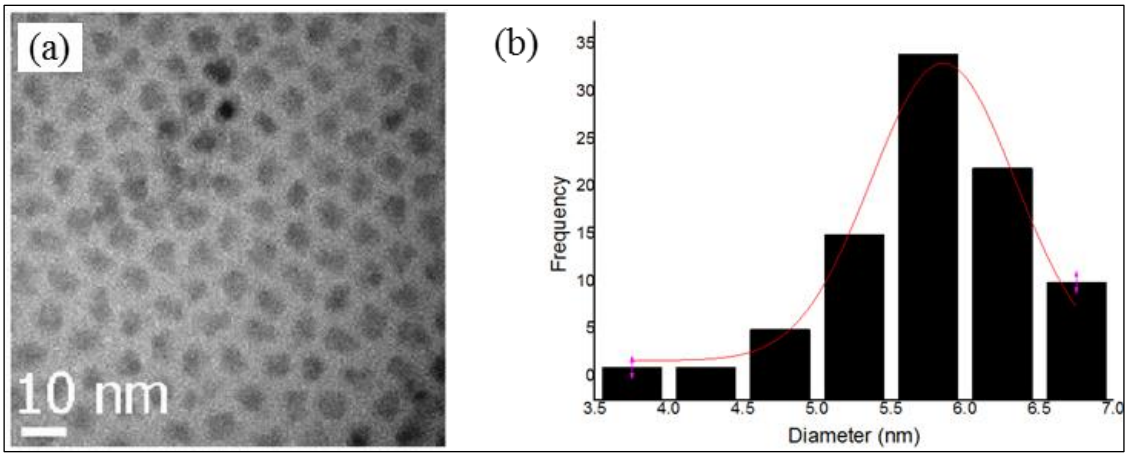

Figure 2-10: CdSe/CdS/ZnS: (a) *TEM image (b) histogram of size distribution [24].*

The calibration tests are performed under static and dynamic conditions using two high pressure diamond anvil cells (DAC) and an optical rheometer, respectively. All the used experimental devices are thermally regulated.

2.5.1 High pressure experiments

High pressure experiments are carried out using two different diamond anvil cells, as illustrated in Table 2-1. The first one is equipped with a diamond anvil and a thin diamond flat window. This particular configuration limits the range of working pressures up to 1.3 GPa, but greatly improves the microscopic observation of the sample. This high pressure cell is chosen to be designated as the low-pressure DAC. The second one is equipped with two diamond anvils with a classical DAC symmetrical design, that can allow experiments up to 3 GPa and more, to cover the whole range of our application. It is refered to as the symmetrical DAC in the following.

Range	F(P→1.3GPa,T)	F(P→3GPa,T)
Scheme	Low-pressure DAC (LaMCoS) 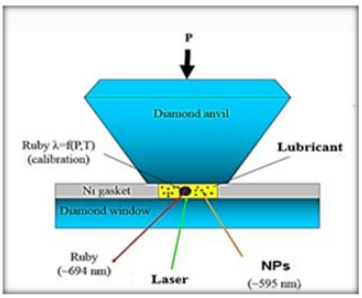	Symmetrical DAC (ILM –Lyon 1) 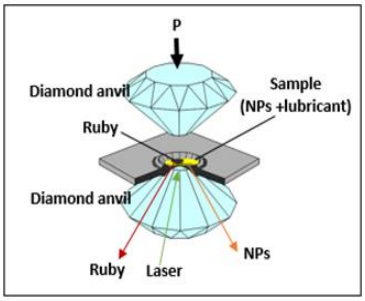
Confined liquid	Gasket thickness=100-300µm Gasket hole diameter=700µm Volume of liquid=0.1 µL	Gasket thickness=65-70µm Gasket hole diameter=200µm Volume of liquid=0.004 µL
Visualization diamond	Diamond window thickness=250-600µm	Diamond anvil thickness=2,2mm

Table 2-1: Characteristics of the used diamond anvil cells (DACs).

The DAC principle consists in two diamonds, (anvil on the upper face and anvil or window on the lower part) between which there is a hollow metal gasket ensuring the cell sealing. To begin with, micro-particles of ruby are introduced into the gasket hole as calibrated pressure sensors which give a precision of ±50 MPa. Afterwards, approximately 1 µL of the sample consisting of the NPs dispersed in squalane is injected into the gasket hole before closing the cell. The pressure is generated in the cell through applying a normal force by inflating a membrane with helium under controlled pressure. The temperature is measured thanks to a thermocouple inserted as close as possible to the sample touching the gasket (at the cutlet face of the anvil). A heating ring, surrounding the DAC, is connected to a heating system (which is linked to the thermocouple) to regulate the temperature with a precision of +/- 0.1 K.

The pressure calibrations are operated at three different temperatures (ambient, 323K and 348 K) for each used DAC in order to evaluate the pressure and temperature sensitivities of the CdSe/CdS/ZnS QDs in ranges encountered in realistic EHD contacts.

2.5.2 Thermal dynamic experiments

An optical rheometer (Physica MCR301, Anton Paar) is used to perform the dynamic thermal calibration on the CdSe/CdS/ZnS QDs dispersed in squalane, at atmospheric pressure. The spectroscopic measurements are carried out while imposing shear rates at constant imposed temperature to the colloidal suspension. The temperature is regulated by a Peltier system and the shear rate is imposed by the rotation of a plate (or a cone or a cylinder) driven by a servo motor. The temperature is typically measured with a precision is of +/- 0.03 K between 296 K and 373 K thanks to a platinum sensor that is located near the sample under the measuring gap. Three rotational geometries are available: plate-plate, cone-plate and coaxial cylinders. Coaxial cylinders are opaque, thereby, this configuration prevents the spectroscopic measurements to be realized. The cone-plate configuration allows maintaining a constant shear; however, the liquid may become turbulent and flows out at high shear rates. In contrast, in the parallel-plates configuration, the liquid is confined between two plates by capillary forces and hardly escape at very high shear rates. That is why, in this work, only the parallel-plates configuration is chosen. This configuration consists in a rotating steel plate and a fixed glass plate, as illustrated in Figure 2-11, which allows performing the spectroscopic measurements. The thickness of the sample introduced into the gap between the two plates, is constant ($H=H_0$). This results in a shear rate ($\dot{\gamma}$) varying linearly with r, the radius from the rotational axis (i.e from the plate center at $r=0$) to the considered measurement point. The maximum radius of the rotating plate (outer edge, $r=R$) is equal to 20 mm. The shear rate varies as follows:

$$\dot{\gamma}(r) = \frac{r\omega}{H_0} \qquad 2.7$$

where ω is the angular velocity of the rotating steel plate.

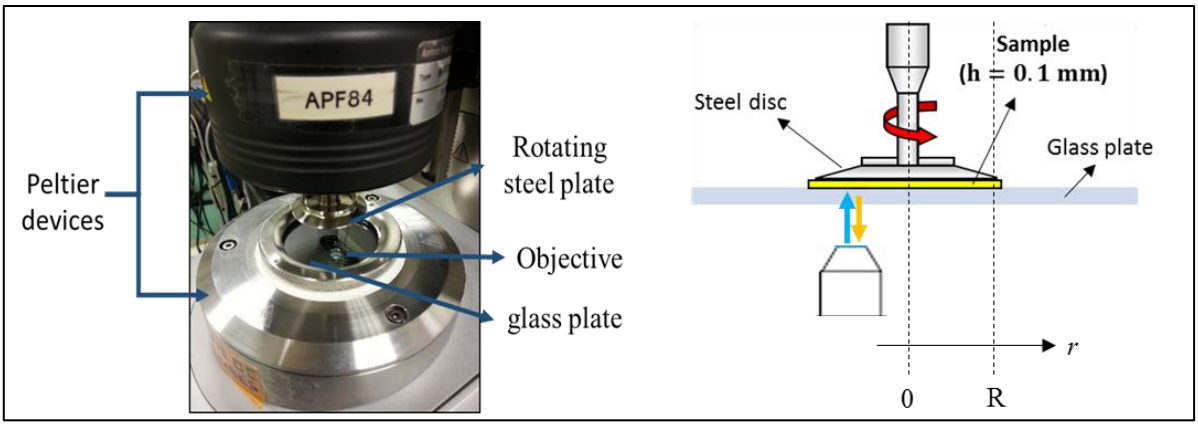

Figure 2-11: Physica MCR301 rheometer (Anton-Paar) using parallel-plates configuration for spectroscopic measurement.

Note also that, due to optical and mechanical constraints, spectroscopic measurements are performed at $r = 2/3\ R$. A small gap of about 0.1 mm is imposed in order to investigate the possible influence of shear stress on the QDs PL. For that, the shear rate in the fluid sample at r=2/3R is varied up to 50,000 s^{-1}.

2.5.3 Fluorescence measurements tools

In all the tests, spectroscopic measurements are carried out using a coupled optical system in the backscattering geometry. This optical system consists of a fluorescence microscope, an argon-ion laser source (Spectra Physics® Stabilite 2017) and a U1000 Horiba Jobin-Yvon spectrometer. The signal captured by the later (coupled by an optical fiber to the fluorescence microscope) is dispersed via a double-additive-stage monochromator equipped with a CCD detector and a 100 gr/mm double grating, yielding a spectral resolution of 0.07 nm/pixel (0.20 meV/pixel).

More into details, the CdSe/CdS/ZnS QDs are excited with the 514.532 nm line of the continuous argon-ion laser source. The laser power delivered at the sample is less than 0.6 mW. This leads to an excitation density of approximately 0.5 kW/cm^2. It is important to know that as such excitation density irradiates the sample for less than 10 second (acquisition time), it has insignificant effect on QDs photo stability [83]–[85].

The backscattered signal is collected using long-working distance objectives mounted on the fluorescence microscope. In order to obtain a sharp focus in the mid-thickness of the sample, two objectives are used:

- Olympus ×50 objective of 10.6 mm working distance (yielding a focused laser spot of about ~10 µm diameter) with the low-pressure DAC.
- Olympus ×20 objective of 12 mm working distance (resulting in a ~20 µm laser spot diameter), for the symmetrical DAC and rheometric experiments.

For that, the fluorescence microscope is set on a motorized micro-positioning xy stage in order to accurately adjust the position of the laser beam over the sample. The micro-positioning xy stage is also associated to a manually driven z stage to focus the incident laser beam at the mid-

thickness of the sample. The analyzed area of the sample is visualized by means of a video camera mounted on the microscope. This stage can be operated with any of the used experimental setup (DACs, rheometer, tribometer). In order to check the validity of the optical settings of the microscope and the spectrometer (sensitive to the fluctuations of the room temperature) and the correctness of the CCD detector, neon and sodium spectral calibration lamps are employed while recording the PL spectra. Hence, all acquired spectra are corrected in terms of wavelength thanks to the reference lamps' characteristic lines.

2.6 QDs pressure and temperature sensitivities - Results and discussion

As mentioned earlier, the pressure and temperature sensitivities of the QDs emission energy and bandwidth are required to extract the pressure and temperature values in working EHD contacts. Analytical functions, namely Pearson 7 (which is a combination of Gaussian and Lorentzian profiles) and Splitpearson (combination of two Pearson 7 functions which handle the peak asymmetry), are chosen to respectively estimate the emission energy and the FWHM, with a coefficient of correlation higher than 0.99. These functions are displayed in annex 5.5. The uncertainty evaluated in the different tests, is equal to 1.5 meV for the emission energy and 1.1 meV for the FWHM (see annex 5.2).The measurement uncertainty on pressure and temperature are detailed in annex 5.4.

2.6.1 High pressure calibration results

Here, the spectroscopic measurements are performed at four different xy positions at the mid-thickness of the sample in the DAC for each pressure and temperature condition, thus under static conditions. These different measurements are conducted to estimate the mean emission energy and the FWHM of the QDs PL response, and their corresponding standard deviations. Before and after each QDs spectrum acquisition, the luminescence shift given by the ruby micro-particles has been checked in order to ensure the accuracy of the pressure measurements.

Results in Figure 2-12 indicate the pressure dependence of the QDs emission energy at 296 K, 323 K and 348 K. The pressure uncertainty refers to the uncertainty of the ruby R1 luminescence line shift under pressure. Signs are the experimental data obtained using both the low-pressure and symmetrical DACs. Notice that there are lacks of data point in some pressure ranges, especially at pressures around 1.2-1.6 GPa. That is because of the gasket (ensuring the cell sealing) which does not deform linearly neither with the applied normal force nor with the imposed temperature. That is why it is difficult to control precisely the pressure in a DAC.

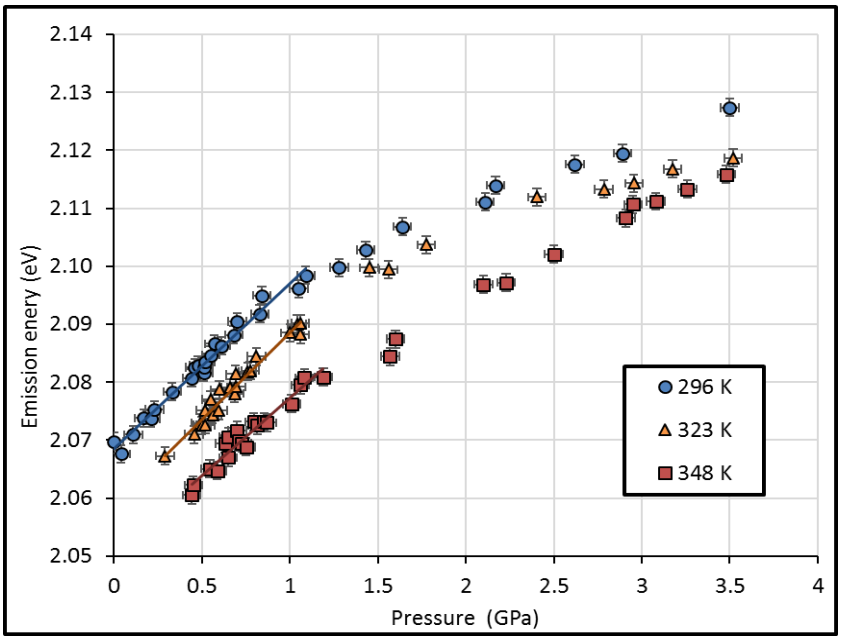

Figure 2-12: Pressure dependence of the emission energy of the CdSe/CdS/ZnS QDs dispersed in squalane at three temperatures (film thickness of the sample in the DAC ≤ 0.07 mm).

The emission energy is found to increase with pressure and decrease with temperature as predicted and shown in existing studies [21], [22], [24], [27]–[29] . This arises from the dependence of the NPs crystalline structure (bulk properties) and size (quantum effect) on the pressure and the temperature changes. The pressure dependence tendency seems to be quadratic over the full pressure range as mentioned by previous researches [21], [28]. Globally, it can be seen that, as the temperature increases, the curves become linear-like. In other words, depending on the temperature of the experiment, the results can show a change in the slope from lower to higher pressures. This might be associated to the phase transition of the carrier liquid (squalane) and not that of the CdSe QDs, which usually appears at pressures well above 3 GPa [30]. This hypothesis is supported by:

-An experiment (inspired from [86]) performed at 296 K using the symmetrical DAC (reaching 3.5 GPa) in which pure squalane is loaded after placing several ruby micro-particles (as pressure sensors) equally distributed (see Figure 2-13(a)). For a purely hydrostatic pressure condition, all ruby micro-particles indicate the same response and thus the same pressure (standard deviation close to 0). In contrast, an increase of the standard deviation refers to the existence of pressure inhomogeneity. This is more likely due to the occurrence of the fluid apparent solidification, thus to a phase change. Due to the limited number of data points in Figure 2-13(b), the slope change (phase transition) for squalane is not defined for a precise pressure value but, at least, it can be argued that the transition lies between 1.5 and 2.3 GPa.

-The work of Bair et al. [25] who demonstrated (using the transient hot wire method described in [87]) that the glass transition lies in the range1.3-1.5 GPa at 296 K and 1.7-2 GPa at 323 K depending on the selected model, as displayed in Figure 2-14.

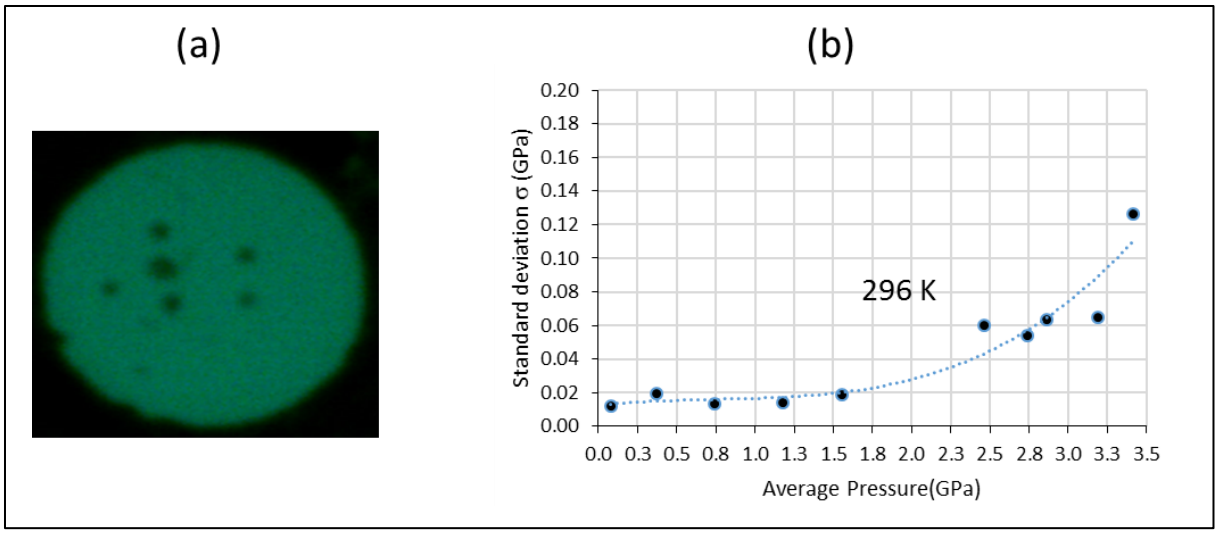

Figure 2-13:(a) Picture of a DAC loaded with ruby micro-particles immersed in squalane.(b) Pressure dependence of the standard deviation of the pressure measurements with the ruby micro-particles in squalane.

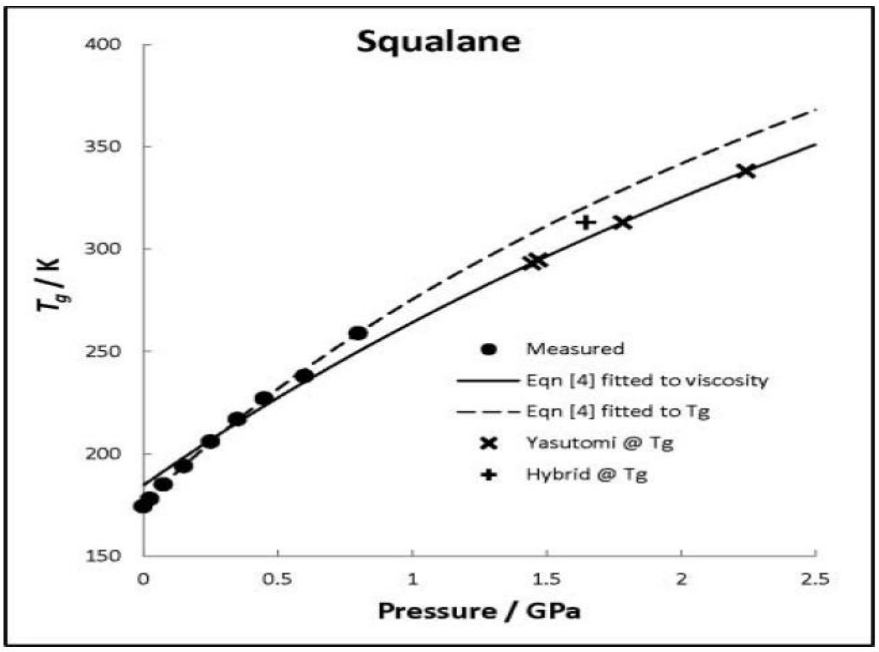

Figure 2-14: Glass transition temperature as a function of pressure. Circles represent the transition detected from thermal properties and correspond to a relaxation time of about 0.3s. The × and + represent the pressures at which the improved Yasutomi and the hybrid models predict the viscosity at the glass transition temperature [25].

Results in Figure 2-15 shows that, under the critical glass transition, the FWHM is almost constant with an increase of pressure and increases with temperature. The plateau witnessed with the increase in pressure suggests that the FWHM is only temperature dependent. Beyond, after the occurrence of a phase change, the FWHM increases with both pressure and temperature.

The discussion on the phase transition of squalane derived from stationary pressure conditions might be misleading and incomplete because it could occur differently under EHD conditions, i.e. under dynamic pressure conditions. That is why our analysis will be focused on the region below 1.3 GPa and for temperature above 296 K. This means that, for our perspective EHD tests, the applied load must be carefully chosen to induce a maximum pressure of 1.3 GPa in the contact.

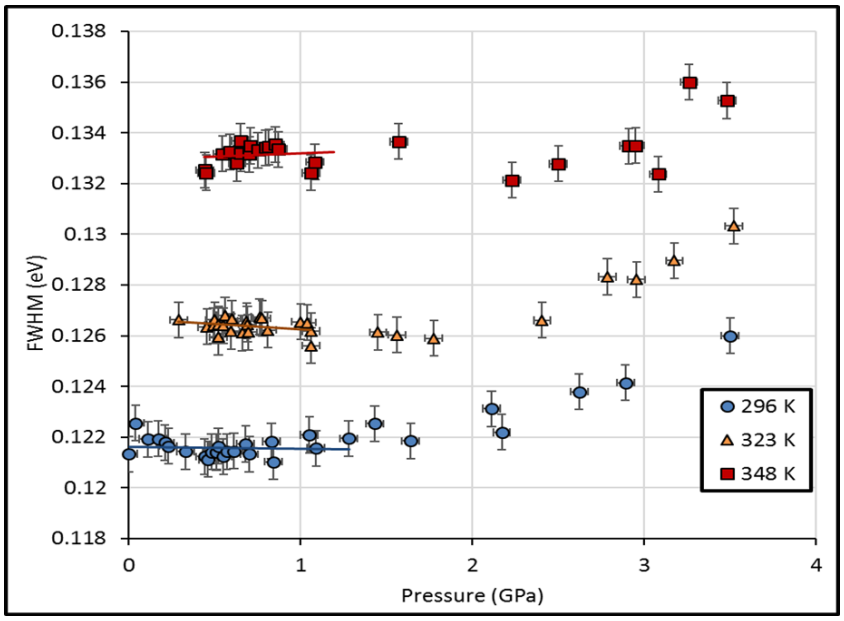

Figure 2-15: Pressure dependence of the FWHM of the PL peak of the CdSe/CdS/ZnS QDs dispersed in squalane at T=296, 323 and 348 K (film thickness of the sample in the DAC ≤ 0.07 mm).

It is important to underline that the low-pressure DAC configuration favors the collection of more photons out of the diamond window as compared to the symmetrical DAC. This enhanced photon collection is due to the larger sample thickness available with the low-pressure DAC and to the limited thickness of the diamond window together with the very large optical aperture and the short working distance, which are characteristics that improve the quality of observations and measurements [88]. In this pressure range on which the regressions are performed, it can be noticed that the calibration curves are linear and have similar slopes for each temperature (see Figure 2-16). These trends yield to two first-order correlations of the pressure and temperature dependencies of the QDs response, one for E_g and the other for the FWHM.

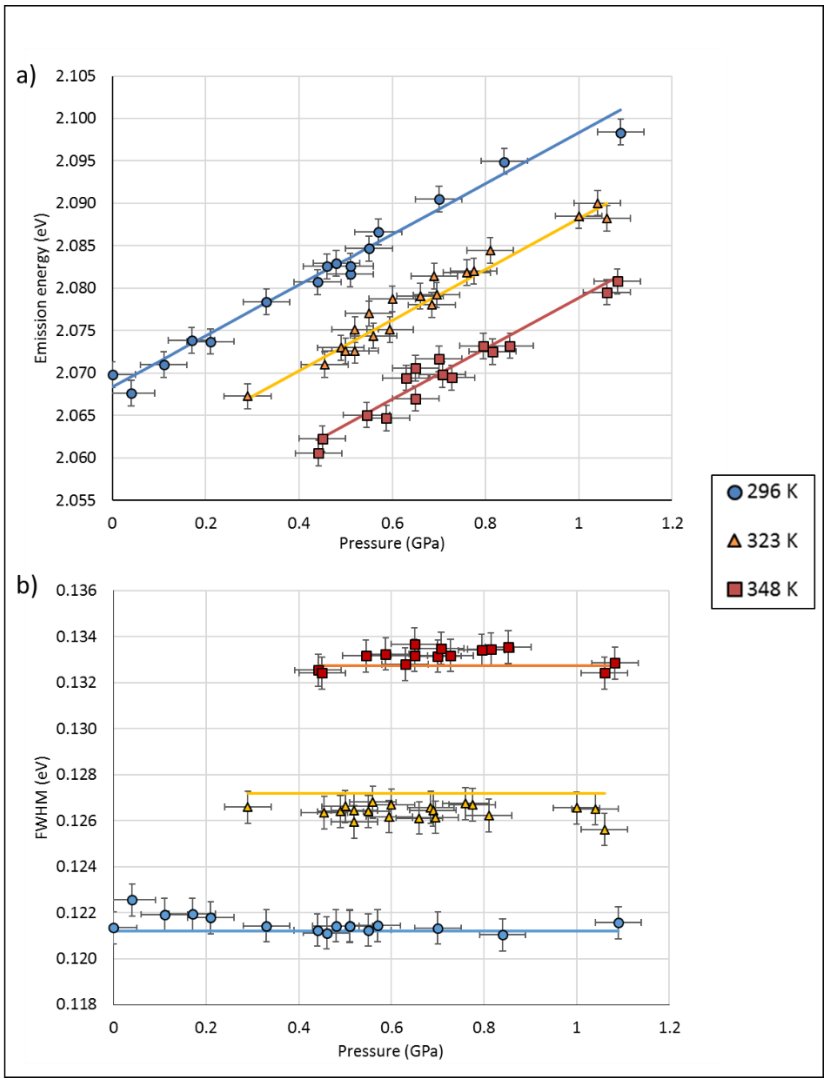

Figure 2-16: Pressure dependence (limited to 1.3 GPa) of a) the emission energy and b) FWHM of the CdSe/CdS/ZnS QDs dispersed in squalane at T=296, 323 and 348 K (film thickness of the sample in the DAC ≤ 0.2 mm).

For E_g, a search for a best regression led to the following relationship:

$$E_g(P,T) = E_{g0} + S_P P + S_T T \qquad 2.8$$

where E_{g0} = 2077 ±1 meV. The bilinear model parameters obtained with a coefficient of correlation R^2_{corr}=0.97 are given in Table 2-2.

Sample	Pressure sensitivity of E_g S_p (meV/GPa)	Temperature sensitivity of E_g S_T (meV/K)
0.125 mg/mL of CdSe/CdS/ZnS QDs dispersed in squalane	29.8 ± 3.7	-0.374 ± 0.041

Table 2-2: Pressure and temperature sensitivities of the emission energy of the CdSe/CdS/ZnS QDs dispersed in squalane.

For the FWHM, the resulted linear relationship can be written as:

$$FWHM(T) = FWHM_0 + S'_T T \quad 2.9$$

Where $FWHM_0$ =116.2 ±1.1 meV and the other regression parameters obtained with a coefficient of correlation R^2_{corr}=0.98 are reported in Table 2-3.

Sample	Temperature sensitivity of FWHM S'_T (meV/K)
0.125 mg/mL of CdSe/CdS/ZnS QDs dispersed in squalane	0.224 ± 0.020

Table 2-3: Temperature sensitivity of the FWHM of the PL peak of the CdSe/CdS/ZnS QDs dispersed in squalane.

Details about the estimation of the pressure and temperature sensitivities and their corresponding uncertainties are shown in annex 5.3.

These equations, obtained for pressures up 1.3 GPa and temperatures between 296 and 348 K, are rather simple and provide a description of the P/T dependence of the CdSe/CdS/ZnS QDs dispersed in squalane photoluminescence properties. In other words, the pressure and temperature influences can be decoupled from a single QDs PL spectrum (at least under static conditions). Indeed, the temperature can be deduced from the FWHM using equation 2.9. Then, it is substituted in equation 2.8, which includes the QDs emission energy, to extract the pressure value.

Nevertheless, these equations must be taken cautiously because their coefficients (QDs P/T sensitivities) may alter by any variation of the QDs concentration (a concentration higher than 0.125 mg/mL may promote parasitic interaction between QDs), QDs size distribution and nature of the lubricant, according to references: [24], [89]. In other words, it should be necessary to make a calibration for each prepared colloidal solution before probing EHD contacts.

2.6.2 Results of the thermal dynamic calibration

Thermal dynamic calibration is conducted using the optical rheometer at ambient pressure. The effect of temperature and shear stress are investigated on the colloidal suspension, realized from 0.125 mg/mL of CdSe/CdS/ZnS QDs dispersed in squalane. This is essential to isolate and identify the possible effect of flow-induced shear stress on the QDs PL response. As mentioned earlier, the shearing is chosen to be driven in the parallel-plates configuration. It is of main interest to calibrate under such conditions because i) the suspension will undergo an intense shearing while performing the *in situ* measurement in EHD contacts and ii) in the rheometer, the temperature is more precisely regulated and more easily controlled than in the DACs. This can provide a further series of experiment to establish the temperature dependence of the QDs PL properties. The sample is also homogenized (by shearing) and thermally stabilized rapidly due to the rotational flow. In addition, with such a low concentration of QDs (of ~ 0.125 mg/mL

in squalane), it is demonstrated that the viscosity of the carrier lubricant remains unaffected [24]. In other words, the QDs does not disrupt the flow of the lubricant and thus the generation of film thickness and friction in EHD contacts.

The results displayed in Figure 2-17 show the variation of the emission energy and FWHM as a function of shear stress at three different temperatures (293, 333 and 373 K). Here, for all applied temperatures, the gap is set at 0.1 mm and the PL spectra are collected at $r = 2/3\ R$. It is important to know that each recorded emission spectrum results from averaging the QDs PL response over a large volume of the sample due to this latter rotation in the rheometer gap.

The emission energy and the FWHM are almost constant despite the effect of flow and shear stress, meaning that the QDs responses are shear stress independent within the range experienced in those experiments. Excluding this parameter supports the application of the linear correlations obtained from static high pressure calibration to probe pressure and temperature under dynamic conditions (EHD contacts).

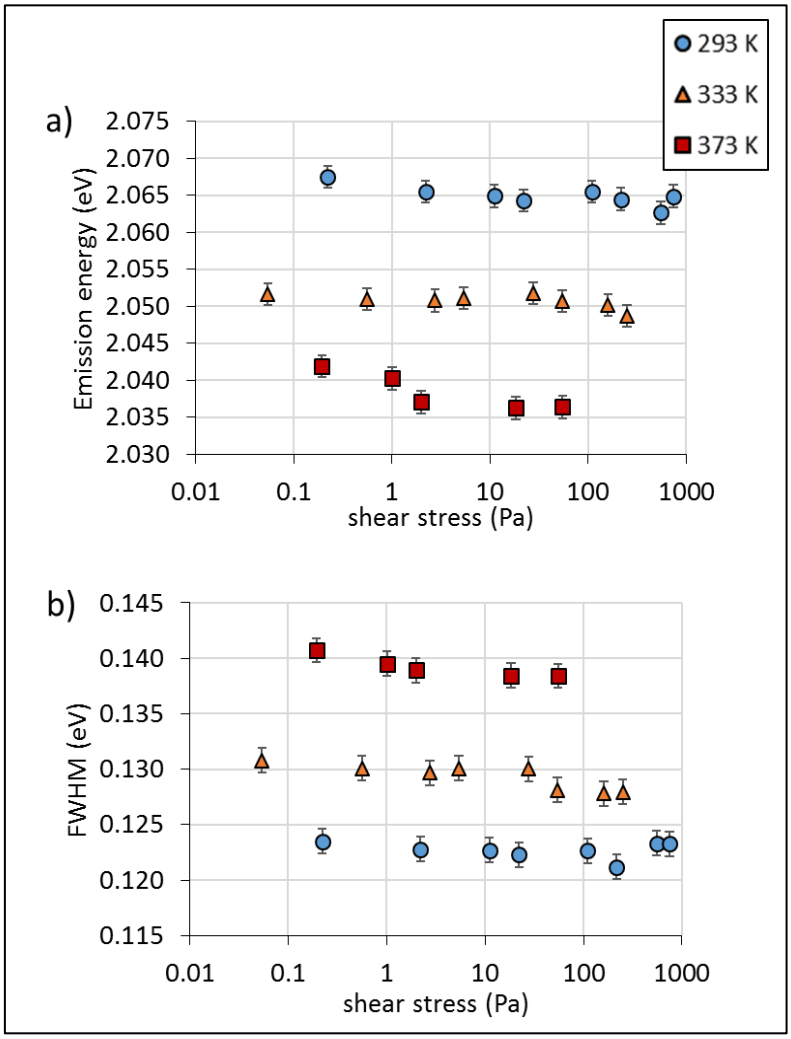

Figure 2-17: Variation of the emission energy and FWHM of CdSe/CdS/ZnS QDs dispersed in squalane as a function of shear stress, at different temperatures.

The small variations of the emission energy and FWHM at different shear stress could arise from the temperature which might increase continuously after a certain number of rotations, depending on the imposed temperature. At low temperature, the viscosity of the dispersion is high thereby the self-heating is more accentuated with shear and number of cycles than at high temperature. That is why, in order to get reliable results, low numbers of cycles and short PL acquisition times (<10 s) are carefully set for each recorded spectroscopic measurement.

Furthermore, in Figure 2-17, the averaged values of the temperature sensitivity of the emission energy is of -0.370 meV/K and that of FWHM is of 0.215 meV/K. These temperature dependencies of the emission energy and the FWHM in these simple dynamic conditions are therefore found to be very similar to those found in the static high pressure experiments carried out with the DACs (see Table 2-2 and Table 2-3).

2.7 Conclusion

This chapter showed essential steps towards the development of a new *in situ* technique allowing simultaneous pressure and temperature measurements in EHD contacts. The technique is based on exploiting the dependence of the photoluminescence properties of CdSe/CdS/ZnS quantum dots (QDs) with pressure and temperature. These QDs are chosen to be dispersed in a model lubricant, namely squalane.

Static and dynamic calibrations are performed in order to evaluate the pressure and temperature sensitivities of a dispersion of 0.125 mg/mL of CdSe/CdS/ZnS QDs in squalane. The static calibration results showed that it is possible to measure simultaneously the pressure and temperature thanks to the emission energy and the Full Width at Half Maximum of the QDs PL spectroscopic response. These latter P/T dependencies are found to be linear for pressures up to 1.3 GPa and for temperatures from 296 K to 373 K (or in ranges below the phase change of the carrier lubricant). This confirms their high potential for probing pressure and temperature in confined lubricating films as those occurring in EHD contacts. Nevertheless, it is important to know that the P/T sensitivities yielded from the calibrations must be applicable only for the employed colloidal solution within the explored pressure and temperature ranges, otherwise, the QDs P/T sensitivities may be modified. For these reasons, it should be necessary to perform a calibration for each prepared QD NPs solution before the EHD contacts can be properly studied in the same pressure and temperature ranges.

Under controlled conditions of temperature and shearing, the rheological analysis (in the parallel-plates configuration) showed that the presence of QDs doesn’t affect the viscosity of the carrier lubricant and that shearing is not perturbative to the QDs PL response. In addition, a very good accordance is found between the temperature sensitivities yielded from the thermal dynamic and the static high pressure calibrations. These results confirm the perspective to perform non-perturbing temperature measurements.

In the next chapter, the potentiality of these CdSe/CdS/ZnS QDs/nanosensors is used to establish pressure and temperature profiles throughout EHD point contacts, simulated in a dedicated tribometer.

Chapter 3: *in situ* measurement of pressure and temperature in EHD contacts

Chapter 3: *in situ* measurement of pressure and temperature in EHD contacts 95
3.1 Experimental setup 97
3.1.1 EHD tribometer 97
3.1.2 Coupling the EHD tribometer with the photoluminescence equipment 99
3.2 Spatial measurement resolution 100
3.2.1 Laser spot size 100
3.2.2 Depth of focus 101
3.2.3 The uncertainty on the position of a measuring point 102
3.3 Experimental preparation 102
3.3.1 QDs suspensions 102
3.3.2 Parameters of importance and operating conditions 104
3.3.2.1 Tests under isothermal conditions 106
3.3.2.2 Tests under non-isothermal conditions 107
3.4 *In situ* pressure and temperature measurement 109
3.4.1 Pressure measurements - Isothermal contacts with dispersion N°1 109
3.4.2 Pressure measurements - Isothermal contacts with non-calibrated dispersions 110
3.4.3 Temperature measurement - Non-isothermal contacts 114
3.5 Summary and conclusion 118

In the previous chapter, the photoluminescence response of the CdSe/CdS/ZnS QDs dispersed in squalane with a concentration of 0.125 mg/mL have been investigated as a function of pressure and temperature in static conditions. Pressure and temperature sensitivities of the emission energy and the FWHM were thus respectively determined for a given colloidal suspension. In this chapter, several dispersions of QDs in squalane are used to probe pressure and temperature in EHD contacts. Various operating conditions such as pure rolling or rolling-sliding, normal load, inlet temperature and contacting solid materials will be investigated. The purpose of this chapter is to evaluate the potentialities of the developed spectroscopic method over a wide range of operating conditions. Comparisons with results obtained from numerical tools will be also proposed. Note that the main features of the employed TEHD numerical model are briefly described in annex 5.1.

3.1 Experimental setup

3.1.1 EHD tribometer

The test-rig used in this work is a ball-on-disc tribometer called "Jerotib" developed by Molimard et al. [31] at LaMCoS. It simulates EHD contacts and allows measuring both film thickness and friction. The contacting bodies (disc and ball) are driven independently by two separate motors to apply any desired slide-to-roll ratio (SRR):

$$SRR = \frac{\Delta u}{u_e} = 2\frac{u_b - u_d}{u_b + u_d} \times 100\% \qquad 3.1$$

where u_e is the entrainment velocity and u_b, u_d the velocities of the ball and the disc, respectively. SRR is equal to zero in pure rolling and different from zero in rolling-sliding conditions.

The contact normal load (w) is applied by means of a lever arm, a spring and a plate in vertical translation linked to a static force sensor. The ball dips into the oil reservoir, insuring fully flooded conditions. The two specimen and the oil are thermally isolated and maintained at a constant temperature by an external thermal controlling system (see Figure 3-1). The temperature is controlled with a precision of 0.1K thanks to a platinum resistance (PT100) immersed in the oil reservoir near the contact zone.

Table 3-1 summarizes the Jerotrib operating characteristics and their precision. Balls which have a radius of 12.7 mm and made of 100C6 steel or silicon nitride (Si_3N_4) are used. They are driven against a transparent disc of 85 mm in diameter and 10 mm thick, made of glass (BK7) or sapphire. Spectroscopic measurements require at least one transparent surface. The glass disc is used for the medium contact pressure range (0.5–0.8 GPa) and the sapphire disc for pressures around or above 1 GPa. In terms of thermal properties, glass can be considered as a thermal insulator material that does not absorb/dissipate heat easily and thus enhance heat generation within the lubricant. On the other hand, sapphire exhibits a thermal diffusivity (D) similar to that of 100C6 steel. Table 3-2 and Table 3-3 display the mechanical and thermal properties of the chosen contacting solid materials. Here, the thermal conductivity and specific heat of the contacting solids are considered constant. It should be recalled that one of the purposes of this

work is to study the influence of the different employed materials on the pressure and the temperature distributions in EHD contacts.

Parameters	Range	Precision
Speed	0.01 to 10 $m.s^{-1}$	0.0005%
Slide-to-roll ratio	0 to $\pm$200 %	<1.2 %
Temperature	-10 to 120 °C	0.1 °C
Normal load	up to 300 N	0.8 %
Friction Force	up to 40 N	0.3 %
Hertzian Pressure	up to 3 GPa	-
Film thickness	Few to 1500 nm	Typically 2 – 5 nm
Materials	Glass – Sapphire Silicon nitride Steel – Tungsten Carbide	σ_{RMS}: 2 – 8 nm σ_{RA}: 10 nm σ_{RMS}: 5 – 20 nm
Contact configuration	Slender – Circular – Large elliptical	

Table 3-1: Jerotrib tribometer operating characteristics.σ_{RA} ,σ_{RMS} are the arithmetical average and the root mean squared values of the surface roughness, respectively.

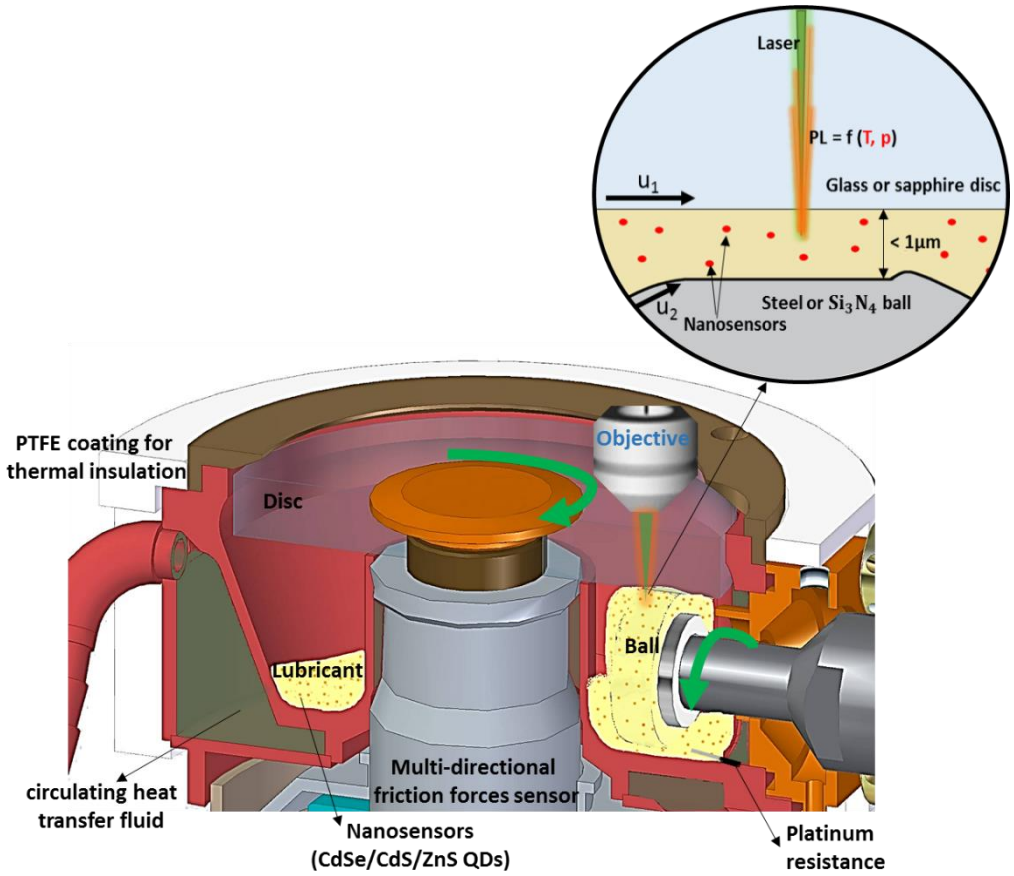

Figure 3-1: Cross-section of the Jerotrib experimental set-up.

	Disc properties	
Parameter [Unit]	Glass (BK7)	Sapphire
$E_d\ [Pa]$	81×10^9	360×10^9
$\nu_d\ [-]$	0.208	0.34
$\rho_d\ [kg.m^{-3}]$	2510	4000
$k_d\ [W.m^{-1}.K^{-1}]$	1.114	40
$C_{pd}\ [J.kg^{-1}.K^{-1}]$	858	750
$D_d\ [m^2.s^{-1}]$	5.17×10^{-7}	1.33×10^{-5}

Table 3-2: Transparent discs properties.

	Ball properties	
Parameter [Unit]	Steel (100C6)	Silicon nitride (Si_3N_4)
$E_b\ [Pa]$	210×10^9	310×10^9
$\nu_b\ [-]$	0.3	0.29
$\rho_b\ [kg.m^{-3}]$	7850	3240
$k_b\ [W.m^{-1}.K^{-1}]$	46	20
$C_{pb}\ [J.kg^{-1}.K^{-1}]$	470	680
$D_b\ [m^2.s^{-1}]$	1.25×10^{-5}	9.08×10^{-6}

Table 3-3: Balls properties.

3.1.2 Coupling the EHD tribometer with the photoluminescence equipment

The ball-on-disc tribometer is operated together with the optical system previously described in Chapter 2, as shown in Figure 3-2. This system comprises a laser source, a microscope and a spectrometer, all coupled by optical fibers. An additional video camera fixed on the microscope and a monitor are used for the contact visualization. The microscope is mounted on a xyz micro positioning stage. The xy-displacements allow to precisely move and position the laser beam over the EHD contact area. The z displacement is used to focus the laser in the mid-film thickness between the transparent disc and the ball and to collect the photoluminescence signal throughout the sample.

An Olympus $\times 50$ objective is employed with a typical 1.8 mW laser power on the sample. This leads to an excitation density of 3.6 kW/cm² which may affect the QDs quantum efficiency for long irradiation times (>1 min) or under static conditions [83]–[85], which is not the case in in situ experiments during which the fluid irradiated by the laser beam is constantly renewed. As with static calibration experiments, all spectra are corrected using the characteristic lines of a sodium spectral lamp.

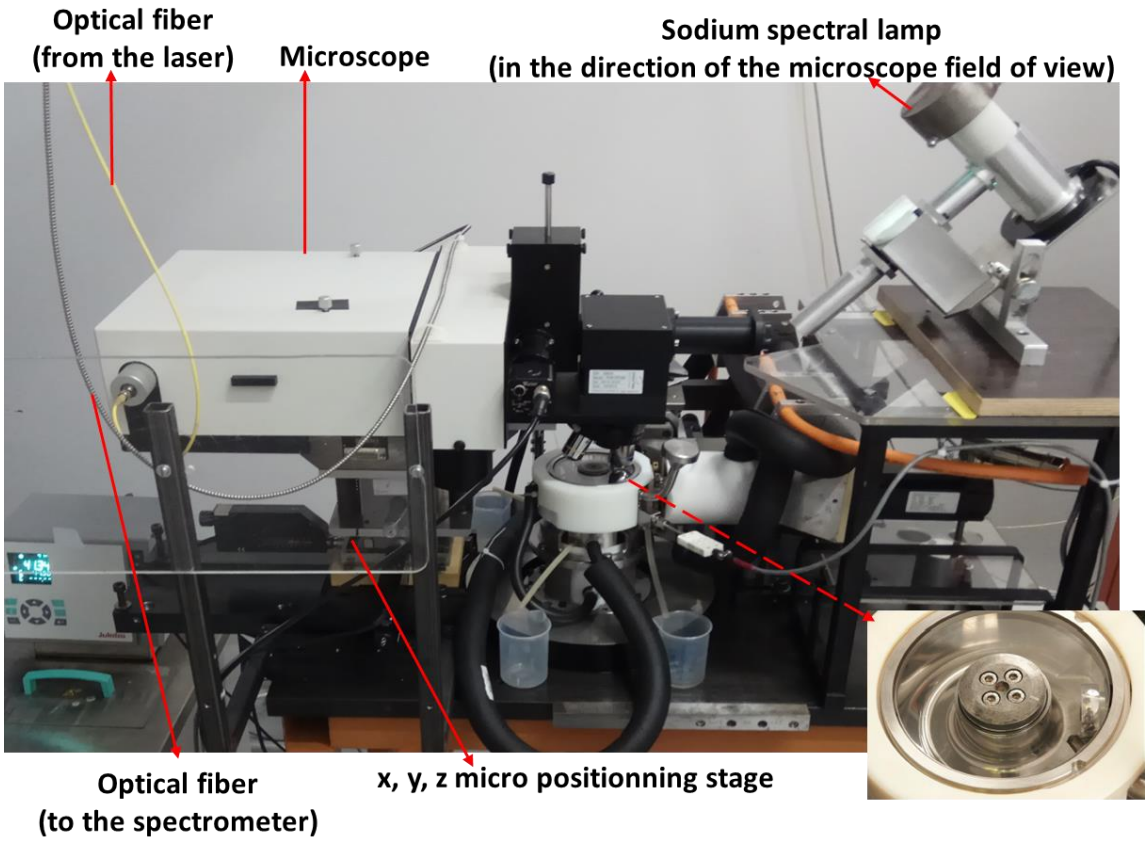

Figure 3-2: The coupling of the Jerotrib test-rig with the optical system (microscope, laser, optical fibers, spectral lamp and spectrometer (not shown here).

3.2 Spatial measurement resolution

The spatial resolution of the *in situ* measurements depends on both the spot size of the laser beam (i.e. the spot diameter of the laser beam through the transparent disc), the stability of the ball-on-disk device (i.e. the spatial stability of the EHD contact) and the accuracy of the xy positioning system.

3.2.1 Laser spot size

Theoretically, the laser spot size depends on the wavelength of the incident radiation and the magnification of the objective. In air, the theoretical value of the laser spot diameter is equal to 2.4 µm using a laser beam of wavelength $\lambda = 514.532$ nm and a ×50 magnification objective (see annex 5.6). Generally, the theoretical diameter of the laser spot is lower than the actual one. For more details, in the case of the performed experiments, the diameter of the laser beam is widened when it passes through:

- The objective lens, which generates longitudinal spherical aberrations.
- The 10 mm thick transparent disc, which is not exempted from optical aberrations.
- Or when reflected by the interfaces.

In order to determine the genuine value of the probe size, an experiment is performed using a cleaved silicon sample to form a steep step underneath the transparent disc (see Figure 3-3). The laser beam passes (by moving the microscope) on both sides of the step, and in turns, the intensity of the 520 cm^{-1} Raman peak emitted by the silicon wafer is measured at different positions. The distance over which the measured intensity varies from 100% to 0% gives the width of the laser spot. The results of this experiment indicate a probe diameter of 4 ± 2 µm in air, 6 ± 2 µm across the glass disc and 8 ± 2 µm across the sapphire disc (see annex 5.6).

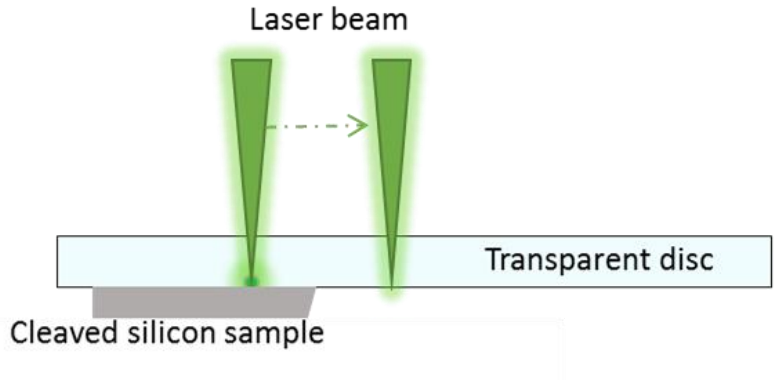

Figure 3-3: Scheme of the laser beam diameter experimental determination.

3.2.2 Depth of focus

The depth of focus depends on the objective magnification and numerical aperture. In this study, the used depth of focus is 1.1 µm for the × 50 magnification objective [90]. Therefore, for film thicknesses of less than 0.5 µm, the magnitude of the spectroscopic parameters will correspond to average values across the film thickness. The depth of focus could be improved by using objectives of higher magnification and adequate corresponding confocal diaphragms. However, decreasing the observed field leads to a significant decrease of the signal-to-noise ratio. Furthermore, as the disc rotation combined with its residual micro-geometrical defects causes (small) vertical fluctuations, it disturbs the focus adjustment, which is extremely sensitive to achieve a satisfactory measurement.

In addition, since the laser beam is travelling through the 10 mm thick sapphire/glass disc, parasitic fluorescent background signal emitted from the transparent disc overlays with the PL QDs spectrum and hides its tails (see Figure 3-4). Moreover, the sapphire fluorescence is found to vary with temperature and stress, as reported in references [91], [92]. This leads to a great difficulty for extracting the accurate QDs full width at half maximum (FWHM) even after applying a baseline correction function. On the other hand, the QDs signal-to-noise ratio allows the evaluation of the QDs emission energy (peak position indicated at top of the QDs spectrum). This latter is not affected by the parasitic background because the QDs does not absorb energy in the range of that emitted by the transparent disc, as reported in reference [23]. For that reasons, the analysis of the FWHM parameter will be not exploited; instead, the emission energy only will be evaluated for studying EHD contacts.

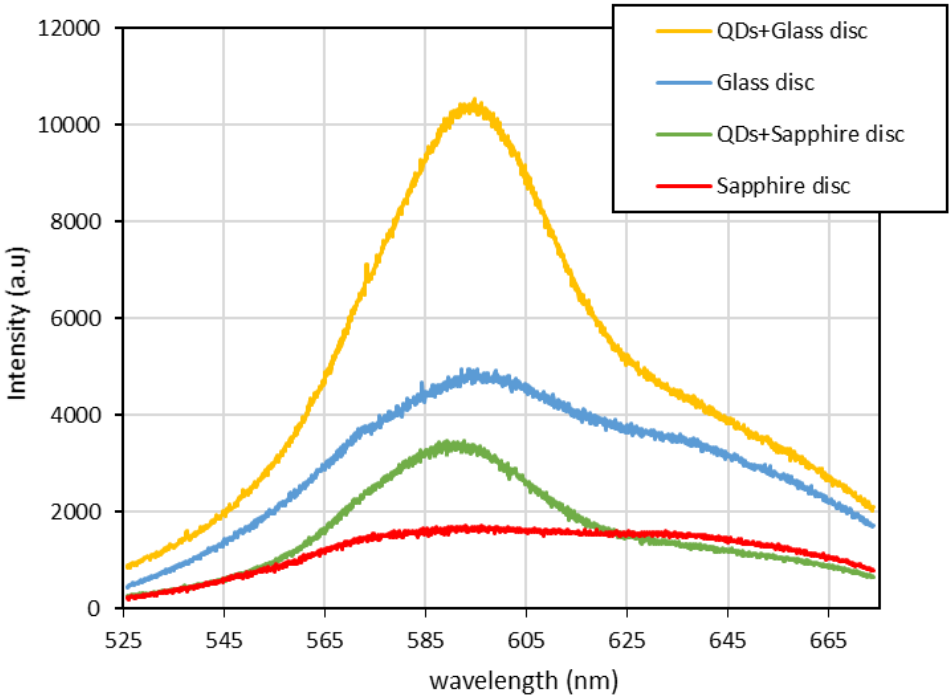

Figure 3-4: QDs PL spectra with background signals of the transparent discs at the contact center. Exploratory tests run at T_0=293 K, u_e=1.5 m/s, SRR=0%. The glass-steel contact is operated at 28N ($P_H = 0.50\ GPa$) and the corresponding lubricant film thickness is of 362 nm. The sapphire-steel contact is operated at 28.5 N ($P_H = 0.90\ GPa$) and the corresponding lubricant film thickness is of 327 nm. For both configurations, the laser is focused at the mid-film thickness of the pressurized zone with a power of 1mW.

3.2.3 The uncertainty on the position of a measuring point

In order to determine the center of the EHD contact, the microscope is moved thanks to the micrometric motorized tables in the xy-plane. At the contact level, the positioning of the laser spot is observed from the B&W image given by the video camera fixed on the microscope. At the center of the contact, the microscope is moved in the z direction to adjust the focus in the mid-thickness, which corresponds relatively to the most intense CdSe/CdS/ZnS QDs PL spectrum along the vertical axis. The uncertainty on the position of a measuring point results from different sources, which can be listed as follows:

- The error on positioning, related to mechanical clearances of the micrometric motorized xy-stage of the fluorescence microscope, is estimated at ± 4 µm.
- The reading error made for determining the position of the contact center (visually on a video screen connected to a camera placed on the microscope) is estimated at ±10 µm.
- Thanks to a very fine mechanical adjustment, a very small error related to the motion of the whole contact over time (geometrical instability) is valued at ± 1 µm.

Hence, the resulting uncertainty on the position of a measuring point is of ± 15 µm.

3.3 Experimental preparation

3.3.1 QDs suspensions

In order to perform various EHD *in situ* experimental campaigns, approximately 50 mL of QDs suspension of 0.125 mg/mL is prepared. Jerotrib oil container must be filled with approximately 11 mL of fluid to ensure a fully flooded EHD contact. The average time of an experiment is about one hour. Due to the rotation of the ball, a small amount of lubricant (~ 0.5 mL) is depleted during the test. Therefore, to compensate this loss, the oil container is refilled with small quantities of pure squalane, i.e. without QDs. This leads to a small reduction in QDs concentration. According to Albahrani [24], for such low initial concentration of 0.125 mg/mL, this should not affect the pressure and temperature sensitivities but only the PL intensity.

It is important to know that the CdSe/CdS/ZnS QDs used to prepare the suspensions in squalane were received in batches of approximately 3 mg. Two batches were then necessary to prepare a sufficient volume of fluid. The prepared and used colloidal suspensions are listed in Table 3-4. It details the batch number (#1 or #2) as well as the estimated dilutions during the EHD tests. Note that the results of the calibrations of Chapter 2 were obtained using batch #1 only.

Figure 3-5 shows a comparison between the PL spectra, obtained at ambient temperature under atmospheric pressure, of the two batches dispersed in squalane under the same conditions: at the same concentration of 0.125 mg/mL and at the same thickness of 0.9 mm between a hollow steel support and a glass lamella. The excitation power is of 0.5 mw and the acquisition time is of 1 second. The spectra are acquired twice and are found replicable.

It can be clearly seen that batch #2 is different compared to the first one in terms of PL emission intensity and wavelength. These differences may arise from:

- The different size distribution of the QDs in the two batches: according to the quantum confinement theory, small QDs emit shorter wavelengths (or higher energies) and bigger QDs emit higher wavelengths (or lower energies) within the emission spectrum.
- The oxidation of batch #2: the oxidation leads to the increase of the QDs emission energy and intensity due to a shrinkage of the CdSe core and a reduction of the defect state by oxygen, respectively [93]. As the first batch was quickly dispersed in squalane and the second one was conserved for a long period in a glass vial contained ambient air (before dispersing it in squalane), this second hypothesis seems to be more probable.

This difference may also lead to a dissimilarity on the QDs pressure and temperature sensitivities between the first and second batches, according to references [24], [94].

N° of colloidal dispersion	Batch	Concentration(mg/mL)	Calibrated
1	#1	0.125	✓
2	#2	0.125	-
3	#2	0.105	-
4	#2	0.098	-
5	#2	0.065	-
6	#2	0.098	-

Table 3-4: The employed colloidal suspensions for in situ measurements.

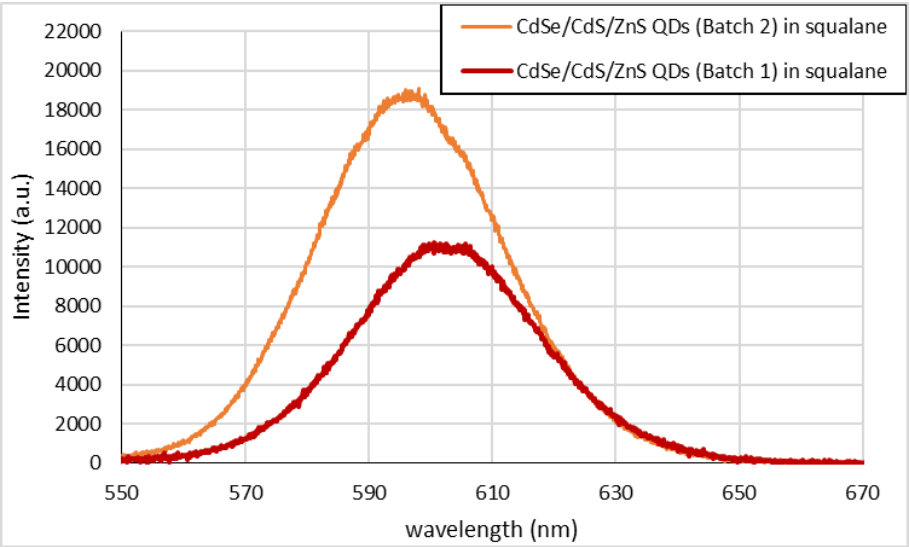

Figure 3-5: Photoluminescence spectra of the two batches of CdSe/CdS/ZnS QDs dispersed in squalane at equal concentration of 0.125 mg/mL, at the same thickness of 0.9 mm between a hollow steel support and a glass lamella, irradiated at 0.5 mW at ambient temperature under atmospheric pressure.

3.3.2 Parameters of importance and operating conditions

With an acceptable level of accuracy, analytical models allocate more flexibility in designing operating conditions (selecting entrainment velocity, normal load, etc.) to predict central & minimum film thicknesses and Hertzian pressure, and to indicate shear heating at the contact inlet without having to run full numerical simulations.

The central film thickness (h_c) is estimated by the Chittenden analytical equation [95].Van Leeuwen [96] and Wheeler et al.[54] demonstrated that this equation is the most accurate to predict central film thickness for circular EHD contacts in case of a Newtonian lubricant operated under pure rolling and isothermal conditions. The Chittenden formula incorporates the contact geometry, the materials properties, the entrainment velocity and the normal load. It can be expressed as follows:

$$H_C = K {U_C}^{0.68} {W_C}^{-0.073} {G_C}^{0.49} \qquad 3.2$$

where H_C, U_C, W_C and G_C are the dimensionless film thickness, speed, load and material parameters respectively. They are calculated as follows:

$$H_C = \frac{h_c}{R_x} \qquad U_C = \frac{\mu_0 u_e}{E_r R_x} \qquad W_C = \frac{w}{E_r {R_x}^2} \qquad G_C = \alpha^* E_r$$

with μ_0 the Newtonian viscosity at atmospheric pressure, α^* the pressure-viscosity coefficient, both parameters being considered at the inlet temperature. They are calculated from a modified WLF model [97]. w is the normal load, R_x the reduced radius is defined as:

$$\frac{1}{R_x} = \frac{1}{R_{dx}} + \frac{1}{R_{bx}}$$

with R_{dx} and R_{bx} the principal curvature radii of the disc (d) and ball (b) along the x-axis and E_r the reduced Young modulus of the contacting solids :

$$\frac{2}{E_r} = \frac{(1-\nu_d^2)}{E_d} + \frac{(1-\nu_b^2)}{E_b}$$

with E_b and ν_b the Young modulus and the Poisson ratio of the ball, and E_d and ν_d the ones of the disc.

Moes [98], [99] defined two analytical parameters, the dimensionless load (M) and material properties (L), to describe EHD contacts. These parameters can be expressed by combining the previous dimensionless Chittenden parameters as:

$$L = G_C(2U_C)^{1/4} \quad 3.3$$

$$M = W_C(2U_C)^{-3/4} \quad 3.4$$

The radius of the contact can be calculated as:

$$a = \sqrt[3]{\frac{3wR_x}{2E_r}} \quad 3.5$$

The Hertzian pressure (P_H) is determined using the following formula:

$$P_H = \frac{3w}{2\pi a^2} \quad 3.6$$

Jubault [4] has analyzed experimentally the evolution of the pressure as a function of M and L and has concluded that the pressure profiles resemble a Hertzian distribution when M>100 and L<17.

The thermal film thickness reduction coefficient φ_T proposed by Cheng [32] represents an indicator on the significance of thermal effects at the contact inlet that lead to the reduction of the lubricant viscosity and thus the reduction of the lubricant film thickness. It is calculated as follows:

$$\varphi_T = \frac{1 - 13.2\left(\frac{P_H}{E_{eq}}\right)Q_{th}^{0.42}}{1 + 0.213(1 + 2.23|SRR|^{0.83})Q_{th}^{0.64}} \quad 3.7$$

with E_{eq} is the equivalent elastic modulus which is expressed as:

$$E_{eq} = \frac{E_b^2 E_d(1+\nu_d)^2 + E_d^2 E_b(1+\nu_b)^2}{\left(E_b(1+\nu_d) + E_d(1+\nu_b)\right)^2}$$

and Q_{th} is the dimensionless thermal parameter:

$$Q_{th} = \left(-\frac{\partial \mu}{\partial T}\right)\frac{u_e^2}{k_f}$$

According to [100], the Cheng formula provides a critical value φ_T= 0.96 under which shear-heating becomes significant at the contact inlet.

Combining the above-mentioned parameters and criteria, it becomes possible to define the actual ranges of operating conditions to apply during *in situ* experiments. They are limited by the possibilities of the measurement technique previously defined by the static and dynamic calibrations of CdSe/CdS/ZnS QDs, by the capabilities of the different set-up used in this work and also by the mechanisms taking place in EHD contacts. In more details, the requirements for selecting these ranges can be listed as follows:

1. The normal loads (w) are chosen to not generate more than ~1.3 GPa as maximum pressure above which the linear slope of the QDs emission energy as function of pressure changes according to the calibration results (shown in chapter 2).
2. The entrainment velocity (u_e) is chosen at the lowest to limit shear heating at the contact inlet for isothermal conditions, but high enough to ensure a sufficient film thickness (central film thickness h_c > 200 nm) in order to collect an adequate PL intensity (adequate signal-to-noise ratio).

Additional constraints have to be accounted for, according the purpose of each *in situ* test: among them, M and L values or φ_T.

The aim of this chapter is to exploit the potentialities of the developed spectroscopic method to measure pressure and temperature in EHD contacts: the selected operating conditions are justified below and summarized in Table 3-5, Table 3-6 and Table 3-7. Note that all the tests are carried out under steady state conditions.

3.3.2.1 Tests under isothermal conditions

A first series of tests is dedicated to evaluate the feasibility of the developed method for measuring the pressure in the absence of significant thermal effects, i.e. under isothermal conditions. To ensure such conditions, the experiments are conducted under operating conditions maintaining the thermal coefficient (φ_T) equal or higher than 0.96. This is achieved under pure rolling (SRR = 0%), at entrainment velocities (u_e) avoiding shear heating at the contact inlet and providing a sufficient film thickness in the contact zone. It is important to note that than the dimensionless load parameter (M) is maintained higher than 100 and L maintained equal or lower than 17, in order to guarantee a quasi-Hertzian pressure distribution, as revealed in [37]. So that, the experimental central pressure can be compared to the Hertzian and numerical central pressures for corroboration.

The isothermal tests are run at 298 and 323K with u_e = 1.8 and 3.1 m/s, respectively, in order to ensure a sufficient film thickness (>200 nm) and thus provide an adequate QDs signal-to-noise ratio. Various combinations of materials are used: sapphire-steel, glass-steel and glass-Si_3N_4. Four normal loads (from 84 to 222 N) are selected leading to Hertzian pressures at the contact center from 0.8 to 1.8 GPa. The tests are labeled with PRI which stands for pure rolling

isothermal and numbered from 1 to 6. All the operating conditions and contact parameters are given in Table 3-5, where the QDs dispersion number is also indicated. Here, only three tests are performed with the calibrated dispersion N°1.

	$\boldsymbol{\varphi_T} \geq 0.96$, SRR= 0%					
Disc material	Sapphire				Glass	
Ball material	100C6				100C6	Si_3N_4
Test number	PRI1	PRI2	PRI3	PRI4	PRI5	PRI6
Colloidal dispersion (N°)	1	1	1	4	2	6
$\mathbf{T_0}$ (K)	298	323	298	298	298	298
$\mathbf{u_e}$ (m/s)	1.8	3.1	1.8	1.8	1.8	1.8
Load w (N)	84	84	222	84	111	92
$\mathbf{P_H}$ (GPa)	1.3	1.3	1.8	1.3	0.8	0.8
a (mm)	0.175	0.175	0.243	0.175	0.257	0.234
h_c (nm) from **[95]**	287.5	201.1	267.8	287.5	311.7	312.7
M, L	152, 13	205, 10	402, 13	152, 13	250, 7	203, 8

Table 3-5: Pure rolling operating conditions allowing isothermal contacts using different solid materials and different colloidal suspensions.

3.3.2.2 Tests under non-isothermal conditions

A second series of tests is dedicated to evaluate the feasibility of the developed method for the temperature measurement at similar Hertzian pressures as for the previous isothermal cases, and using different contacting solids materials: glass-steel, glass-Si_3N_4, sapphire-steel and sapphire-Si_3N_4.

The non-isothermal tests are conducted at 313 K using non-calibrated colloidal dispersions. Four different normal loads (from 53 to 111 N) are applied to generate Hertzian pressures at the contact center from 0.8 to 1.3 GPa. The tests are carried out at high entrainment speed (u_e=5 m/s) in order to promote shear-heating at the contact inlet. Besides, according to equation 3.2, this high entrainment speed should provide a significant increase in the colloidal suspension film thickness and thus increases the detected PL signal-to-noise ratio. However, an opposite effect on the film thickness occurs because shear heating generates a viscosity drop in the inlet area. The tests are performed under two different values of SRR:

- One series of tests run under pure rolling (SRR= 0%) with shear heating occurring at the contact inlet, as indicated by the thermal Cheng coefficient in Table 3-6. For this series, the tests are labeled with PRNI which stands for pure rolling non-isothermal and numbered from 1 to 4.
- Another series of tests is performed in rolling-sliding conditions with SRR=10% (see Table 3-7) in order to induce an additional increase of temperature but in the central

pressurized zone. Typically, such moderate SRR is more likely to occur in engineering conditions [101]. The tests are labeled with RSNI which stands for rolling-sliding non-isothermal and numbered from 1 to 4.

The calculated Cheng coefficient, contact radius, M & L parameters and the central film thickness (for isothermal Newtonian conditions) are given in Table 3-6 and Table 3-7. The QDs dispersion number is also indicated.

	$\mathbf{T_0}$= 313 K $\mathbf{u_e}$= 5 m/s SRR= 0%			
Disc material	Glass		Sapphire	
Ball material	100C6	Si_3N_4	100C6	Si_3N_4
Test number	PRNI1	PRNI2	PRNI3	PRNI4
Colloidal dispersion (N°)	2	6	4	6
w (N)	111	92	84	53
$\mathbf{P_H}$ (GPa)	0.8		1.3	
a (mm)	0.257	0.234	0.175	0.139
h_c (nm) from **[95]**	393.7	395.0	363.1	365.6
M, L	182, 7	148, 8	111, 13	66, 16
$\boldsymbol{\varphi_T}$ (-)	~0.92		~0.93	

Table 3-6: Pure rolling conditions leading to non-isothermal contacts using different solids materials and different non-calibrated colloidal dispersions.

	$\mathbf{T_0}$= 313 K $\mathbf{u_e}$= 5 m/s SRR= 10%			
Disc material	glass		sapphire	
Ball material	100C6	Si_3N_4	100C6	Si_3N_4
Test number	RSNI1	RSNI2	RSNI3	RSNI4
Colloidal dispersion (N°)	2	6	4	6
w (N)	111	92	84	53
$\mathbf{P_H}$ (GPa)	0.8		1.3	
a (mm)	0.257	0.234	0.175	0.139
h_c (nm) at SRR=0% from **[95]**	393.7	395.0	363.1	365.6
M, L	182, 7	148, 8	111, 13	66, 16
$\boldsymbol{\varphi_T}$ (-)	~0.91		~0.92	

Table 3-7: Rolling-sliding cases leading to non-isothermal contacts using different solids materials and different non-calibrated colloidal dispersions

3.4 *In situ* pressure and temperature measurement

In this section, *in situ* measurements of pressure (at isothermal conditions, Table 3-5) and temperature (at non-isothermal conditions, Table 3-6 and Table 3-7) are presented and discussed. Indeed, as the fine detection of the QDs FWHM is prevented by the disc parasitic fluorescence in the background, only the QDs emission energy is analyzed. Firstly, in pure rolling under isothermal conditions in order to derive the variation of pressure. Then, for the same operating conditions but in rolling-sliding, the part of the change in the emission energy due to the heating of the lubricant can be estimated and thus the temperature could be measured.

In order to track the position of the measuring points, a Cartesian coordinate system is defined in the contact zone. The measurements are performed along the contact centerline (y=0) in the rolling direction (x direction). The measurement steps are adapted to the contact diameter which increases with the applied load, following equation 3.5. Its origin is determined by visualization, thanks to the CCD camera, and taken at the geometrical center of the contact operated in the EHD regime.

Besides, as mentioned earlier, the focus in the z direction is adjusted at mid-film thickness, which corresponds to the most intense CdSe/CdS/ZnS QDs PL spectrum across the colloidal suspension thin film. The smaller the analyzed thickness is, the longer the acquisition time required to get a sufficient signal-to-noise ratio. This is why, the acquisition time is 3 min at the contact center and 30 s -1 min at the inlet. It is important to note that such acquisition time is much larger than that used for the IR technique, estimated at a few microseconds.

Since the fluorescence microscope provides a depth of field higher than the lubricant film thickness, the detected emission energy is averaged through the full lubricant film thickness, for each given position on the contact centerline (along x-axis at y=0). Thus, in this section, all the reported temperatures are averaged over the lubricant film thickness, the pressure being constant through the lubricant film. Dimensionless x-axis scale is maintained thorough this section to facilitate comparisons between the different combinations of contacting solids. The uncertainties on temperatures and pressures measurements are given in annex 5.4.

3.4.1 Pressure measurements - Isothermal contacts with dispersion N°1

According to the static calibration model, the pressure under isothermal conditions (at T_0) can be determined as follows:

$$P = \frac{E_g(P,T_0) - E_g(P_0,T_0)}{S_P} \qquad 3.8$$

with

$$E_g(P_0,T_0) = E_{g0} + S_T T_0$$

where E_{g0} is the bandgap energy at zero kelvin and at atmospheric pressure, S_P, S_T are the QDs pressure and temperature PL sensitivities, respectively.

It is important to note that the emission energy at atmospheric pressure for a given environmental temperature $E_g(P_0,T_0)$ can be also determined experimentally, by simply

averaging the values of the QDs emission energies recorded at the contact inlet (for x/a ≤ -2). As regards to the colloidal dispersion N°1 and according to the static calibration described in chapter 2, the QDs pressure sensitivity S_P is equal to 0.0298 +/- 0.0037 eV/GPa. By implementing this value into equation 3.8, it is possible to convert the emission energy variations between the contact inlet (at ambient pressure) and the contact center in order to deduce the central pressure values.

Table 3-8 reports comparisons between experimental and simulated central pressure values in sapphire-steel contacts operated under isothermal and pure rolling conditions, at 1.8 m/s and 298K and at 3.1 m/s and 323K, for an applied normal load of w=84 N leading to P_H=1.3 GPa. The experimental pressures are estimated using the linear model obtained from the static calibration limited to 1.3 GPa. These first results, obtained for two inlet temperatures and entrainment velocities, show a very good accordance between experimental, numerical as well as analytical central pressures with a relative deviation of less than 3%, whereas the range of uncertainty on S_p for dispersion N° 1 is 12%. This demonstrates the feasibility of the technique to measure central pressures in isothermal EHD contacts.

	Sapphire-steel, w= 84N, SRR=0%, P_H=1.30 GPa	
	T_0=298K u_e=1.8 m/s	T_0=323K u_e=3.1 m/s
P_{exp}(GPa)	1.27 ± 0.15	1.34 ± 0.16
P_{num}(GPa)	1.32	1.32

Table 3-8: Measured and simulated central pressure values using the calibrated colloidal dispersion (N°1) for sapphire-steel contacts operated under isothermal conditions at applied loads: (a) w=84 N (P_H=1.3 GPa) at 298K (1.8m/s) and 323K (3.1m/s). The contact parameters are detailed in Table 3-5 (Tests N°: PRI1 and PRI2).

However, for a higher normal load of 222 N (P_H=1.8 GPa) applied to a sapphire-steel contact in test N°PRI3, the experimental central pressure obtained with the same methodology as before is 1.48 ± 0.15 GPa whereas the one obtained numerically is equal to 1.82 GPa. This means that, in this case, the pressure is experimentally underestimated by ~18%, compared to the numerical and analytical predictions. This disability to correctly measure pressures higher than 1.3 GPa at 298 K is found because the linearity of the calibration model is no longer valid above 1.3 GPa, according to the static calibrations results (ranging from 0.1 to 3 GPa) shown in chapter 2.

3.4.2 Pressure measurements - Isothermal contacts with non-calibrated dispersions

Based on the accordance between the measured, simulated and analytically calculated central pressures lower or equal to 1.3 GPa, as shown in Table 3-8 and in reference [68], some EHD isothermal tests are performed in order to deduce the pressure sensitivity S_P of the QDs in the non-calibrated colloidal dispersions (N° 2, 4 & 6) as follows:

$$S_P = \frac{E_g(P_{center}, T_0) - E_g(P_0, T_0)}{P_H} \qquad 3.9$$

where P_H is the Hertzian pressure calculated analytically, $E_g(P_{center}, T_0)$ is a set of three QDs emission energies recorded at the contact central zone at x/a =0 and y=0, and $E_g(P_0, T_0)$ represents a set of four QDs emission energies recorded at the contact inlet at x/a = {-5,-4,-3,-2} and y=0.

For more details, the tests operating conditions are listed in Table 3-5 (tests N°: PRI4, PRI5 and PRI6). A S_P value of 0.0266 ± 0.0013 eV/GPa is found with a coefficient of correlation of 0.98 for the different isothermal tests operated under three different normal loads and solid materials. Note that this S_P value falls within the uncertainty range obtained from the static calibrations performed with dispersion N°1 (0.0298 ± 0.0037 eV/GPa).

Once a S_P value determined for dispersions N°2, 4 & 6, and in order to extend the investigation and extract representative pressure profiles, thirteen to twenty-five spectra (some duplicated twice or three times) are recorded from the contact inlet to the contact outlet, as shown in

Figure 3-6. Note that the contrasted interferogram displayed in Figure 3-6 does not represent what is observed during experiments (actually B&W images with weak contrast between interference fringes (no chromium layer on the disc that could disturb the PL and reduce the signal-to-noise ratio)), given by the video camera fixed on the microscope.

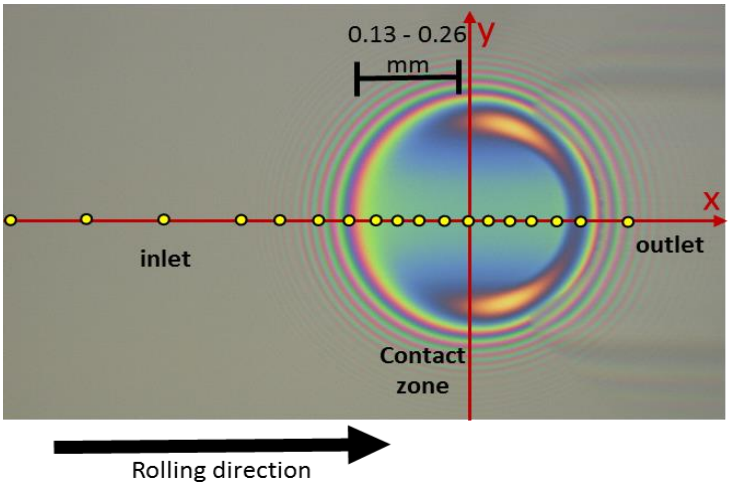

Figure 3-6: Typical measurement positions along the contact centerline.

The left side of Figure 3-7 shows the QDs emission energy variations recorded along the contacts centerline in the rolling direction from the inlet to the outlet edge, for different isothermal configurations (glass-steel, glass-Si_3N_4 and sapphire-steel) using dispersions N°2, 4 and 6. The operating conditions are detailed in Table 3-5 (tests N° PRI4, PRI5 and PRI6). The emission energy variations seem to be consistent with the well-known pressure variations expected from the EHL theory: the PL energy distributions approach the elliptical Hertzian distribution. Indeed, one can notice the existence four distinct zones from Figure 3-7:

- The inlet zone (for x/a ≤ -2) where the emission energy is constant as the colloidal suspension is subjected to atmospheric pressure and shearing. This is an important result: it shows that the photoluminescence response of the QDs is insensitive to shear rate, because in pure rolling it is in the inlet area that the latter is most intense, from 10^{+5} to 10^{+7} s^{-1}.
- The contact vicinity where a gradual increase of the pressure arises as the gap between the moving solids is reduced.
- The central pressure zone at the contact center where the maximum pressure and thus maximum energy are reached.
- The outlet zone where the pressure drops down. It is important to underline that, at the outlet, the QDs signal-to-noise ratio becomes very low because the sudden decompression causes the breakdown of the lubricating film and thus leads to the formation of a liquid/vapor meniscus. Notice that downstream the outlet, at the film thickness restriction (required for maintaining the continuity of mass flow), the pressure spike is not observed very likely because it is much narrower than the scanning measuring steps, of the order de 25 to 50 µm.

By implementing the deduced S_P value (0.0266 ± 0.0013 eV/GPa), it is then possible to convert the emission energy variations into pressure variations between the contact inlet (at ambient pressure) and each measuring point using equation 3.8. The right side of Figure 3-7 shows comparisons between of the measured pressure values and the pressure profiles along the contact centerline (y = 0) in the *x*-direction, obtained using the numerical model, for different normal loads and contacting materials: glass-steel, glass-Si_3N_4 and sapphire-steel.

The experimental pressures are in good agreement with predicted ones using the numerical model and this with a deviation less than 3% at the contact center. Globally, it can be seen that the emission energy/measured pressure values are replicable for different measuring positions.

The profiles are quasi-Hertzian; as M>100 and L<17, the contacting surfaces are almost flat and parallel leading to a pressure profile close to that of Hertz at the central pressure zone, according the numerical simulation. It can also be noticed that, as the load increases or more precisely as M increases and L decreases, the pressure profiles tend towards a Hertzian pressure distribution, as revealed by the experimental analysis done in [4]. This tendency is also pointed out in the previous works of Kagerer et al. [12], Safa et al. [13] and Habchi et al. [33].

In addition, as expected, the pressure profiles' coordinate system are relatively in similar proportions to the actual geometry of the contact. However, one can notice that the experimental pressure profiles are slightly oversized, in terms of contact diameter in the direction of the dimensionless x-axis, compared to the simulated ones: of ~14% for glass-steel, ~13% for the glass-Si_3N_4 and ~14% for the sapphire-steel contacts.

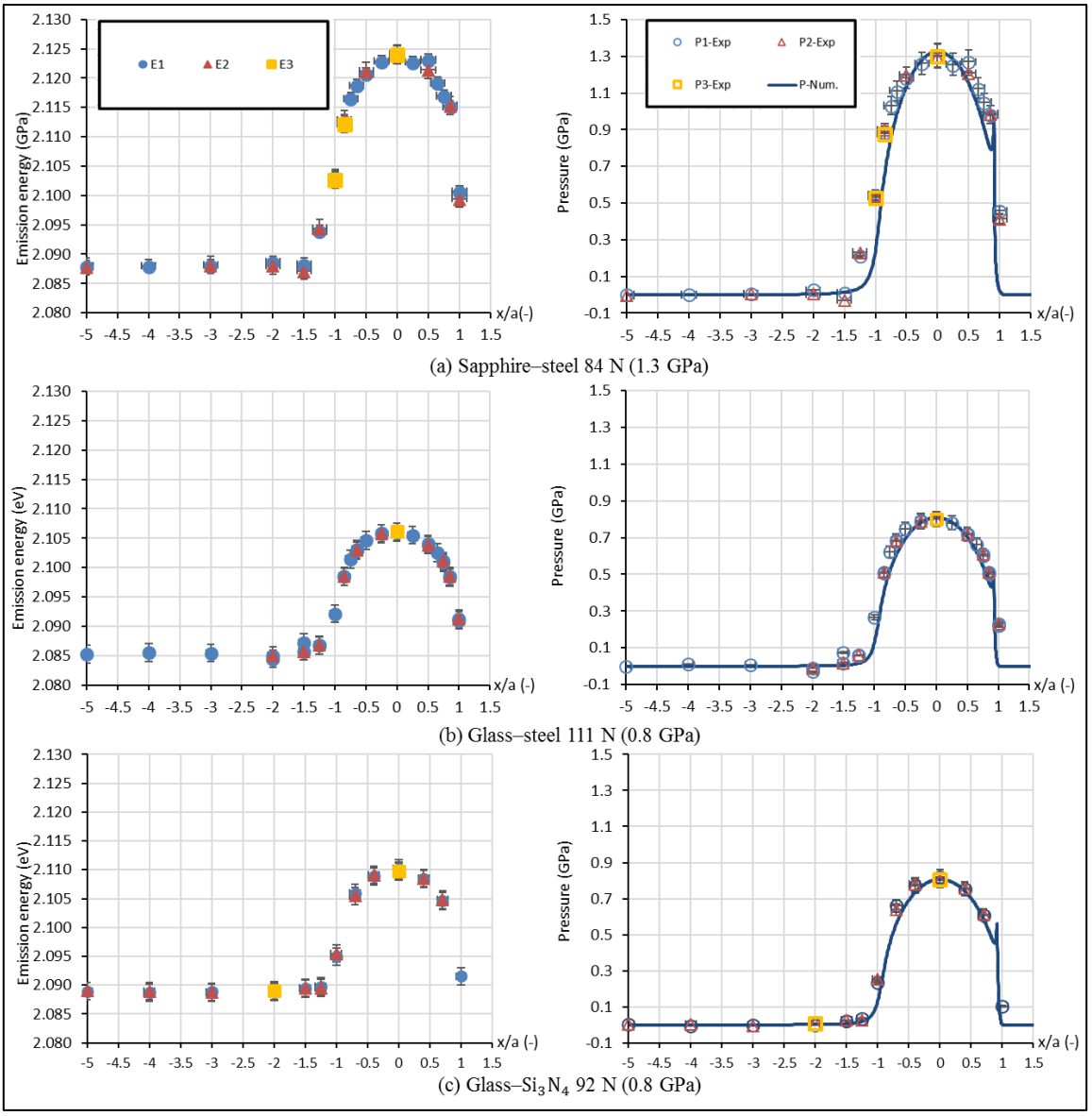

Figure 3-7: Comparison between emission energy profiles (left side) and measured vs. simulated pressure profiles (right side) along the dimensionless x-axis at y=0 for (a) sapphire-steel, (b) glass-steel and (c) glass-Si_3N_4 isothermal contacts operated at T_0 =298 K with u_e =1.8 m/s in pure rolling. More details about operating conditions are listed in Table 3-5 (tests N° PRI4, PRI5 and PRI6). E_i represents the detected emission energy and P_i-Exp represents the measured pressure values, with "i" the number of measurements recorded at the dimensionless x position of the same test.

3.4.3 Temperature measurement - Non-isothermal contacts

The QDs emission energy is sensitive to both pressure and temperature variations and the full width at half maximum cannot be exploited in our measurements. This means that 2 unknowns (P and T) must be determined from a single equation describing their influence on the QDs emission energy. Hence, in order to determine the latter change due to temperature variations only during the passage of the nanosensors through the non-isothermal EHD contact, the change of the global emission energy has to be corrected from the consequence of the pressure variations. To do this, using the linear calibration model (equation 3.8), the measurement of temperature becomes possible by substituting the experimental pressure values (P_{iso}) obtained under isothermal conditions operated under lower entrainment velocity or pure rolling. Indeed, according to Jubault [4], Jolkin et al. [36], Kagerer et al. [12], for a given load and contacting solids, a moderate increase of the slide-to-roll ratio should not alter significantly the characteristic shape of the pressure distribution, especially the central pressure. This outcome is also demonstrated in the case of a slight increase of the entrainment velocity by Jubault [4], especially for M>100 and L<17. Basically, the differences are mostly located at the horseshoe shaped constriction, i.e. in the amplitude/shape of the pressure spike at the outlet. On this basis, the experimental temperature can be deduced as a first approximation as follows:

$$T = \frac{E_g(P,T) - E_{g0} - S_P P_{iso}}{S_T} \qquad 3.10$$

However, since non-calibrated colloidal dispersions are used, their temperature sensitivity is necessary in order to perform *in situ* temperature measurement. The temperature sensitivity is evaluated by analyzing the QDs emission energies at the contact entrance (x/a= {-5,-4,-3}) at 298 K and 313 K. Thus, the temperature sensitivity is simply approximated for the non-calibrated suspension (N° 2, 4 and 6) as follows:

$$S_T = \frac{E_{inlet}(P_0, T_1 = 313K) - E_{inlet}(P_0, T_2 = 298K)}{\Delta T = 313K - 298K} \qquad 3.11$$

A resulted S_T of -0.000268 ± 0.000018 eV/K is found with a coefficient of correlation of 0.76 from six tests (in which the non-calibrated colloidal dispersions are employed) whose operating conditions are detailed in Table 3-5 (Test n° PRI4, PRI5 and PRI6) and Table 3-6.

For each of the operating conditions detailed in Table 3-6 and in Table 3-7, several spectra are recorded along the rolling direction. As displayed in Figure 3-8, three spectra are recorded at the contact entrance (at x/a= [-5, -2[) and three to four spectra are recorded at the contact center (at x/a= [-0.5, 0.5]). Some of the measurements are performed twice or three times to check the reproducibility of the tests.

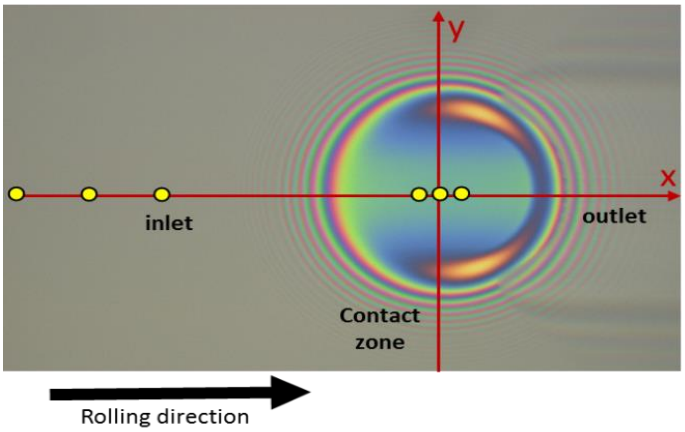

Figure 3-8: Measurement positions throughout the non-isothermal contact.

Figure 3-9 shows a comparison between the measured and simulated temperatures of (a) glass-steel, (b) glass-Si_3N_4, (c) sapphire-steel and (d) sapphire-Si_3N_4 contacts performed at 5 m/s and 313 K in pure rolling (see Table 3-6) for different applied normal loads.

Overall results in Figure 3-9 shows that the operating conditions indicated in Table 3-6 do not allow to definitely qualifying the method for temperature sensing, the temperature variations are too low and of the same order of magnitude as the measurement uncertainties, indicated by the error bars. However, there is a good agreement for cases (b) and (d) and, while variations remain weak, larger differences for cases (a) and (c).

For all operating conditions, the simulations reveal a very small rise of temperature (by a few degrees K) at the contact vicinity (x/a= - 1). This stems from i) the inlet shear heating promoted by the relatively high entrainment velocity, as predicted by the Cheng thermal film thickness reduction coefficient (shown in Table 3-6), and ii) the lubricant compression at the contact inlet.

Moreover, the deviation of the measured temperatures from their mean value is of ±3K, comparable to simulated temperature variations. Therefore, although a rather good repeatability of the test results for each contact position and configuration, quantitative comparison on the dominance of frictional or compressional heating cannot be inferred from the measurements. Finally, from Figure 3-9, it is found that there is no significant difference in terms temperature amplitude/tendency, between the different combinations of normal loads and contacting solids. Under pure rolling and high entrainment velocity, shear heating is more pronounced than the compressive heating; the shear heating is governed at x/a = [-3.5, -1] (i.e upstream of the contact), where lubricant layers is moving at different speeds and rubbing against each other across the lubricant film. In contrast, the compression is manifested in a limited zone (at the contact center).

The simulated temperature profiles are in a good accordance with the previous results of simulation by Habchi et al. [33] and measurement by Safa et al. [13]. In all cases, the viscous heating effect appeared at the contact inlet is pursued by a cooling step during the passage of the lubricant in contact high pressure zone, then by a second small rise in temperature near the

outlet, in the conjunction region. These trends are qualitatively similar to that obtained by Cheng et al. [9].

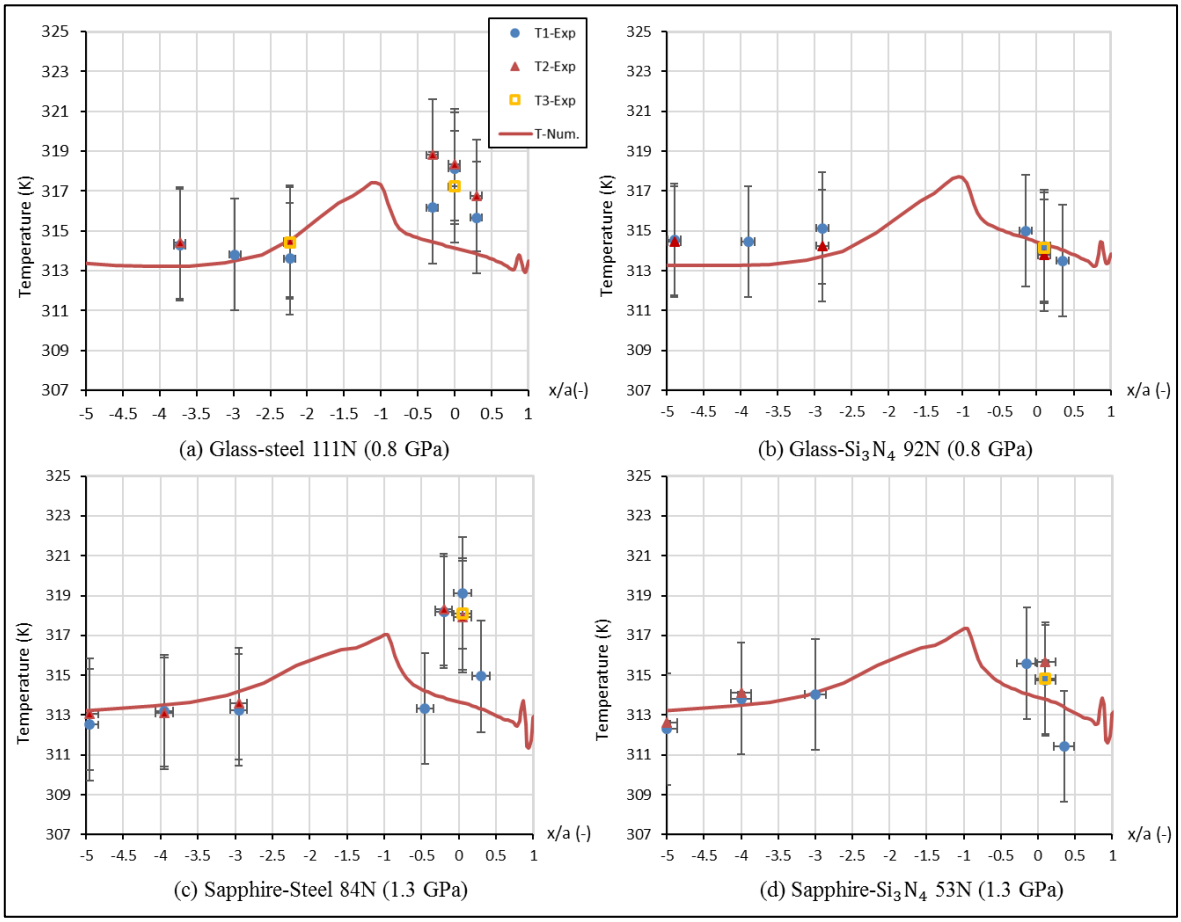

Figure 3-9: Comparison between measured and simulated temperature profiles along the dimensionless x-axis at y=0 for (a) glass-steel, (b) glass-Si_3N_4, (c) sapphire-steel and (d) sapphire-Si_3N_4 non-isothermal contacts operated at T_0 =313 K with u_e =5 m/s in pure rolling. More details about operating conditions are listed in Table 3-6 (tests N° PRNI1, PRNI2, PRNI3 and PRNI4).T_i-Exp represents the measured temperature values, with "i" the number of measurements performed at the dimensionless x position of the same test.

In contrast, the results displayed in Figure 3-10 show larger temperature changes and a better agreement between the measured and the simulated temperature rises in glass-steel, glass-Si_3N_4, sapphire-steel and sapphire-Si_3N_4 contacts operated at 5 m/s but with a SRR of 10% and for different applied normal loads. Globally, the gap between experimental and simulated temperature rise is less than 5K, whereas the temperature uncertainty is of 7%. Again, the experimental results are found reproducible.

At the contact inlet, the simulated temperature rise caused by shear heating still exists in rolling-sliding condition with no substantial change in amplitude compared to the ones obtained under pure rolling for the same entrainment speed, as predicted by the Cheng coefficients reported in Table 3-7. Afterwards, within the pressurized region, the temperature rise becomes more intense and reaches its maximum value at the contact center mostly due to shear under high pressure, as the surface velocities of the contacting bodies are now different. Subsequently, the

temperature falls steeply at the outlet zone. The temperature profiles, very likely influenced by the pressure distribution (see the appearance of a temperature spike at 1.3 GPa), are comparable to those found in previous works [11]–[14], [34], [35].

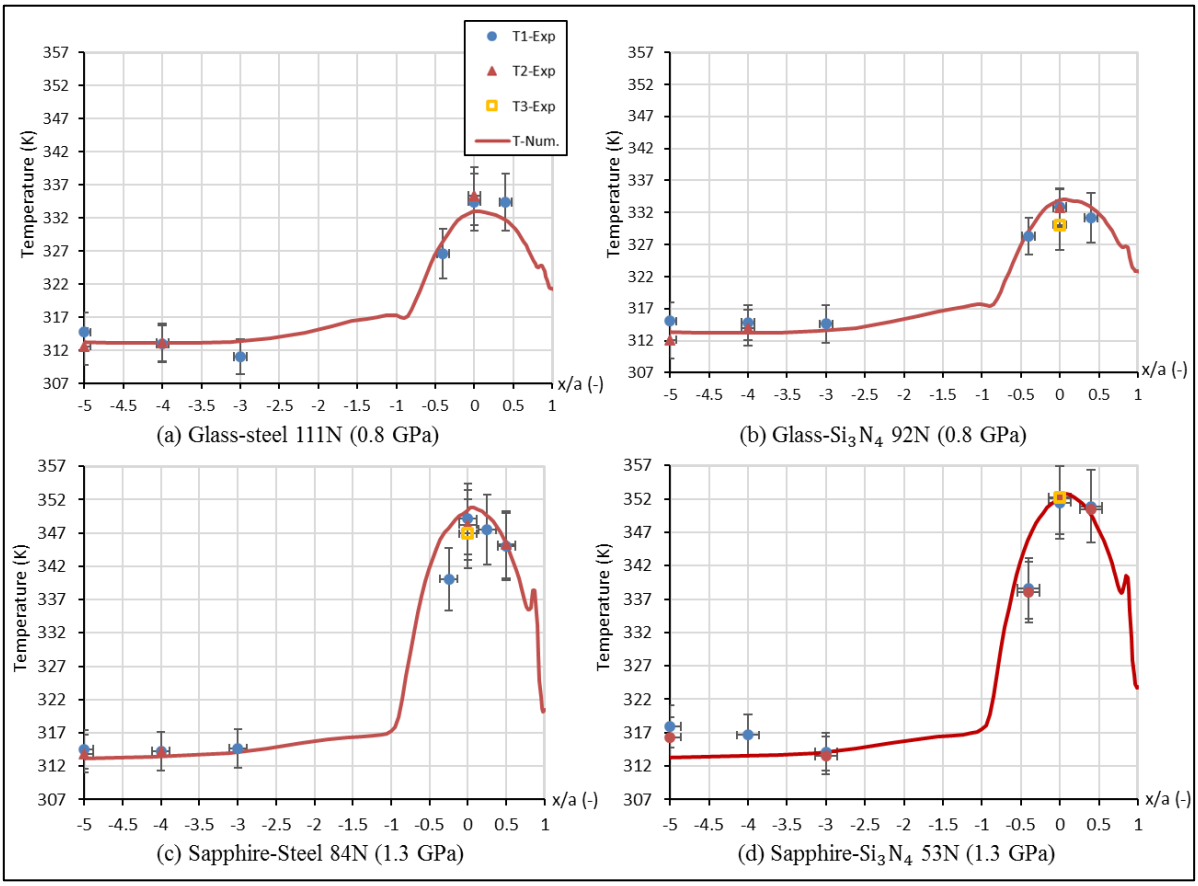

Figure 3-10: Comparison between measured and simulated temperature profiles along the dimensionless x-axis at y=0 for (a) glass-steel, (b) glass-Si_3N_4, (c) sapphire-steel and (d) sapphire-Si_3N_4 non-isothermal contacts operated at T_0 =313 K with ue =5 m/s in rolling-sliding conditions (SRR=10%). More details about operating conditions are listed in Table 3-7 (tests N° RSNI1, RSNI2, RSNI3 and RSNI4). T_i-Exp represents the measured pressure values; with "i" number of measurements performed at the dimensionless x position of the same test.

By increasing the Hertzian pressure from 0.8 GPa (in glass-steel and glass-Si_3N_4) to 1.3 GPa (in sapphire-steel and sapphire-Si_3N_4), the temperature rise increases by 20K at the contact center. This pronounced heating is due to the amplification, by a higher pressure, of the shear heating of the lubricant, itself induced by the application of a non-zero SRR and a relatively high speed (u_e=5 m/s), according to [33].

At constant Hertzian pressure, the oil temperature rises using a Si_3N_4 ball appeared to be slightly higher (of ~1.5K) than those using a steel ball, as shown in Figure 3-10, for both glass and sapphire discs. However, as these small differences are comparable with the deviation of the measured temperatures from their mean value, definite conclusions cannot be draw from our results measurements at this level, even if Si_3N_4 presents a lower thermal conductivity than steel, as mentioned in Table 3-3. Nevertheless, at constant normal load this time, the

temperature increase with a Si_3N_4 ball is expected to be greater than with a steel ball, because of the high pressure effect on shear heating. Example of simulated oil temperature rises due to thermal insulating effect shown by Ebner et al. [14] and Kaneta et al. [34], are displayed in Figure 3-11 and in Figure 3-12 respectively.

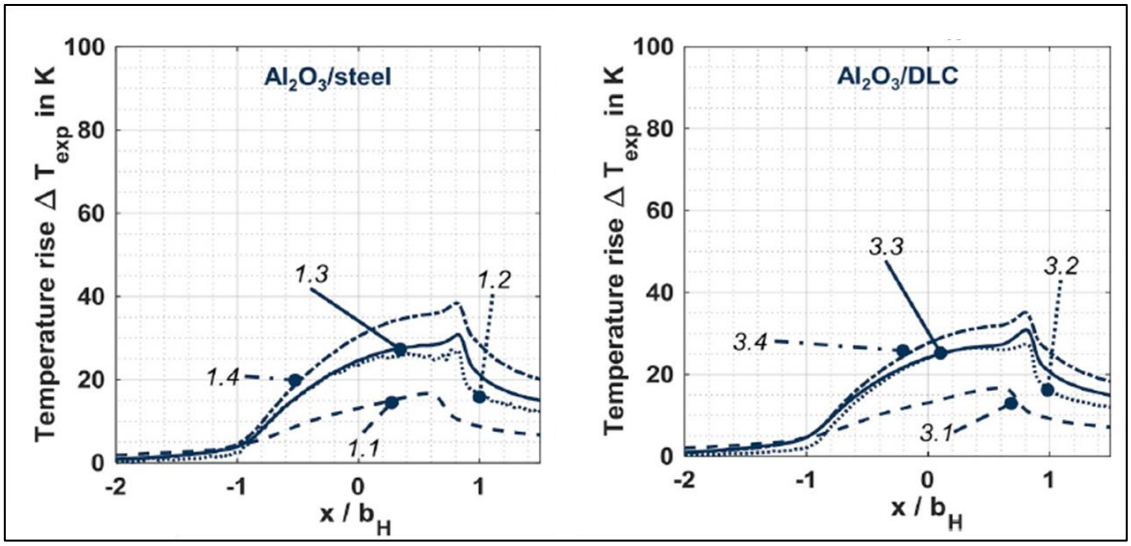

Figure 3-11: Comparison between the measured oil temperature rise in sapphire/steel and in sapphire/DLC contacts operated under various rolling-sliding conditions[14]. Note that each line type refers to the same conditions in terms of central Hertzian pressure, entrainment speed and sliding.

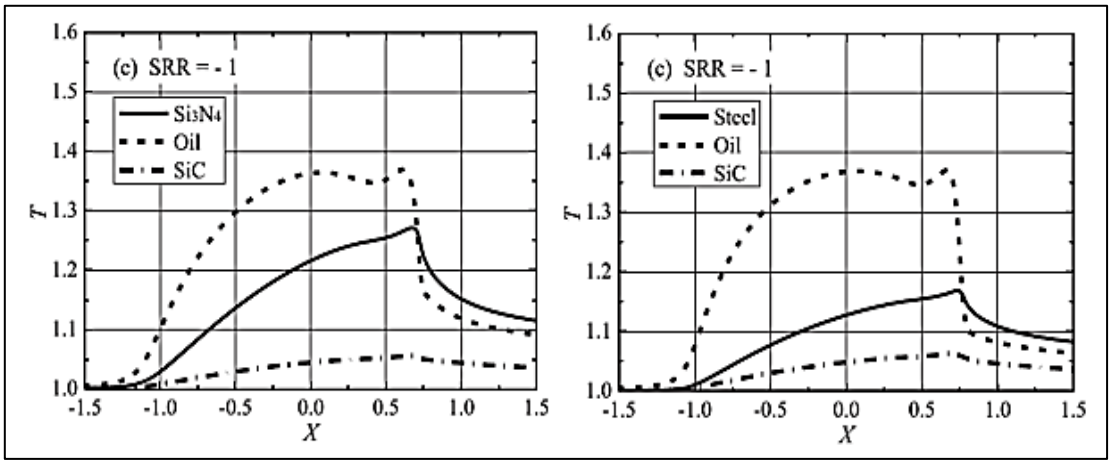

Figure 3-12: Comparison between the simulated dimensionless temperature rise of oil and contacting solids: Steel-SiC and Si_3N_4-SiC contacts for P_H=0.75 GPa at T_0=333K operated at u_e=5m/s with SRR=-100% [34].

3.5 Summary and conclusion

In this chapter, the Jerotrib test-rig and the main features of the methodology employed to carry out *in situ* pressure and temperature measurements in EHD contacts are briefly described. Various circular EHD contacts of different combination of contacting solids (glass-steel, glass-

Si_3N_4, sapphire-steel and sapphire-Si_3N_4) are explored through experiments and numerical simulations.

The purpose of that study is to demonstrate the feasibility of the spectroscopic method using the photoluminescence of CdSe/CdS/ZnS QDs to measure pressure and temperature in a wide range of EHD operating conditions. These latter are carefully selected to ensure a first series of isothermal experiments (under pure rolling at relatively low entrainment velocity) in order to extract the maximum pressures. This is achieved by implementing the detected QDs emission energy at the contact inlet and center into the empirical law obtained thanks to the static calibration established in Chapter 2. In case of the non-calibrated colloidal dispersion, the QDs pressure sensitivity is deduced via the predicted central Hertzian pressure and the variation of the emission energy at the contact inlet and center. Hence, the pressure values are obtained by recording the QDs photoluminescence throughout the centerline of the contact. As regards to the temperature sensitivity of the non-calibrated colloidal dispersion, it is deduced via the variation of the emission energy as function of different imposed temperatures at the contact inlet. The series of non-isothermal experiments are driven at higher entrainment velocity under pure rolling and rolling-sliding conditions, in order to perform temperature measurement. This is done by substituting the experimental isothermal pressures at the contact inlet and in the central region into the empirical calibration law to determine the part of change of QDs emission energy due to temperature only; as the pressure obtained under isothermal conditions does not vary much at moderate rolling-sliding and/or entrainment velocity conditions, according to previous studies.

A global satisfying agreement is revealed from comparisons of the measured pressures and temperatures with numerical predictions. The effect of normal load (or Moes parameters M and L) on the pressure distribution is pointed out. Under isothermal conditions, pressure measurements have proven to be quite accurate, as long as the QDs suspension used in *in situ* tests has been calibrated before. Under non-isothermal conditions, the numerical simulation shows a weak influence of the thermal insulation effect by employing Si_3N_4 instead of a steel ball. However, this effect cannot be quantified easily because it generates a variation which is of the same of order of magnitude as the measurement uncertainty and because the material thermal properties are not so different each other. Nevertheless, it can be concluded that these overall findings proved the potential of the method based on the photoluminescence response of nanosensors to probe pressure and temperature in EHD contacts.

The performance of the developed method among the state of the art competing techniques can be described by means of spatial resolution, level of reliability, accuracy, intrusiveness and complexity. This is detailed in the following paragraphs and summarized in Table 3-9.

- Intrusiveness

Dispersible in small concentration, the nanosized QDs are non-perturbative to the lubricant rheology. Given the typical film thicknesses during *in situ* spectroscopic measurements, this highlights the non-intrusiveness of the CdSe-based quantum dots photoluminescence method which is comparable to Raman spectroscopy, as long as the used laser density is not too high. The developed method can also be considered as less intrusive and less perturbative than

infrared thermography which requires the use of infrared reflective coating(s) like chromium and/or aluminum overlay(s), of different thermal diffusivity than that of the transparent disc, to be applied to reject some undesirable or parasitic radiations. In addition, although electrical resistance method has been for a long time the only one to provide pressure and temperature profiles, they are considered intrusive since the dimension of the electrical sensor (deposited on an electrical insulating layer in case of metallic samples) may perturb to the lubricant flow inside the contact.

- Reliability

Discarding the effect of high shear and pressures, the reproducibility of the pressure and temperature measurements reflects the fact that the used QDs are reliable sensors. Their reliability is very close to that of the Raman spectroscopy. On the other hand, electrical sensors are not reliable because they are susceptible to be rapidly deteriorated by the typical EHD film thicknesses (< 1 µm) and the severe conditions of shearing and pressure.

- Spatial resolution

With a low probe size, the developed technique is characterized by its relatively high spatial resolution as Raman spectroscopy and recent infrared thermography. In contrast, electrical resistance methods have a poor spatial resolution as the dimensions of the deposited sensors are not negligible compared to the contact size.

- Accuracy and complexity

The complexity of the proposed technique lies in the fact that it requires performing isothermal contacts in pure rolling to determine the contribution of the variation in QDs emission energy due to pressure, before measuring temperature under non-isothermal conditions. It is important to note that the ability of the QDs to withstand severe conditions makes the technique outperforms the electrical resistance method in measuring both temperature and pressure. Besides, the developed technique pressure and temperature uncertainties are in the same range as that of the electrical resistance method.

Regarding temperature sensing, the complexity of the proposed technique appears to be lower than that of IR thermography for which the radiations of the contacting solids, lubricant and environment need to be isolated or rejected by performing previous experiments using different coating materials and film thicknesses as the lubricant emissivity depends on both temperature and film thickness. In addition, the developed technique can cover a temperature range similar to the one of IR thermography.

Regarding pressure sensing, the developed method appears to be close in accuracy to Raman spectroscopy. However, Raman spectroscopy can cover a wider range of pressure compared to the developed technique, which is limited to 1.3 GPa only in the case of squalane. Nevertheless, the QDs can be functionalized with suitable ligands to ensure affinity with a wide range of lubricants, in contrast to Raman technique which is restricted to a very limited number of lubricants that exhibit intense Raman signal, which is usually much weaker than in any other spectroscopic method.

Technique	Parameter	Spatial resolution	Parameter resolution	Level of intrusiveness	Level of complexity
IR thermography [35], [60], [102]	T	6-36 µm	0.01K	Medium	High
IR absorption spectroscopy [103], [104]	P/T	100 µm	-	Medium	High
Raman spectroscopy [55], [100]	P	5-10 µm	30 MPa	Low	low
Electrical resistance [12]–[14], [105]	P&T	5-35 µm width	~63-105 MPa ~1-3K	High	Medium
CdSe-based QDs photoluminescence [68]	P&T	5-10 µm	50 MPa on P 3-2 K on T	Low	Medium

Table 3-9: Performance of the developed method among the state of the art techniques for pressure and temperature sensing.

In the next chapter, the spectroscopic method will be further exploited to quantify temperature rise as a function of the slide-to-roll ratio at equivalent normal load or Hertzian pressure. Again, the numerical predictions will be used for validation. In addition, the investigation will be extended further to compare heat generation and power losses in steel-steel and steel-Si_3N_4 EHD contacts in order to tackle the industrial challenge.

Chapter 4: Comparison between all-steel and hybrid EHD contacts

Chapter 4: Comparison between all-steel and hybrid EHD contacts 123
4.1 Effect of sliding and normal load in sapphire-steel and sapphire-Si_3N_4 contacts 125
4.1.1 Operating conditions 125
4.1.2 Temperature rise 126
4.2 Effect of sliding and normal load in steel-steel and steel-Si_3N_4 contacts 130
4.2.1 Operating conditions 130
4.2.2 Pressure distribution 131
4.2.3 Temperature rise 133
4.2.4 Heat generation 135
4.2.5 Heat fluxes 137
4.3 Summary and discussion 140

In the previous chapters, *in situ* pressure and temperature measurements in EHD contacts have been presented for different combinations of contacting solids: glass-steel and glass-Si_3N_4, sapphire-steel and sapphire-Si_3N_4. These results showed the feasibility of the methodology developed in this work. In particular, thanks to the photoluminescence emission energy of nanosensors, based on QDs, it was possible to estimate pressure and temperature in nominal isothermal and non-isothermal conditions, respectively. These experimental results were corroborated with predictions obtained numerically using a TEHD model and results taken from the literature.

This chapter is dedicated to study the effect of the nature of the contacting materials on EHD rolling-sliding contact temperatures. In particular, the effect of the sliding ratio and normal load on temperature rise, generated heat and power losses will be quantified and compared for all-steel and hybrid (Si_3N_4-steel) EHD contacts. Experimental measurements will be compared with numerical results. Furthermore, thanks to the use of a TEHD numerical model, the partition of the generated heat between the contacting solids will be investigated through the assessment of the heat fluxes transferred to the contacting surfaces.

4.1 Effect of sliding and normal load in sapphire-steel and sapphire-Si_3N_4 contacts

4.1.1 Operating conditions

As mention previously, spectroscopic techniques require deploying at least one transparent contacting body. Therefore, a sapphire disc is used to conduct PL measurements. Note that the thermal diffusivity, which gives a measure of both the rate of heat transfer through a material and the capacity of the material to absorb heat, of sapphire ($D=1.24\times10^{-5}$ m^2/s) is nearly identical to that of the 100C6 steel ($D=1.33\times10^{-5}$ m^2/s). In order to study the effect of sliding on the temperature rise, three rolling-sliding tests, whose operating conditions are reported in Table 4-1, are conducted on Jerotrib. The experiments are carried out at high speed under a compromising range of slide-to-roll ratios which both promote shear heating and cover low and moderate slide-to-roll ratios that are most likely to occur in bearings and gears, respectively [101]. It is also important to highlight that the maximum Hertzian pressure is carefully selected to be lower or equal to 1.3 GPa because the pressure measurement technique was not demonstrated above this value, according to the results presented in the previous chapter. This analysis is conducted with sapphire-steel and sapphire-Si_3N_4 contacts under the same external load generating different central Hertzian pressures, and under different normal loads generating the same central Hertzian pressure. Indeed, from an engineering point of view, depending on the industrial application, an all-steel bearing can be either replaced:
-by a hybrid bearing of same dimensions to carry the same external loading.
-or by a carefully adapted geometry of hybrid bearing to support the same local pressure as the all-steel bearing.

	T_0=313 K u_e=5 m/s SRR=[0 ; 50%]		
Disc material	Sapphire		
Ball material	Steel (100C6)	Si_3N_4	Steel (100C6)
Colloidal dispersion (N°)	4	6	4
w (N)	84	53	53
P_H (GPa)	1.3	1.3	1.1
a (mm)	0.175	0.139	0.151
h_c (nm) at SRR=0%	363.1	365.65	375.49
M, L	111, 13	66, 16	70,13
$\varphi_T(-)$ at SRR=0 %	~0.93	~0.93	~0.93

Table 4-1: Operating conditions for measuring the temperature rise at sapphire-steel and sapphire-Si_3N_4 contacts center.

4.1.2 Temperature rise

As mentioned in the previous chapter, it was not possible to measure pressure and temperature simultaneously since only one spectroscopic parameter (emission energy) can be use. In the following, all spectra are recorded at the contact center (x=0, y=0), as shown in Figure 4-1 where the pressure is assumed to remain almost unchanged for the same load and contacting materials, but for varying SRR. This was demonstrated using a TEHD model and by previous pressure measurements reported in reference [4], [36]. For each applied SRR value two spectra are recorded successively at the same location to check the reproducibility of the measurements. Roughly, twenty minutes have elapsed between two consecutive SRR values to ensure stationary conditions. The total time of a sliding test, with slide–roll ratios varying from 0 to 50%, is roughly two hours.

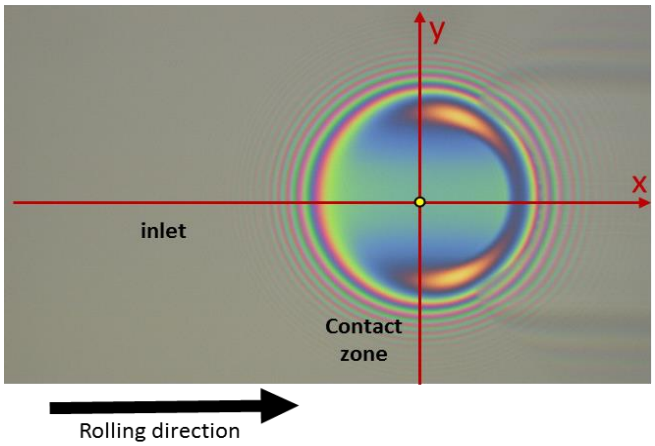

Figure 4-1: Central position for measuring the temperature rise under various SRR values.

According to the temperature profiles reported in Figure 3-12 (in chapter 3) in pure rolling, the temperature change at the contact center is negligible meaning that the temperature is closed to the inlet temperature (i.e. T=T_O at SRR=0%). Therefore, the temperature rise at the contact

center can be calculated as the difference between the temperature at the contact center at SRR = 0% (here 313K) and the temperature at the contact center at a given SRR. It can be expressed as follows:

$$\Delta T = \frac{E_g(P_{centre}, T_0) - E_g(P_{center}, T)}{S_T} \qquad 4.1$$

with $E_g(P_{centre}, T_0)$ the emission energy at the contact center at SRR=0%, $E_g(P_{center}, T)$ the emission energy at the contact center at |SRR|> 0 %. S_T, the QDs temperature sensitivity was determined in chapter 3 for the non-calibrated dispersions n°2, 4 and 6: S_T= -0.000268 ± 0.000018 eV/K.

Figure 4-2 displays the variations of the emission energy and the corresponding temperature variations, together with the results given by the numerical model. All measurements are taken at the contact center with SRR varying from 0 to 50%. The measured and calculated temperature variations represent the changes in average temperatures through the film thickness.

It can be clearly seen that the measured temperature rises with increasing SRR, as expected. This effect is caused by the shear heating of the lubricant caused by the sliding speed between the contacting bodies. For the same concentration of colloidal suspension, in the case of the sapphire-steel contacts, one can notice that the emission energy at the lower central pressure (1.1 GPa, w=53N) is reduced compared to one at higher central pressure. This is attributed to the expected pressure dependence of the emission energy. Note that the less the concentration of quantum dots is, the higher the QDs emission energy (unlike the QDs pressure and temperature sensitivities which are constant for concentrations below 0.125 mg/mL), according to Albahrani [24]. This can be clearly shown by comparing the emission energies at SRR= 0% and 1.3 GPa of the sapphire-steel and sapphire-Si_3N_4 cases, at the left side of Figure 4-2 (a) and (b). Besides, globally, the experimental results (in terms of emission energy and thus in terms of temperature rise) are found reproducible. This reflects the fact that the used QDs have a reliable photostability and very good ability to withstand high shear and high pressures.

The measured and simulated temperature rises at P_H=1.3 GPa are in good accordance: within a ~25% deviation for SRR ≤ 10 % and within 3% or less for SRR ≥ 25%. Under a reduced pressure of 1.1 GPa, the deviation between measured and simulated temperature rises is estimated at ~52% for SRR ≤ 10 % and at less than 20% for SRR ≥ 25%. Despite that rather large deviation, a rather acceptable agreement is obtained with the less highly loaded sapphire-steel contact. These deviations might be attributed to different sources: the experimental method itself presents limitations and uncertainties (see Chapter 3) and deficiencies in the modeling approach with regard to the limiting shear stress, not taken into account here and which should impact the shear heating of the lubricant. This is why the simulated temperature rises might be slightly overestimated compared to the experimental ones. Nevertheless, the numerical model represents a helpful mean to quantitatively predict temperature rise, especially, at high central pressure and SRR.

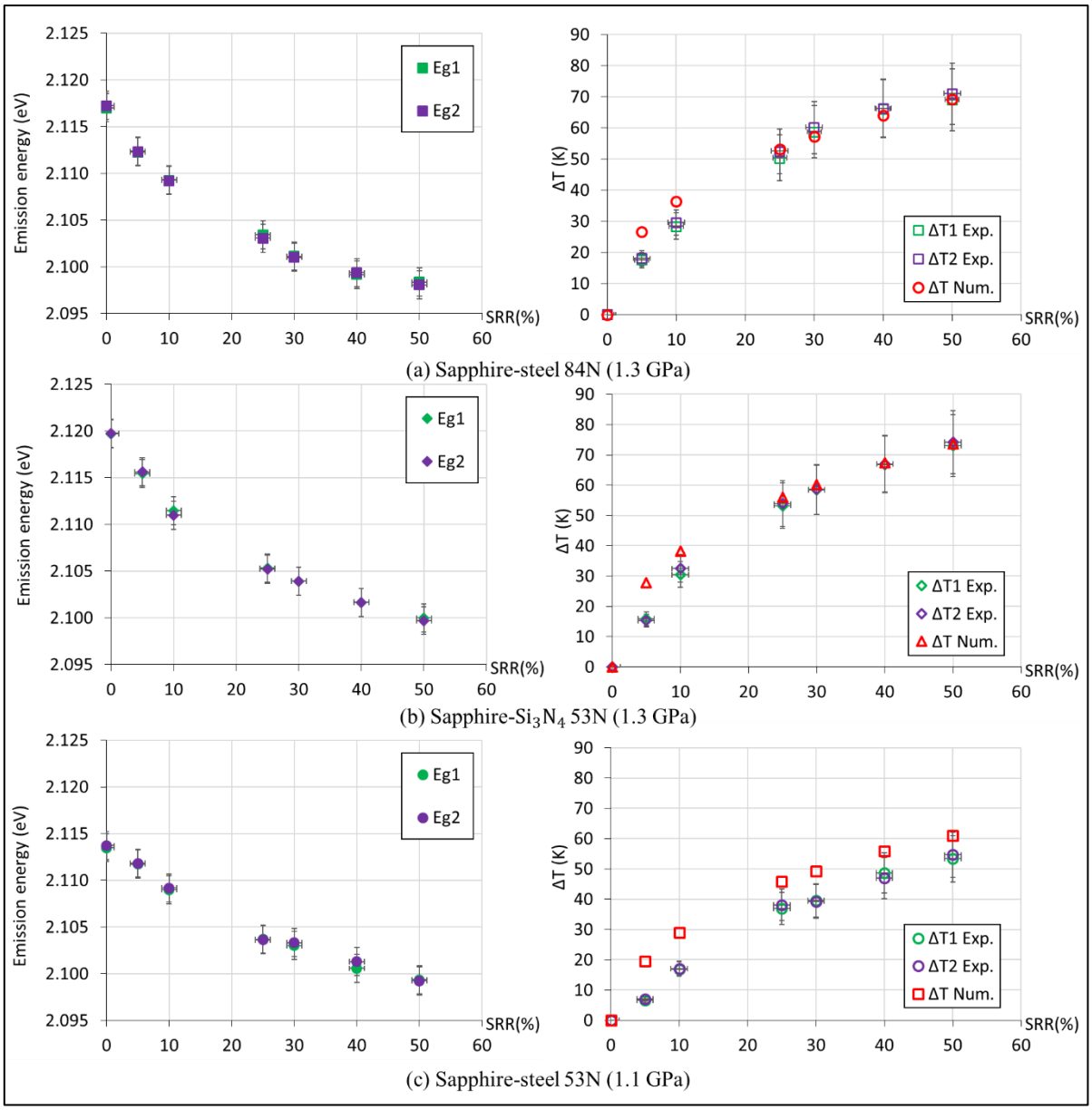

Figure 4-2: Variation of the emission energy (left) and of the averaged measured and simulated temperature rises (right) as functions of the slide-to-roll ratio for: (a) sapphire-steel (84N), (b)sapphire-Si_3N_4 (53N) and (c) sapphire-steel (53N) contacts operated at T_0=313 K and u_e=5 m/s. Eg_i and ΔT_i Exp represent repeated measurements at the contact center for the same operating conditions.

The results are plotted in Figure 4-3 but in a different way. They show, for the same central pressure (P_H=1.3 GPa), that the measured and simulated temperature rises in the sapphire-Si_3N_4 contact are slightly higher by ~1 to 5K than the ones obtained in the sapphire-steel case. However, this difference is close to the temperature measurement uncertainty.

At lower central pressure P_H=1.1 GPa, both simulated and measured temperature rises in sapphire-steel contacts are reduced by ~10-15K, respectively, compared to the cases where the applied loads generate 1.3 GPa as Hertzian pressure. These experimental and numerical results underline the significant effect of pressure combined with shear in enhancing the temperature rise at the contact center. The results also seem in coherence with the thermal properties of the

solids but the effect here is limited and of the same range as the uncertainties, numerical and experimental. Indeed, the significance of this effect can have ben clearly observed by employing contacting solid with very low thermal diffusivity like glass ($D=0.05\times10^{-5}$ m^2/s).

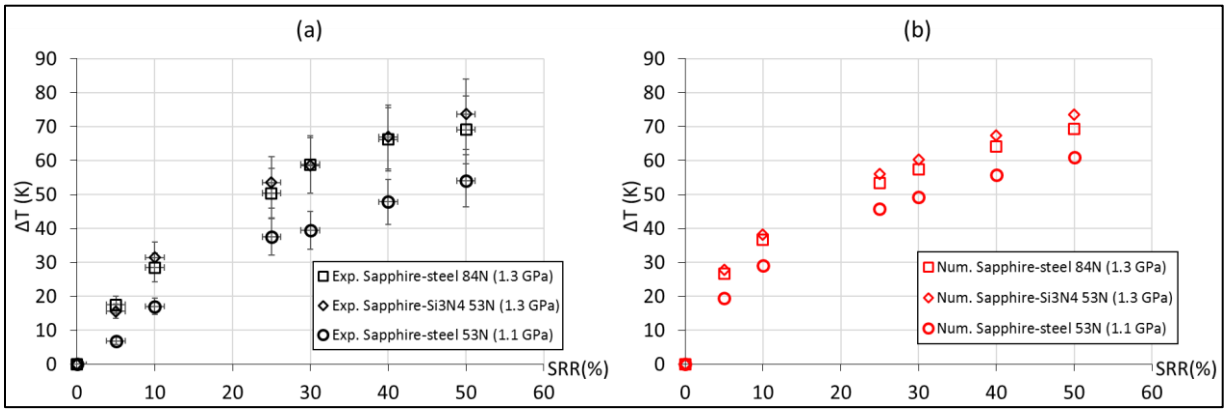

Figure 4-3: (a) measured and (b) simulated average temperature rises as functions of slide-to-roll ratio.

The tendency of the temperature rise as a function of the slide-to-roll ratio is in good accordance with previous measurements of Lu et al. [35] (Figure 4.4) and surface temperature results obtained by Reddyhoff et al. [61], [102] using the infrared thermography technique (Figure 4.5). This tendency looks very much like the non-linear tendency of the shear stress as a function of the slide-to-roll ratio: At some point, for a sufficiently high pressure and shear rates conditions, shear stress reaches a maximum value and becomes shear rate-independent. This behavior results in plateau-like regime, known as limiting shear stress, in which the friction saturates to a limit value. Consequently, this limits the ability of the lubricant to dissipate heat, as illustrated in reference [43]. This may explain the resulted tendency, shown in Figure 4-3.

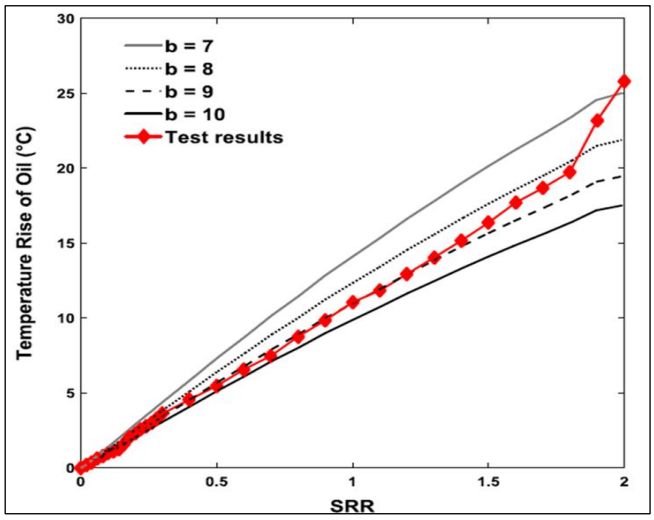

Figure 4-4:Temperature rise of oil Santotrac 50 versus sliding–rolling ratio [35].

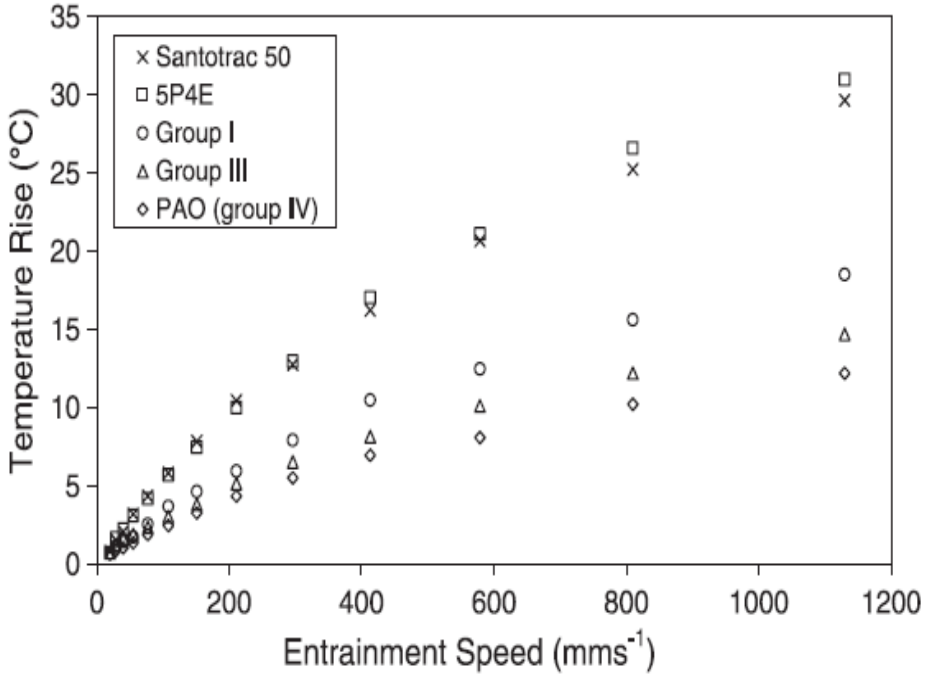

Figure 4-5: Average temperature rise of the steel ball and the sapphire disc surfaces versus entrainment speed for the range of oils tested in EHD contacts, with w= 20 N, SRR = 50 %, and T_0=40°C [102].

4.2 Effect of sliding and normal load in steel-steel and steel-Si_3N_4 contacts

4.2.1 Operating conditions

This section provides clues for the understanding of pressure, temperature rise and heat dissipation in steel-steel and in steel-Si_3N_4 contacts. Note that for such opaque contacting solids, the spectral methodology using QDs photoluminescence cannot be used anymore for performing *in situ* measurements. Instead, friction tests are carried out to evaluate the power losses which refer to the heat generated in these contacts (details will be reported in section 4.2.4). Besides, as the use of QDs is discarded, the criteria for selecting pressure equal or lower than 1.3 GPa is excluded. Therefore, the normal loads can be chosen to generate high pressures closely similar to that produced inside rolling element bearings. The sliding and normal loading effects are studied by applying rolling-sliding conditions, presented in Table 4-2 and Table 4-3, on Jerotrib test rig. The first series of rolling-sliding tests described in Table 4-2 are also simulated using the TEHD model. The mechanical and thermal properties of the contacting solids materials are reported in (Table 3-3, chapter 3). Note that 100C6 steel discs have the same properties as 100C6 balls.

	T_0=298 K u_e=0.5 m/s SRR=[0 ; 50%]		
Disc material	Steel (100C6)		
Ball material	Si_3N_4	Steel (100C6)	Si_3N_4
Colloidal dispersion (N°)	Pure SQ	5	Pure SQ
w (N)	256	256	181
P_H (GPa)	1.8	1.6	1.6
a (mm)	0.260	0.276	0.232
h_c (nm) at SRR=0 and 298K	111.83	114.13	114.70
M, L	1234, 9	1289, 8	872, 9
$\varphi_T(-)$ at SRR=0%	~0.99	~0.99	~0.99

Table 4-2: First series of rolling-sliding tests for comparing the effect of sliding on steel-steel and hybrid (steel- Si_3N_4) contacts operated at T_0=298 K.

	T_0=313 K u_e=5 m/s SRR=[0 ; 50]%		
Disc	Steel (100C6)		
Ball	Si_3N_4	Steel (100C6)	Si_3N_4
Colloidal dispersion (N°)	Pure SQ	5	Pure SQ
w (N)	256	256	181
P_H (GPa)	1.8	1.6	1.6
a (mm)	0.260	0.276	0.232
h_c (nm) at SRR=0 and 313K	337.49	344.40	346.14
M, L	344, 13	360, 11	244, 13
$\varphi_T(-)$ at SRR=0%	~0.92	~0.92	~0.92

Table 4-3: Second series of rolling-sliding tests for comparing the effect of sliding on steel-steel and hybrid (steel- Si_3N_4) contacts operated at T_0=313 K.

4.2.2 Pressure distribution

Figure 4-6 shows a comparison between the simulated pressure profiles along the x-direction for steel-steel and steel-Si_3N_4 contacts, at the same normal load (256 N) and at different loads generating the same maximum pressure (1.6 GPa) at the contact center, for three different slide-to-roll ratios (SRR=5, 25, 50%) at 298K.

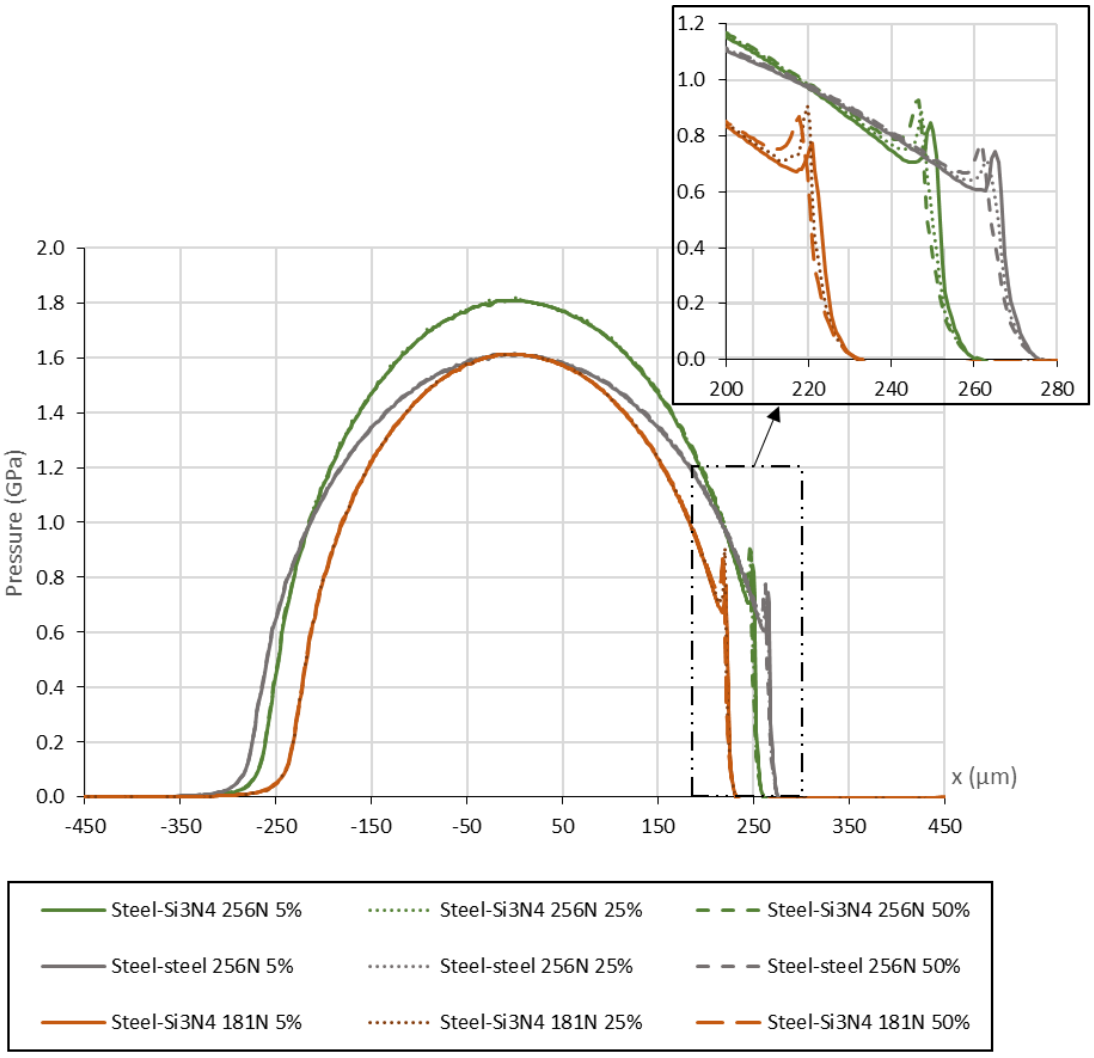

Figure 4-6: Simulated pressure profiles along the contact centerline for: steel-Si_3N_4 (w=256N P_H=1.8 GPa), steel-steel (w=256N P_H=1.6 GPa) and steel-Si_3N_4 (w=181N P_H=1.6 GPa) contacts operated at T_0=298 K, u_e=0.5 m/s and SRR= 5, 25, 50%.

All these plotted profiles are originated from the elastic properties of the contacting bodies (and their corresponding deformations) induced by the application of normal loads. Indeed, as predicted, it is found that:

- The central pressure corresponds to that predicted by Hertz as M>100 and L<17, according to [37].
- For the same contacting materials (steel-Si_3N_4 in this case), as the load increases the EHD pressure becomes higher and its distribution becomes larger. In this given case, a 41% increase of the normal load leads to a 12% increase in pressure and 11% increase in contact width.
- Under equivalent applied normal load, the maximum pressure in a hybrid contact is higher than in an all-steel contact (of 12% here).

- The pressure distribution in all-steel contact is larger (in width) than in steel-Si_3N_4 contact either under identical normal load (by 6% wider) or for same generated central pressure (by 16% wider).

More importantly, it can be clearly noticed that the characteristic EHD pressure distribution shape remains almost unchanged within the applied SRR range, at least up to SRR=50%. The differences are mainly found in the location and amplitude of the pressure spike at the contact outlet. These results are in accordance with the results published in [12], [36], [37]. One can notice that, as SRR increases, the position of the pressure spike moves further into the contact area. This is in good accordance with the experimental results of Kagerer et al. [12].

4.2.3 Temperature rise

Figure 4-7 shows the simulated temperature profiles along the rolling direction (x-axis) in steel-steel (w=256N) and steel-Si_3N_4 (w=256N, 181N) contacts operated in rolling-sliding (SRR=5, 25, 50%) and at an entrainment speed of 0.5 m/s. Note that the displayed temperatures are average values across the lubricant film thickness.

Globally, in contrast to the pressure profiles, the temperature starts to increase at the inlet to reach its maximum beyond the contact center, then, it decreases as a tail at and beyond the contact outlet zone. The results shows also that the temperature profile is a little perturbed where the small pressure spike is located, according to pressure profiles displayed in Figure 4-6. These results are in a good agreement with the experimental and numerical work of Ebner et al. [14].

The results emphasize the effect of normal load in the steel-Si_3N_4 configuration. For the same combination of contacting bodies at constant velocity and SRR, the increase of normal load and thus in contact pressure enhances the temperature rise within the lubricant. Here, the 41% increase of normal load and thus of 12.5% in contact pressure corresponds to a temperature rise of approximatively 9K for SRR=50%, 4.5K for SRR=25% and 1K for SRR=5%. Also, at constant normal load and materials configuration, an increase of SRR leads to an increase of the average temperature.

Regarding the steel-steel contact, the temperature rise is lessened compared to the steel-Si_3N_4 case either under equivalent load or under same central pressure. Due to a higher contact pressure, the deviation from the average temperature rise in steel-steel configuration is obviously higher under equivalent load than under same central pressure in steel-Si_3N_4 contact. The deviation from the average temperature rise of the steel-steel contact compared to the steel-Si_3N_4 contact operated at equivalent normal load is estimated at 18K for SRR=50%, at 9K for SRR=25% and at 2K for SRR=5%.

To summarize, the difference between the average temperature rises in steel-steel and in steel-Si_3N_4 is twofold higher in the case of equivalent normal load than in the case of equivalent central pressure.

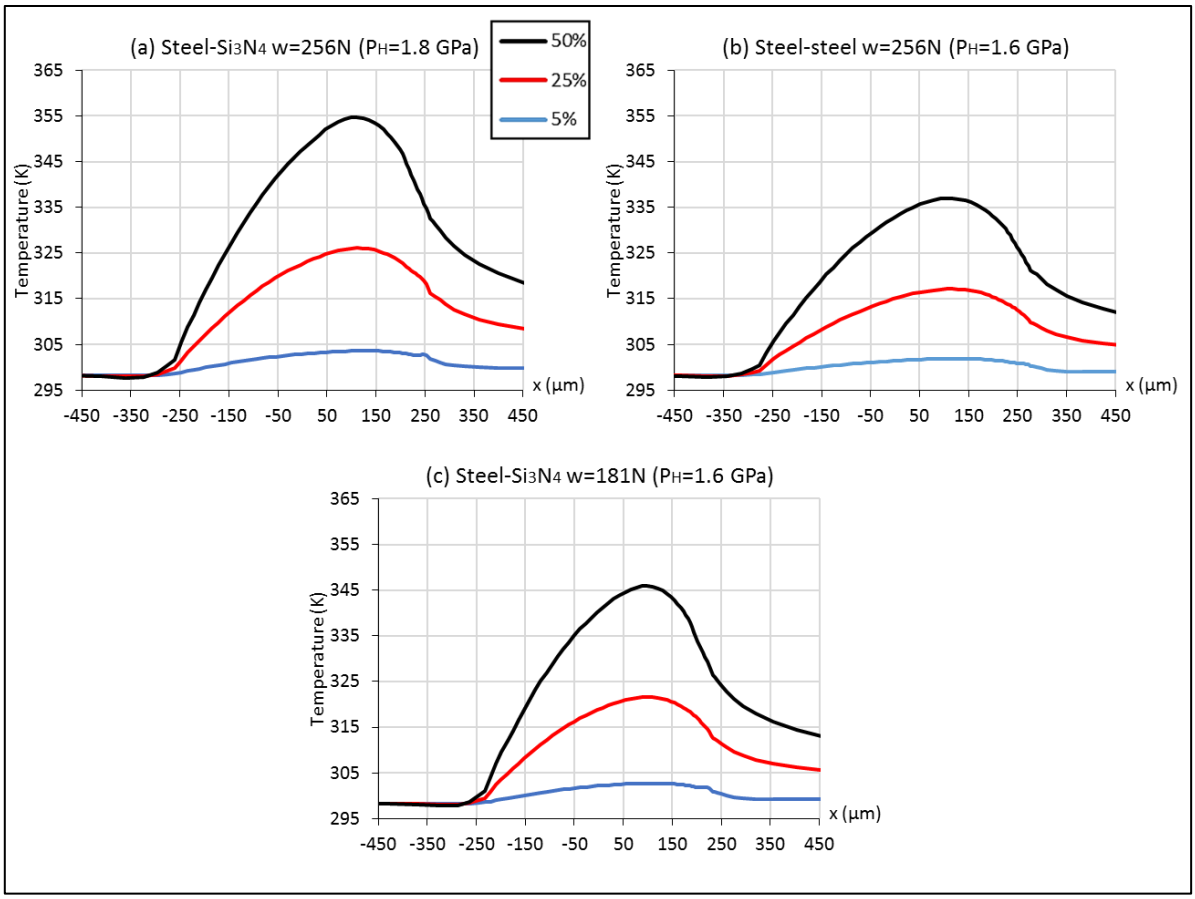

Figure 4-7: Simulated average temperature profiles at the centerline of*: (a) steel-Si_3N_4 (w=256N P_H=1.8 GPa), (b) steel-steel (w=256N P_H=1.6 GPa) and (c) steel-Si_3N_4 (w=181N P_H=1.6 GPa) contacts operated at T_0=298 K, u_e=0.5 m/s with SRR=5, 25 and 50%.*

This might be assigned to a thermal effect stemming from the solid materials properties: Si_3N_4 material does not conduct and absorb so easily the heat generated by the lubricant shearing as it has a lower thermal diffusivity compared to 100C6 steel. As a result, the temperature increases more within the lubricant, especially, at the Si_3N_4-lubricant interface as indicated in Figure 4-8. All these findings are in a good accordance the temperature measurement presented in section 4.1.2.

Beyond the contacting surfaces, the temperature inside the solids increases accordingly with the heating of the highly confined lubricant as displayed in Figure 4-8, which shows the deformed contacting solids.

It can be concluded that the contact pressure, the slide-to-roll ratio and, to a lower extend, the difference in thermal properties of the solid materials contribute in altering the temperature distribution within EHD contacts.

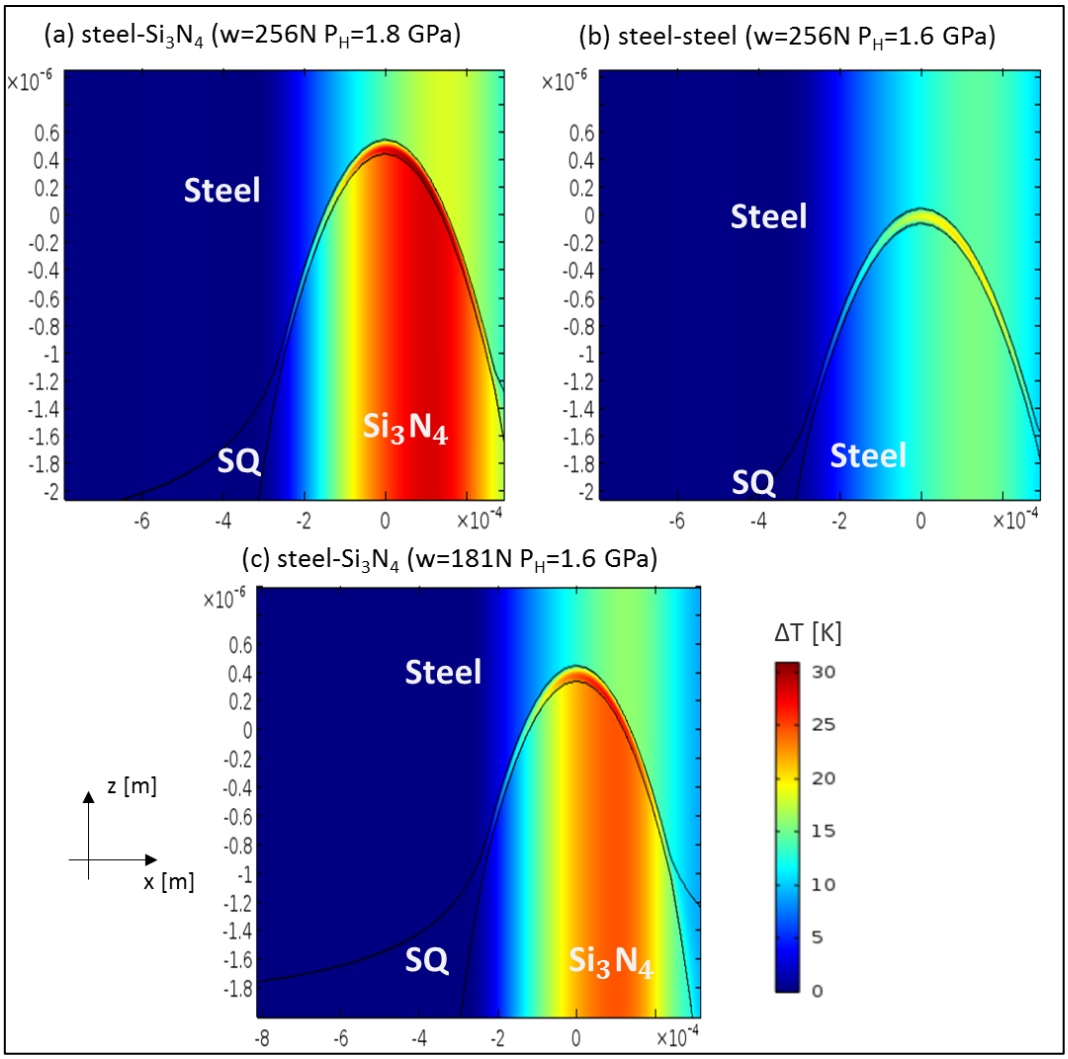

Figure 4-8: Temperature rise distribution for: (a) steel-Si_3N_4 (w=256N P_H=1.8 GPa), (b) steel-steel (w=256N P_H=1.6 GPa) and (c) steel-Si_3N_4 (w=181N P_H=1.6 GPa) contacts operated at T_0=298 K, u_e=0.5 m/s with SRR=25%.

4.2.4 Heat generation

In order to validate the previous results (in sections 4.2.2 and 4.2.3), an alternative approach assessing the energy balance through EHD is adopted by comparing experimental power losses and numerical heat generation. Indeed, at the conjunction between the contacting solids, the power is transmitted via the heavily loaded EHD contacts which, in turn, generate power losses due to the shearing action of the lubricant, considered as a localized heat source.

The experimental power losses (PWL), in the x direction, can be expressed as follows:

$$PWL = F_x \times |u_d - u_b| \qquad 4.2$$

with F_x the tangential force measured thanks to a multi-axis strain-gauge sensor installed in the test rig Jerotrib, u_d and u_b the velocities of the disc and the ball, respectively. In the numerical model, the generated heat is calculated by the integration of equation 5.12 (reported in annex 5.1) over the pressurized fluid volume.

Figure 4-9 displays comparisons between the measured power losses and simulated heat generation in steel-steel and steel-Si_3N_4 contacts under varying sliding conditions. An overall good agreement is found and reveals a proportionality of both parameters to sliding. These results highlight the consistency between the transmitted mechanical energy and the internally generated energy within these tested contacts.

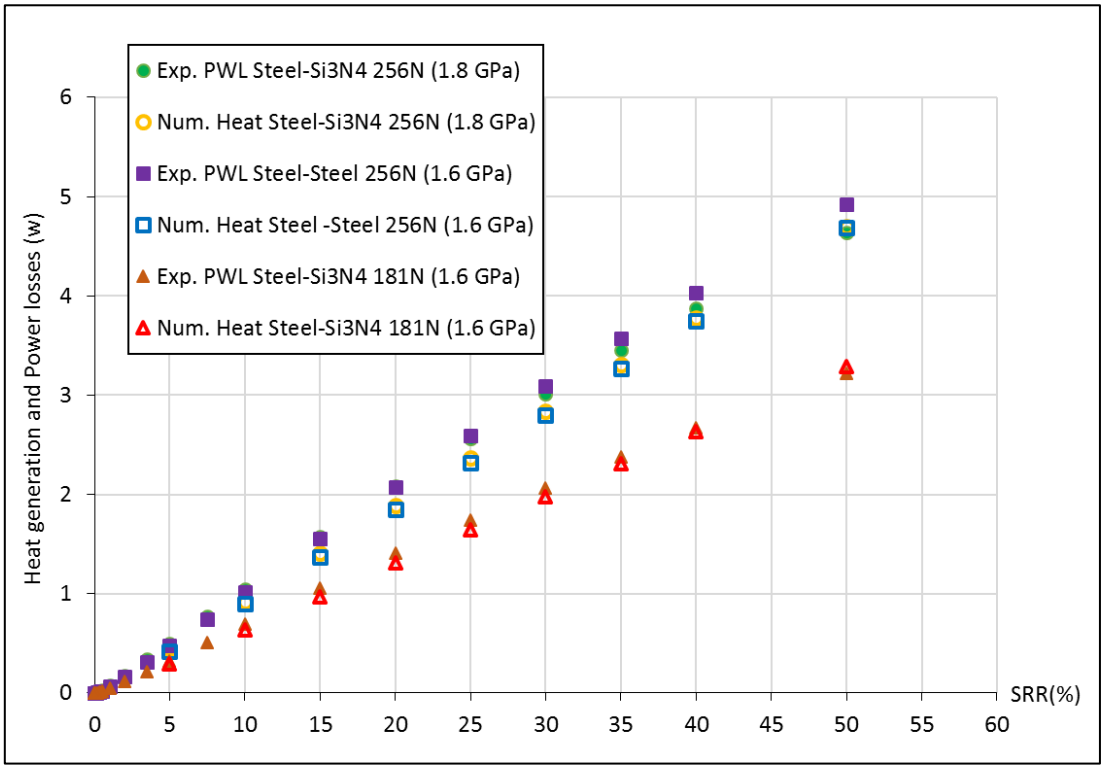

Figure 4-9: Measured power losses and simulated heat generation versus slide-to-roll ratio for: steel-Si_3N_4 (w=256N P_H=1.8 GPa), steel-steel (w=256N P_H=1.6 GPa) and steel-Si_3N_4 (w=181N P_H=1.6 GPa) contacts operated at T_0=298 K and u_e=0.5 m/s.

Indeed, the results shows that, under a constant normal load of 256 N, the generated heat in the steel-Si_3N_4 (P_H=1.8 GPa) contact, are slighty higher than in steel-steel (P_H=1.6 GPa) one, over the whole range of applied SRR [0; 50%]. On the other hand, at lower normal load of 181 N, the heat generated in the steel-Si_3N_4 (P_H=1.6 GPa) contact is reduced, by approximately 30% over the whole applied SRR range, compared to the other higher load case (w=256 N). In other words, one can say that the normal load dominates the pressure effect on heat generation regardless the combined contacting solids are steel-steel or steel-Si_3N_4. Note that the temperature rise concept is closely related to the heat generation one, but should not be confused. Unlike the temperature, the amount of heat is proportional to the mass of the considered lubricant, itself dependent of the contact dimensions. This involves the implication of the pressurized fluid volume (contact area and film thickness) and the heat transfer into the contacting solids.

It can be notice that, under higher SRR (above 35% in Figure 4-9 and above 25% in Figure 4-10), the experimental power losses in the steel-Si_3N_4 configuration starts to slightly decrease compared to the steel-steel case. This could be related to the thermal properties of Si_3N_4 which

could lead in higher temperature rise and thus a decrease of the lubricant viscosity which might lessen the frictional force (F_x) and, ultimately, reduce the power losses.

Results, in Figure 4-10, emphasizes not only the significance of normal load effect but also the influence of the sliding speed on the power losses. Indeed, by comparing results in Figure 4-9 and Figure 4-10, it can be argued that by increasing 10-fold the sliding velocity, the power losses increase by more than 5 times. This statement must be considered with caution *because* the inlet temperatures are not the same for both cases (see and compare the Cheng film thickness reduction factors (even calculated at SRR=0) reported on the last lines of Tables 4-2 and 4-3).

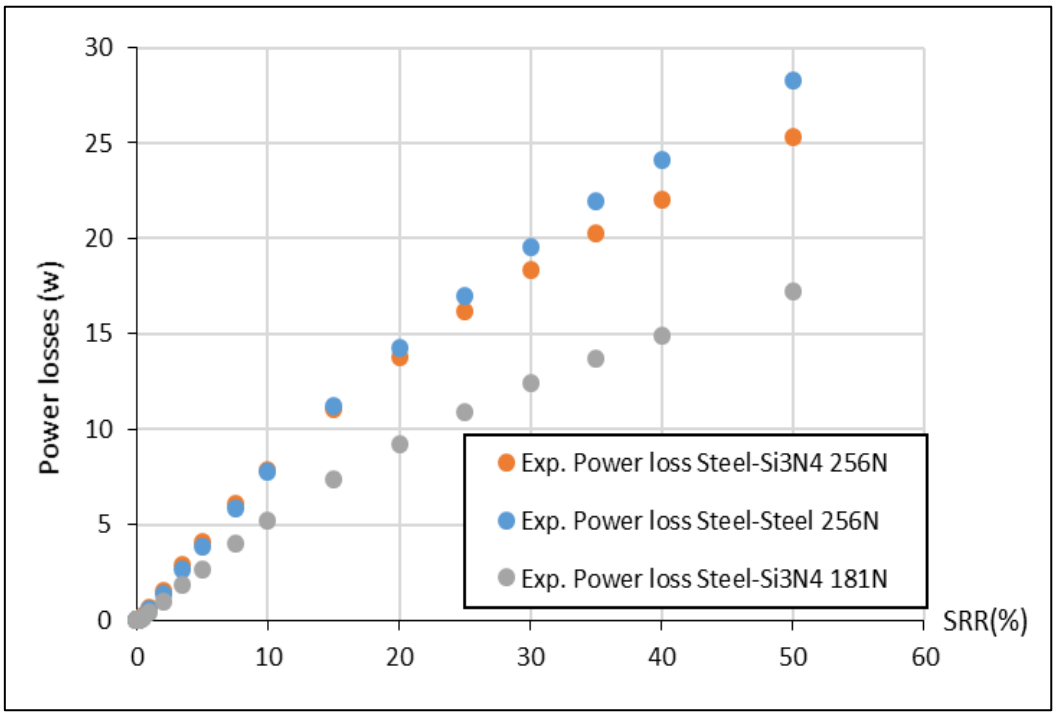

Figure 4-10: Experimental power losses versus slide-to-roll ratio for: steel-Si_3N_4 (w=256N P_H=1.8 GPa), steel-steel (w=256N P_H=1.6 GPa) and steel-Si_3N_4 (w=181N P_H=1.6 GPa) contacts operated at T_0=313 K and u_e=5 m/s.

Validations shown in chapter 3 with regard to pressure and temperature measurements on one side, and, Figure 4-2 and in Figure 4-9 on the other side, both reflect the credibility of the TEHD model. Hence, this makes the numerical model a helpful complementary mean to go further in the investigation. This will be the subject of the next section.

4.2.5 Heat fluxes

This section explores how frictional heat, generated by lubricant shearing, is transferred and evacuated in steel-steel and in steel-Si_3N_4 contacts. This is realized through the assessment of heat fluxes at the interfaces of the solid surfaces in some of the tests presented in Table 4-2. It is important to note that, within the fluid, convective heat in the z-direction (i.e. across film thickness) is neglected compared to conductive heat, as demonstrated by Spikes et al. [7].

As illustrated in Figure 4-11 where SRR=25%, the conductive surface heat fluxes are concentrated at the contacts center. The magnitude of the heat fluxes is more pronounced at the

steel-lubricant interface than in the Si_3N_4-lubricant interface. This is due to the superior thermal conductivity of the 100C6 steel (46 $W.m^{-1}.K^{-1}$) compared to that of Si_3N_4 (20 $W.m^{-1}.K^{-1}$).

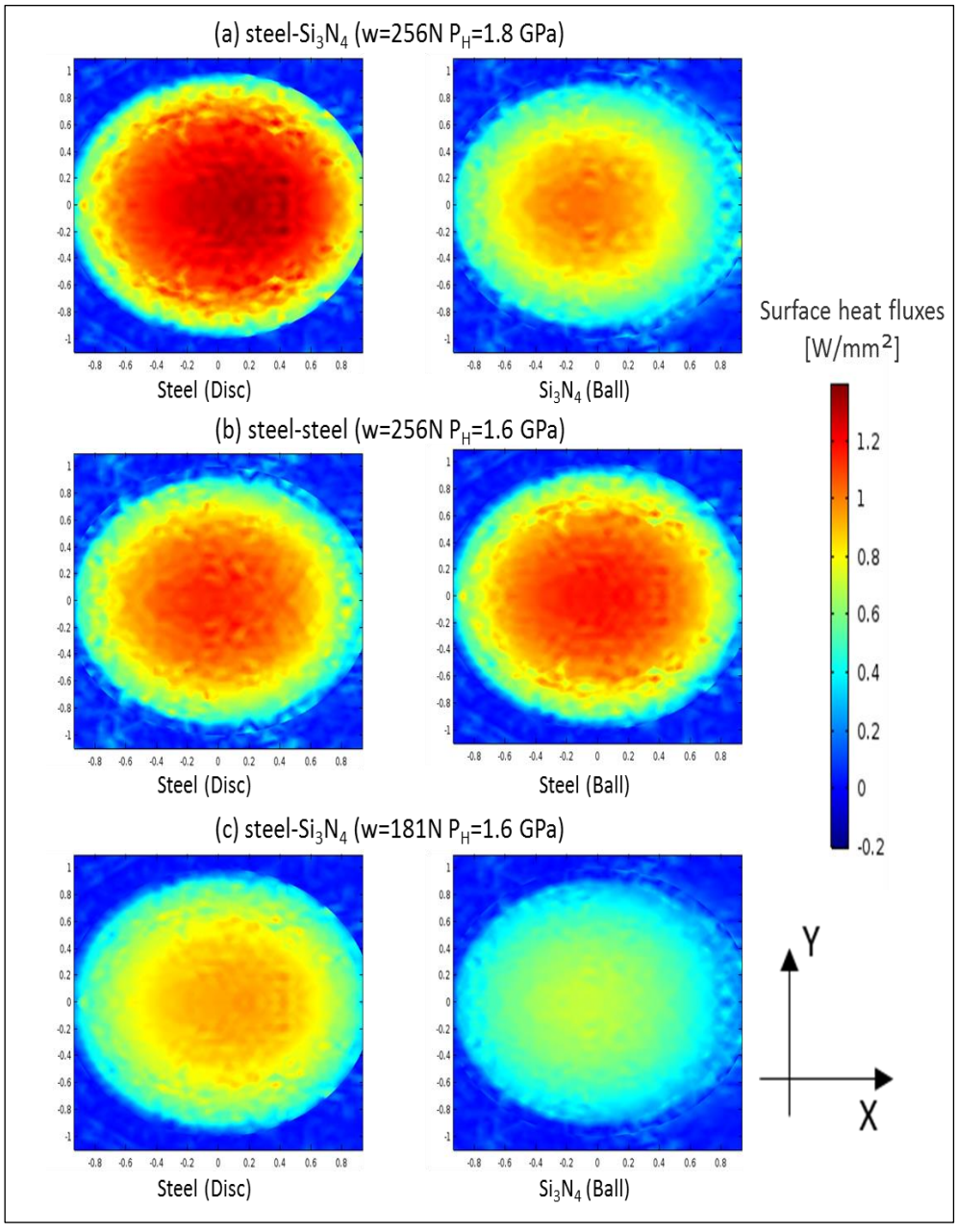

Figure 4-11: Comparison between the absolute values of the heat fluxes at the specimen/lubricant interfaces in: (a) steel-Si_3N_4 (w=256N P_H=1.8 GPa), (b)steel-steel (w=256N P_H=1.6 GPa) and (c) steel-Si_3N_4 (w=181N P_H=1.6 GPa) contacts operated at T_0=298 K, u_e=0.5 m/s with SRR=25%.

In the steel-steel case, the heat fluxes are almost equally balanced between the disc and the ball surfaces. Precisely, the conductive heat fluxes are slightly higher on the upper surface (the disc). The reason of this is that, for SRR>0, the steel ball moves faster than the steel disc. This gives less time to the ball to be heated up compared to the disc, and therefore, the ball becomes cooler than the disc. And as heat flow transfers from the hot to the cool zone, the magnitude of conductive heat fluxes at the ball surface is higher than at the disc surface.

At the same normal load of 256 N as for the steel-steel contact but applied to the steel-Si_3N_4 case, the heat fluxes are larger at the steel surface because heat transfers are reduced on the Si_3N_4 ball surface. Furthermore, at a lower load of 181 N, still in the case of steel-Si_3N_4 contacts, both of the steel and Si_3N_4 surface heat fluxes are lessen compared to the previous configuration, but also compared to the steel-steel case under the same contact pressure (1.6 GPa).

Complementary to the results presented in Figure 4-11, in order to globalize all the heat transfers concerning each contacting body and the lubricating film, the different heat fluxes can be integrated. They can be presented as plotted in Figure 4-12, for SRR =5, 25 and 50% of the tests presented in Table 4-2. It can be noted that, in these simulations, the energy balance is fully satisfied: the heat generated within the lubricant is transferred by the different fluxes to the 3 elements that constitute the lubricated contact.

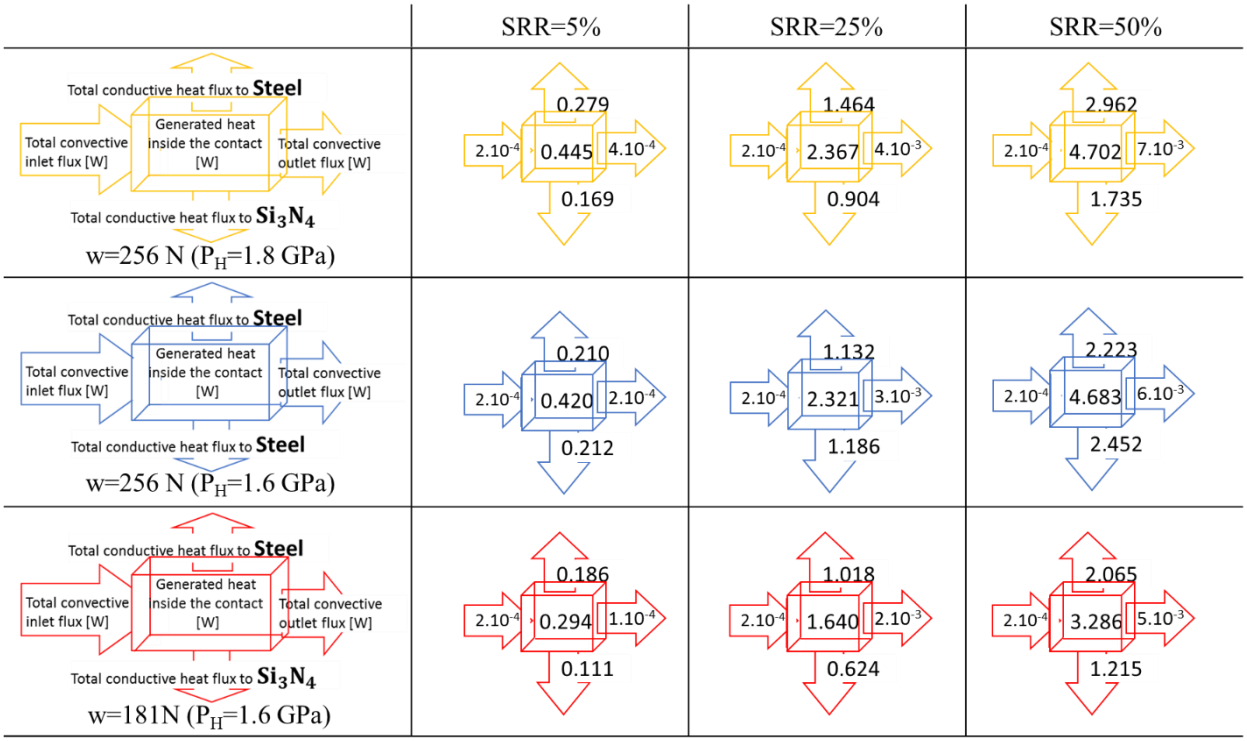

Figure 4-12: Convective & conductive heat fluxes and generated heat *in the lubricant volume for steel-Si_3N_4 (w=256N P_H=1.8 GPa), steel-steel (w=256N P_H=1.6 GPa) and steel-Si_3N_4 (w=181N P_H=1.6 GPa) contacts operated at T_0=298 K, u_e=0.5 m/s for SRR=5, 25 and 50%.*

For further exploration, one can deduce the integrated heat fluxes disc to ball ratios to compare the influence of sliding and normal load on the heat transfer between the different combinations of contacting solid materials. As shown in Figure 4-13, these ratios are quite constant for a given combination of contacting solids and applied normal load, independently of the SRR value. Indeed, in the steel-steel contacts, the ratios are close to 1 because the disc and the ball specimen are made from the same material. On the other hand, in the case of steel-Si_3N_4 contacts, the ratio is higher than 1 because the heat is more easily conducted into the steel disc.

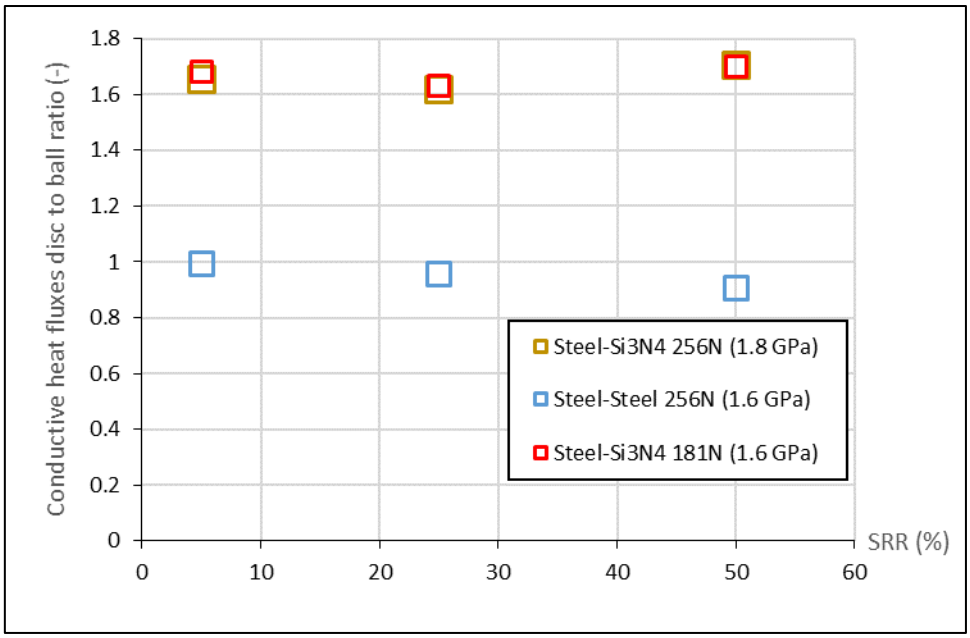

Figure 4-13: Conductive heat fluxe disc to ball ratios *for: steel-Si_3N_4 (w=256N P_H=1.8 GPa), steel-steel (w=256N P_H=1.6 GPa) and steel-Si_3N_4 (w=181N P_H=1.6 GPa) contacts operated at T_0=298 K, u_e=0.5 m/s with SRR=5, 25 and 50%.*

4.3 Summary and discussion

In order to tackle the industrial objective of this work, the last chapter aims to compare pressure, temperature and heat generation in all-steel and hybrid (steel-Si_3N_4) contacts under rolling-sliding conditions and different normal loads.

The first part of this chapter is dedicated to the measure of the temperature rise in sapphire-steel and sapphire-Si_3N_4 contacts using the CdSe/CdS/ZnS QDs. Both measured and simulated temperature rises at the contact center increase with the same tendency with respect to an increase of the slide-to-roll ratio. For different normal loads inducing the same central pressure, the temperature rise in a sapphire-Si_3N_4 contact is found to be slightly higher than in a sapphire-steel contact (with less than 5K). This is attributed to the lower thermal diffusivity of the Si_3N_4 material compared to that of 100C6 steel. Under the same normal load, the difference in temperature rise becomes more pronounced (of ~10K) because pressure in a sapphire-Si_3N_4 contact is higher than in the sapphire-steel case. This means that contact central pressure, sliding and solid material thermal properties have an influence on the temperature rise within the lubricant.

The validation and reproducibility of the experimental results highlights the reliability of the QDs used as nanosensors to measure pressure and temperature under severe shearing and pressure conditions. The developed method is non-intrusive and has an appropriate spatial resolution (~10 µm) compared to the size of a typical EHD contact. However, the main drawback of this technique lies in the necessity of using one transparent material like glass or sapphire through which the exciting laser beam and the detected QDs photoluminescence signal pass. This is nevertheless an inherent characteristic of all optical methods. In our case, however,

it can be noted that it is not necessary to coat the transparent surface with a metallic coating, as is the case for interferometric or infrared thermography techniques. Another issue is that, before sensing temperature, it is required to perform an isothermal contact in pure rolling conditions to determine the part of QDs emission energy change due to pressure. In addition, using squalane in this study, it was found that the methodology is applicable up to 1.3 GPa only.

The main section of this chapter presents comparisons between the evolution of pressure and temperature profiles as well as heat generation in steel-steel and steel-Si_3N_4 contacts, operated under various slide-to-ratios, at equivalent normal load or at different loads generating the same central pressure.

Regarding the pressure distribution, it corresponds to that expected from the Hertz theory. For the same combination of contacting bodies, as the load increases, the pressure and its distribution (contact size) increase. The pressure distribution in steel-steel contacts is wider than in steel-Si_3N_4 contacts, of 6% under the same normal load or of 16% for the same generated central pressure. The characteristic shape of the pressure profiles remains unchanged except at the position of the pressure spike because which moves gradually towards the contact center with an increase of the slide-to-roll ratio.

Regarding the temperature rise, it exhibits a clear evolution in magnitude as a function of the slide-to-roll ratio. For same combination of contacting bodies, the temperature increases with contact pressure. Under the same normal load, the temperature rise is higher in the case of steel-Si_3N_4 contacts than for steel-steel contacts. The difference between temperature rises in steel-steel and in steel-Si_3N_4 contacts is doubled when the normal load is kept constant, compared to the case when the central pressure is kept constant.

Concerning heat generation, it is found to be in good accordance with the experimental power losses derived from friction measurements. This corroborates the coherence between the transmitted mechanical energy and the internally generated energy within the contact. At constant normal load, the heat generated inside Si_3N_4-steel contacts is slightly higher than in steel-steel contacts. Under a normal load generating the same central pressure as in steel-steel contacts, the heat generation in Si_3N_4-steel contacts is reduced by ~30% compared to the steel-steel case.

With regard to heat transfer, the convective and the conductive heat fluxes are evaluated using the TEHD numerical model. The convective heat fluxes are very low compared to the conductive ones: the largest amount of heat is conducted into the contacting solids. The ratio between the integrated conductive heat fluxes into top (disc) and bottom (ball) bodies is found to be almost constant and equal to 1 in the steel-steel configuration, constant and close to ~1.7 in the steel-Si_3N_4 configuration, and in all cases nearly independent of the applied slide-to-roll ratio and normal load.

From a broader perspective, these overall results to some extent provide instruction for a better selection of REBs design and material depending on the operating conditions of the application.

General conclusion

The work presented in this manuscript was motivated by an industrial need to measure the local pressures and temperatures and to compare the heat generation in all-steel and hybrid elastohydrodynamic (EHD) contacts. Overcoming such challenges represents a very useful route for a better selection of rolling element bearings (REBs) design, material and lubrication conditions.

To meet this objective, a non-intrusive *in situ* method, exploiting the sensitivity of the photoluminescence of quantum dots (QDs) to pressure and temperature, was developed. This method has the potential to be more efficient in terms of detectability, accuracy and reliability than the previously developed techniques such as Raman spectroscopy, infrared thermography and electrical resistance, respectively. Moreover, a thermal-EHD numerical model is used as a helpful mean to validate measurements.

The first step of this work was intended to calibrate the QDs photoluminescence to pressure and temperature variations under static conditions and to analyze the influence of shear stress on their response under controlled conditions of temperature and shearing. These characterizations confirm the theoretical capability of the photoluminescence spectroscopy to allow pressure and temperature measurements, thanks to the quantification of the emission energy and full width at half maximum of the QDs response, discarding the effect of flow or shearing. The pressure and temperature dependencies were found to be linear for pressures up to 1.3 GPa and for temperatures from 296 K to 373 K (or in ranges below the phase change of the carrier lubricant).

The next step was dedicated to performing *in situ* pressure and temperature measurements in EHD contacts using a ball-on-disc tribometer. To operate the photoluminescence technique, it is absolutely imperative to use at least one transparent material (made of glass or sapphire) through which both the incident laser beam and the photoluminescence emission by the QDs pass. However, it turned out that through the transparent disc, the fine detection of the QDs full width at half maximum is prevented by the disc parasitic fluorescence in the background. The methodology initially conceived had be modified to overcome this situation. The solution consisted in evaluating the emission energy in pure rolling under isothermal conditions in order to extract the variations of the pressure only. Thus, for the same normal load but in rolling-sliding, the contribution of the variation in emission energy due to the heating of the lubricant could be determined and thus temperature could be deduced.

The *in situ* measurements were conducted for different combinations of contacting solids: glass-steel, sapphire-steel, glass-Si_3N_4 and sapphire-Si_3N_4. The experimental-numerical comparisons in terms of pressure and temperature revealed a good consistency which demonstrates the feasibility of the proposed methodology.

A numerical investigation was elaborated to quantify pressure, temperature as well as heat generation in steel-steel and steel-Si_3N_4 EHD contacts. The effects of sliding, normal loading and material thermal properties were underlined. The main outcomes are the following:

-For a given combination of contacting solids, the increase of normal load increases the local pressure, temperature and generated heat within the pressurized lubricant volume.
-Under same normal loads, the employment of Si_3N_4 ball instead of 100C6 steel ball causes an increase on both local pressure (due to a higher Young modulus) and temperature (due to the (higher) pressure influence of the lubricants properties and the specific thermal properties of the ceramic).
-Whether the combined contacting solids are steel-steel or steel-Si_3N_4, the applied normal load and sliding speed are the key parameters that alter the generation of heat within the contact.
- The proportionality of the conductive heat fluxes between the disc and ball remains constant despite the effect of sliding and normal loading.

The validity of these results was successfully corroborated through comparisons between the simulated heat in the contact and the experimental power losses in rolling-sliding conditions. Indeed, equality found between mechanical energy and internal thermal energy (heat) demonstrates the conservation of energy.

Recommendations for future work

In spite of demonstrating the feasibility of the developed technique through the quantification of the QDs photoluminescence properties, it would be of great interest to carry out simultaneous pressure and temperature independent measurements. This could be achieved by means of an additional fine spectrum processing to extract QDs full width at half maximum from the transparent disc (glass or sapphire) overlaid fluorescence. Another option would be to use diffraction gratings with a density well below 100 gr/mm, to provide a larger spectral range and thus more accurate processing of the spectra baselines. In our case this would require a different spectrometer than the one available. It is also important to reduce the pressure and temperature uncertainties. This can be done by using more sensitive quantum dots and/or by performing further calibration with more sensitive reference sensor than the ruby micro particles. In addition, the uncertainty on the position of a measuring point can be improved I) by employing a high resolution camera for a better observation of the contact and the laser spot, II) by optimizing the xyz micro positioning stage of the microscope.

Moreover, from an engineering point of view, it would be very informative to perform pressure and temperature measurements and simulations for different types of lubricants. Besides, it is particularly necessary to properly model the limiting shear stress behavior corresponding to each lubricant, in order to use a numerical model rich of physical considerations allowing a representative simulation of EHD contacts.

On top of that, as the rolling element bearing contacts do not instantaneously share the same kinematics and loading conditions, it would be extremely interesting to carry out extensive local temperature measurements within the lubricant covering the REBs surfaces (i.e. cage, inner/outer rings or even on rolling elements in case of full complement REBs). This would provide information on the locations of the power losses, which would be very useful for understanding heat generation mechanisms occurring in such mechanisms.

Annexes

Annexes **147**
5.1 Themo-elastohydrodynamic Numerical model 149
5.1.1 Lubricant Transport Properties 149
5.1.2 Numerical computation 151
5.2 Emission energy and Full width at half maximum uncertainties 154
5.3 Pressure and temperature sensitivities uncertainties 154
5.4 Pressure and temperature uncertainties 155
5.4.1 High pressure cell 155
5.4.2 Elastohydrodynamic contact 155
5.5 Pearson VII and SplitPearson VII functions 155
5.6 Determination of the laser spot size using cleaved silicon sample 156

5.1 Themo-elastohydrodynamic Numerical model

In this study, a numerical model is used as a validation/complementary tool to compare the experimental results to full simulations. In addition to analytical formulas considering a Newtonian lubricant behavior for predicting shear heating at the contact inlet and the central film thickness, numerical simulations allocate more accuracy by i) implementing advanced models based on lab measurements on the lubricant transport properties and their dependence on pressure, temperature and shear stress, and ii) by solving the full equations of the EHD problem.

The resolution of the non-Newtonian thermal EHD model was inspired by the work of Habchi [67] and developed by Doki-Thonon [106] and Wheeler [44]. In this study, the appropriate physical considerations such as the chosen lubricant rheological and thermal behaviour laws are implemented to perform proper simulations. The QDs are not considered in the modelling because their presence doesn't affect squalane rheology, as demonstrated in the previous chapter and in reference [68].

The simulations are carried out with a three-dimensional model in steady state, fully flooded, thermal, non-Newtonian conditions and considering smooth surfaces. As the Reynolds equation is part of the model, all its classical assumptions are implicitly satisfied.

5.1.1 Lubricant Transport Properties

5.1.1.1 Lubricant density

The variations of the lubricant density with pressure and temperature are taken into account by the Tait relation [107]. The Tait model relates the density variation for a given volume V to V_0 volume at ambient pressure and to V_R volume at ambient pressure and at a reference temperature T_R. It is written as follows:

$$\rho(P,T) = \rho_R \left(\frac{V_R}{V_0} \times \frac{V_0}{V}\right) \qquad 5.1$$

with

$$\frac{V_0}{V} = 1 - \frac{1}{1+K_0'} ln\left[1 + \frac{P}{K_0}(1+K_0')\right]$$

$$\frac{V_0}{V_R} = 1 + a_v(T - T_R)$$

$$K_0 = K_{00}\exp(-\beta_k T)$$

where K_0 is the isothermal bulk modulus at atmospheric pressure, K_0' = 11.74 is the pressure rate of change of the isothermal bulk modulus, K_{00}= 8.658 GPa is the isothermal bulk modulus at zero absolute temperature. The coefficient of thermal expansion a_v = 8.36×10^{-4} K^{-1} and the bulk modulus-temperature coefficient β_k= 6.332×10^{-3} K^{-1} are obtained with a standard deviation of 0.05% from Bair experimental results [107].

5.1.1.2 Lubricant viscosity

Viscosity is another parameter that strongly depends on pressure and temperature. A hybrid model [25] is used to represent accurately the viscosity-pressure-temperature dependence of squalane. It is considered as a more enhanced correlation (between the viscosity measured thanks to a viscometer and pressure at different temperatures) than the so-called improved Yasutomi model. It can be written as follows:

$$\mu = \mu_0 \left(1 + \frac{\alpha_0}{q} P\right)^q \exp\left(\frac{C_F P}{P_\infty - P}\right) \qquad 5.2$$

with

$$\mu_0 = \mu_{0\infty} \exp\left(\frac{D_F\, T_\infty}{T - T_\infty}\right)$$

$$\alpha_0 = a_2 \left(\frac{1}{T}\right)^2 - a_1 \left(\frac{1}{T}\right) + a_0$$

$$q = b_1 \left(\frac{1}{T}\right) + b_0$$

$$P_\infty = c_2 \left(\frac{1}{T}\right)^2 + c_1 \left(\frac{1}{T}\right) + c_0$$

where $\mu_{0\infty}$ is the low-shear (or Newtonian) viscosity for zero argument of the exponential, D_F the fragility parameter and T_∞ the divergence temperature, according to [25] .

The values of the hybrid model parameters of squalane are listed in Table 5-1.

Hybrid Model-Squalane	
Parameter [Unit]	**Value**
$\mu_{0\infty}[Pa.s]$	3.93×10^{-5}
$D_F[-]$	6.09
$T_\infty[K]$	154.82
$a_0[1/GPa]$	2.34
$a_1[K/GPa]$	-166.78
$a_2[K^2/GPa]$	1.48×10^6
$b_0[-]$	-2.18
$b_1[K]$	2.33×10^3
$C_F[-]$	6.09
$c_0[GPa]$	24.46
$c_1[K.GPa]$	-1.17×10^4
$c_2[K^2/GPa]$	1.54×10^6

Table 5-1: The hybrid model parameters of the squalane from [25].

Squalane, as most of lubricants, is a shear sensitive material. At high shear stress, shear thinning phenomenon occurs and contributes to decrease the apparent viscosity and thus to friction reduction. The shear dependence of viscosity is expressed by Carreau equation:

$$\eta = \mu\left[1 + \left(\dot{\gamma}\,\lambda_R \frac{\mu}{\mu_R}\frac{T}{T_R}\frac{V_0}{V_R}\right)^2\right]^{(n-1)/2} \quad 5.3$$

where $\mu_R = 15.6$ mPa.s is the low shear viscosity at reference temperature and ambient pressure, λ_R =2.26×10^{-9} s the relaxation time and n =0.463 the Carreau exponent [108].

5.1.1.3 Lubricant thermal properties

In order to properly simulate the thermal and frictional behavior of the EHD contact, the temperature and pressure dependencies of the lubricant thermal conductivity (k_f) and volumetric heat capacity (ρC_{pf}) are implemented. The formulation of empirical relations are described in the work of Björling et al. [109]. The different parameters are measured using the transient hot-wire method (Håkansson et al. [110]). For the squalane, the equations are written as:

$$k_f = C_k\,\kappa_f^{-s} \quad 5.4$$

with

$$\kappa_f = \left(\frac{V}{V_R}\right)\left[1 + A_k\left(\frac{T}{T_R}\right)\left(\frac{V}{V_R}\right)^{q^*}\right]$$

where C_k= 0.074 W/mK, s= 4.5, $q^* = 2$ and $A_k = -0.115$.

$$C_v = \rho C_{pf} = C_0 + m^*\chi \quad 5.5$$

with

$$\chi = \left(\frac{T}{T_R}\right)\left(\frac{V}{V_R}\right)^{-3}$$

where C_0= 0.94×10^6 J/m^{3}K and m^*= 0.62×10^6 J/m^{3}K.

5.1.2 Numerical computation

In order to obtain the solution to the circular non-Newtonian TEHD contact problem, the model solves simultaneously the generalized Reynolds, solids' deformation, load balance and energy equations.

The Generalized Reynolds equation represents the flow of the lubricant and provides the pressure along the contact. It takes into account the density and viscosity variations within the film thickness and can be expressed as follows:

$$\frac{\partial}{\partial x}\left[\left(\frac{\rho}{\eta}\right)_e \frac{\partial P}{\partial x}\right] - \frac{\partial}{\partial y}\left[\left(\frac{\rho}{\eta}\right)_e \frac{\partial P}{\partial y}\right] + \frac{\partial}{\partial x}(\rho_x^*) + \frac{\partial}{\partial y}(\rho_y^*) = 0 \quad 5.6$$

with

$$\left(\frac{\rho}{\eta}\right)_e = \frac{\eta_e}{\eta_e'}\rho_e' + \rho_e''$$

$$\rho_x^* = \rho_e'\,\eta_e(u_{tx} - u_{bx}) - \rho_e u_{bx}$$

$$\rho_y^* = \rho_e'\,\eta_e(u_{ty} - u_{by}) - \rho_e u_{by}$$

where u_{tx}, u_{bx}, u_{ty} and u_{by} are the solids speed along x and y directions, respectively. The variables carrying the index $()_e$ represent equivalent terms taking into account the variations of the lubricant properties in the film thickness. These latter are written:

$$\rho_e = \int_0^{h(x,y)} \rho(P,T)dz$$

$$\rho'_e = \int_0^{h(x,y)} \rho(P,T)\left(\int_0^z \frac{1}{\eta(P,T,\tau)}dz'\right)dz$$

$$\rho''_e = \int_0^{h(x,y)} \rho(P,T)\left(\int_0^z \frac{z'}{\eta(P,T,\tau)}dz'\right)dz$$

$$\frac{1}{\eta_e} = \int_0^{h(x,y)} \frac{1}{\eta(P,T,\tau)}dz$$

$$\frac{1}{\eta'_e} = \int_0^{h(x,y)} \frac{z}{\eta(P,T,\tau)}dz$$

The film thickness is given by the sum of the rigid bodies' separation h_0, the initial shape of the solids which is approximated by parabolic curves and the solids deformation. As the elastic deformation is larger than film thickness, the rigid bodies' separation h_0 is constantly negative. The film thickness expression is set as follows:

$$h(x,y) = h_0 + \frac{x^2}{2R_x} + \frac{y^2}{2R_y} - \delta(x,y) \qquad 5.7$$

with δ(x,y) the sum of the vertical deformations of the two solids in contact.

This deformation, due to the pressure generated in the contact, is calculated according to the linear elasticity theory:

$$\nabla.\sigma(u,v,w) = 0 \qquad 5.8$$

The pressure field carries the normal load applied on the contact, so that the load balance equation writes:

$$w = \iint_S P(x,y)dxdy \qquad 5.9$$

where S represents the contact area.

The piezoviscous and non-Newtonian effects are not the only major consequences of the strong pressure and strong shear that govern inside the contact. In addition to these two rheological phenomena, the implication of heat generation by compression and shearing must be considered. Depending on the nature of the fluid and the operating conditions (entrainment

speed, sliding, normal loading), the resulting temperature rise may have a strong impact on the lubrication parameters (reduction of film thickness and coefficient of friction).

The lubricant is subjected to a severe compression at the contact inlet, as high as several gigapascals. This action generates a heat source that can be calculated as:

$$Q_{comp} = -\frac{T}{\rho}\frac{\partial \rho}{\partial T}\left(\overrightarrow{u_f}.\vec{\nabla}p\right) \qquad 5.10$$

where

$$\overrightarrow{u_f} = \begin{pmatrix} u_{f,x} \\ u_{f,y} \end{pmatrix}$$

with

$$u_{f,i} = \frac{\partial p}{\partial i}\left(\int_0^z \frac{z}{\mu}dz - \frac{\mu_e}{\mu_e'}\int_0^z \frac{1}{\mu}dz\right) + \mu_e\left(u_{d,i} - u_{b,i}\right)\int_0^z \frac{1}{\mu}dz + u_{b,i} \text{ for } i = \{x, y\}$$

The indices f, d and b stand for the fluid, disc and ball, respectively.

More importantly, due to the kinematics conditions especially the relative sliding produced the velocity difference of the solid surfaces, the lubricant experiences shear stresses which can reach dozens of megapascal (MPa). This causes a significant heat generation whose contribution is more pronounced than that produced by compression. The shear-heating source is written as:

$$Q_{shear} = \mu\left(\left(\frac{\partial u_{f,x}}{\partial z}\right)^2 + \left(\frac{\partial u_{f,y}}{\partial z}\right)^2\right) \qquad 5.11$$

The generation of heat within the lubricant film and the heat dissipation through the lubricant and the contacting bodies are modelled by the energy equation. This equation guarantees the conservation of heat fluxes in the whole system and allows to determine the temperature distribution within the contact. By neglecting the volumetric forces and the radiative thermal exchanges, the stationary heat equation of the lubricant denoted (f) is formulated as follows:

$$-\nabla.\left(k_f \nabla T\right) + \rho C_{pf}\overrightarrow{u_f}.\nabla T = Q_{comp} + Q_{shear} \qquad 5.12$$

where k_f, ρ and C_{pf} are, respectively, the thermal conductivity, density and heat capacity of the fluid.

For the two contacting solids, the heat equation writes:

$$-\nabla.\left(k_i \nabla T\right) + \rho_i C_{pi}\overrightarrow{u_i}.\nabla T = 0 \qquad 5.13$$

where k_i, ρ_i, u_i and C_{pi} are, respectively, the thermal conductivity, density, velocity and heat capacity of the solid i=$\{d, b\}$.

Note that the heat conduction along xy-plane (the lubricant film plane) is neglected compared to heat convection. On the other hand, as the film thickness is very thin and small compared to

the other dimensions of the contact, the heat convection is considered negligible compared to the heat conduction along the z-direction, in agreement with Yang et al. [111]. More details on the model domain, boundary conditions, numerical stability method and cavitation treatment can be found in the work of Habchi et al. [112].

5.2 Emission energy and Full width at half maximum uncertainties

-The uncertainty is estimated as the standard deviation ($\sigma_{deviation}$) of all experimental data obtained from the static calibration: emission energy and full width at half maximum (FWHM) as a function of pressure and temperature. It can be defined as the square root of the squared differences from the Mean and can be expressed as:

$$\sigma^2_{deviation} = \frac{SCE}{n_t - DoF} = \frac{1}{n_t - DoF} \times \sum_{i=1}^{n_t} (x_i - \mu_{mean})^2 \qquad 5.14$$

with sum-of-squares of deviations SCE= 0.0006641 , Degree of freedom (P, T) DoF=107, x_i value of the statistical series, μ_{mean} the mean value of the statistical series and the total number in the series n_t=390.

The resulted uncertainty of the emission energy is δE_g= 0.0015 eV.

The resulted uncertainty of the FWHM is $\delta FWHM$= 0.0011 eV.

5.3 Pressure and temperature sensitivities uncertainties

The emission energy (E_g) and the full width at half maximum (FWHM) dependence to the pressure (P) and temperature (T) are related as follows:

$$E_g(P,T) = E_{g0} + S_p P + S_T T \qquad FWHM(T) = FWHM_0 + S'_T T \qquad 5.15$$

where the pressure and temperature sensitivities are calculated as:

$$S_p = \frac{n_t \sum P\, E_g - \sum P \sum E_g}{\Lambda_p} \qquad S_T = \frac{n_t \sum T\, E_g - \sum T \sum E_g}{\Lambda_T}$$
$$S'_T = \frac{n_t \sum T\, FWHM - \sum T \sum FWHM}{\Lambda_T} \qquad 5.16$$

with

$$\Lambda_p = n_t \sum p^2 - \left(\sum P\right)^2 \qquad \Lambda_T = n_t \sum T^2 - \left(\sum T\right)^2$$

where n_t is the total number of data.

The resulted uncertainty of the pressure and temperature sensitivities can be expressed as:

$$\delta S_p = \delta E_g \sqrt{\frac{n_t}{\Lambda_p}} \qquad \delta S_T = \delta E_g \sqrt{\frac{n_t}{\Lambda_T}} \qquad \delta S'_T = \delta FWHM \sqrt{\frac{n_t}{\Lambda_T}} \tag{5.17}$$

5.4 Pressure and temperature uncertainties

5.4.1 High pressure cell

The uncertainty of the temperature corresponds to the magnitude obtained from multiple measurements under the same measurement conditions. it is estimated at 1K using the high-pressure cell. As regards to the pressure uncertainty, in literature, it is reported that uncertainty of the ruby (calibrated pressure sensors used in the static calibration) due to the influence of pressure is 30 MPa. In addition, the uncertainty of the ruby due to the influence of temperature is about 20 MPa/K. Therefore, as the temperature uncertainty is estimated at 1K, this results in an uncertainty of 50 MPa.

5.4.2 Elastohydrodynamic contact

From equation 5.15, the pressure uncertainty on the emission energy is estimated under elastohydrodynamic isothermal conditions as follows:

$$\frac{\delta P}{P} = \frac{\delta E_g}{E_g} + \frac{\delta S_p}{S_p} \tag{5.18}$$

the Temperature uncertainty on the emission energy can be expressed in non-isothermal conditions as follows:

$$\frac{\delta T}{T} = \frac{\delta E_g + P\delta S_p + S_p \delta P}{E_g - S_p P} + \frac{\delta S_T}{S_T} \tag{5.19}$$

5.5 Pearson VII and SplitPearson VII functions

Historically, the Pearson VII function is used for characterizing peak shapes from conventional X-ray powder diffraction patterns. It can be expressed as follows:

$$I(E) = \frac{I_{max}}{\left[1 + \left(\frac{\left(E - E_g\right)}{HWHM}\right)^2 \left(2^{\frac{1}{m_{Per}}} - 1\right)\right]^{m_{Pear}}} \qquad 5.20$$

where m_{Pear} is the peak shape parameter, I_{max} the maximum peak intensity, $HWHM$ the half width at half maximum ($HWHM = FWHM/2$), E_g is the central emission energy. Note that the shape parameter (m_{Pear}) handles different tail-shapes of a peak. Indeed, as shown in Figure 5-1, Pearson VII function approaches a:

- Lorentzian distribution as $m_{Pear} \rightarrow 1$
- Gaussian distribution as $m_{Pear} \rightarrow \infty$ (e.g. $m_{Pear} > 10$)

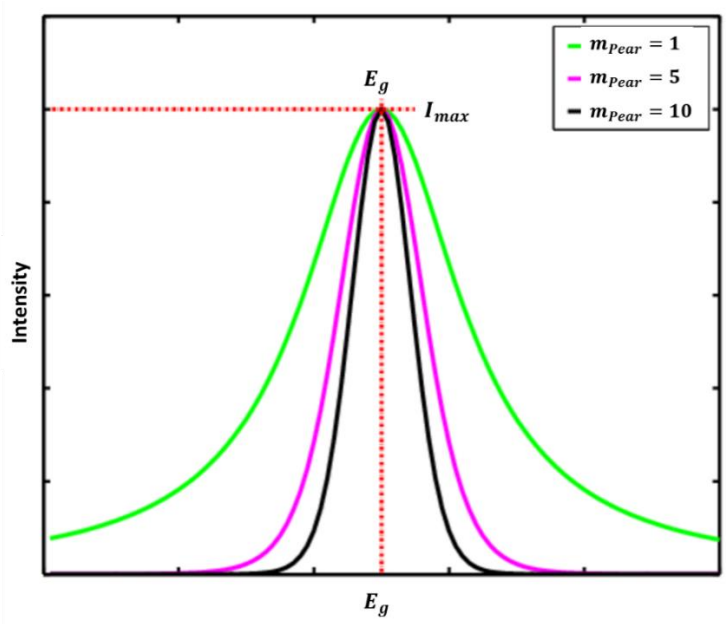

Figure 5-1: Pearson VII function versus shape parameter.

Regarding SplitPearson VII function, it results simply from merging two halves of Pearson VII distributions.it is defined as follows:

$$I(E) = \begin{cases} PearsonVII\left(E; E_g, I_{max}, HWHM1, m_{Pear}1\right) x \leq E_g \\ PearsonVII\left(E; E_g, I_{max}, HWHM2, , m_{Pear}2\right) x > E_g \end{cases} \qquad 5.21$$

The resulted Full width at half maximum is equal to $FWHM = HWHM1 + HWHM2$.

5.6 Determination of the laser spot size using cleaved silicon sample

Theoretical value: the theoretical value of the laser spot diameter (see Figure 5-2) can be calculated using the following formula:

$$d_{spot} = \frac{4 \times \lambda \times f}{\pi \times d_{beam}} \qquad 5.22$$

where the laser beam of wavelength λ=514.532 nm with an entrance diameter d_{beam} equal to 1mm by means of a focal length f=3.67 mm specific to the ×50 magnification objective used for our measurements. This results to a spot size d_{spot}=2.4 µm.

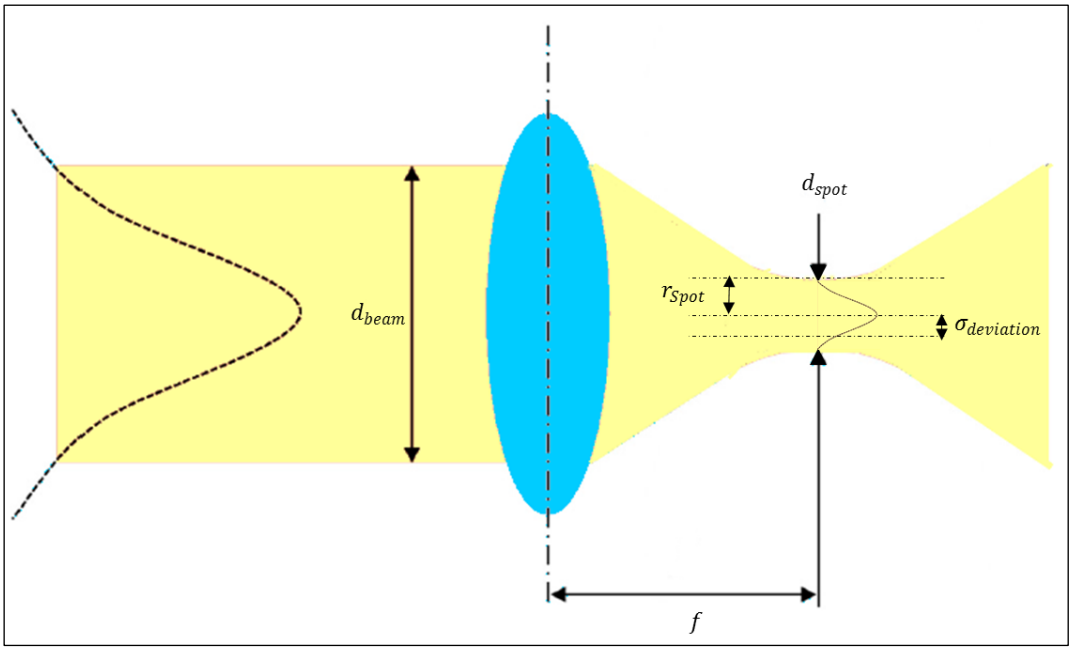

Figure 5-2: Propagation of the incident beam through focusing lens.

The theoretical diameter of the laser spot is generally lower than the realistic one, especially, for *in situ* measurements where the laser beam is focused (in the contact thin film) through a 10 mm thick transparent disk. In other words, the diameter of the focusing spot is widened when it passes through the objective lens, which generates longitudinal spherical aberration.A way to determine the effective value of the beam spot size is by performing the following silicon step experience.

Silicon step experience: in this experiment, a cleaved silicon sample is used as to produce a step. First, the laser beam is focused on the surface of the silicon by the ×50 objective long working distance used for *in situ* experiments. Then, the microscope is moved in the x-direction using a motorized table, so that the laser beam passes on both sides of the step (see Figure 5-3). While the spectrometer is centered on the Raman line of silicon at 520 cm^{-1}, the intensity of this line is measured as a function of the x position. Measurements are made every one to two micrometer.

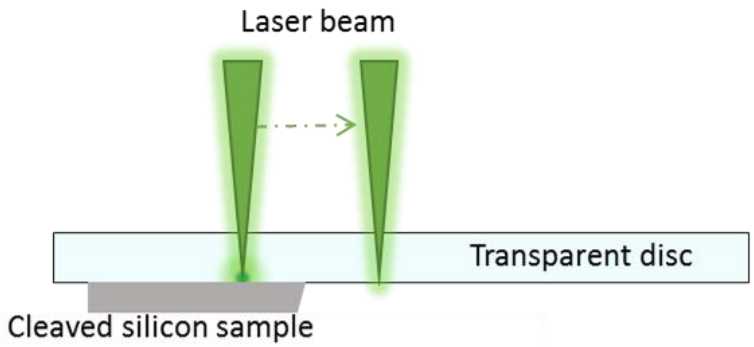

Figure 5-3: Scheme of the laser beam diameter experimental determination.

The intensity in a plane perpendicular to the direction of propagation of the laser beam, is assumed to follow a Gaussian variation law as a function of the distance r_{spot} (the radius of the beam spot) to the axis:

$$I(r_{beam}) = I_0 \times e^{\left(\frac{-r_{spot}^2}{2\sigma_{deviation}}\right)} \qquad 5.23$$

where $\sigma_{deviation}$ is the standard deviation, and here, r_{beam} corresponds to 2 $\sigma_{deviation}$,as shown in Figure 5-2.

The intensity of the signal emitted by the silicon is analyzed: the distance over which the measured intensity varies from 100% to 0% gives the spot diameter. The profile of the intensity decay (when passing over the silicon step) depends on the distribution of the light intensity inside the beam spot, which is not uniform. The decay can be expressed by a cumulative distribution function as follows:

$$\phi(x) = \frac{1}{2} \times \left[1 + erf\left(\frac{x - \mu_{decay}}{\sigma_{deviation}\sqrt{2}}\right)\right] \qquad 5.24$$

where x is the position and μ is the mean (center of the decay).

The results, shown in Figure 5-4, Figure 5-5 and Figure 5-6, indicate a probe size on the sample of (4 ± 2) μm in air, of (6 ± 2) μm with BK7 glass disk and of (8 ± 2) μm with the sapphire disk respectively. These values are fundamental for *in situ* experiments because they determine the spatial resolution of the measurements.

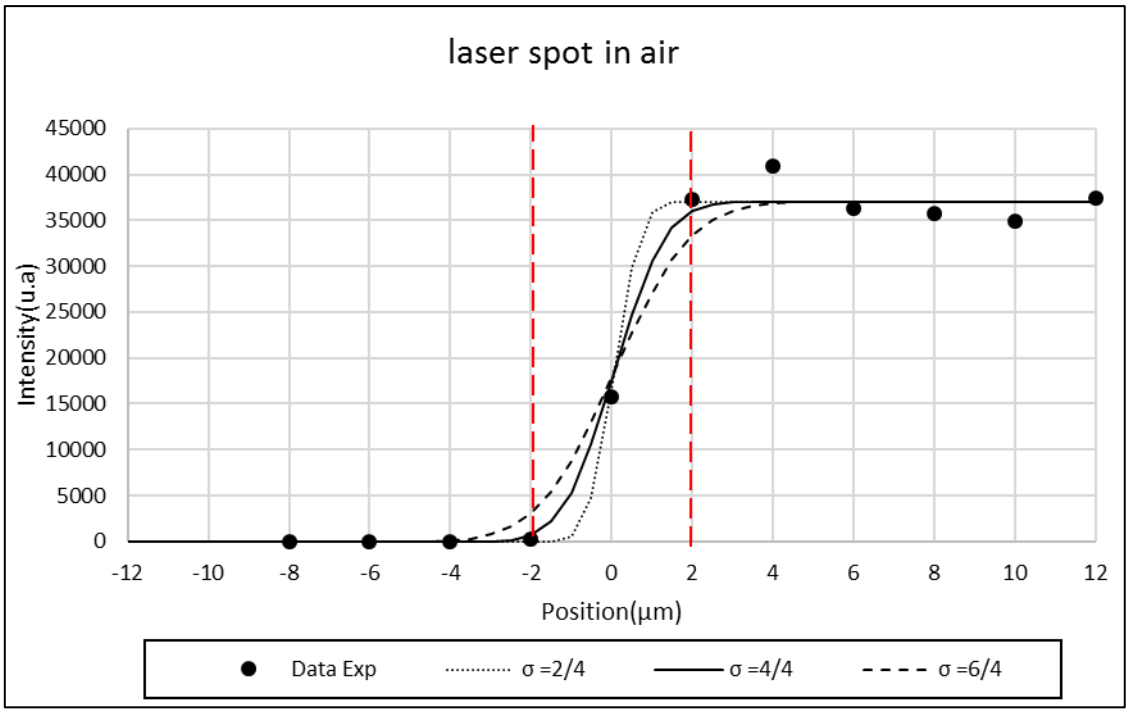

Figure 5-4: Laser spot size in air.

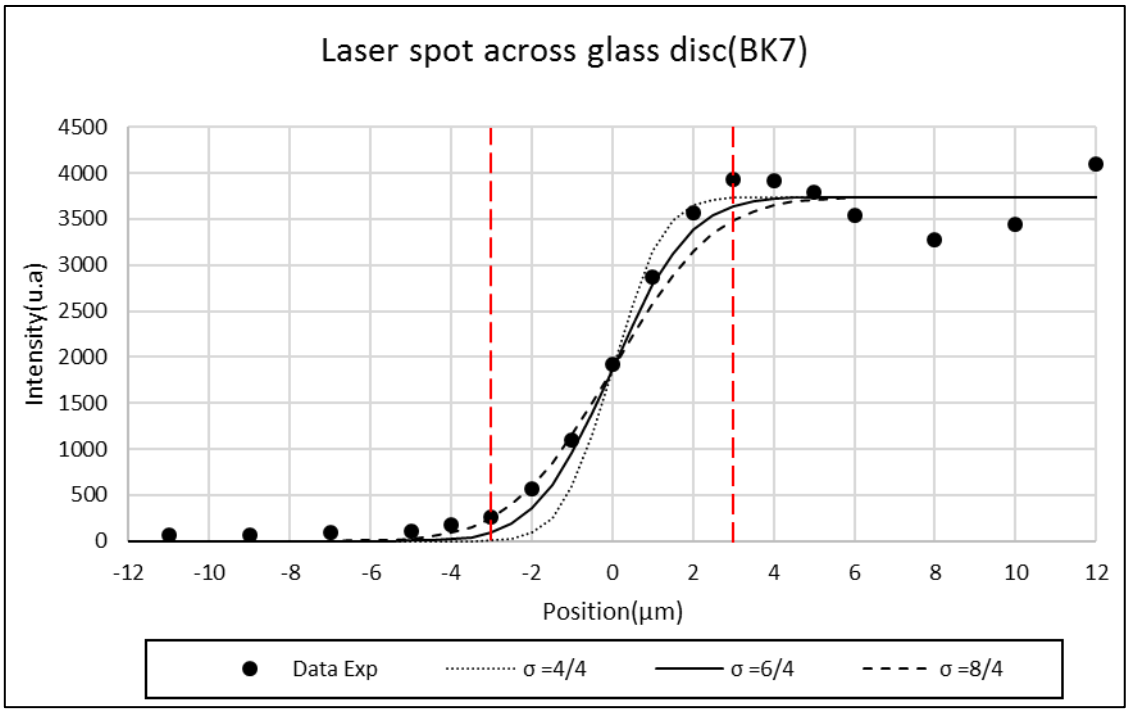

Figure 5-5: Laser spot size across the glass disc.

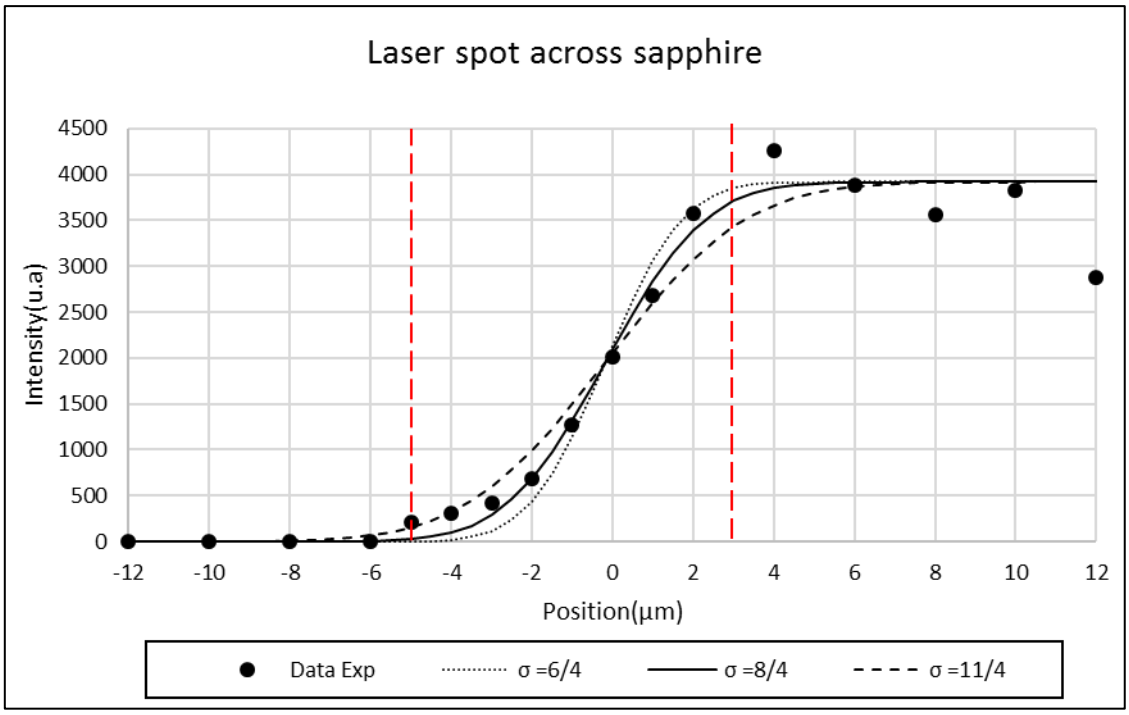

Figure 5-6: Laser spot size across the sapphire disc.

References

[1] H. A. Spikes, “Thin films in elastohydrodynamic lubrication: The contribution of experiment,” Proceedings of the Institution of Mechanical Engineers, Part J: Journal of Engineering Tribology, vol. 213, no. 5, pp. 335–352, May 1999, doi: 10.1243/1350650991542712.

[2] S. M. B. Albahrani, D. Philippon, P. Vergne, and J. Bluet, “A review of in situ methodologies for studying elastohydrodynamic lubrication,” Proceedings of the Institution of Mechanical Engineers, Part J: Journal of Engineering Tribology, vol. 230, no. 1, pp. 86–110, Jan. 2016, doi: 10.1177/1350650115590428.

[3] R. Kumar, M. S. Azam, S. K. Ghosh, and S. Yadav, “70 years of Elastohydrodynamic Lubrication (EHL): A Review on Experimental Techniques for Film Thickness and Pressure Measurement,” MAPAN, vol. 33, no. 4, pp. 481–491, Dec. 2018, doi: 10.1007/s12647-018-0277-1.

[4] I. Jubault, “Application de la microspectrometrie raman aux mesures in situ dans les contacts dynamiques. Contribution a l’etude du contact elastohydrodynamique.,” PHD thesis, l’Université des Antilles et de la Guyane, 2002.

[5] S. D. Rassat and E. J. Davis, “Temperature Measurement of Single Levitated Microparticles Using Stokes/Anti-Stokes Raman Intensity Ratios,” Appl Spectrosc, vol. 48, no. 12, pp. 1498–1505, Dec. 1994, doi: 10.1366/0003702944027921.

[6] I. Jubault, J. L. Mansot, P. Vergne, A. A. Lubrecht, and J. Molimard, “In situ pressure measurements in an elastohydrodynamically lubricated point contact using Raman microspectrometry. Comparison with numerical calculations,” in Tribology Series, vol. 41, Elsevier, 2003, pp. 663–673.

[7] H. A. Spikes, V. Anghel, and R. Glovnea, “Measurement of the Rheology of Lubricant Films Within Elastohydrodynamic Contacts,” Tribology Letters, vol. 17, no. 3, pp. 593–605, Oct. 2004, doi: 10.1023/B:TRIL.0000044509.82345.16.

[8] J. W. Kannel, J. C. Bell, and C. M. Allen, “Methods for Determining Pressure Distributions in Lubricated Rolling Contact,” A S L E Transactions, vol. 8, no. 3, pp. 250–270, Jan. 1965, doi: 10.1080/05698196508972099.

[9] H. S. Cheng and F. K. Orcutt, “Paper 13: A Correlation between the Theoretical and Experimental Results on the Elastohydrodynamic Lubrication of Rolling and Sliding Contacts,” Proceedings of the Institution of Mechanical Engineers, Conference Proceedings, vol. 180, no. 2, pp. 158–168, Jun. 1965, doi: 10.1243/PIME_CONF_1965_180_076_02.

[10] T. A. Dow, R. D. Stockwell, and J. W. Kannel, “Thermal Effects in Rolling/Sliding EHD Contacts: Part 1—Experimental Measurements of Surface Pressure and Temperature,” Journal of Tribology, vol. 109, no. 3, pp. 503–510, Jul. 1987, doi: 10.1115/1.3261486.

[11] M. O. A. Mokhtar and A. A. Abdel Ghany, “Elastohydrodynamic Behavior of Rolling Elliptical Contacts: Part I: Pressure and Temperature Distributions,” Journal of Tribology, vol. 107, no. 3, pp. 343–348, Jul. 1985, doi: 10.1115/1.3261071.

[12] E. Kagerer and M. E. Königer, “Ion beam sputter deposition of thin film sensors for applications in highly loaded contacts,” Thin Solid Films, vol. 182, no. 1–2, pp. 333–344, Dec. 1989, doi: 10.1016/0040-6090(89)90269-1.

[13] M. M. A. Safa, J. C. Anderson, and J. A. Leather, “Transducers for pressure, temperature and oil film thickness measurement in bearings,” Sensors and Actuators, vol. 3, pp. 119–128, Jan. 1982, doi: 10.1016/0250-6874(82)80013-9.

[14] M. Ebner, A. Ziegltrum, T. Lohner, K. Michaelis, and K. Stahl, “Measurement of EHL temperature by thin film sensors – Thermal insulation effects,” Tribology International, vol. 128, pp. 1–9, Dec. 2018, doi: 10.1016/j.triboint.2018.12.015.

[15] J. M. Reddecliff and R. Valori, “The Performance of a High-Speed Ball Thrust Bearing Using Silicon Nitride Balls,” Journal of Lubrication Technology, vol. 98, no. 4, p. 553, 1976, doi: 10.1115/1.3452925.

[16] R. Miner, “F117–PW–100 Hybrid Ball Bearing Ceramic Technology Insertion,” New York, NY, ASME Paper 95GT-390, 1995.

[17] V Paleu, D N Olaru, and Sp Cretu, “Power loss prediction for a hybrid rolling bearing,” Conference Paper, Gheorghe Asachi Technical University of Iasi, 2000.

[18] H. Aramaki, Y. Shoda, Y. Morishita, and T. Sawamoto, “The Performance of Ball Bearings With Silicon Nitride Ceramic Balls in High Speed Spindles for Machine Tools,” Journal of Tribology, vol. 110, no. 4, p. 693, 1988, doi: 10.1115/1.3261715.

[19] B. R. Jorgensen and Y. C. Shin, “Dynamics of Machine Tool Spindle/Bearing Systems Under Thermal Growth,” Journal of Tribology, vol. 119, no. 4, p. 875, 1997, doi: 10.1115/1.2833899.

[20] Y. Shoda, S. Ijuin, H. Aramaki, H. Yui, and K. Toma, “The Performance of a Hybrid Ceramic Ball Bearing Under High Speed Conditions with the Under-Race Lubrication Method,” Tribology Transactions, vol. 40, no. 4, pp. 676–684, Jan. 1997, doi: 10.1080/10402009708983708.

[21] H. M. Fan, Z. H. Ni, Y. P. Feng, X. F. Fan, J. L. Kuo, Z. X. Shen, and B. S. Zou, “High pressure photoluminescence and Raman investigations of CdSe⁄ZnS core/shell quantum dots,” Appl. Phys. Lett., vol. 90, no. 2, p. 021921, Jan. 2007, doi: 10.1063/1.2430772.

[22] D. Valerini, A. Cretí, M. Lomascolo, L. Manna, R. Cingolani, and M. Anni, “Temperature dependence of the photoluminescence properties of colloidal Cd Se ⁄ Zn S core/shell quantum dots embedded in a polystyrene matrix,” Physical Review B, vol. 71, no. 23, Jun. 2005, doi: 10.1103/PhysRevB.71.235409.

[23] M. Protière, N. Nerambourg, O. Renard, and P. Reiss, “Rational design of the gram-scale synthesis of nearly monodisperse semiconductor nanocrystals,” Nanoscale Research Letters, vol. 6, no. 1, p. 472, 2011, doi: 10.1186/1556-276X-6-472.

[24] S. M. B. Albahrani, “Photoluminescent CdSe/CdS/ZnS quantum dots for temperature and pressure sensing in elastohydrodynamic,” PHD thesis, INSA Lyon, 2016.

[25] S. Bair, O. Andersson, F. S. Qureshi, and M. M. Schirru, “New EHL Modeling Data for the Reference Liquids Squalane and Squalane Plus Polyisoprene,” Tribology Transactions, vol. 61, no. 2, pp. 247–255, Mar. 2018, doi: 10.1080/10402004.2017.1310339.

[26] W. Zhang, D. Dai, X. Chen, X. Guo, and J. Fan, “Red shift in the photoluminescence of colloidal carbon quantum dots induced by photon reabsorption,” Applied Physics Letters, vol. 104, no. 9, p. 091902, Mar. 2014, doi: 10.1063/1.4867487.

[27] W. Shan, W. Walukiewicz, J. W. Ager, K. M. Yu, J. Wu, and E. E. Haller, “Pressure dependence of the fundamental band-gap energy of CdSe,” Applied Physics Letters, vol. 84, no. 1, pp. 67–69, Jan. 2004, doi: 10.1063/1.1638879.

[28] J. R. Mei and V. Lemos, “Photoluminescence on CdSe and CdTe under hydrostatic pressure,” Solid State Communications, vol. 52, no. 9, pp. 785–788, Dec. 1984, doi: 10.1016/0038-1098(84)90005-X.

[29] B. Li, W. Liu, L. Yan, X. Zhu, Y. Yang, and Q. Yang, “Revealing mechanisms of PL properties at high and low temperature regimes in CdSe/ZnS core/shell quantum dots,” Journal of Applied Physics, vol. 124, no. 4, p. 044302, Jul. 2018, doi: 10.1063/1.5031056.

[30] A. San-Miguel, “Nanomaterials under high-pressure,” Chemical Society Reviews, vol. 35, no. 10, p. 876, 2006, doi: 10.1039/b517779k.

[31] J. Molimard, M. Querry, and P. Vergne, “New tools for the experimental study of EDH and limit lubrications,” Tribology Series, pp. 717–726, 01-Jan-1999.

[32] H. S. Cheng, “A Refined Solution to the Thermal-Elastohydrodynamic Lubrication of Rolling and Sliding Cylinders,” ASLE TRANSACTIONS, 1965, doi: 10.1080/05698196508972110.

[33] W. Habchi and P. Vergn--(1+x)^n=1+nx/1!+(n(n-1) x^2)/2!+⋯, “On the compressive heating/cooling mechanism in thermal elastohydrodynamic lubricated contacts,” Tribology International, vol. 88, pp. 143–152, Aug. 2015, doi: 10.1016/j.triboint.2015.03.025.

[34] M. Kaneta, P. Sperka, P. Yang, I. Krupka, P. Yang, and M. Hartl, “Thermal Elastohydrodynamic Lubrication of Ceramic Materials,” Tribology Transactions, vol. 61, no. 5, pp. 869–879, Sep. 2018, doi: 10.1080/10402004.2018.1437492.

[35] J. Lu, T. Reddyhoff, and D. Dini, “3D Measurements of Lubricant and Surface Temperatures Within an Elastohydrodynamic Contact,” Tribology Letters, vol. 66, no. 1, pp. 3–16, Mar. 2018, doi: 10.1007/s11249-017-0953-2.

[36] A. Jolkin and R. Larsson, “Film Thickness, Pressure Distribution and Traction in Sliding EHL Conjunctions,” Tribology and Interface Engineering Series, pp. 505–516, Dec-1999.

[37] I. Jubault, J. Molimard, A. A. Lubrecht, J. L. Mansot, and P. Vergne, “In Situ Pressure and Film Thickness Measurements in Rolling/Sliding Lubricated Point Contacts,” Tribology Letters, vol. 15, no. 4, pp. 421–429, Nov. 2003, doi: 10.1023/B:TRIL.0000003068.07650.2e.

[38] B. J. Hamrock, L. R. Center, O. S. U. R. Foundation, and U. S. N. A. and S. A. S. and T. I. Program, Fundamentals of fluid film lubrication. NASA Office of Management, Scientific and Technical Information Program, 1991.

[39] E. V. Zaretsky, Y. P. Chiu, and T. E. Tallian, “Ceramic bearings for use in gas turbine engines,” J. Mater. Eng., vol. 11, no. 3, pp. 237–253, Dec. 1989, doi: 10.1007/BF02834841.

[40] A. Sawaguchi, K. Toda, and K. Niihara, “Mechanical and Electrical Properties of Silicon Nitride-Silicon Carbide Nanocomposite Material,” Journal of the American Ceramic Society, vol. 74, no. 5, pp. 1142–1144, May 1991, doi: 10.1111/j.1151-2916.1991.tb04357.x.

[41] P. Cann and A. A. Lubrecht, “An analysis of the mechanisms of grease lubrication in rolling element bearings,” Lubrication Science, vol. 11, no. 3, pp. 227–245, May 1999, doi: 10.1002/ls.3010110303.

[42] G. Stachowiak and A. W. Batchelor, Engineering Tribology. Butterworth-Heinemann, 2013.

[43] S.-N. Ndiaye, L. Martinie, D. Philippon, N. Devaux, and P. Vergne, “A Quantitative Friction-Based Approach of the Limiting Shear Stress Pressure and Temperature Dependence,” Tribology Letters, vol. 65, no. 4, Dec. 2017, doi: 10.1007/s11249-017-0929-2.

[44] J.-D. Wheeler, “Non-Elliptical Point Contacts: the Torus-on-Plane Conjunction,” PHD Thesis, INSA Lyon, Lyon, France, 2016.

[45] D. Dowson and G. R. Higginson, “A Numerical Solution to the Elasto-Hydrodynamic Problem,” Journal of Mechanical Engineering Science, vol. 1, no. 1, pp. 6–15, Jun. 1959, doi: 10.1243/JMES_JOUR_1959_001_004_02.

[46] B. Najji, B. Bou-Said, and D. Berthe, “New Formulation for Lubrication With Non-Newtonian Fluids,” Journal of Tribology, vol. 111, no. 1, p. 29, 1989, doi: 10.1115/1.3261875.

[47] W. Habchi, “A Full-System Finite Element Approach to Elastohydrodynamic Lubrication Problems : Application to Ultra-Low-Viscosity Fluids,” PHD Thesis, INSA Lyon, 2008.

[48] Y. Peiran and W. Shizhu, “A Generalized Reynolds Equation for Non-Newtonian Thermal Elastohydrodynamic Lubrication,” J. Tribol, vol. 112, no. 4, pp. 631–636, Oct. 1990, doi: 10.1115/1.2920308.

[49] C. H. Venner and A. A. Lubrecht, “Revisiting film thickness in slender elasto-hydrodynamically lubricated contacts,” Proceedings of the Institution of Mechanical Engineers,

Part C: Journal of Mechanical Engineering Science, vol. 224, no. 12, pp. 2549–2558, Dec. 2010, doi: 10.1243/09544062JMES2316.

[50] A. Canzi, C. H. Venner, and A. A. Lubrecht, “Film thickness prediction in elastohydrodynamically lubricated elliptical contacts,” Proceedings of the Institution of Mechanical Engineers, Part J: Journal of Engineering Tribology, vol. 224, no. 9, pp. 917–923, Sep. 2010, doi: 10.1243/13506501JET717.

[51] R. Gohar and A. Cameron, “Optical Measurement of Oil Film Thickness under Elasto-hydrodynamic Lubrication,” Nature, vol. 200, no. 4905, p. 458, Nov. 1963, doi: 10.1038/200458b0.

[52] L. Gustafsson, E. Höglund, and O. Marklund, “Measuring Lubricant Film Thickness with Image Analysis,” Proceedings of the Institution of Mechanical Engineers, Part J: Journal of Engineering Tribology, vol. 208, no. 3, pp. 199–205, Sep. 1994, doi: 10.1243/PIME_PROC_1994_208_371_02.

[53] F. J. Westlake and A. Cameron, “Fluid Film Interferometry in Lubrication Studies,” Nature, vol. 214, no. 5088, pp. 633–634, May 1967, doi: 10.1038/214633a0.

[54] J.-D. Wheeler, P. Vergne, N. Fillot, and D. Philippon, “On the relevance of analytical film thickness EHD equations for isothermal point contacts: Qualitative or quantitative predictions?,” Friction, vol. 4, no. 4, pp. 369–379, Dec. 2016, doi: 10.1007/s40544-016-0133-7.

[55] D. J. Gardiner, E. M. Baird, C. Craggs, M. P. Dare-Edwards, and J. C. Bell, “Raman microspectroscopy of a working elastohydrodynamic contact,” Lubrication Science, vol. 1, no. 4, pp. 301–313, Jul. 1989, doi: 10.1002/ls.3010010402.

[56] E. J. Hutchinson, D. Shu, F. Laplant, and D. Ben-Amotz, “Measurement of Fluid Film Thickness on Curved Surfaces by Raman Spectroscopy,” Applied Spectroscopy, vol. 49, no. 9, pp. 1275–1278, Sep. 1995, doi: 10.1366/0003702953965371.

[57] I. Jubault, J. Molimard, A. A. Lubrecht, J. L. Mansot, and P. Vergne, “In Situ Pressure and Film Thickness Measurements in Rolling/Sliding Lubricated Point Contacts,” Tribology Letters, vol. 15, no. 4, pp. 421–429, Nov. 2003, doi: 10.1023/B:TRIL.0000003068.07650.2e.

[58] F. LaPlant, E. J. Hutchinson, and D. Ben-Amotz, “Raman Measurements of Localized Pressure Variations in Lubricants Above the Glass Transition Pressure,” J. Tribol, vol. 119, no. 4, pp. 817–822, Oct. 1997, doi: 10.1115/1.2833891.

[59] V. K. Ausherman, H. S. Nagaraj, Sanborn, D.M., and W. O. Winer, “Infrared Temperature Mapping in Eiastohydrodynamic Lubrication,” Journal of Lubrication Technology, p. 7, 1976.

[60] V. Turchina, D. M. Sanborn, and W. O. Winer, “Temperature Measurements in Sliding Elastohydrodynamic Point Contacts,” J. of Lubrication Tech, vol. 96, no. 3, pp. 464–469, Jul. 1974, doi: 10.1115/1.3452005.

[61] T. Reddyhoff, H. A. Spikes, and A. V. Olver, “Compression Heating and Cooling in Elastohydrodynamic Contacts,” Tribol Lett, vol. 36, no. 1, pp. 69–80, Oct. 2009, doi: 10.1007/s11249-009-9461-3.

[62] J. Lu, T. Reddyhoff, and D. Dini, “3D Measurements of Lubricant and Surface Temperatures Within an Elastohydrodynamic Contact,” Tribology Letters, vol. 66, no. 1, Mar. 2018, doi: 10.1007/s11249-017-0953-2.

[63] G. E. Morales-Espejel and A. Gabelli, “Application of a rolling bearing life model with surface and subsurface survival to hybrid bearing cases,” Proceedings of the Institution of Mechanical Engineers, Part C: Journal of Mechanical Engineering Science, vol. 233, no. 15, pp. 5491–5498, Aug. 2019, doi: 10.1177/0954406219848470.

[64] A. A. Wereszczak, W. Wang, Y. Wang, M. Hadfield, W. Kanematsu, T. P. Kirkland and O. M. Jadaan, “Rolling Contact Fatigue of Ceramics,” Oak Ridge National Laboratory, Oak Ridge, TN, USA, ASME Paper, 2006.

[65] T. Gkinis, R. Rahmani, H. Rahnejat, and M. O’Mahony, “Heat generation and transfer in automotive dry clutch engagement,” Journal of Zhejiang University-SCIENCE A, vol. 19, no. 3, pp. 175–188, Mar. 2018, doi: 10.1631/jzus.A1700481.

[66] K. Yan, B. Yan, B. Q. Li, and J. Hong, “Investigation of bearing inner ring-cage thermal characteristics based on CdTe quantum dots fluorescence thermometry,” Applied Thermal Engineering, vol. 114, pp. 279–286, Mar. 2017, doi: 10.1016/j.applthermaleng.2016.11.205.

[67] W. Habchi, D. Eyheramendy, P. Vergne, and G. Morales-Espejel, “A Full-System Approach of the Elastohydrodynamic Line/Point Contact Problem,” J. Tribol, vol. 130, no. 2, p. 021501, Apr. 2008, doi: 10.1115/1.2842246.

[68] S. M. B. Albahrani, T. Seoudi, D. Philippon, L. Lafarge, P. Reiss, H. Hajjaji, G. Guillot, M. Querry, J.-M. Bluet, and P. Vergne, “Quantum dots to probe temperature and pressure in highly confined liquids,” RSC Advances, vol. 8, no. 41, pp. 22897–22908, 2018.

[69] A. S. Stodolna,A. Rouzée, F. Lépine, S. Cohen, F. Robicheaux,A. Gijsbertsen, J. H. Jungmann, C. Bordas, and M. J. J. Vrakking, “Hydrogen Atoms under Magnification: Direct Observation of the Nodal Structure of Stark States,” Physical Review Letters, vol. 110, no. 21, May 2013, doi: 10.1103/PhysRevLett.110.213001.

[70] B. Streetman and S. Banerjee, Solid State Electronic Devices. Pearson Education, 2014.

[71] “Semiconductors,” Mapping Ignorance, 25-Feb-2016. [Online]. Available: https://mappingignorance.org/2016/02/25/semiconductors/. [Accessed: 05-Aug-2019].

[72] R. Koole, E. Groeneveld, D. Vanmaekelbergh, A. Meijerink, and C. de Mello Donegá, “Size Effects on Semiconductor Nanoparticles,” in Nanoparticles: Workhorses of Nanoscience, C. de Mello Donegá, Ed. Berlin, Heidelberg: Springer, 2014, pp. 13–51.

[73] D. A. Neamen, Semiconductor physics and devices: basic principles, 3rd ed. Boston: McGraw-Hill, 2003.

[74] “CdSe Quantum Dots - Michael C. Hughes.” [Online]. Available: http://web.michaelchughes.com/projects/cdse-quantum-dots. [Accessed: 29-May-2019].

[75] A. M. Smith and S. Nie, “Semiconductor Nanocrystals: Structure, Properties, and Band Gap Engineering,” Accounts of Chemical Research, vol. 43, no. 2, pp. 190–200, Feb. 2010, doi: 10.1021/ar9001069.

[76] A. P. Alivisatos, “Semiconductor Clusters, Nanocrystals, and Quantum Dots,” Science, N ew Series, vol. 271, no. 5251, 1996.

[77] M. Chamarro, C. Gourdon, P. Lavallard, O. Lublinskaya, and A. I. Ekimov, “Enhancement of electron-hole exchange interaction in CdSe nanocrystals: A quantum confinement effect,” Phys. Rev. B, vol. 53, no. 3, pp. 1336–1342, Jan. 1996, doi: 10.1103/PhysRevB.53.1336.

[78] M. Thambidurai, N. Muthukumarasamy, S. Agilan, N. Murugan, S. Vasantha, R. Balasundaraprabhu and T. S. Senthil, “Strong quantum confinement effect in nanocrystalline CdS,” J Mater Sci, vol. 45, no. 12, pp. 3254–3258, Jun. 2010, doi: 10.1007/s10853-010-4333-7.

[79] H. Tang, G. Xu, L. Weng, L. Pan, and L. Wang, “Luminescence and photophysical properties of colloidal ZnS nanoparticles,” Acta Materialia, vol. 52, no. 6, pp. 1489–1494, Apr. 2004, doi: 10.1016/j.actamat.2003.11.030.

[80] D. U. Lee, D. H. Kim, D. H. Choi, S. W. Kim, H. S. Lee,K-H Yoo, and T. W. Kim, “Microstructural and optical properties of CdSe/CdS/ZnS core-shell-shell quantum dots,” Optics Express, vol. 24, no. 2, p. A350, Jan. 2016, doi: 10.1364/OE.24.00A350.

[81] P. Reiss, S. Carayon, J. Bleuse, and A. Pron, “Low polydispersity core/shell nanocrystals of CdSe/ZnSe and CdSe/ZnSe/ZnS type: preparation and optical studies,” Synthetic Metals, vol. 139, no. 3, pp. 649–652, Oct. 2003, doi: 10.1016/S0379-6779(03)00335-7.

[82] Y. P. Varshni, “Temperature dependence of the energy gap in semiconductors,” Physica, vol. 34, no. 1, pp. 149–154, Jan. 1967, doi: 10.1016/0031-8914(67)90062-6.

[83] C.-F. Wang, F. Fan, R. P. Sabatini, O. Voznyy, K.Bicanic, X. Li, D. P. Sellan, M. Saravanapavanantham, N. Hossain, K. Chen, S. Hoogland,and E. H. Sargent, “Quantum Dot Color-Converting Solids Operating Efficiently in the kW/cm2 Regime,” Chem. Mater., vol. 29, no. 12, pp. 5104–5112, Jun. 2017, doi: 10.1021/acs.chemmater.7b00164.

[84] E. V. Lutsenko, A. G. Voinilovich, N. V. Rzheutskii, V. N. Pavlovskii, G. P. Yablonskii, S. V. Sorokin, S. V. Gronin, I. V. Sedova, P. S. Kop’ev, S. V. Ivanov, “Optically pumped quantum-dot Cd(Zn)Se/ZnSe laser and microchip converter for yellow—green spectral region,” Quantum Electron., vol. 43, no. 5, p. 418, 2013, doi: 10.1070/QE2013v043n05ABEH015164.

[85] O. V. Chashchikhin and M. F. Budyka, “Photoactivation, photobleaching and photoetching of CdS quantum dots − Role of oxygen and solvent,” Journal of Photochemistry and Photobiology A: Chemistry, vol. 343, pp. 72–76, Jun. 2017, doi: 10.1016/j.jphotochem.2017.04.028.

[86] S. Klotz, J.-C. Chervin, P. Munsch, and G. Le Marchand, “Hydrostatic limits of 11 pressure transmitting media,” Journal of Physics D: Applied Physics, vol. 42, no. 7, p. 075413, Apr. 2009, doi: 10.1088/0022-3727/42/7/075413.

[87] B. Håkansson, P. Andersson, and G. Bäckström, “Improved hot-wire procedure for thermophysical measurements under pressure,” Review of Scientific Instruments, vol. 59, no. 10, p. 2269, Jun. 1998, doi: 10.1063/1.1139946.

[88] P. M. Oger, I. Daniel, and A. Picard, “Development of a low-pressure diamond anvil cell and analytical tools to monitor microbial activities in situ under controlled P and T,” Biochimica et Biophysica Acta (BBA) - Proteins and Proteomics, vol. 1764, no. 3, pp. 434–442, Mar. 2006, doi: 10.1016/j.bbapap.2005.11.009.

[89] M. Lunz, A. L. Bradley, W.-Y. Chen, V. A. Gerard, S. J. Byrne, Y. K. Gun’ko, V. Lesnyak, and Nikolai Gaponik, “Influence of quantum dot concentration on Förster resonant energy transfer in monodispersed nanocrystal quantum dot monolayers,” Phys. Rev. B, vol. 81, no. 20, p. 205316, May 2010, doi: 10.1103/PhysRevB.81.205316.

[90] “Olympus Microscope components Guide. [Online]: http://earth2geologists.net/Microscopes/Olympus_documents/Components_brochure_Aug2005.pdf [Accessed: 07-Dec-2019].” .

[91] J. D. Brewer, B. T. Jeffries, and G. P. Summers, “Low-temperature fluorescence in sapphire,” Physical Review B, vol. 22, no. 10, pp. 4900–4906, Nov. 1980, doi: 10.1103/PhysRevB.22.4900.

[92] Q. Ma and D. R. Clarke, “Optical fluorescence from chromium ions in sapphire: A probe of the image stress,” Acta Metallurgica et Materialia, vol. 41, no. 6, pp. 1811–1816, Jun. 1993, doi: 10.1016/0956-7151(93)90201-3.

[93] W. G. J. H. M. van Sark, P. L. T. M. Frederix, D. J. Van den Heuvel, H. C. Gerritsen, A. A. Bol, J. N. J. van Lingen, C. de Mello Donegá, and A. Meijerink, “Photooxidation and Photobleaching of Single CdSe/ZnS Quantum Dots Probed by Room-Temperature Time-Resolved Spectroscopy,” The Journal of Physical Chemistry B, vol. 105, no. 35, pp. 8281–8284, Sep. 2001, doi: 10.1021/jp012018h.

[94] A. Narayanaswamy, L. F. Feiner, A. Meijerink, and P. J. van der Zaag, “The Effect of Temperature and Dot Size on the Spectral Properties of Colloidal InP/ZnS Core−Shell Quantum Dots,” ACS Nano, vol. 3, no. 9, pp. 2539–2546, Sep. 2009, doi: 10.1021/nn9004507.

[95] Chittenden R. J., Dowson D., Dunn J. F., and Taylor C. M., “A theoretical analysis of the isothermal elastohydrodynamic lubrication of concentrated contacts. II. General case, with

lubricant entrainment along either principal axis of the Hertzian contact ellipse or at some intermediate angle," Proceedings of the Royal Society of London. A. Mathematical and Physical Sciences, vol. 397, no. 1813, pp. 271–294, Feb. 1985, doi: 10.1098/rspa.1985.0015.

[96] H. van Leeuwen, "The determination of the pressure–viscosity coefficient of a lubricant through an accurate film thickness formula and accurate film thickness measurements. Part 2: high L values," Proceedings of the Institution of Mechanical Engineers, Part J: Journal of Engineering Tribology, vol. 225, no. 6, pp. 449–464, Jun. 2011, doi: 10.1177/1350650111398405.

[97] S. Bair, C. Mary, N. Bouscharain, and P. Vergne, "An improved Yasutomi correlation for viscosity at high pressure," Proceedings of the Institution of Mechanical Engineers, Part J: Journal of Engineering Tribology, vol. 227, no. 9, pp. 1056–1060, Sep. 2013, doi: 10.1177/1350650112474394.

[98] H. Moes, "Optimum similarity analysis with applications to elastohydrodynamic lubrication," Wear, vol. 159, no. 1, pp. 57–66, Nov. 1992, doi: 10.1016/0043-1648(92)90286-H.

[99] G. Nijenbanning, C. H. Venner, and H. Moes, "Film thickness in elastohydrodynamically lubricated elliptic contacts," Wear, vol. 176, no. 2, pp. 217–229, Aug. 1994, doi: 10.1016/0043-1648(94)90150-3.

[100] I. Jubault, J. L. Mansot, P. Vergne, A. A. Lubrecht, and J. Molimard, "In situ pressure measurements in an elastohydrodynamically lubricated point contact using Raman microspectrometry. Comparison with numerical calculations," in Tribology Series, vol. 41, D. Dowson, M. Priest, G. Dalmaz, and A. A. Lubrecht, Eds. Elsevier, 2003, pp. 663–673.

[101] V. Brizmer, H. R. Pasaribu, and G. E. Morales-Espejel, "Prediction of Micropitting Performance of Oil/Additive Solutions in Rolling and Sliding Contacts," presented at the 5th World Tribology Congress, WTC 2013, 2013, vol. 3.

[102] T. Reddyhoff, H. A. Spikes, and A. V. Olver, "Improved infrared temperature mapping of elastohydrodynamic contacts," Proceedings of the Institution of Mechanical Engineers, Part J: Journal of Engineering Tribology, vol. 223, no. 8, pp. 1165–1177, Aug. 2009, doi: 10.1243/13506501JET499.

[103] J. L. Lauer and M. E. Peterkin, "Infrared Emission Spectra of Elastohydrodynamic Contacts," J. of Lubrication Tech, vol. 98, no. 2, pp. 230–235, Apr. 1976, doi: 10.1115/1.3452805.

[104] P. M. Cann and H. A. Spikes, "In Lubro Studies of Lubricants in EHD Contacts Using FTIR Absorption Spectroscopy," Tribology Transactions, vol. 34, no. Issue 2, pp. 246–258, 1991, doi: 10.1080/10402009108982033.

[105] S. Miyata, B.-R. Höhn, K. Michaelis, and O. Kreil, “Experimental investigation of temperature rise in elliptical EHL contacts,” Tribology International, vol. 41, no. 11, pp. 1074–1082, Nov. 2008, doi: 10.1016/j.triboint.2008.01.006.

[106] T. Doki-Thonon, N. Fillot, G. E. Morales Espejel, M. Querry, D. Philippon, N. Devaux, and P. Vergne, “A Dual Experimental/Numerical Approach for Film Thickness Analysis in TEHL Spinning Skewing Circular Contacts,” Tribol Lett, vol. 50, no. 1, pp. 115–126, Apr. 2013, doi: 10.1007/s11249-013-0122-1.

[107] S. Bair, “Reference liquids for quantitative elastohydrodynamics: selection and rheological characterization,” Tribol Lett, vol. 22, no. 2, pp. 197–206, May 2006, doi: 10.1007/s11249-006-9083-y.

[108] S. Bair, C. McCabe, and P. T. Cummings, “Comparison of Nonequilibrium Molecular Dynamics with Experimental Measurements in the Nonlinear Shear-Thinning Regime,” Phys. Rev. Lett., vol. 88, no. 5, p. 058302, Jan. 2002, doi: 10.1103/PhysRevLett.88.058302.

[109] M. Björling, W. Habchi, S. Bair, R. Larsson, and P. Marklund, “Towards the true prediction of EHL friction,” Tribology International, vol. 66, pp. 19–26, Oct. 2013, doi: 10.1016/j.triboint.2013.04.008.

[110] B. Håkansson, P. Andersson, and G. Bäckström, “Improved hot-wire procedure for thermophysical measurements under pressure,” Review of Scientific Instruments, vol. 59, no. 10, pp. 2269–2275, Oct. 1988, doi: 10.1063/1.1139946.

[111] P. Yang, S. Qu, Q. Chang, and F. Guo, “On the Theory of Thermal Elastohydrodynamic Lubrication at High Slide-Roll Ratios—Line Contact Solution,” J. Tribol, vol. 123, no. 1, pp. 36–41, Jan. 2001, doi: 10.1115/1.1330738.

[112] W. Habchi, D. Eyheramendy, S. Bair, P. Vergne, and G. Morales-Espejel, “Thermal Elastohydrodynamic Lubrication of Point Contacts Using a Newtonian/Generalized Newtonian Lubricant,” Tribol Lett, vol. 30, no. 1, p. 41, Mar. 2008, doi: 10.1007/s11249-008-9310-9.

Publications and conferences

Publication:

‘’Quantum dots to probe temperature and pressure in highly confined liquids” RSC Adv., vol. 8, no. 41, pp. 22897–22908, 2018. S. M. B. Albahrani, T. Seoudi, D. Philippon, L. Lafarge, P. Reiss, H. Hajjaji, G. Guillot, M. Querry, J.-M. Bluet, and P. Vergne,

Poster:

- T. Seoudi, D. Philippon, S.M.B. Albahrani, P. Reiss, H.Diaf , A.San-Miguel, J.-M. Bluet and P. Vergne “Local mapping of temperature and pressure throughout the EHD contacts” TRIBOUK- London,UK, 27-28/04/2017.

Oral presentation:

- T. Seoudi, D. Philippon, S.M.B. Albahrani, P. Reiss, H.Diaf , A.San-Miguel, J.-M. Bluet and P. Vergne “Towards a local mapping of Temperature and Pressure in Elastohydrodynamic contacts”6th World Tribology Congress WTC-Pékin, Chine, 17-22/09/2017.

- T. Seoudi, D. Philippon, S.M.B. Albahrani, P. Reiss, H.Diaf , A.San-Miguel. and P. Vergne “Local Measurement of Temperature and Pressure in Elastohydrodynamic Contacts” LEEDS-LYON 45th,Leeds, UK, 1-4 /09/2018.

- T. Seoudi, D. Philippon, N. Fillot, S.M.B. Albahrani, P. Reiss, A.Mondelin, Y. Maheo and P. Vergne “A novel non-intrusive in situ technique for mapping temperature and pressure throughout lubricated contacts” Tribology Frontiers Conference, Chicago, USA, 28-31/10/2018.

FOLIO ADMINISTRATIF

THESE DE L'UNIVERSITE DE LYON OPEREE AU SEIN DE L'INSA LYON

NOM : SEOUDI DATE de SOUTENANCE : 20/02/2020

Prénom : Tarek

TITRE : Non-intrusive CdSe-based quantum dots for sensing pressure and temperature in lubricated contacts

NATURE : Doctorat Numéro d'ordre : 2020LYSEI009

Ecole doctorale : Mécanique, Energétique, Génie Civil, Acoustique

Spécialité : Mécanique

RESUME :
Cette thèse est dédiée à la mesure des pressions et des températures locales et à la comparaison de la génération de chaleur dans les contacts élastohydrodynamiques (EHD) de type tout acier et hybride (nitrure de silicium-acier). Le but ultime de ce travail est de développer une nouvelle technique in situ non-intrusive, exploitant la sensibilité de la photoluminescence (PL) des boîtes quantiques (QDs) de CdSe/CdS/ZnS aux variations de pression et température, afin de cartographier ces deux paramètres dans les contacts EHD. Dispersible à faible concentration dans les lubrifiants, il est montré que les QDs ne modifient pas le comportement rhéologique du fluide porteur et que le cisaillement n'est pas perturbateur à la réponse en PL. La calibration des QDs en suspension confirme la dépendance de la réponse en PL des QDs à la pression et à la température. Les mesures in situ sont effectuées en utilisant un banc d'essai bille-disque. La comparaison entre les mesures in situ de pression et de température et celles prédites à l'aide d'un modèle éléments finis TEHD interne montre une bonne concordance, ce qui démontre la faisabilité de la méthodologie proposée. Les effets du glissement et du chargement normal sur la pression, la température et la chaleur générée sont reportés. L'effet des propriétés thermiques des solides est souligné et la répartition de la chaleur générée entre les solides en contact est étudiée. L'équilibre énergétique entre l'énergie mécanique et l'énergie thermique interne générée par compression et cisaillement est démontré en comparant les pertes de puissance expérimentales et la chaleur générée issue du modèle numérique, pour des contacts acier-acier et hybrides.

MOTS-CLÉS : Lubrification élastohydrodynamique, contacts hybrides, mesure *in situ*, photoluminescence, boîtes quantiques, mesure de pression et température, pertes de puissances et génération de chaleur

Laboratoire (s) de recherche : Laboratoire de Mécanique des Contacts et des Structures

Directeur de thèse : Philippe Vergne et David Philippon

Président de jury : Prof. Robert DWYER-JOYCE

Composition du jury :

Prof. Robert DWYER-JOYCE (Examinateur)
Prof. Martin HARTL (Rapporteur)
Prof. Alfonso SAN-MIGUEL (Examinateur)
Dr. Janet WONG (Rapporteur)
Dr. David PHILIPPON (Co-Directeur)
Dr. Philippe VERGNE (Directeur)